Systems Integration for Biosensing: Design, Fabrication, and Packaging of Microelectronics, Sensors, and Microfluidics

by

David Welch

A Dissertation Presented in Partial Fulfillment
of the Requirements for the Degree
Doctor of Philosophy

Approved November 2012 by the
Graduate Supervisory Committee:

Jennifer Blain Christen, Chair
Jitendran Muthuswamy
David Frakes
Jeffrey LaBelle
Michael Goryll

ARIZONA STATE UNIVERSITY

December 2012

ABSTRACT

Over the past fifty years, the development of sensors for biological applications has increased dramatically. This rapid growth can be attributed in part to the reduction in feature size, which the electronics industry has pioneered over the same period. The decrease in feature size has led to the production of microscale sensors that are used for sensing applications, ranging from whole-body monitoring down to molecular sensing.

Unfortunately, sensors are often developed without regard to how they will be integrated into biological systems. The complexities of integration are underappreciated. Integration involves more than simply making electrical connections. Interfacing microscale sensors with biological environments requires numerous considerations with respect to the creation of compatible packaging, the management of biological reagents, and the act of combining technologies with different dimensions and material properties.

Recent advances in microfluidics, especially the proliferation of soft lithography manufacturing methods, have established the groundwork for creating systems that may solve many of the problems inherent to sensor-fluidic interaction. The adaptation of microelectronics manufacturing methods, such as Complementary Metal-Oxide-Semiconductor (CMOS) and Microelectromechanical Systems (MEMS) processes, allows the creation of a complete biological sensing system with integrated sensors and readout circuits. Combining these technologies is an obstacle to forming complete sensor systems.

This dissertation presents new approaches for the design, fabrication, and integration of microscale sensors and microelectronics with microfluidics. The work addresses specific challenges, such as combining commercial manufacturing processes into biological systems and developing microscale sensors in these processes. This

work is exemplified through a feedback-controlled microfluidic pH system to demonstrate the integration capabilities of microscale sensors for autonomous microenvironment control.

ACKNOWLEDGEMENTS

My time at Arizona State University has been filled with learning, maturing, and, as is usual for a graduate student, countless hours of frustration. Reflecting back, I realize that numerous individuals have aided me in both completing this dissertation and overcoming all of the challenges that accompany it. I will do my best to thank them all here.

First, I could not have completed this work without the guidance, support, and friendship of my mentor, Dr. Jennifer Blain Christen. She has been both a great teacher and a great role model. It has truly been an honor to receive my graduate education with her as my advisor.

The joy in my life throughout this journey has been Alyson Vivattanapa. Her love, strength, and encouragement have enabled me to accomplish what I never thought possible. I would also like to thank Sumi for all the happiness she brings to both Alyson and me.

My parents, John and Annette, have given me constant love and support throughout my entire life. I am forever grateful.

Thanks also to Alyson's parents, Vorapote and Wantana, for their encouragement and kindness.

The members of my committee have been helpful throughout my dissertation work. Dr. Jitendran Muthuswamy deserves thanks for serving as a co-chair when my committee was first formed. Thanks to Dr. David Frakes for remaining on my committee ever since my comprehensive exam and for providing excellent comments. A special thanks to Dr. Jeffrey LaBelle for his continued advice ever since I first arrived at ASU. Many thanks to Dr. Michael Goryll, who has been an invaluable resource

throughout my research endeavors. His knowledge and willingness to discuss ideas has been a great help.

A number of ASU staff members have provided assistance through my work. Evie Selberg has been extremely helpful with every administrative task, and I appreciate her patience with my numerous purchases. The CSSER staff have also been very helpful, especially Dr. Stefan Myhajlenko, Carrie Sinclair, Jon Martin, and Todd Eller. Many thanks to James Laux for his excellent support with everything related to Cadence and design submission.

Finally, I would like to thank Dr. Stephen Johnston, Dr. Neal Woodbury, and Maria Hanlin for all of their work with the Biodesign Institute Graduate Program. The Biodesign program provided me with initial support during my studies at ASU and helped to match me with Dr. Blain Christen for the completion of my Ph.D.

TABLE OF CONTENTS

LIST OF TABLES

LIST OF FIGURES

Figure Page

Figure Page

Chapter 1

INTRODUCTION

Biological sensing technology has seen tremendous advancements since Leland C. Clark Jr. introduced the electronic glucose sensor 50 years ago. Since his presentation on electrochemical glucose monitoring, sensors for biological applications have become ubiquitous in our daily lives. The extensive usage of biological sensors is mainly due to the development of sensors which are smaller, more accurate, more sensitive, and more reliable. These advancements are largely due to the rise of the microelectronics industry. The advancements in microelectronics have natural parallels to the needs of biological sensing. Smaller feature sizes allow sensors that are better matched to the sizes of the biological features they are measuring. The heavily controlled manufacturing procedures for electronics also coincide with the desire for highly reliable and reproducible biological sensors. The batch processing and high yield manufacturing practices significantly reduce the per device cost of sensor production. Additionally, the advancements in microelectronic circuit technology have increased the signal readout and processing capabilities of new biological sensors. The field of biological sensors continues to grow thanks to these advances and shows no sign of slowing. However, many of the advancements in biological sensing technology have been developed without regard to their use within an actual sensing system. Sensing systems can become so burdensome, either by increasing size or decreasing accuracy, sensitivity, or reliability, that many of the original advantages of the new sensors alone are completely lost. To fully harness all of the advancements of the past 50 years, biological sensor development needs to be approached on a systems level as well as the sensor level.

System integration is challenging for a variety of reasons. The first is the size of the sensors. Sensors can now be on the order of nanometers, but they still require interfacing with larger components to be effectively used anywhere other than the ideal

laboratory setting. Difficulties arise when making connections to read a signal. Managing analyte interaction with miniature sensors is also a problem.

Another issue with new sensors is working with the signals they produce. Small sensors often produce small signals. Getting as much information as possible out of a signal often requires filtering, amplifying, and computational processing. Microelectronics are well-suited for all of these tasks. However, interfacing electronics with sensors is not straightforward. Care has to be taken to ensure the electronics do not interfere with the sensor or analyte and vice versa. For the best results, sensors should be located as close to possible to the readout circuits associated with them. Bringing components together reduces noise therefore making the sensor more effective. Many challenges arise from combining different technology effectively.

Additional problems emerge for continuous monitoring applications. Some biological sensors, such as glucose monitors and pregnancy tests, are designed with single use components. Systems that perform multiple time-point measurements offer more information than single-use sensors. The additional time dependent data provides means for the analysis and prediction of the response to change within a biological system. However, additional information requires more complex signal conditioning and processing.

The sensor environment is also important. The sensors should be protected from outside disturbances, and care should be taken to ensure that the sensor is actually making the desired measurement. Microscale and nanoscale sensors naturally lend themselves to placement in a microscale environment for effective control. The most common way to create a microscale biological environment is through a microfluidic device. Microfluidics offer unprecedented control over microscale reactions and are becoming increasingly popular in biological technology. Effectively placing sensors

within microfluidics is not easy and presents many challenges in both packaging and fabrication.

This dissertation presents new methods for creating sensor systems. Intricacies in the design, fabrication, and packaging of sensor systems are discussed as a complete problem. Solutions for combining microelectronic circuits, microscale sensors, and microfluidics are also presented.

The work presented here is organized on the sensing scale of the system discussed. Chapters 4 and 5 present systems for whole-body level sensing. These chapters show the ability of adapting commercial microelectronics processes for sensing applications while still maintaining a small size. Chapters 6 and 7 detail work on cellular level sensing applications. The systems sense cellular impedance or cellular electrical activity to demonstrate interfacing capabilities and integrated processing. Chapters 8, 9, and 10 discuss the ion sensitive field effect transistor as a pH sensor for molecular level sensing. Device characteristics are examined and a system to mitigate drift is presented. A complete feedback controlled pH system is presented to highlight the capabilities of combining sensors, microelectronics, and microfluidics. Chapters 11 and 12 present information on the use of commercially available CMOS processes for microscale sensing systems. Designs for CMOS integrated sensors are shown along with a novel method for interfacing CMOS circuits with microfluidic environments.

Prior to discussing sensor systems, this dissertation begins with brief introductions to two topics commonly addressed through the remainder of this work: cell culture (Chapter 2) and soft lithography microfluidics (Chapter 3).

Chapter 2

CELL CULTURE

The first tissue culture experiments in 1907 used small pieces of frog spinal cord placed on clotted tissue in a warm, moist chamber to show that cells could proliferate in artificial environments [1]. Since those experiments, cell culture has been an integral part of biological research. Cell culture provides a means to study the behavior of animal cells, either under normal conditions or the stress of an experiment. The growing use of cell culture in fields including cancer research, stem cell research, and vaccine production, has also created a substantial financial impact. A report by Global Industry Analysts Inc. projects the global market for cell and tissue culture supplies to surpass $6 billion by 2015 [2]. Cell culture usage shows no signs of slowing in the coming years either.

While the cell culture market has seen extraordinary prosperity in the past 100 years, many of the methods for performing cell culture research have been largely unchanged. This chapter examines the current status of cell culture practices. Requirements for effective cell culture are presented. Many of the problems addressed throughout the remainder of this work incorporate biological analysis, often with the aim of improving cell culture applications. A thorough understanding of cell culture is therefore essential.

2.1 Basics

Cell culture, the *in vitro* growth of cells, begins with harvesting cells from intact or dissociated tissues or organs from a living subject [3]. These freshly harvested cells are known as a primary culture. Cells are kept in a controlled environment and proliferate until they are ready to passage. Passaging is the term for transferring cells from an ongoing culture into a new culture to allow further propagation. The continued passaging of cells is dependent on the type of cell. After primary cells have been passaged, they can be considered a cell line.

Primary cell lines often show behavior dependent on the passage number. Different harvesting methods or different harvesting sources can also lead to variations in behavior. Primary cell lines are preferred when a specific cell behavior, such as electrical activity, is of interest. However, when the specific behavior is of less interest, cells that exhibit consistent behavior through repeated passaging are preferred. This repeatability is possible by using cells which have been transformed. Transformation is the alteration of cell characteristics such as cell cycle time, anchorage dependence, response to growth factors, or most importantly the lifespan of the cell. Cells can be transformed to have an infinite lifespan, thus allowing specific cell lines to be maintained with well-known characteristics. There are some differences in the behavior of primary cells and immortalized cells, but the culture and analysis methods are largely the same.

2.2 Cell Growth

There are four basic stages of cell growth in culture: lag, log, plateau, and decline. Immediately after plating of cells (primary or immortalized) into a new vessel, cells undergo a lag phase during which they do not divide. The length of the lag phase mostly depends on the growth phase of the cells when they were passaged and the seeding density. During the lag phase, cells adapt to their surroundings. The next phase, log phase, is characterized by logarithmic proliferation. The plateau phase occurs when the cells have grown sufficiently to take up all the space available. This culture state is known as confluent. After reaching plateau phase, the cells go into decline with the rate of cell death exceeding the rate of cell division.

During all phases of cell growth, cells consume glucose and oxygen and produce carbon dioxide (CO_2) and lactic acid. The balanced production of CO_2 and lactic acid is important to maintain a physiological pH of 7.2 to 7.4. The lag phase of growth presents culture problems because these factors are unbalanced, with lactic acid

production outpacing CO_2 production. Therefore, most cell culture systems provide an elevated CO_2 environment to provide balance. But providing elevated CO_2 levels is not the only means of regulating pH; cell culture media can also aid in pH maintenance.

2.3 Media

Initially, cell culture media were composed of natural media extracted from tissues and body fluids. With the increased utilization of cell culture, and thus increased media demands, chemically defined media have been developed. These media have been formulated to maintain proper pH, osmolarity, and nutrition. The media comprise a combination of a basal medium and serum. The serum provides the necessary growth factors while the basal medium contains nutrients and a balanced salt solution. The balanced salt solution provides pH buffering for the system, usually by the inclusion of sodium bicarbonate. As CO_2 dissolves into the media, it causes the pH to rise by the reaction

$$H_2O + CO_2 \Leftrightarrow H_2CO_3 \Leftrightarrow H^+ + HCO_3^- \tag{2.1}$$

The presence of sodium bicarbonate helps drive this equation back to the left because sodium bicarbonate dissociates,

$$NaHCO_3 \Leftrightarrow Na^+ + HCO_3^- \tag{2.2}$$

producing excess bicarbonate. This system manages to maintain pH at the ideal biological value of 7.4. Some media have been developed which do not require increased CO_2 concentrations to stabilize pH; instead they operate with atmospheric CO_2. These media usually incorporate pyruvate, an amino acid, or phosphate-based solutions for buffering. Another common buffer system is HEPES, 4-(2-hydroxyethyl)-1-piperazineethanesulfonic acid. HEPES is a strong buffer in the 7.2 to 7.6 range, but is both toxic and expensive so efforts are made to minimize its use.

2.4 Incubation

While the media can provide nutrients and pH control, external sources are used to maintain CO_2 concentration and temperature. An incubator is commonly employed to create a proper culture environment. The incubator keeps a stable temperature, $37\,^{\circ}C$, and humidity, 100%. Temperature stability is very important because just a $2\,^{\circ}C$ change for a short period can cause cell death [4]. The humidity is necessary to prevent changes in media concentration due to evaporation.

2.5 Microfluidic Cell Culture

Much work has been performed to advance cell culture methods using the growing fields of microfluidics and microfabrication [5]. Many devices have been developed for cellomics including cell sampling, cell trapping and sorting, cell treatments such as lysis and transfection, and cellular analysis [6–10]. Microfluidic platforms are now widely produced using poly(dimethylsiloxane) (PDMS) [11]. PDMS has good bio-compatibilty, optical properties, and a quick turnaround time in fabrication, so it is well-suited for biological applications [12]. Instead of merely performing cellomics in PDMS microfluidic devices, recent work has focused on creating systems capable of maintaining cell cultures over time or incorporating sensors [13–20]. Hung et al. demonstrated the ability to perform high-throughput assays on cultures of cells [21]. Automated cell culture systems have been developed which have maintained viable cells in 96 independent culture chambers for weeks at a time with mixers and pumps incorporated into the microfluidic design [22]. Other systems have been created to work toward minimizing human interaction with cells in the culture [23]. Recently, 3-dimensional culture in PDMS devices without the use of hydrogels for suspending cells has been demonstrated [24, 25]. PDMS cell culture is becoming more common in scientific research; guides to performing standardized PDMS cell culture work have been published [26]. However, PDMS cell culture devices still require a great deal of

human involvement and lack sufficient sensor systems to give information about the culture microenvironment.

Chapter 3

SOFT LITHOGRAPHY MICROFLUIDICS

Many of the advances of the microelectronics industry in the past 50 years have hinged on the ability to make devices smaller. Near the end of the century, the same miniaturization techniques began to find applications in biological research. George Whitesides pioneered many of the advances through his work with polydimethylsiloxane, commonly referred to as PDMS. Whitesides presented ideas such as elastomeric printing and micromolding, which were referred to collectively as "soft lithography" [27]. The field of soft lithography matured very quickly, with many biological oriented devices being developed [28]. Soft lithography also continued to adopt many of the advances of the microelectronics industry, including large scale integration [29]. Soft lithography microfluidics are now widely used with entire journals devoted to advances in the field. This chapter gives a brief introduction to the techniques commonly used to create PDMS microfludics. Many of these techniques are applied throughout the rest of this dissertation.

3.1 PDMS

PDMS is a type of silicone rubber. Chemically, PDMS consists of repeating monomer $[SiO(CH_3)_2]$ units. It is basically a $Si-O-Si-O$ polymer backbone with each silicon atom bearing two methyl groups. The chemical structure of PDMS is shown in Figure 3.1. PDMS has a number of uses ranging from contact lenses to shampoo. It has numerous properties that make it well-suited for biological applications, such as being optically clear, inert, gas permeable, non-toxic, and non-flammable.

PDMS is used to make microfluidics because it is mixed as a viscous liquid and then slowly cures to become solid. The chemical structure of PDMS allows for easy conversion to a solid by cross-linking the polymer backbone. The slow curing time, typically an hour or more depending on temperature, allows for the viscous solution

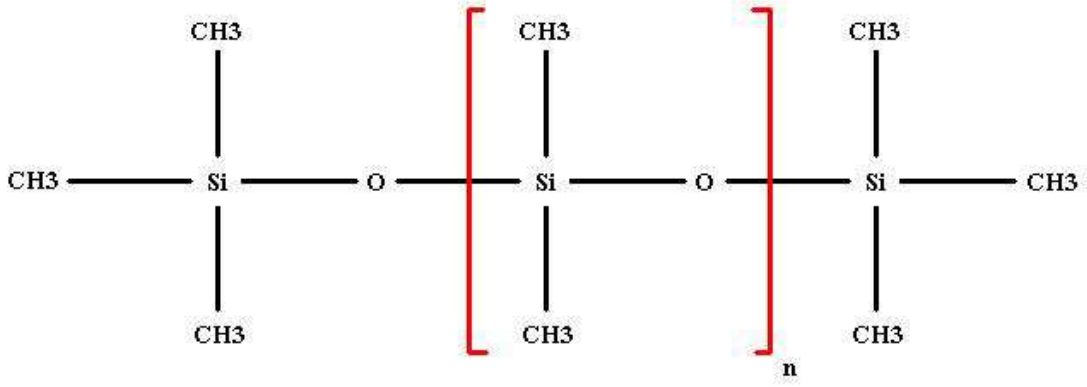

Figure 3.1: Chemical structure of PDMS.

to be molded. PDMS molds to the contours of the container holding it during curing, even maintaining micrometer or smaller features. The elastomeric properties also allow PDMS to be easily peeled away from a mold.

Additionally, the surface properties of PDMS can be modified. Exposing PDMS to an oxygen plasma treatment creates exposed hydroxyl groups in place of the surface methyl groups. These hydroxyl groups can be transformed to allow a number of reactions to occur at the surface, such as the attachment of self assembled monolayers. Perhaps the most useful consequence of surface activation is the ability to permanently bond the PDMS to another surface. Plasma treatment of PDMS allows it to form a covalent bond with another piece of activated PDMS. This surface modifying reaction can also be easily performed with activated glass substrates or any material with free hydroxyl groups.

3.2 Microfluidic Fabrication

Fabrication techniques for soft lithography microfluidics all follow the same basic procedure. Briefly, the procedure is to create a master mold using lithography techniques, pour PDMS over the mold, allow it to cure, remove the PDMS, then attach the molded

PDMS to another material to complete the channels. Of course, more elaborate fabrication methods are available to create complex designs.

The more specific fabrication process for a simple microfluidic device is as follows:

1. A mask is designed, often in a computer aided drafting software. Here the geometry of the device is defined including channels, input and output ports, and any other microfluidic feature.

2. A silicon wafer is cleaned in preparation for lithography. It will be used to create the mold.

3. Photoresist is spin coated onto the wafer. Either positive or negative resists will function to create a mold. Positive photoresists are sometimes preferred because they can heated after processing to “reflow”. This reflow action causes the sharp edges of the design to be smoothed. This is often helpful in creating valves as will be discussed later. Negative resists, such as SU-8, are often used because of their ability to create high aspect ratio patterns.

4. The resist is baked, exposed, and developed according to the procedure for the resist used. The mask design is thus patterned in the resist.

5. The patterned resist is hard baked. This step helps the adhesion of the resist to the wafer. In the case of positive resist, this also causes reflow.

6. PDMS is prepared by mixing the two part resin. The mixture is typically 10 : 1, part A : part B. The two parts are thoroughly mixed to ensure an even reaction throughout.

7. The mixture is degassed to remove bubbles. Bubbles naturally occur during the mixing process so it is essential to remove them to create homogeneous devices.

8. The liquid PDMS is poured over the prepared patterned resist mold.

9. The mixture is allowed to cure. It will cure overnight at room temperature or in approximately two hours at $70\,^{\circ}C$.

10. The cured PDMS is peeled away from the master mold.

11. The PDMS is cut down to include the desired shape containing the microfluidic device.

12. A blunt needle is used to punch holes for access to the microfluidic channels. Typically port areas have been defined in the design to signify the location of these ports.

13. A glass slide is cleaned with isopropyl alcohol and water, then dried.

14. Both the PDMS and the glass slide are treated with oxygen plasma. The typical treatment uses a Harrick Plasma System (Harrick Plasma, Ithaca, NY). Oxygen is used as the process gas and "high" RF power is used for $30 - 60$ seconds. The pressure should be kept lower than 600 mTorr; a light purple plasma should be visible during treatment. A bright pink plasma indicates a nitrogen plasma, usually due to room air inside the chamber.

15. Immediately upon completion of the plasma treatment, the activated PDMS surface is placed on the activated glass surface. The two pieces instantly bond.

16. The pieces are left in an oven at $70\,^{\circ}C$ for about 10 minutes to allow a strong bond to form.

The completed microfluidic structure can then be used for the designed purpose. More advanced microfluidic structures often consist of multiple layers. More layers allow for channels to cross without mixing. Multilayer devices also allow for the

creation of valves. The easiest type of valve to make is a normally open configuration. This means that flow will pass through the valve unless the valve is activated. There are two common methods to create normally open valves: push up configurations and push down configurations. The difference is illustrated in Figure 3.2. The fluid layer contains the fluid of interest. The control layer is either filled with air or water that can be compressed by air. The general operation of both valves is identical - a pressure is applied to the control channel which causes the thin layer of PDMS separating the channels to flex into the fluid channel and block flow. Reflow of the patterned resist can help to create rounded channel shapes. This is helpful in preventing leakage around the valve in the corners of the fluid channel that the membrane does not fully block.

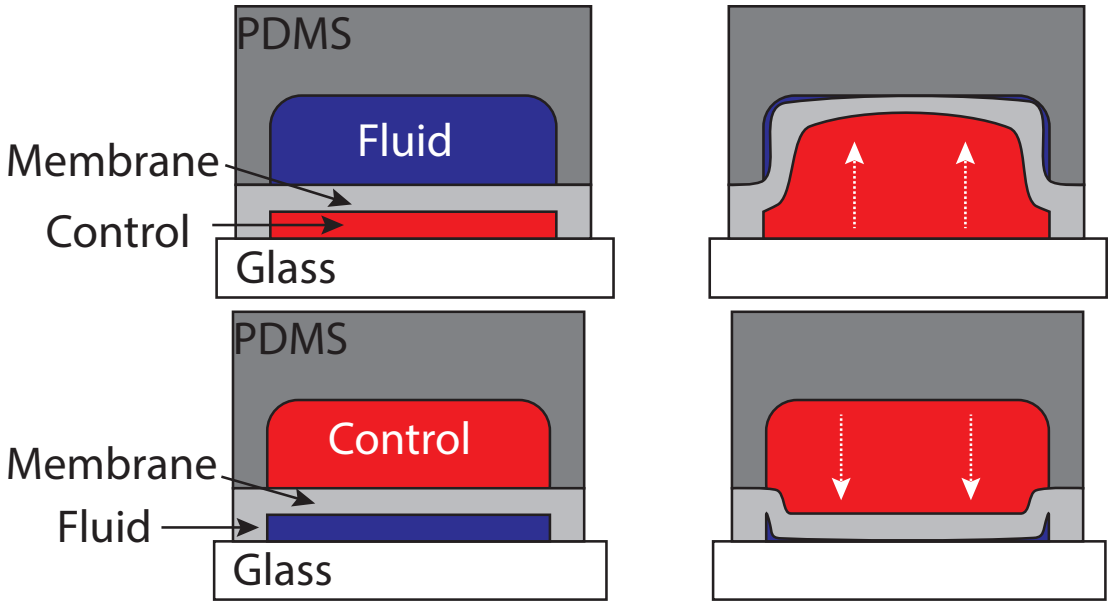

Figure 3.2: Push up (top) and push down (bottom) microfluidic valve configurations. Both designs are normally open valves.

The process for making valves involves added steps to the simple device fabrication sequence presented earlier. The process for push down valves is stated here. The procedure for push up valves simply switches the fluid and control layers.

1. Two masks are designed, one for the fluid layer and one for the control layer. The mask needs to include channel crossings where valves will be created. In general, the valve layer should be 10 times wider than the depth of the fluid layer when a valve is desired. A crossing without a valve can be created by using a thinner valve layer [29].

2. Both masks are used to create molds with patterned resist. The fluid layer should be approximately $10\,\mu m$ tall. The control layer height is not as important as long as it does not become blocked. A height of $10\,\mu m$ to $40\,\mu m$ is usually sufficient.

3. PDMS is mixed and poured over the control depth to a usual device thickness, approximately $5\,mm - 10\,mm$.

4. Uncured PDMS is spun onto the fluid layer at 3500 RPM. This creates a thin PDMS layer over the entire wafer. Areas over the patterned resist are even thinner and will act as the flexible membrane when the control layer crosses a channel layer.

5. Both wafers are allowed to cure for about two hours at $70\,^{\circ}C$.

6. The control layer is removed from the mold and the excess PDMS is removed from the sides so the molded surface is flat.

7. Both the fluid layer (still on the wafer) and the control layer are plasma treated.

8. Immediately upon completion of plasma treatment, the control layer is aligned with the fluid layer and brought into contact to form a bond.

9. The pieces are left in an oven at $70\,^{\circ}C$ for about 10 minutes to allow a strong bond to form.

10. The two bonded layers are then peeled from the fluid design wafer. Access ports are then punched. The design is then ready for bonding to glass.

These basic soft lithography techniques are used throughout this work to form microfluidic devices.

Chapter 4

MEMS TILT SENSOR

Tilt measurement is ubiquitous to a range of research and industrial fields including automotive, aerospace, mechanical, and civil engineering. Biomedical engineering research also employs tilt sensors. Recent research used tilt data to analyze the gait in persons with stroke or spinal cord injury [30] [31] and for advancing human-computer interface capabilities [32] [33]. A particularly interesting application area is replacing the function of the human vestibular system, commonly known as the inner ear.

According to the Food and Drug Administration [34], at the end of 2006, more than $112,000$ people worldwide had received cochlear implants. Many of the individuals receiving cochlear implants also suffer from dizziness and balance disorders from loss of inner ear functions. The inner ear's vestibular system provides cues about self-motion and helps stabilize vision during movement. Augmentation of cochlear implants to include restoration of vestibular function would aid these individuals. It has been estimated that approximately $30,000$ Americans are coping with profound loss of inner ear balance [35]. Restoration of balance could be achieved by bypassing a dysfunctional element in the vestibular pathway using artificial stimulation. There are a number of sites along the vestibular pathway that can be tapped into: the ampullae, the scarpa's ganglion, and individual nerve bundles.

The vestibular system in human physiology, illustrated in Figure 4.1, senses the head's motion and orientation using the ampullary (within semicircular canals) and otolith (utricle and saccule) end organs. Three orthogonally oriented semicircular canals sense angular acceleration while the otolith organs oriented perpendicular to one another sense tilt and linear acceleration. Both of these systems are based on natural microfluidic technology, in which motion or otolith displacement is detected by

cilia. The cilia, which are tiny hairs, signal the displacement angle by modulating the firing frequency of the underlying neurons.

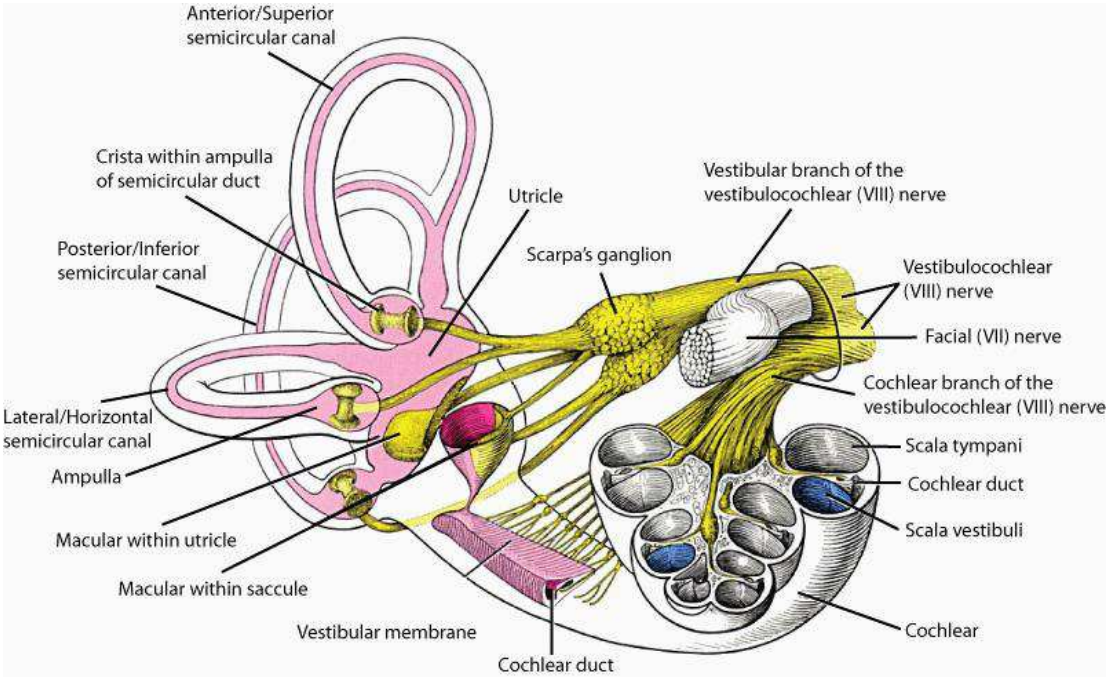

Figure 4.1: Illustration of the inner ear with the ampullary and otolith end organs indicated [36]. Changes in head position cause movement of fluid in the inner ear resulting in cilia deformation. The deformation generates an electrical signal that is interpreted as motion by the brain. This is the body's natural fluidic microelectromechanical system (MEMS).

Advanced applications such as a vestibular replacement require a tilt sensor that produces a readout signal so data can be collected and analyzed. The tilt sensor also needs to function at angles other than flat with respect to gravity. Additionally, many applications such as vestibular implants desire low power consumption and a small device size; other application areas value a device with robust operation that is resistant to environmental noise. Of course the most important quality for such a sensor is a precise and accurate measurement of tilt with an adequately high sensitivity.

This chapter describes the complete design, fabrication, and testing of a new tilt sensor design. The device utilizes a commercial MEMS process to create a unique

device. This novel adaptation of microfabrication technology for biosensing focuses on measurements at the whole-body level.

4.1 Background

Generally, tilt sensors can be classified by the pendulum (the material which responds to changes in inclination) and the method of obtaining a signal. There are three basic categories for pendulums: solid-mass pendulum, liquid pendulum, and gas pendulum [37]. All of the pendulum types function similarly by responding to the direction of the gravitational force. The methods for detecting changes in the pendulum state have much more variety and include resistance [37–42], capacitance [43–46], inductance [47–49], magnetism [50], fiber optics [51–53], and optical measurement [54–58]. Many different configurations of tilt sensors have been made for each detection method.

Fluid pendulums have been used to cause resistance changes by shifting the position of liquid mercury [38] or by changing the amount of conductive fluid [39] [40]. Clever designs by Billat *et al.* [41] and Milanović *et al.* [42] used heat transfer through a gas to cause thermal changes in resistance. Other recent designs measured deformation of a solid pendulum using piezoresistance [37]. Resistance-based devices have good sensitivity and stability but their performance is susceptible to external and internal influences.

Capacitance changes are often used to detect relative differences in the height of a liquid pendulum [43] [46], with permittivity sometimes improved by the addition of nanoparticles to the detection fluid [44]. Other capacitive sensing setups utilize a solid proof mass similar to the operation of an accelerometer [45]. Generally, these devices perform well, but temperature and humidity can tamper with the results.

Less common sensing techniques include measurement of tilt with inductance, magnetism, or fiber optics. Inductance-based tilt sensors utilize a ferrofluid as a pen-

dulum [47–49]. Magnetic sensors use a pair of magnets to alter a magnetic field when tilted [50]. Fiber optic methods involve the use of a liquid pendulum [51] or solid pendulum [52] [53]. However, these less common sensing techniques require complicated measurement setups with expensive or large components.

Optical methods have been used in combination with many different types of pendulums. The refraction of light through a liquid pendulum has been measured optically to determine inclination [56]. Ragazzoni *et al.* measured the deflection of light through an array of prisms to determine tilt [57]. Another optical method utilized a freely rotating, solid-mass pendulum atop a circular photodiode array for one dimensional tilt detection with accompanying on-chip readout circuitry [54]. Work by Kato *et al.* [55] uses a liquid pendulum and detects the position of a bubble by use of a photodiode array. The device by Kato *et al.* has a similar operation to the device presented in this work, but their design used a spirit level (commonly available in hardware stores) placed on top of a photodetector array to create a macroscale system requiring manual assembly. A spirit level is a common tool for carpenters, masons, or anyone that simply wants to hang a picture. The tool uses bubble movement within a vial to indicate deviations in inclination with respect to the force of gravity. A user simply has to visually inspect if the bubble is centered in the vial to determine if a surface is flat. The information gathered from the device is useful for hanging a picture but it does not satisfy the needs of scientific applications.

4.2 Design and Operation

We began the design of our tilt sensor with the natural operation of the human vestibular system as a model. However, it is impossible to create an exact replica of the vestibular system using MEMS technology. This is impossible because there is not a soft, flexible material in commercial MEMS processing that can replicate biological tissue material. Ideally we would produce flexible transducers to mimic the mechanotransduction prop-

erties of the cilia within the inner ear; instead, we had to determine an alternate method to produce a signal. The vestibular system relies on fluid movement to detect tilt using the otolith organs so we developed a design under the same premise of sensing fluidic motion. Noting the operation of spirit levels inspired us to replicate their function within a MEMS microfluidic environment.

Our design was constrained by the fabrication steps available in the SensorNor MultiMEMS process. The process involves standard silicon wafer processing technology but with the addition of isotropically etched borosilicate glass. The process is summarized in Figure 4.2. The MultiMEMS process offers a p-substrate wafer with n-well and n-epitaxial layers. Also offered are an n+ layer and four types of p-doping: p-surface resistor, p-surface conductor, p-buried resistor, and p-buried conductor. It is a single metal layer process and includes anodic bonding of both top and bottom side glass layers. The glass is bonded to the wafer after silicon processing and allows the formation of sealed cavities as well as access to the silicon surface.

Based on the constraints of the process we developed a MEMS microfluidic tilt sensor, the principle of operation of the sensor is illustrated in Figure 4.3. The MEMS tilt sensor consists of a square cavity that is partially filled with an opaque liquid. The remaining volume in the cavity is occupied by an air bubble. Tilting the device changes the position of the bubble within the cavity. The fluid cavity is located directly on top of four equal-area triangular p-n junction photodiodes. The photodiodes are rotated 45° off-axis from the square sides of the cavity so the base of each triangle aligns against one side. Light is projected from a light-emitting diode onto the device from above. Light passes through the bubble and fluid in the chamber, and the photodiodes measure the number of photons reaching the bottom of the cavity. The magnitude of the current produced in each photodiode depends on the number of photons reaching the sensor, allowing the position of the bubble to be determined.

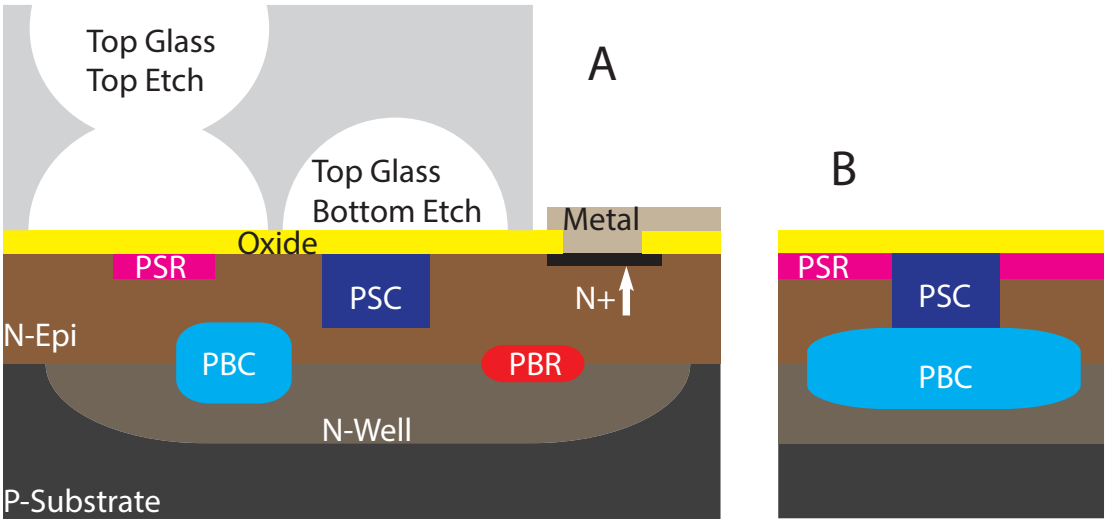

Figure 4.2: Cross-section schematic showing each of the doping regions available in the SensoNor MultiMEMS process (A). Definable layers include n-well, n-epitaxial, n+, and four p-doped layers: p-surface resistor (PSR), p-surface conductor (PSC), p-buried resistor (PBR), and p-buried conductor (PBC). Both a top and bottom layer of glass can be isotropically etched from both the top and bottom sides before anodic bonding. The bottom glass layer is not pictured. The cross-section for the photodiode structure is shown in (B). Three p-doped regions, PSR, PSC, and PBC, are stacked to maximize the depletion region. The pattern of stacked layers is repeated throughout the photodiode area.

Fluid-Light Interaction

The number of photons passing through liquid to the photodiodes is reduced according to Beer's Law,

$$A = \varepsilon bc \tag{4.1}$$

which states that the absorption (A) of a fluid is dependent on its the molar absorptivity (ε), the distance the light travels through the fluid (b), and the fluid's concentration (c). Simply put, the farther light travels through a liquid the more the intensity decreases because some of the light is absorbed by the liquid. Areas covered with more liquid will have lower current outputs because the number of photons hitting the photodiode

is decreased. More light reaches sensing areas directly below the bubble which allows the bubble location to be determined.

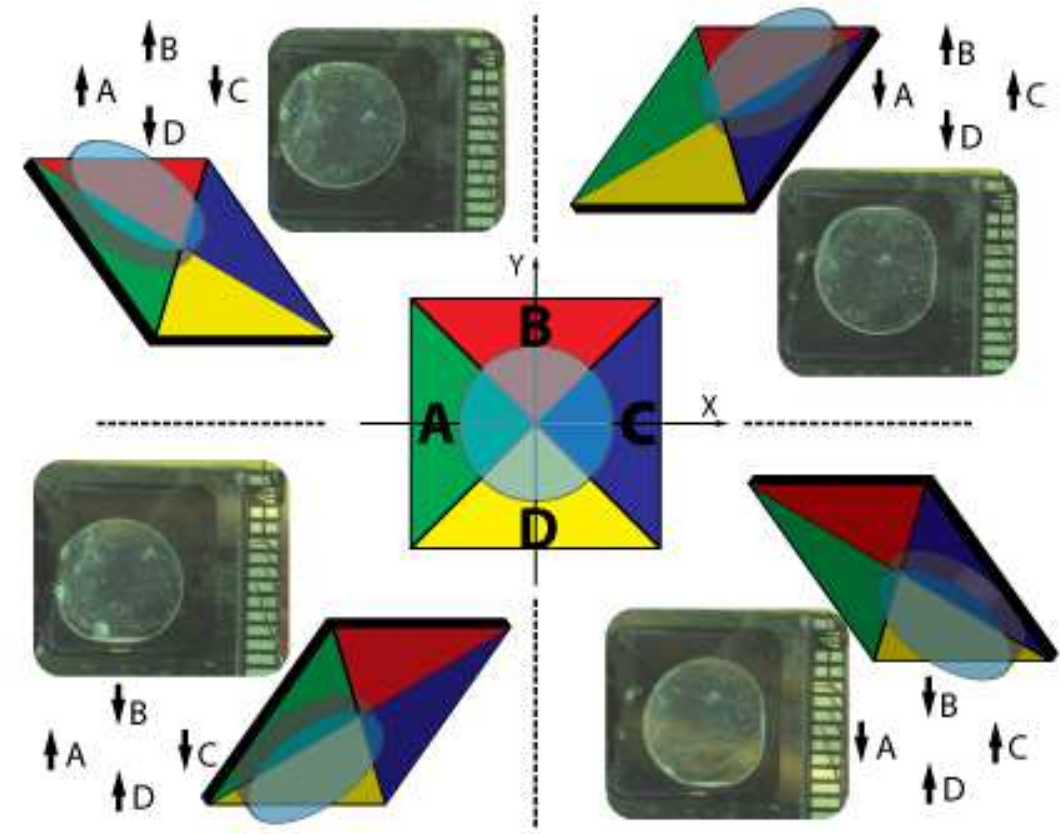

Figure 4.3: The sensing region consists of four equal-area triangular regions. The bubble is located in the center when the device is aligned normal to gravity. As the device tilts the bubble moves to expose different areas of each photodiode. Micrographs and corresponding illustrations of the device show the bubble moving to contact the wall when tilted toward each corner.

Sensor Operation and Output

The bubble position depends on the orientation of the device with respect to gravity. The bubble will be centered at the top of the cavity when the base of the device is normal to the gravitational force. As the device tilts, the bubble moves along the ceiling of the cavity and therefore changes which photodiodes are more illuminated. The operation

is illustrated in Figure 4.4. Since all four photodiodes are equal area and oriented 45° off-axis from the square cavity (which we assume to be oriented with the x and y axes), the four output currents I_A, I_B, I_C, and I_D are related to the bubble position on the x and y axis with:

$$x = \frac{I_C - I_A}{I_C + I_A} \tag{4.2}$$

$$y = \frac{I_B - I_D}{I_B + I_D} \tag{4.3}$$

Dividing by the sum of the two regions in equations (4.2) and (4.3) normalizes the output. The tilt angle and inclination direction can be calculated from the measured x and y position of the bubble. If we assume the top of the cavity is hemispherical and the shape of the bubble remains circular, then the relationship between current output and tilt angle, θ_x, is approximated with $x = arctan(\theta_x)$ [55]. Because our device is symmetric, this relationship also holds for tilt measured in the y direction, θ_y.

4.3 Fabrication and Testing

Design Layout

We designed two versions of MEMS tilt sensors and various photodiode test structure to be included on our test chip. The only difference between the two tilt sensor designs is the etching of the glass above the photodiodes. One of the designs has a fully open cavity. The other design only has the bottom side of the top glass etched, forming an enclosed cavity. The enclosed cavity is accessible through access ports which were also incorporated into the glass etching design. Both designs have an identical photodiode layout in the silicon below the cavity. The full sensor layout, generated using L-Edit, is shown in Figure 4.5.

The tilt sensor's fluidic cavity has a pan (rectangular prism) shape formed by creating an open area in the top glass, $2360\mu m \times 2360\mu m$. The open cavity design maximizes the total depth of the pan. This will be defined by the thickness of the glass, $525\mu m$. These dimensions give a total volume of approximately $2.9\mu L$. The enclosed

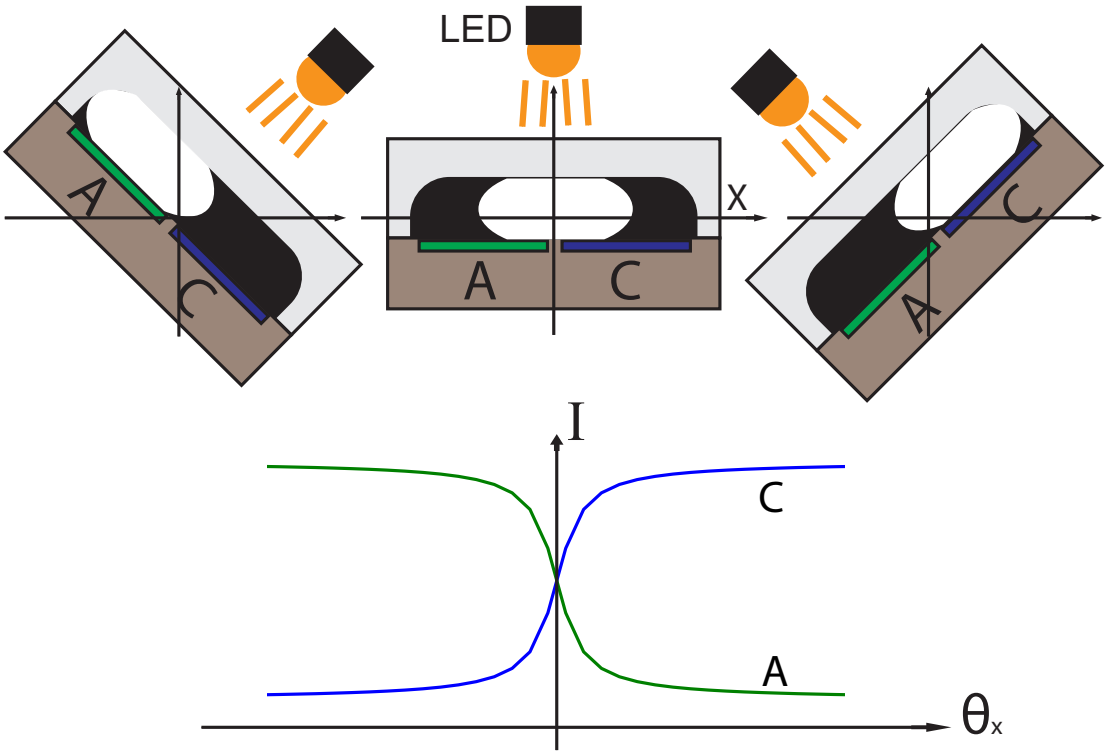

Figure 4.4: A cross-section of the device tilting along the x axis shows bubble movement. As the inclination angle increases in the positive direction, the bubble exposes photodiode C more than photodiode A, which increases I_C and decreases I_A. Approximating the top surface of the device as a hemisphere allows us to predict a relationship between angle and output current that is close to $I = arctan(\theta_x)$, shown in the graph.

cavity design only etched on the bottom side of the top glass to create a pan depth of $310\mu m$; this causes the total volume to drop to $1.7\mu L$. While the total volume of fluid for each device varies between the two designs, their operation is analogous.

The optical detection for the tilt sensor is composed of four p-n photodiodes. The p-doped side of the diodes is designed with overlapping p-surface resistor, p-buried conductor, and p-surface conductor; the n-doped side is n-epi. The configuration and choice of doping regions was determined by examining the relative doping levels of each layer and the photon penetration depth for silicon [59]. The optical detection occurs in the depletion regions formed at the junctions between the p-doped and n-epi

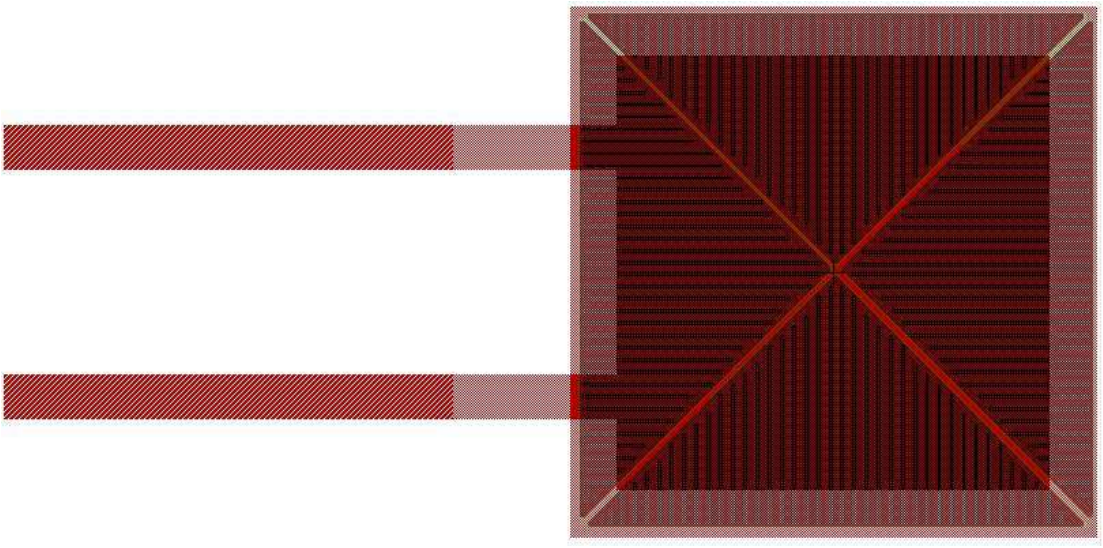

Figure 4.5: Layout of the enclosed cavity design is shown. The four photodiode areas are the triangular regions with a common vertex in the center. The fluidic ports extend to the left from the sensing region for access to the cavity. The layout for the open cavity is identical except the ports are not included. Each triangular region has a base of $2\,mm$ and an altitude of $1\,mm$.

regions. Stacked p-doped regions allows for the largest depletion region to maximize photocurrent over a given area. A cross-section of the photodiode layout is shown in Figure 4.2. The configuration is repeated across the entire photodiode region. Each photodiode is a triangular area with a base of $2\,mm$ and an altitude of $1\,mm$. The photodiodes are arranged with a separation of $14\,\mu m$. Photodiode test structures were included on the device to allow characterization of each combination of p-n photodiode separately. We defined equal areas of the four p-doped regions independent of any other doping so geometry differences did not exist to vary the characterization results.

The completed chip fabrication is shown in Figure 4.6. The open cavity design is not shown in this picture but is identical in size.

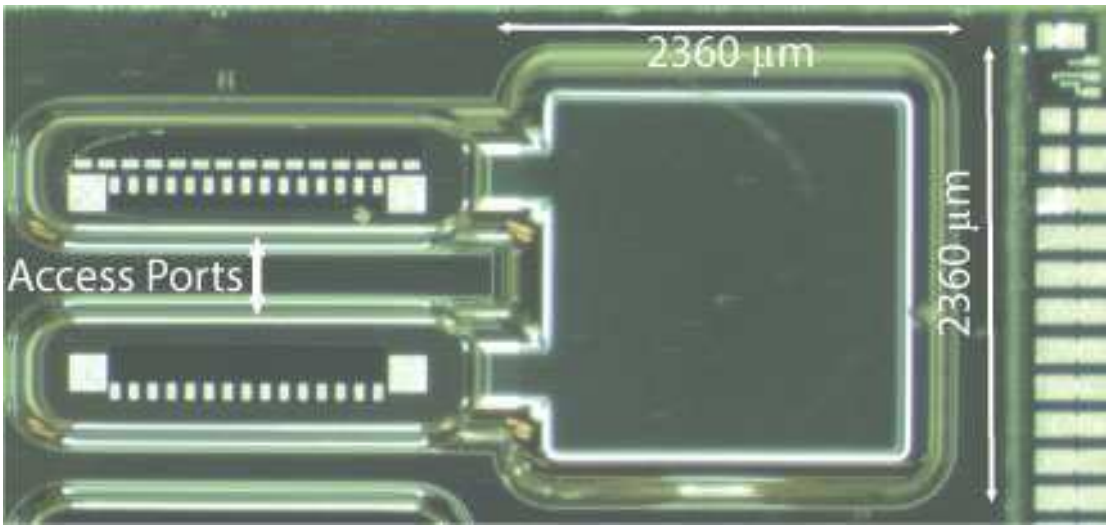

Figure 4.6: Micrograph of tilt sensor before fluid addition and sealing. The access ports extend from the left of the sensing region. Bondpads for electrical connections are shown on the right.

Photodiode Characterization

Initial characterization of the photodiodes was performed using test structures. These structures were designed such that p-n junctions were formed between the n-type epitaxial layer and the four p-type layers as described in section 4.3. The p-type layers each had different junction areas as a result of different doping ratios, and they were at different depths within the final structure. It was expected that the photodiodes would have different current-voltage characteristics and would exhibit different sensitivities to optical stimulation.

The photodiode test structures were probed using a Semiprobe probe station and measurements were performed using a Keithley 2636A source-measurement unit. All measurements were performed in a dark room so ambient light was eliminated. With the light source turned off, current-voltage measurements were performed for each of four single-layer photodiodes on each die. As demonstrated in Figure 4.7,

each of the four photodiodes shows a slightly different current-voltage characteristic. The difference is expected considering the difference in p-n junction depths for each photodiode combination layout. The classic features of a forward biased diode are quite evident and confirm that we did in fact make good diode connections. Results for reverse bias performance are shown in Figure 4.8. As expected, we observed a linear correlation between light intensity and photocurrent. Our results confirmed that our multilayered photodiode design increased the photocurrent over just using one p-n junction photodiode.

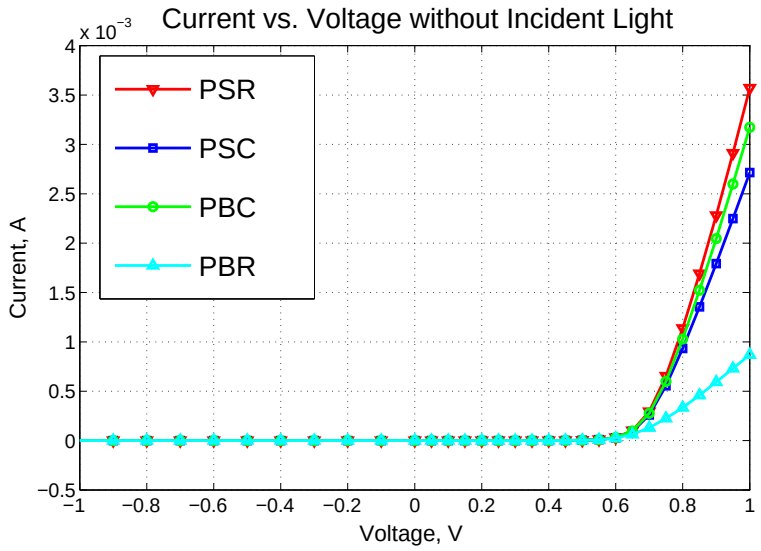

Figure 4.7: Photodiode characterization data showing the current versus voltage behavior for all four devices. All devices have a turn-on voltage of approximately $0.7V$.

Fluid Selection

The properties of the fluids used within the device are very influential on the performance. There were three properties that we analyzed in selecting a fluid: viscosity, surface tension, and opacity. The viscosity and surface tension of the fluid determines how quickly the bubble moves and settles. The response time is inversely proportional to the viscosity of the fluid. Because of the small scale of the device, surface tension forces will have a significant effect. We also desired a liquid that was opaque to block

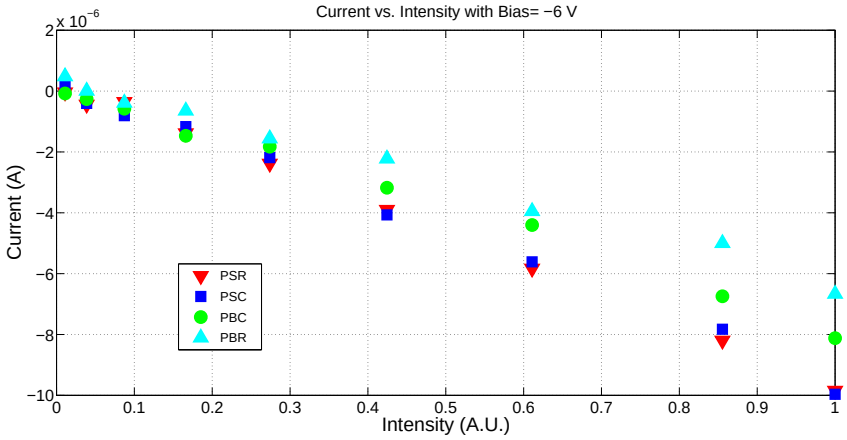

Figure 4.8: The relationship between intensity and current was characterized for the four photodiodes with a bias of -6.0 V. Because the devices are reversed bias there is a nearly linear relationship between light intensity (arbitrary units) and photocurrent.

light and therefore increase the contrast for the bubble area. These same fluid properties are desirable in commercially available spirit levels. Traditional spirit levels utilize an alcohol (hence the "spirit" nomenclature) because of their low values for surface tension and viscosity. The alcohol is also colored, though it is usually yellow or green, to provide contrast when viewed by the user.

Water was first examined as a possible fluid because it is non-toxic and could be easily dyed to increase the opacity. Water was found to be inadequate due to the high surface tension and viscosity values ($72\,dynes/cm$ [60] and $1\,cP$ [61] at 298.15 K, respectively). We instead selected methanol as the alcohol to fill the tilt sensor cavity. It was chosen because it has low surface tension ($22.1\,dynes/cm$) and viscosity ($0.54\,cP$). Another option, ethanol, has a surface tension nearly identical to methanol ($22.27\,dynes/cm$) but about twice the viscosity ($1.07\,cP$). Because surface forces play such large roles in fluid-surface interactions we sought to minimize all these values and hence chose methanol.

The issue with the choice of methanol lies in trying to make it opaque. The position of the bubble is better defined when there is a large difference in the absorptivity of the fluid and the bubble. Methanol is received as clear liquid so there is little contrast from an air-filled bubble. In accordance with Beer's Law (Equation (4.1)), we increase the absorption of the fluid by increasing the molar absorptivity, which is accomplished by adding a dye. However, methanol is actually a solvent used to dissolve and remove many common water-based dyes, such as food coloring. We therefore had to dye the methanol using a solvent-based dye. Solvent dyes are used in permanent markers. We accomplished methanol dying by dipping the felt tip of a a black Mark-tex Film Opaquer pen (ITW Dymon, Olathe, KS, USA) directly into 100% methanol (VWR International, Radnor, PA, USA) until the methanol was a uniform black color. The dye remained in solution as long as the methanol did not evaporate (thus illustrating the need to re-cap markers!).

Device Sealing

Preliminary sealing tests were performed on the open cavity design because fluid could simply be pipetted directly into the cavity. However there were a number of difficulties associated with the sealing of the device while keeping the solution contained. A major problem was the volatility of the methanol. The methanol is evaporated quickly, leaving little time to physically cover and seal the device. The volatility of the methanol also excluded sealing using heat. The second issue was the choice of an adhesive. Methanol reacts with most epoxies preventing them from fully curing. If the methanol was not sequestered from the glue used to seal the cavity, then an imperfect seal would form. Poor sealing either led to the cover falling off or methanol evaporation due to leakage.

Due to the difficulty in sealing the open cavity, the focus was shifted to the enclosed cavity with access ports. Filling of the small cavity through the access ports was initially very difficult. The effects of surface tension on a device with such small

dimensions were apparent through the solution clinging to the glass walls of the ports. We found that fluid could be injected into the device using a Fisherbrand Elite Pipetter with an Ultra Micro Pipet Tip (Fisher Scientific, Waltham, MA, USA) capable of dispensing volumes down to $0.1\,\mu L$. Dyed methanol was injected until a bubble with a diameter of over $1.2\,mm$ was present and moving freely within the cavity. The bubble could be trapped in the device by tilting so the bubble would move away from the ports. Although the fluid was contained, it still evaporated slowly through the access ports. We were still unable to use an epoxy to seal the device because it would not cure when in contact with the methanol, even with the small area of the access ports. The solution was to plug the holes into the cavity using small pieces of Parafilm "M" (Pechiney Plastic Packaging, Chicago, IL, USA). The parafilm is resistant to methanol and forms an airtight seal allowing the use of epoxy to seal the outside and hold the parafilm in place. The parafilm was covered with Loctite 3335 UV curable epoxy (Henkel Corporation, Westlake, OH, USA) and cured with an EN-180 handheld 8W UV-A longwave lamp (Spectroline, Westbury, NY, USA). The fully cured epoxy ensured that the Parafilm would maintain a sealed cavity without leakage. The sealed device is shown in Figure 4.9. Finally, the fully assembled MEMS device was wire bonded to a 24 pin side-braze DIP (KD-S86898-B-1, Kyocera, Kyoto, Japan) for electrical access and ease of handling.

Tilt Testing

Testing of various angles of inclination was performed with a Hi-Tech HS-645MG servo motor (Hitec, Poway, CA, USA) attached to a moveable platform as shown in Figure 4.10. The servo motor is controlled with Motor-Bee control software (PC Control Limited, Kettering, Northamptonshire, UK) and is able to adjust the angle of inclination in 1.25° steps using a graphical user interface. The packaged chip was placed into a socket mounted on a board on the tilt platform. Attaching the chip to the board

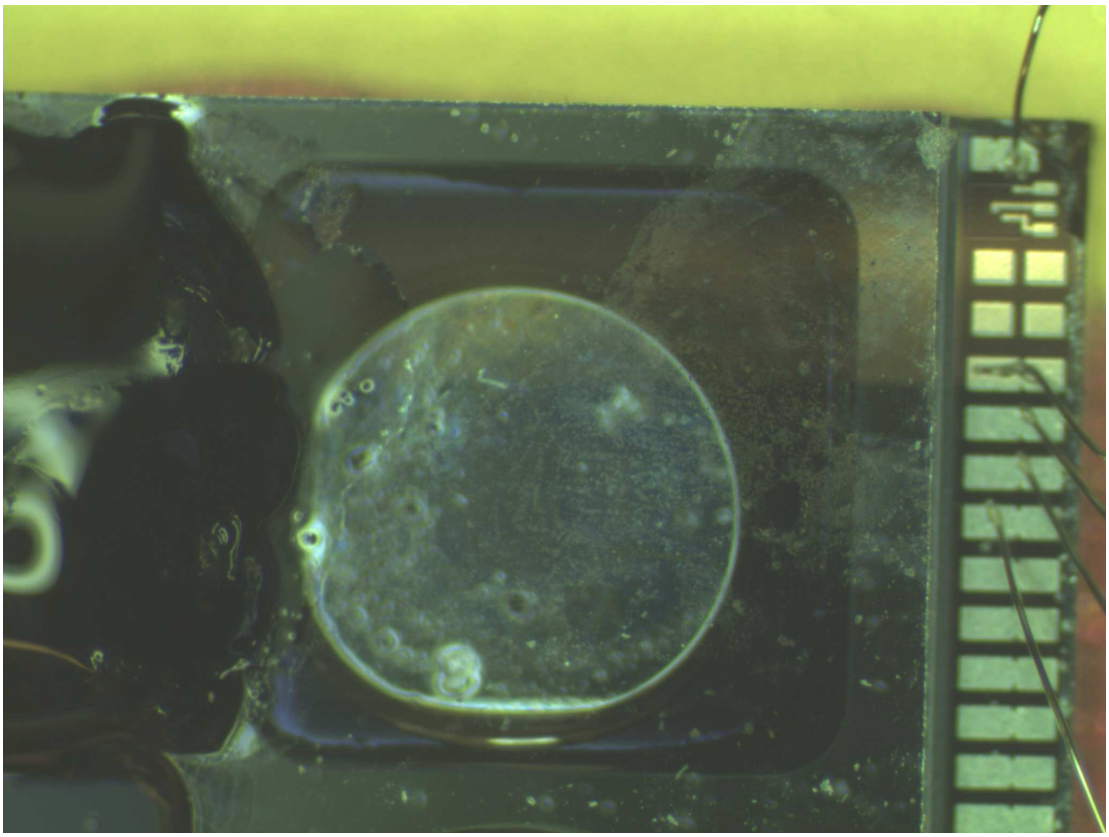

Figure 4.9: Micrograph of tilt sensor after fluid addition and sealing. The parafilm (not visible) is held in place by the UV-cured epoxy. Wire bond connections are visible on the right. The device is shown in a tilted state so the bubble is located toward one corner of the cavity. The cavity is $2360\mu m \times 2360\mu m$.

with a socket also ensured that the package, and therefore the chip itself, is aligned correctly with the axis of tilt. Electrical leads from the board allowed connections for measurements. A light-emitting diode is suspended $1\,cm$ above the chip to aim light through the fluid cavity from directly above the device.

Photodiodes were operated in photoconductive mode during testing by applying a $5V$ reverse bias with a DC power supply. The p-doped side of each diode was connected to one channel of a Keithley 2636A source measurement unit (Keithley Instruments, Inc., Cleveland, OH, USA). Each channel on the source measurement unit was set to source a value of $0V$ and measure current.

The rotated layout of the photodiodes within the cavity allows for easy testing of the inclination along the x and y axis independently. The device is easily aligned within the DIP. Therefore, the x and y axes are aligned with the socket on the test platform. The alignment enabled us to sweep the tilt angle in one direction independent of the other to fully characterize the relationship between the output of the photodiodes and the inclination. Testing was performed by tilting the stage from -45° to $+45^\circ$ along the x axis and recording the current in each photodiode. The dual-axis capability of the system was tested by fixing the inclination of the device perpendicular to the servo-controlled stage tilt path (therefore setting the y axis tilt) and again sweeping from -45° to $+45^\circ$. The tilt in the perpendicular direction, x, was performed with fixed y inclinations of $-31^\circ, -21^\circ, -13^\circ, +13^\circ, +21^\circ$, and $+31^\circ$. Sweeps were performed with both increasing and decreasing inclination to allow us to observe any hysteresis in the system.

4.4 Experimental Results

Results from sweeping the inclination along the x axis are shown in Figure 4.11. As expected, increasing the tilt angle increases the value of I_C and decreases the value of I_A. Both curves have been fit to a sigmoid function,

$$y(x) = a + \frac{b}{1 + e^{\frac{-(x-m)}{s}}} \tag{4.4}$$

where $y(x)$ is the current (I_A or I_C), x is the value of θ, a is the value at the minimum θ, b is the maximum θ minus a, m is the center value of θ, and s is the total width of the function. The coefficients of determination, R^2, are 0.99623 for photodiode A and 0.99549 for photodiode C.

Equations (4.2) and (4.3) map the output current to the angle of inclination. Figure 4.12 shows the results of mapping the output values to θ_x. This data was also fitted with a sigmoid function giving an R^2 value of 0.99595. The sigmoid fitting function

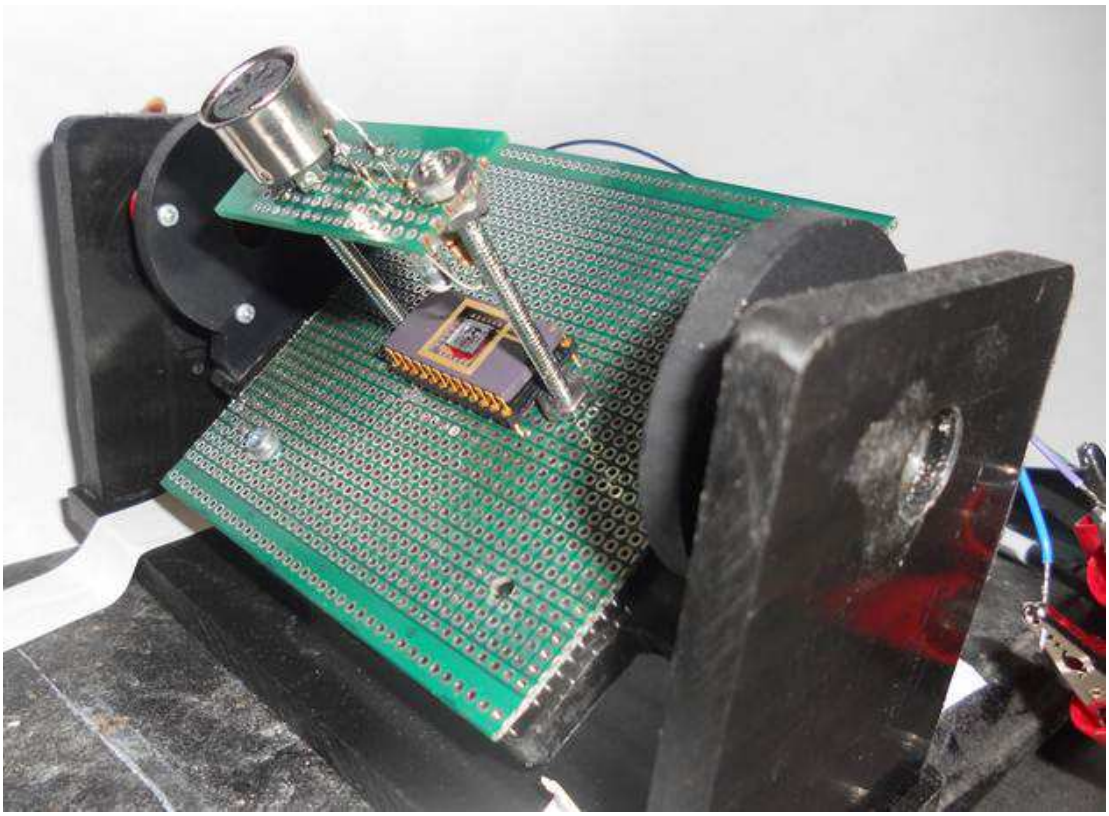

Figure 4.10: Tilt testing platform shown with an inclination of 45°. The tilt angle is controlled through a computer and allows 1.25° steps. An LED is suspended directly above the device, maintaining alignment of the light through all inclination angles.

can be inverted to allow the calculation of θ_x, given the values for I_A and I_C, using

$$y(x) = m + s\ ln\left(\frac{x-a}{a+b-x}\right) \tag{4.5}$$

with $a = -0.1261$, $b = 0.4081$, $m = 2.0237$, $s = 6.6582$, and x from equation (4.2).

We adjusted the inclination of the tilt platform to test changes in x and y tilt that occur simultaneously. The value of θ_x was swept at various values for θ_y to determine the performance of the tilt sensor using all four photodiode regions concurrently. The normalized output currents for all four photodiodes output are shown in Figure 4.13. The current through each photodiode increases or decreases as predicted in Figure 4.3. The bubble freely moves in all four directions allowing measurement of tilt along two

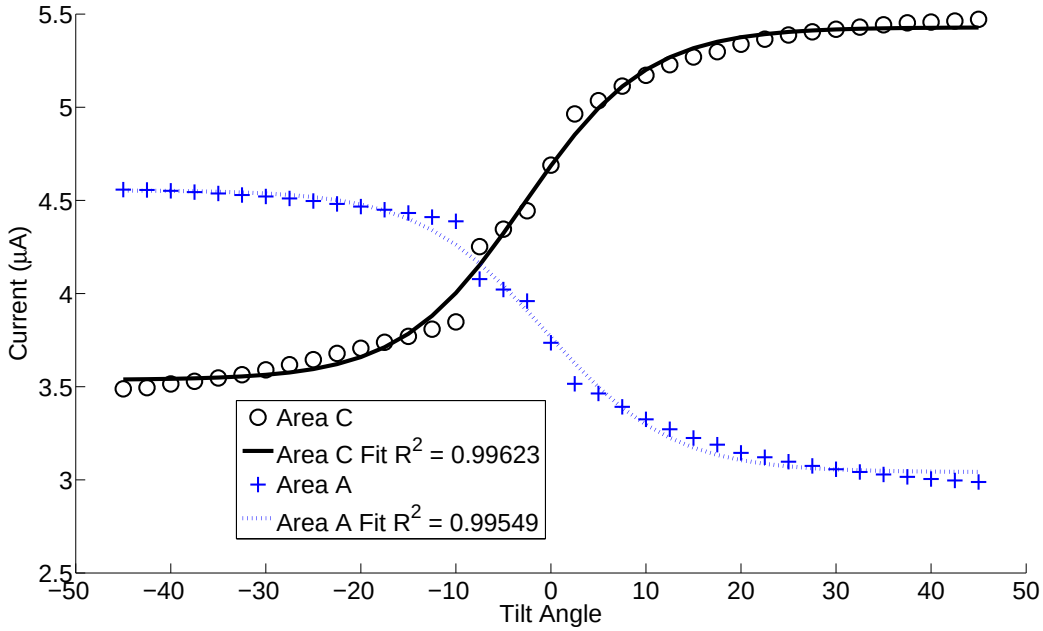

Figure 4.11: Outputs of photodiodes A and C as the angle of inclination changes from -45° to $+45^\circ$.

axes. The data from each region can be mapped to tilt angle using equations (4.2) and (4.3) and a sigmoid fitting function.

The dimensions of this device are small so there are potential irregularities during operation due to various surface forces. Surface tension forces tend to dominate in cavities on the scale of this device. In the evolution of this sensing system, water was tested as a possible fluid. The surface tension forces of water were too high to allow free movement of a bubble within a cavity of this size. Methanol and other alcohols are common choices for other fluid pendulum tilt sensing devices. As temperature decreases, their viscosity and surface tension will increase. Increased viscosity and surface tension can be a potential limitation to this type of tilt sensing mechanism. The glass cavity is formed using isotropic etching with hydrofluoric acid (HF). Wet etching with HF generates a rough surface, and non-uniformities are often observed at the bot-

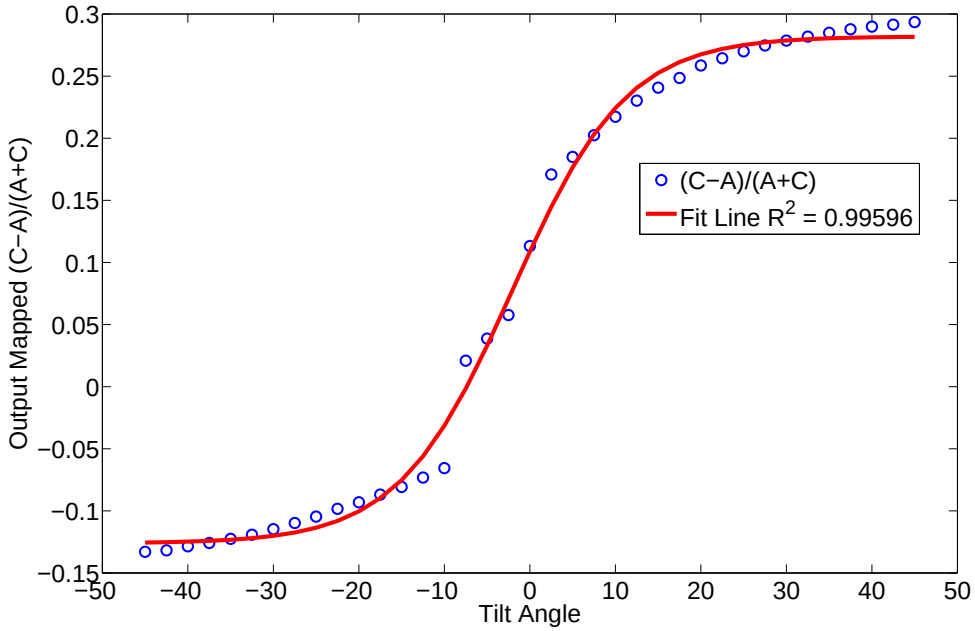

Figure 4.12: Outputs of photodiodes A and C mapped to θ_x using equation (4.2). The fit line is derived from equation (4.4).

tom of etched cavities. Distortions to the surface could affect the ability of the bubble to traverse the cavity. Data in Figure 4.14 show an output dependent upon which direction the tilt angle θ_x is swept. These variations are slight, but nevertheless suggest hysteresis in our system.

The profile of our glass cavity is not perfectly hemispherical because the width of the cavity is greater than twice the depth of the HF wet etch. This fabrication step creates a relatively flat surface at the top of the cavity. The bubble is in constant contact with the top surface as it traverses the cavity so the relationship $x = arctan(\theta_x)$ is not a perfect model for this system. The flat surface allows the device to be very sensitive when the device is nearly orthogonal to gravity. This sensitivity is demonstrated by the maximum slope of the mapped output signal occurring around $\theta_x = 0$ in Figure 4.12. The sensitivity of our device is best quantified by examining the number of bits of

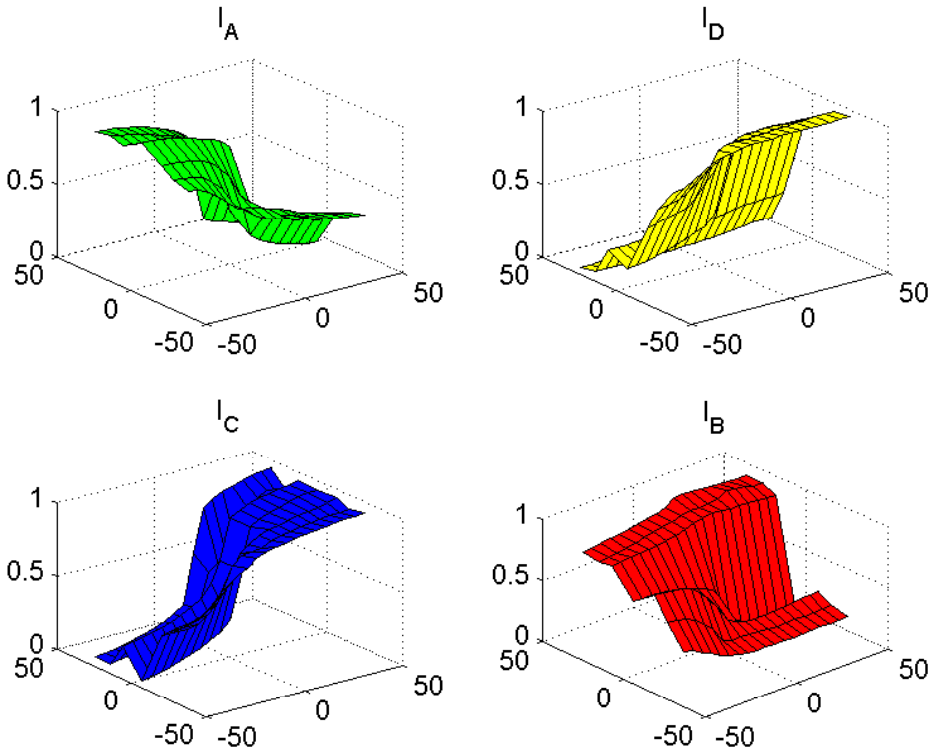

Figure 4.13: Normalized output currents for all four photodiodes with colors corresponding to each region, as in Figure 4.3. Measurements were made sweeping both θ_x and θ_y.

an analog-to-digital converter (ADC) needed to distinguish a 1° change in inclination (Table 4.1). A large measurement range, $\pm 36.25^\circ$, is possible with just a 12 bit ADC.

Each photodiode in our system produces a current which is used to find the *x* and *y* positions using equations (4.2) and (4.3). These calculations in the current domain can be implemented through translinear circuit principles [62]. Translinear circuits rely on an exponential relationship between current and voltage; therefore, they are commonly implemented using either bipolar transistors in the forward-active region or MOS transistors operated in subthreshold. Analyzing the multiplier/divider circuit

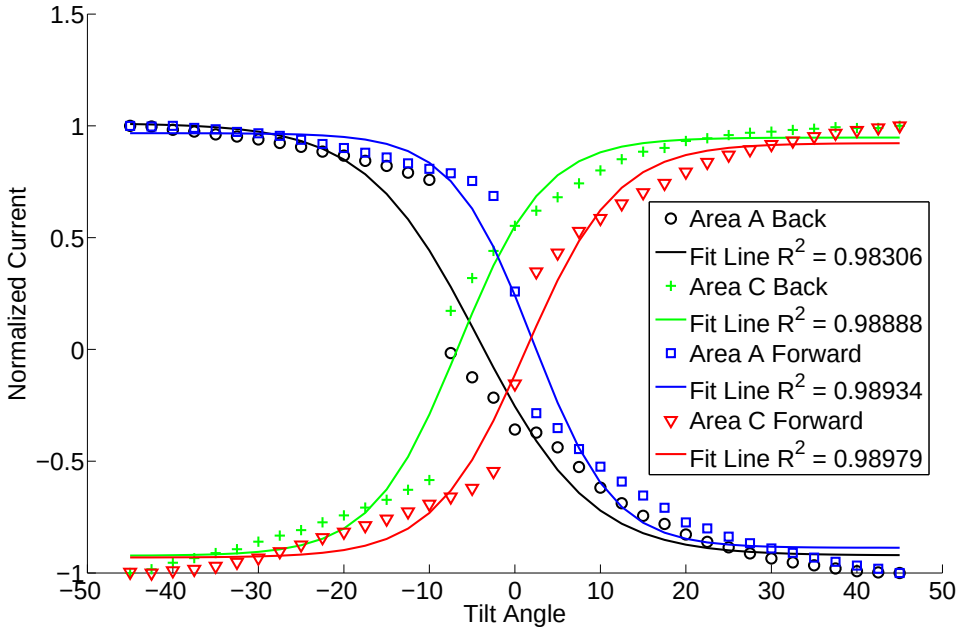

Figure 4.14: Normalized output currents for photodiodes A and C as the inclination is swept in both the increasing (forward) and decreasing (backwards) directions.

Table 4.1: Measurement range where a 1° tilt change can be distinguished for a given number of ADC bits.

ADC bits	Inclination range
6-bits	$\pm 3.75^\circ$
8-bits	$\pm 18.75^\circ$
10-bits	$\pm 28.75^\circ$
12-bits	$\pm 36.25^\circ$
14-bits	$\pm 43.75^\circ$

shown in Figure 4.15 gives the translinear relationship

$$I_M(I_C - I_A) = I_{OUT}(I_C + I_A) \tag{4.6}$$

and by rearranging we get

$$I_M\left(\frac{I_C - I_A}{I_C + I_A}\right) = I_{OUT} \tag{4.7}$$

which is equivalent to equation 4.2 with I_{OUT} equal to the x position value multiplied by a constant current I_M. Completing the calculation with just a few transistors reduces the complexity of a system using our sensor. Furthermore, the translinear circuit has very low power consumption compared to operational amplifier signal operations. Future implementations of this tilt sensor could incorporate the circuit within the device to reduce the readout complexity and processing.

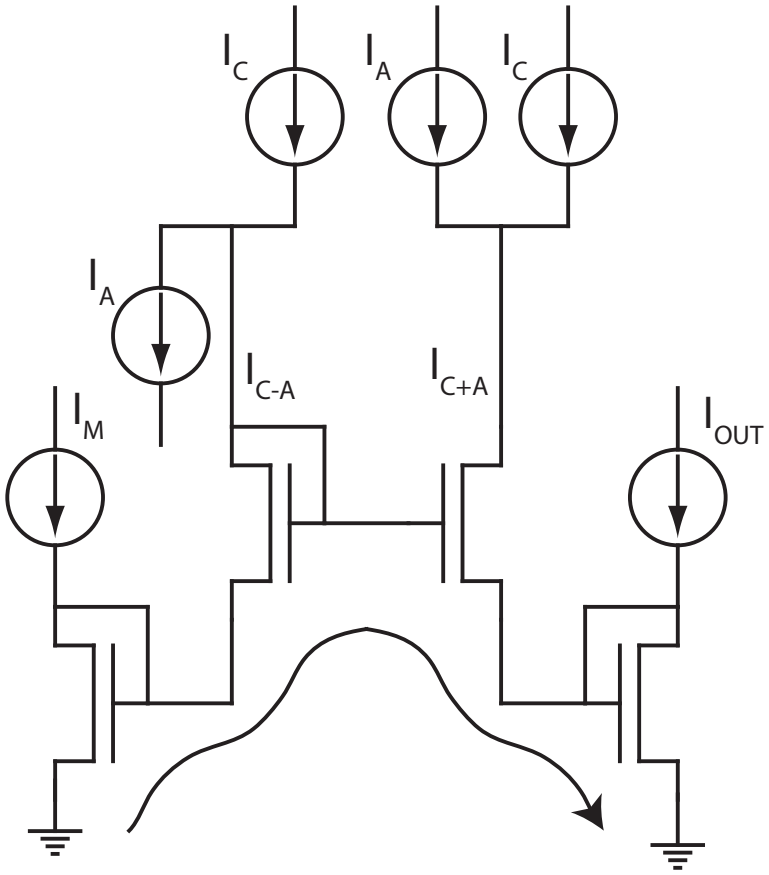

Figure 4.15: A schematic for a multiplier/divider circuit is shown with the translinear loop indicated using an arrow. The output current, I_{OUT}, is equal to the result of equation (4.2) multiplied by a constant current I_M.

This system presents a significant advance in tilt sensor systems. The system utilizes a fluid pendulum design for optical measurement. The system is not susceptible to many of the environmental noise problems that occur in other systems that measure

capacitance or resistance. Additionally, our fully-differential measurement allows for variations in bubble size if that were to occur. The system size and operating principle make it very attractive for numerous tilt sensing applications. Accelerometers are often used for tilt measurement, but they contain fragile parts which are prone to break when dropped or vibrated violently. Our design has no moving parts so it is more robust and therefore better suited for certain applications.

The position of the bubble is determined by a differential measurement of pairs of diodes so there are no restrictions on the intensity of light required to operate. The simple bubble-positioning method used for this sensor allows easy system integration without the use of complex readout circuits. The device also has potential to be self-powered by energy harvesting through the operation of the photodiodes in photovoltaic mode in conjunction with the use of optics instead of an LED. Operating without an external power supply would be advantageous for applications in long-term monitoring where constant powering is not available. The majority of the device fabrication is done in a commercially available MEMS process which allows for mass production and a low cost per device.

Chapter 5

MEMS SUN TRACKER

Solar energy has emerged as one of the best options for alternative energy. It is widely used in both industrial and domestic applications with increasing popularity. Data from the U.S. Energy Information Administration indicates that solar panel production in the U.S. in 2009 was more than 14 times the production in 2000 [63]. The number of companies producing solar modules increased from 21 to 101 over the same time frame. As solar photovoltaics become more efficient, these numbers are sure to continue rising.

The amount of power produced by solar photovoltaics is of course dependent on the amount of sunlight striking the device. Solar cells need to be in direct sunlight as much as possible to optimize power production. The sun is constantly moving across the sky, thus systems for tracking the position of the sun and adjusting solar panels to account for sun movement have received considerable attention, both for terrestrial collection systems [64–66] and satellite collection modules [67] [68]. The principle component of a sun tracking system is a sunlight position sensor. There are a number of different setups for solar tracking including both active and passive systems. Passive solar trackers provide an elegant solution for solar tracking: heat from the sun moves a low boiling point fluid from side to side and then relies on gravity to adjust the mounted panels. An example of a passive solar tracker is shown in Figure 5.1. Passive solar trackers have no motors, gears, or other controls that can fail but still require complicated damping cylinders and the entire setup can still be expensive. Passive systems also take time to reset from the evening position in the morning thus losing some solar radiation (*i.e.* the trackers don't like mornings, just like me). Passive systems are also susceptible to strong winds and can lack accuracy.

Figure 5.1: A commercial passive tracking system manufactured by Zomeworks Corporation is pictured [69]. Low boiling point fluid is contained in the tubing running along the left and right sides of the solar panels. Solar heating causes the system to track sun position.

Active trackers come in many different configurations classified by the directions the panel alignment can be adjusted. The two methods for controlling the panel position are open-loop tracking systems or a closed-loop tracking systems [65]. Open-loop systems simply adjust the position of a solar panel by a predetermined amount without knowledge of the quality of this adjustment. These algorithm-based control systems utilize a solar irradiation geometry model which adjusts the position of the tracker given the date, time, and location of the solar panel. The systems do not observe the output of the process being controlled so there is no adjustment for errors. While these systems are less expensive, they require complex microprocessor programming and can still produce alignment errors.

A closed-loop tracking system uses feedback control principles to ensure the correct position of the panels. Closed-loop systems sense the position of the sun, calculate the error, then adjust the position to minimize error. The feedback configuration

ensures that the panels are always aimed directly at the sun. However, these systems are not without fault. The sensors could give an incorrect position due to interference and reflections from passing clouds. These systems typically employ photodiode sensors to determine sun position. A closed-loop system is especially necessary for satellite-based solar applications. Because of the zero gravity environment and unpredictable position and orientation, passive and open-loop tracking options are not possible.

The following work presents a novel method of creating a miniature sun position sensor for use in a closed-loop sun tacking system. Most of the device fabrication is performed in a commercial MEMS process. Using a commercial process allows us to take advantage of the regulated manufacturing process to create miniature sensors with precision control over their dimensions and therefore higher repeatability. Because the design is made almost entirely in a commercial MEMS fabrication process, the device can be mass produced at a low cost.

5.1 Background

Recent work in sunlight positioning sensors has yielded large, complicated devices [67]. However, a straightforward method of creating a sun position sensor is well-known. The uncomplicated design uses a pinhole to allow a small light spot to reach the surface of a detector [70] [71]. A position-sensitive detector (PSD) is a common device for detecting the position of such a light spot.

PSDs function by comparing relative magnitudes of photocurrents produced when light strikes a photosensitive region. There are two main designs for PSDs: lateral effect photodiodes, made from a single photodiode area with multiple connection points, and quadrant detectors, made from four equal-area photodiodes [72]. Both designs determine position by taking a differential measurement. Lateral effect photodiodes utilize the lateral photoelectric effect to produce a position-dependent differential photocurrent [73]; quadrant detectors rely on the spatial arrangement of four photodi-

odes to allow subtraction of opposing areas. Both types of devices have widespread uses in sensing motion, vibration, alignment, and leveling. Quadrant photodetectors have seen especially widespread use in laser centering applications for CD and DVD players.

Recent research on pinhole type sun position sensors has focused on improving the complete sensing system while still using a PSD. Advances thus far have focused on concurrent measurement of light at different frequencies [74] or utilizing multiple pinholes to get a more accurate measurement [75–77]. The work by Chen *et al.* recognized the nonlinearity in the output of pinhole sun position detectors and therefore modified the shape of the pinhole to compensate [78]. However, improvements to sun position sensors in terms of a smaller device size and uncomplicated manufacturing have received less attention. Work by Quero *et al.* demonstrated adapting microelectromechanical system (MEMS) technologies to create sun sensors without unreliable macroscale components [64]. However, their devices still required significant assembly since the pieces were all produced separately.

5.2 Principle of Operation

The presented sun sensor uses a negative pinhole design to cast a shadow on a quadrant PSD. Larger photocurrents are produced with this design because light strikes a larger portion of the PSD. Generating larger currents also achieves a higher signal to noise ratio. The larger signal comes at the cost of some device sensitivity. However, because the energy of a direct incident light beam drops off as a function of cosine [79], a 1° misalignment only causes a 0.015% loss in power. The low loss from a slight misalignment indicates that a high accuracy is not imperative for sun position sensing applications and can be sacrificed to create a smaller device. Furthermore, our device produces analog outputs which allow for simple incorporation into a feedback tracking system.

Our sun position detector uses a quadrant photodetector layout to determine the position of a shaded area. The photodetector region is covered with a layer of borosilicate glass. An opaque circular shield on top of the glass blocks light from reaching the surface. The operation is illustrated in Figure 5.2. Inclination relative to the direction of a uniform light source (such as the sun) causes complementary exposure and shading of opposing photodiodes. The relationship between outputs is used to find the centroid of the shaded area. The position of the centroid determines the angle between the normal orientation of the device and the light source. The design has two pairs of opposing photodiodes allowing for simultaneous measurement along two axes.

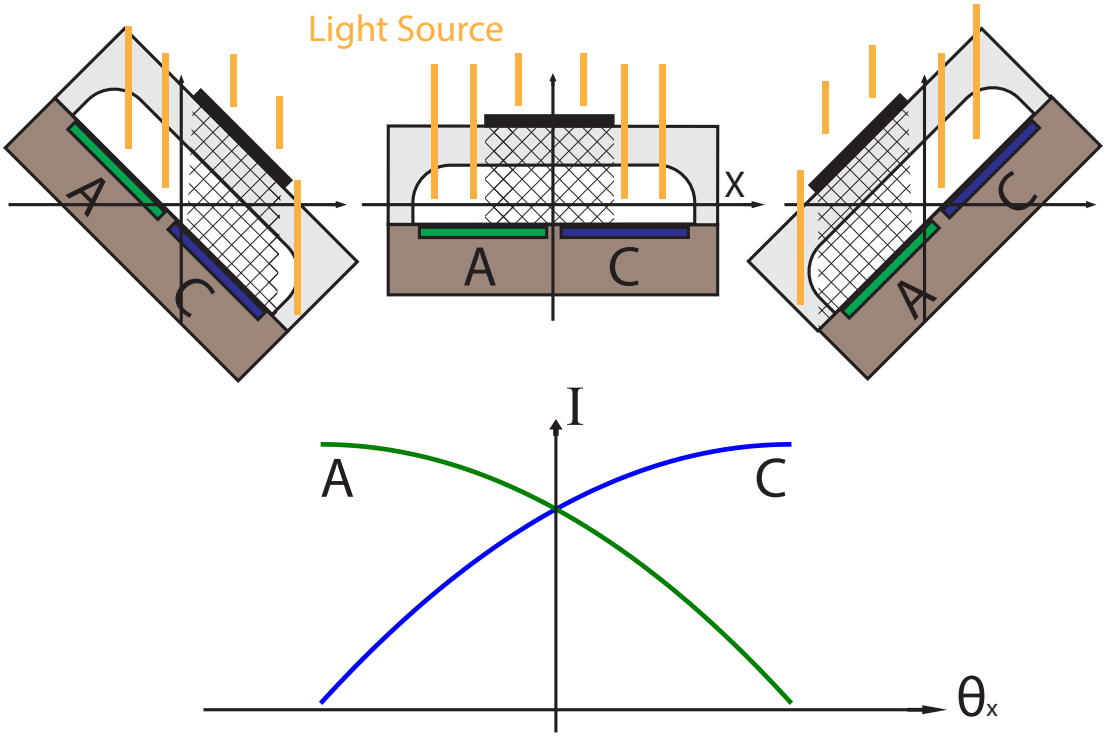

Figure 5.2: Principle of operation for the sun position detector. The output current (I) of opposing photodiodes changes due to variations in the orientation relative to a uniform light source. The lower half of the glass over the photodetectors was isotropically etched for a different device using the same sensors. The cavity is not needed for this system to operate.

There are a number of trade-offs in the design of a spot (or shadow) PSD quadrant photodetector. The size of the spot affects both the resolution and the range of the device. A smaller circle gives a greater resolution but decreases the range of the device. The distance between the shield and the photodetectors also affects both resolution and range; a larger distance causes a faster moving spot and therefore greater resolution at the expense of range. Other factors that affect either resolution or range are the size of the photodetector area, the gap in between adjacent photodiodes, and the parameters of the photodiodes themselves (*i.e.* noise, gain, etc.). We chose to design our device to achieve a good balance between range and resolution while minimizing the total size. We minimized size by placing the shield very close to the photodiodes. The close proximity along with a large shield area gives a large working range while the resolution is still adequate for sun position sensing.

Device Geometry

Each quadrant of the PSD design is a $45-45-90$ right triangle with a base of $b = 2\,mm$ and an altitude of $a = 1\,mm$ as illustrated in Figure 5.3. The shield is placed on top of a $500\,\mu m$ thick layer of glass that was anodically bonded to the surface, therefore the shield distance is $d = 500\,\mu m$. We chose a shield size of $1\,mm$ across to allow the device to have an operating range between -45° and $+45^\circ$ along each axis of tilt. We selected a circular shield shape for easy fabrication.

The expected area exposed to light is estimated using the geometry shown in Figure 5.3. The distance h, the height of the exposed region of the photodiode, changes with the angle from the uniform light source. The value of h relates to the inclination, Θ, by a cosine function. Because our device only operates from -45° to $+45^\circ$ we can approximate the change in h to be linear to a change in Θ. If we ignore the curved shape of the shadow caused by the circular shield we can further simplify the exposed region to be a trapezoid. This assumption allows us to calculate the exposed area, A, to

be

$$A = bh - h^2 \tag{5.1}$$

With the given dimensions of the device we expect the exposed area, and therefore the output current I, to vary with angle as seen in the graph in Figure 5.2. The output current (I) of each photodiode region is not linear with a change in angle. The non-linearity causes the theoretical output current of each photodiode to be approximately 75% of its maximum current when aligned normal to the light source.

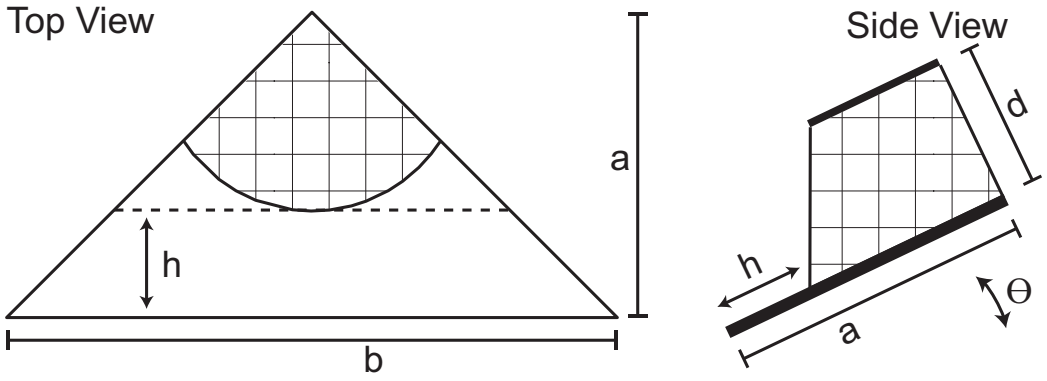

Figure 5.3: Top and side view geometry for one of the photodiode regions. The distance h changes relative to the device orientation.

All four photodiodes are oriented 45° off-axis from the square photosensitive region (which we assume to be oriented with the x and y axes) and have equal area. The photodiode arrangement is shown in Figure 5.4. The four output currents I_A, I_B, I_C, and I_D are used to find the position of the centroid of the shadow on the x and y axis with the same equations ((4.2) and (4.3)) as used in the tilt sensing device in chapter 4. The angle of inclination from a uniform light source can be calculated from the measured x and y values after the device has been calibrated. Using the expected results shown in Figure 5.2 with equation (4.2) gives a nearly linear relationship between x and Θ_x. The symmetry of our device gives a similar linear relationship between y and Θ_y.

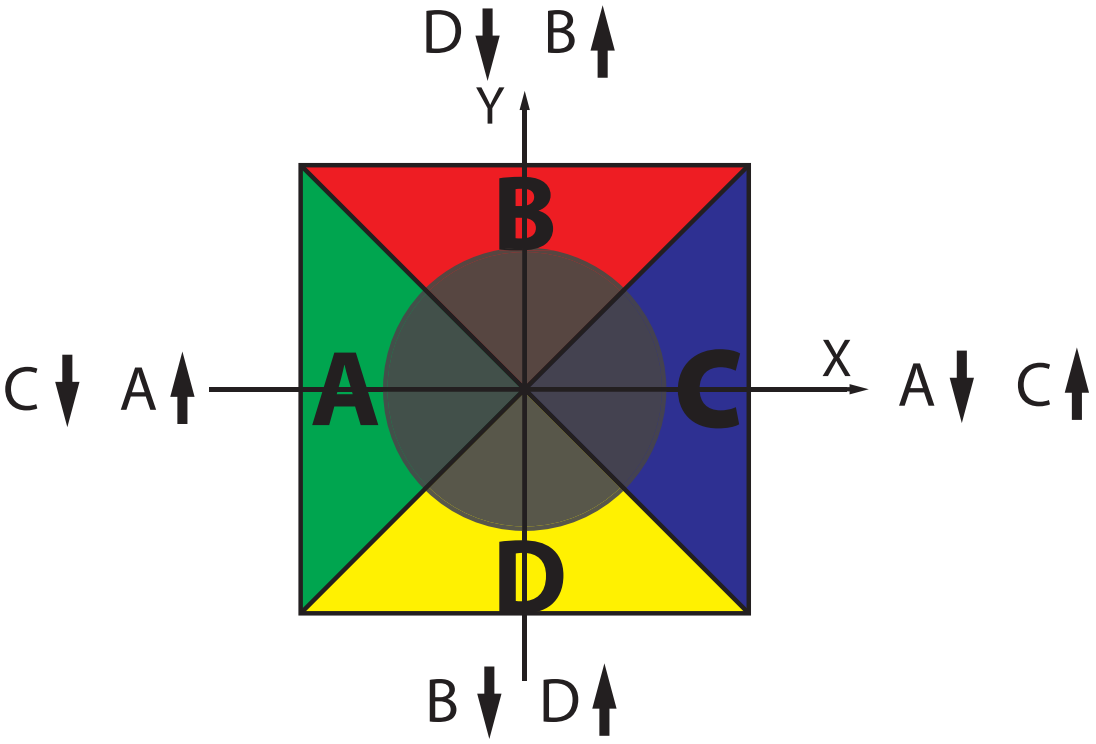

Figure 5.4: Top view of photodiode layout. A circular shield is centered over the detection region. The currents in each region increase and decrease as indicated with changes in angle of incidence of a uniform light source.

5.3 Fabrication

The sun position sensor was designed and fabricated in the same SensoNor Multi-MEMS process described in section 4.2. The same photodiode layout was also used. However, only the closed cavity design was used for our sun position sensor because it allowed us to attach a shield directly over our sensing region at a close distance controlled by the fabrication process.

A circular shield was made using a $1mm$ round punch (Syneo, West Palm Beach, FL, USA) to cut a hole in copper foil tape (Techni-Tool, Worcester, PA, USA). The circular piece of copper tape was adhered to the top glass surface with the aid of a dissection microscope. The shield is shown attached to the glass in Figure 5.5. We

also attempted to form a shield using aluminum foil. The aluminum was more flexible than the copper so it was harder to cut evenly. The aluminum also required superglue to attach the shield to the glass. The attachment proved messy and difficult so we instead proceeded with copper tape. The fully assembled MEMS device was wire bonded to a 24 pin sidebraze DIP (KD-S86898-B-1, Kyocera, Kyoto, Japan) for electrical access and ease of handling.

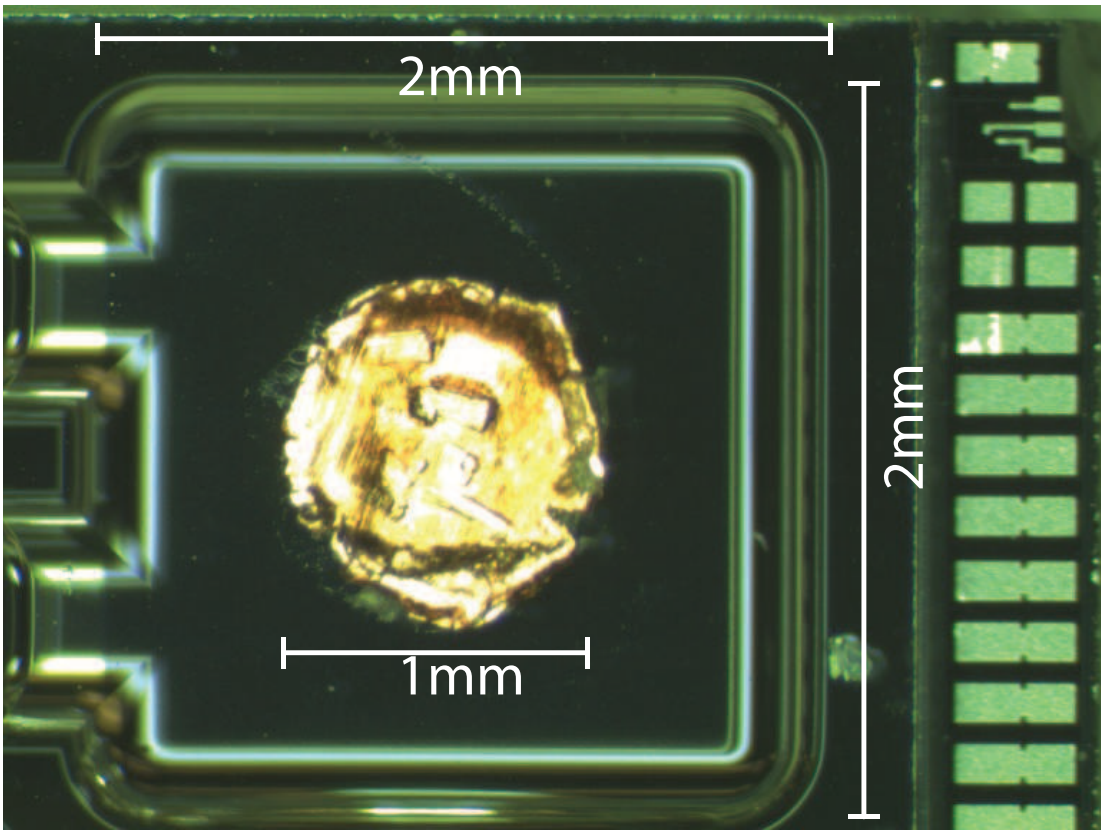

Figure 5.5: Micrograph of MEMS chip after application of circular shield. The base device is identical to the tilt sensor described in chapter 4.

5.4 Experimental

Testing of various angles of inclination was performed with a Hi-Tech HS-645MG servo motor (Hitec, Poway, CA, USA) attached to a moveable platform. A model of the platform is shown in Figure 5.6. The servo motor is controlled with Motor-Bee

control software (PC Control Limited, Kettering, Northamptonshire, UK) and is able to adjust the angle of inclination in 1.25° steps using a graphical user interface. The packaged chip was placed into a socket mounted on a board on the tilt platform. Attaching the chip to the board with a socket also ensured that the package, and therefore the chip itself, is aligned with the axis of tilt. Electrical leads from the board allowed connections for measurements.

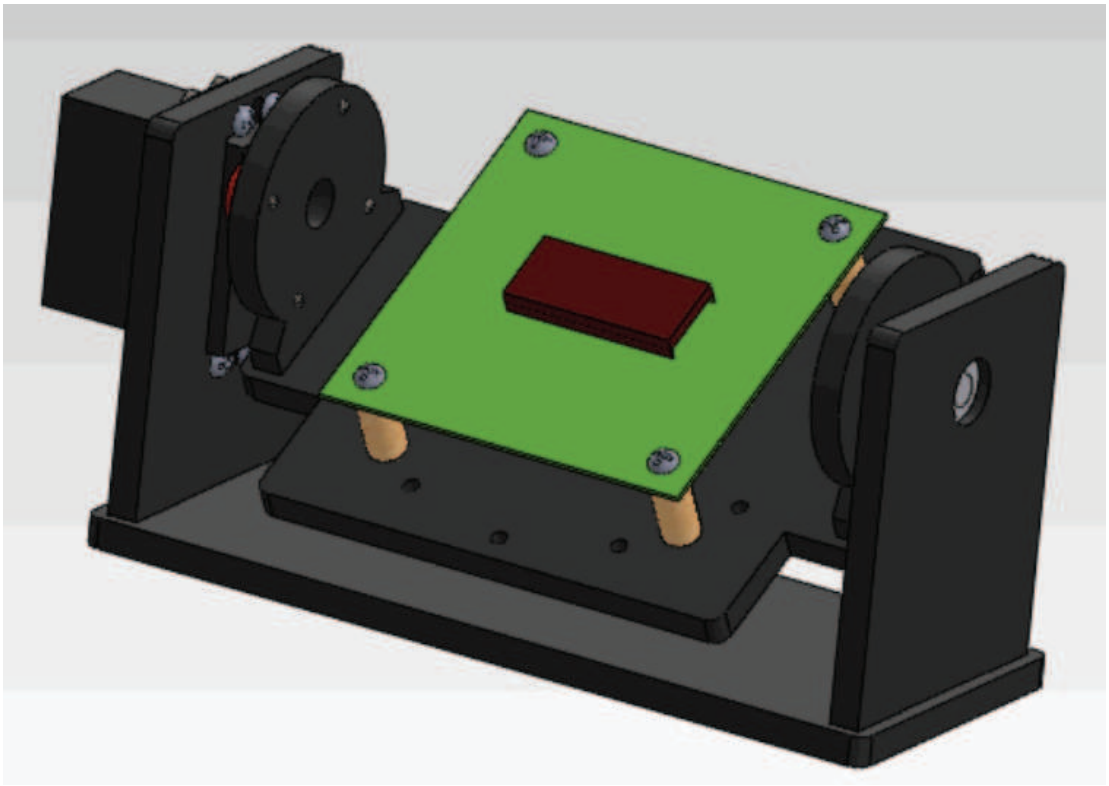

Figure 5.6: A model of tilt testing platform shows the location of the DIP package containing the MEMS chip. A light is suspended above the device to simulate a uniform light source (not shown). The tilt angle is controlled through a computer and allows 1.25° steps.

Photodiodes were operated in photoconductive mode during testing by applying a $5V$ reverse bias with a DC power supply. The p-doped side of each diode was connected to one channel of a Keithley 2636A source measurement unit (Keithley In-

struments, Inc., Cleveland, OH, USA). Each channel on the source measurement unit was set to source $0V$ and measure current.

The rotated layout of the photodiodes within the cavity allows for simple testing of the inclination along the x and y axes independently. The device is easily aligned within the DIP, therefore the x and y axes are aligned with the socket on the test platform. The alignment enabled us to sweep the tilt angle in one direction independent of the other to fully characterize the relationship between the output of the photodiodes and the angle of incidence of a uniform light source. Testing was performed by tilting the stage from -45° to $+45^\circ$ along the x axis and recording the current in each photodiode. A uniform light source was simulated by suspending a spot light approximately $0.5m$ directly above the chip during testing. The light source was a simple lab light using an MB-1142 miniature bulb rated to 18.4 Watts. All testing was performed in a dark room to prevent interference from indirect light sources.

5.5 Results

The results from testing changes in angle of incidence in the x direction are shown in Figure 5.7. As the angle is increased, I_A decreases and I_C increases; this was due to the shadow covering and uncovering the two regions. The shapes of I_A and I_C are close to the predicted shapes but shifted toward the positive Θ_x side. The shift suggests misalignment of the shield or the testing setup. I_A and I_C reach an equivalent point much closer to their maximum values than their minimum value which also agrees with our calculated prediction. As expected, I_B and I_D are nearly identical. The difference in output levels for I_B and I_D suggests misalignment of the circular shield in the y direction.

Mapping of the results using equation (4.2) is shown in Figure 5.8. Because our individual channel results, shown in Figure 5.7, are shifted to the positive x direction, our mapped results show a similar shift. A fit line for the linear region gives an R^2 value

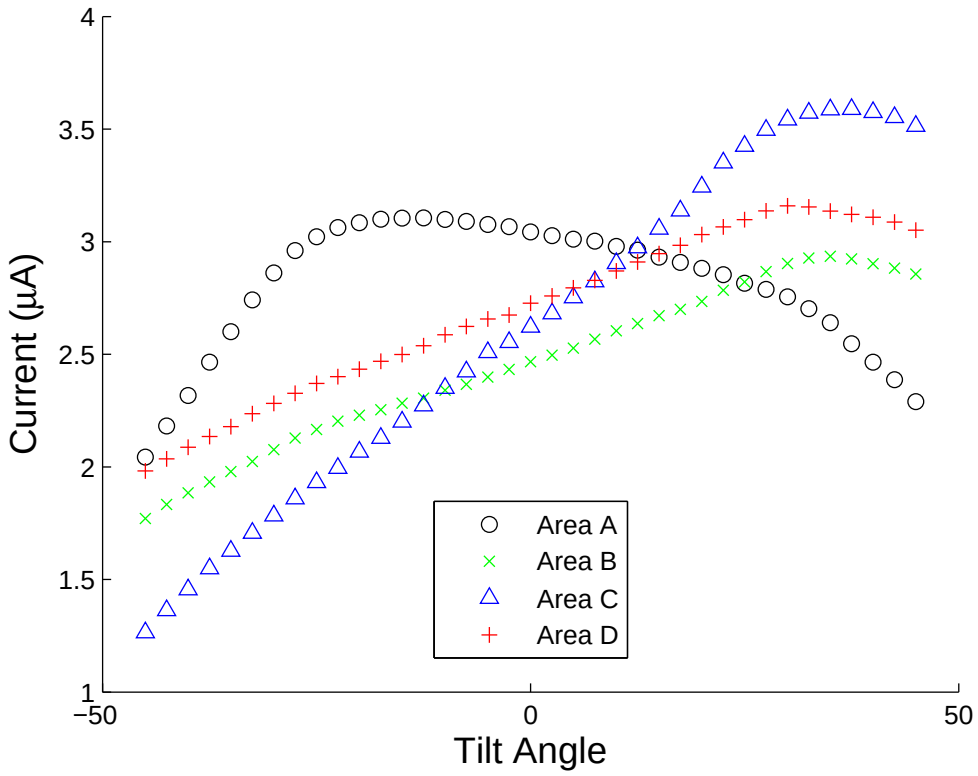

Figure 5.7: Current of the four photodiode regions as the angle of incident light changes in the x direction. I_A and I_C show inverse behavior as the angle is changed. I_B and I_D are nearly equivalent throughout angular changes because there is no change in the y direction. Offsets and non-ideal shapes are likely due to misalignment of the shield.

of 0.995 suggesting a very good correlation. The sensitivity of the device is the slope of the fit line. Over the total output range of the mapped signal, the slope is equivalent to a 1.33% change in output per degree.

Our sensor showed some irregularities in operation that can be attributed to our post-processing. The shield cutting process yielded an imperfect circle. The irregular shape affects the shadow geometry and therefore the measured signal. Additionally, centering the shield over the quadrant photodiodes was difficult. Misalignment on the order of tens of microns can affect the measured light angle by multiple degrees. A more controlled shield size and placement could be created by a lithographically de-

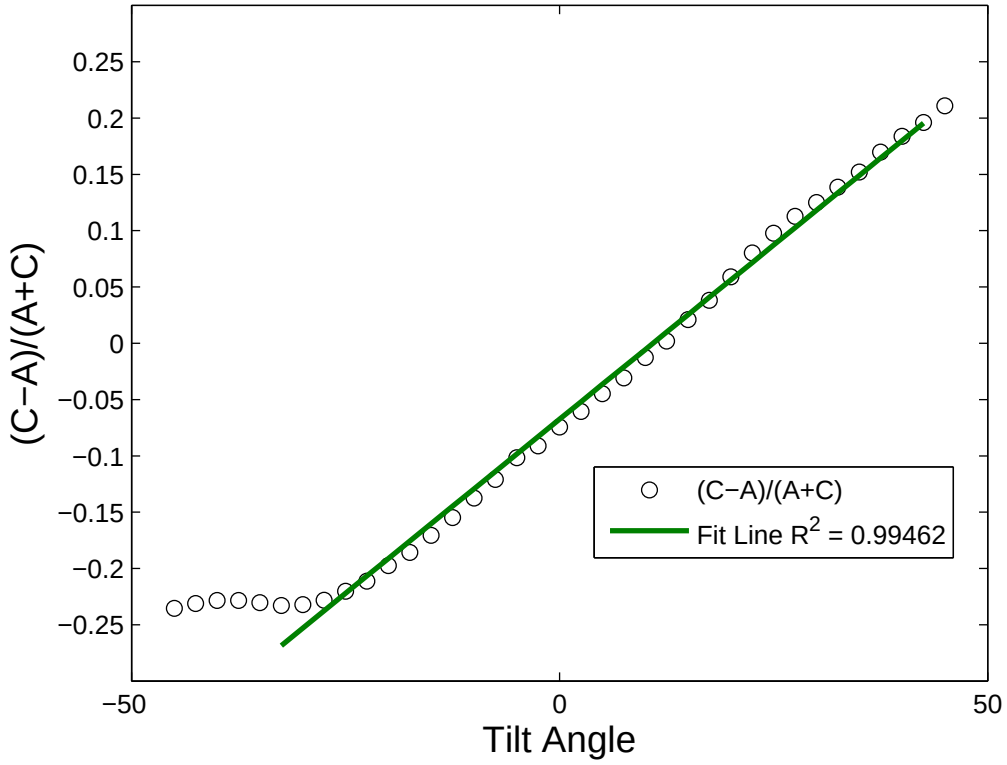

Figure 5.8: Outputs of photodiodes A and C mapped to angle of incident light using equation (4.2). The mapped output is shifted toward the positive Θ_x side, probably due to poor shield alignment. The flat portion of the graph demonstrates the limit to the sensing range.

fined metal deposition, but this would add significant complexity to the device post-processing. Error caused by misalignment could be compensated by addition of an offset or through implementation of the sensor in a closed-loop feedback system [64].

Additional error in the center value of our output signal can be attributed to our method of providing a uniform light source. During testing we used a stationary lamp to simulate a uniform distribution of photons. However, the lamp has imperfect alignment with the inclination of the device. The lamp intensity was also non-uniform. Thus the photon distribution varied as the device was swept through various inclinations. We expect better results when using the device with a uniform source, such as sunlight.

The MEMS chip used for this study was also used for other experiments (Chapter 4). In the other work, the glass over the sensing region was etched on the bottom side to create both a cavity and accompanying access ports. The access ports and cavity are visible in Figure 5.5. The cavity was made with isotropic etching so the corners of the cavity have a curved profile. Light passing through the glass is refracted and therefore affects the output profile of the photodetectors. Future designs of a sun tracking sensor would not include etched regions.

This sensor is unique because of the small size, uncomplicated design, and minimal power consumption. The device was fabricated almost entirely in a commercial process, so it can be reliably reproduced. Placement of the shield is the only post-processing needed to complete the sensor. The angle of incident light striking the device is determined by a differential measurement. The differential measurement setup allows the device to operate independent of the intensity of the light. The output of the differential measurement shows a linear relationship between output and angle of incident light. The device has an operating range of $\pm 45^\circ$. Multiple devices positioned at different angles could provide a larger field of view. This device has the potential to be inexpensive to produce, therefore helping to decrease the total cost of a sun tracking system.

Chapter 6

CAPACITANCE MEASUREMENT

Capacitive sensing techniques have a wide range of uses including antibody-antigen recognition, bacterial growth monitoring, DNA detection, toxic gas detection, and cell localization and monitoring [80]. Regardless of the application, all capacitive sensing techniques have the same general principles of operation. The sensors, usually made with two closely placed metal areas, are exposed to an analyte, and the capacitance is measured. The addition of charged biological particles (proteins, antibodies, cells etc.) between the sensing structures changes the capacitance. Changes in capacitance occur due to changing either the distance term (d) in the standard capacitance equation $C = \frac{\varepsilon_R \varepsilon_0 A}{d}$ or the relative permittivity (ε_R). In biological applications, the charged electrode surface allows attachment of various particles; this is illustrated in Figure 6.1. The sensitive area can also be immobilized with antibodies for detecting the attachment of specific antigens.

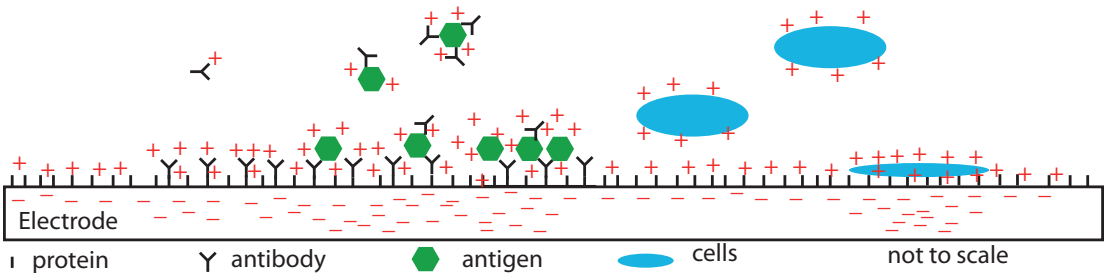

Figure 6.1: Capacitance sensors can be used to detect the presence of biological materials from protein or antibodies to cells.

This chapter presents two systems for capacitive sensing. The first system was designed to be used for a wide range of capacitive sensing applications. The other system was designed specifically for analysis of cellular level monitoring. Both systems have included design and packaging considerations for their integration into biological analysis systems.

6.1 Adjustable Dynamic Range Capacitive Sensing

The biological particles and agents that are potential targets for capacitive sensing vary in size and charge, making a universal system with a variable dynamic range very desirable. The capacitance sensor presented in this section is capable of providing accurate measurements over a large variation in sensing values. The system can switch from sensing capacitance changes down to the attofarad range, as was seen in some permittivity sensing [81], up to the nanofarad range, usual with sensing cell attachment [18] and proliferation [19]. The design of a circuit capable of functioning over such a large range can be accomplished using a single large dynamic range configuration. However, for applications with only small capacitance changes, the majority of this range would be unused resulting in an inefficient system. Additionally, the analog output from the system needs to be converted to a digital signal for recording. A single large range system would provide poor accuracy because the quantization error would be large compared to the signal's dynamic range. This system used a programmable gain circuit capable of matching the dynamic range of the circuit to that of the desired capacitance range. This means that regardless of the capacitance change for the experiment range, the specified capacitance range will utilize the full output voltage by tuning the gain of the system. This also means that the number of bits for an analog-to-digital can remain the same regardless of operation range.

Capacitance Sensing Circuit

The capacitance sensor circuit was implemented using a switched capacitor design and is shown in Figure 6.2. The circuit has two capacitors, the sensing capacitor C_S and the reference capacitor C_{ref}, which were designed with identical initial capacitance values. Exposing the sensing capacitor to a biological material (e.g. proteins, antibodies, cells, etc.) causes a capacitance change for the sensing capacitor only. That value was

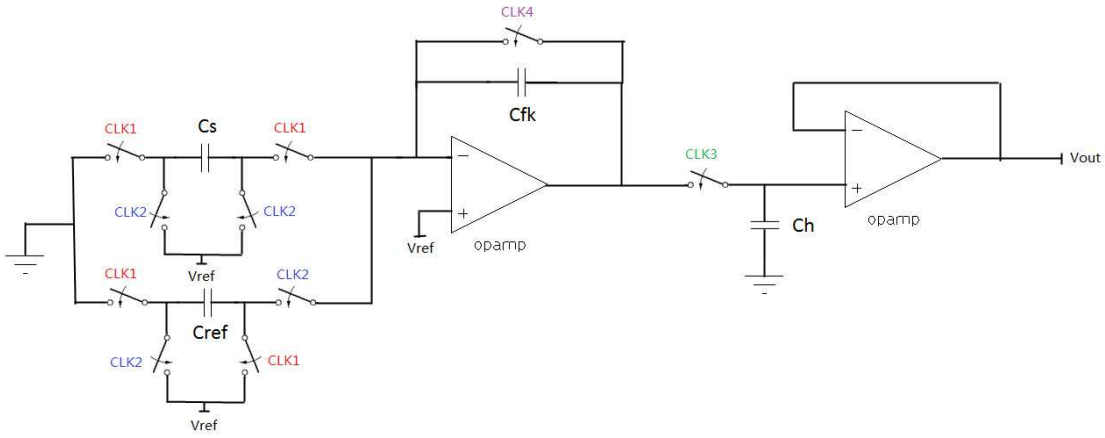

Figure 6.2: Switched capacitor circuit implementation of the capacitance sensor.

compared to a reference capacitance and the difference was calculated. The differences were summed to give a total capacitance measurement. Repeating this process an arbitrary number of times allows adjustment of the dynamic range.

To operate the circuit, both capacitors are charged using the same reference voltage, V_{ref}. All of the charge on the sensing capacitor is used to charge the large feedback capacitor C_{fk}, then the reference capacitor C_{ref} is used to discharge the same feedback capacitor C_{fk}. If there is a capacitance difference between the C_S and the C_{ref}, ΔQ charge will be left on the feedback capacitor C_{fk}. Therefore, after one cycle of charging and discharging, $\Delta Q = V_{ref}(C_S - C_{ref})$. This assumes the capacitance change on C_S is positive. If the charging and discharging repeat N times, the resolution of our sensor is increased N times since the total charge integrated on the feedback capacitor is $\Delta Q = N \cdot V_{ref}(C_S - C_{ref})$. For different applications, capacitance change may vary and the number of cycles N can be user-controlled with external clock signals (CLK3 and CLK4). The dynamic range of the sensor can be optimized by providing the correct external clock signals. The relationship between the voltage output and the capacitance change ΔC on C_S can be described as $V_{out} = N \cdot \frac{V_{ref}(C_S - C_{ref})}{C_{fk}}$. This equation assumes that all components are ideal. This assumption means that the non-zero resistance of

switches, the potential offset of the sample and hold circuit, any layout mismatch, any parasitic capacitances and all noise sources are not considered.

On-Chip Capacitance Structures

The chip was designed for direct interface with the analyzed biological solution with considerations for packaging and sensor interaction. The bond pads were isolated at one end of the chip instead of a normal ring of pads around the perimeter. This was designed to move the electrical connections as far away from the sensing structures as possible. An area without chip surface structures was also included between the bond pads and the sensing region to make sealing along the chip surface easier.

The chip capacitance structures were designed using the top metal of the process. Both capacitance sensing structures on the chip have identical interdigitated electrode designs and dimensions. The equal sizes are required for accurate difference measurements. The capacitance of the two sensors was not an issue because they are used in a differential measurement. The adjustable range design also allows adjustment for smaller or larger values. The total capacitance also depended on the permittivity of the solution the sensors contact, so exact values could not be calculated. The two sensing regions were placed with a gap between them to allow for greater flexibility in isolating the two sensors for difference measurements.

Circuit Simulation

The capacitance sensor was designed and fully simulated with transistor level components. The simulation environment tool used was Cadence IC 6 analog simulator; Cadence Spectre simulation models are provided by MIT/Lincoln Labs 3D SOI 0.15 μm technology design kit version is 3DIC 3.3.5. All of the switches were implemented with PMOS or NMOS transistors with minimum width and length for the 0.15 μm technology. The operational amplifier was a two stage design with an on-chip constant

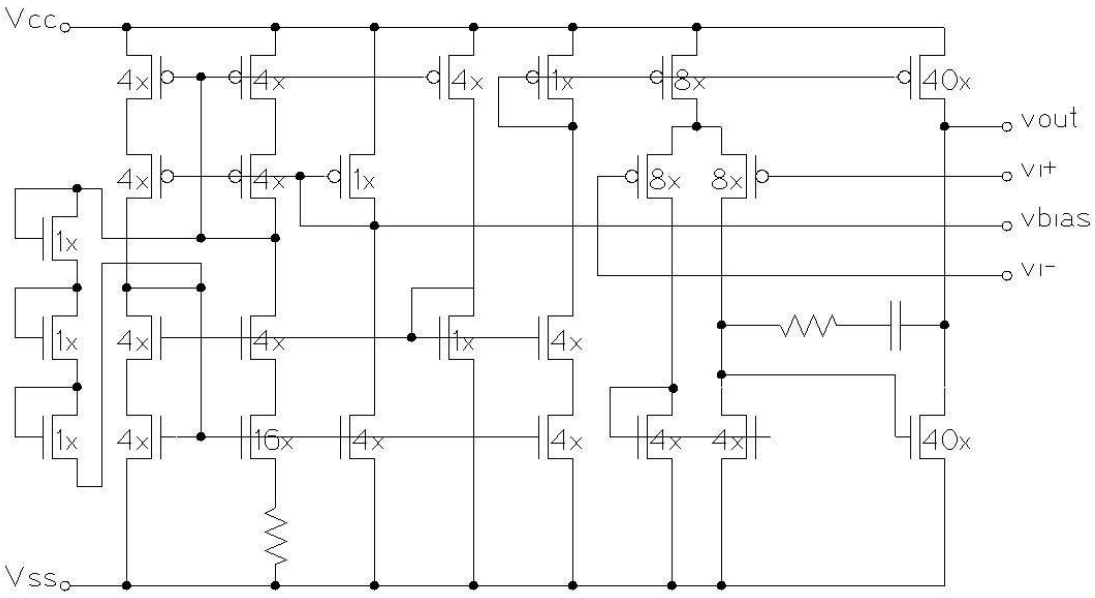

Figure 6.3: Two stage operational amplifier with on-chip constant Gm biasing schematic.

Gm biasing circuit. A startup circuit was also included to guarantee the working state of the current biasing circuit. The circuit schematic is shown in Figure 6.3.

Figure 6.4 (left) shows the results of a small capacitance change simulation where Vout (output node voltage at steady state) took slightly over 10 seconds to stabilize. Figure 6.4 (right) shows 3 complete cycles of charging and discharging simulation with the *voltage at feedback cap* waveform showing voltage changes from the difference in C_S and C_{ref}. The charging period started on the rising edge of the first pulse of the *charging phase* waveform after the *reset signal* goes to zero (in this figure it was the second pulse of the *charging phase* waveform). After *charging phase* goes to zero, *discharging phase* goes high, which makes the waveform at *voltage at feedback cap* go down. After one complete cycle of charging and discharging, a slightly increased voltage can be seen from *voltage at feedback cap*. This difference is caused by the difference in capacitance between C_S and C_{ref} which is determined by $\Delta V = \frac{V_{ref}(C_S - C_{ref})}{C_{fk}}$. Before the *sample clock* goes high, there are 3 cycles of charging and discharging which

makes the total voltage change at *voltage at feedback cap* $\Delta V = 3 \cdot \frac{V_{ref}(C_S - C_{ref})}{C_{fk}}$. The four-clock signals shown in Figure 6.4 are all generated on-chip. For different applications, the number of cycles of charging and discharging can be accurately controlled with two external clock signals.

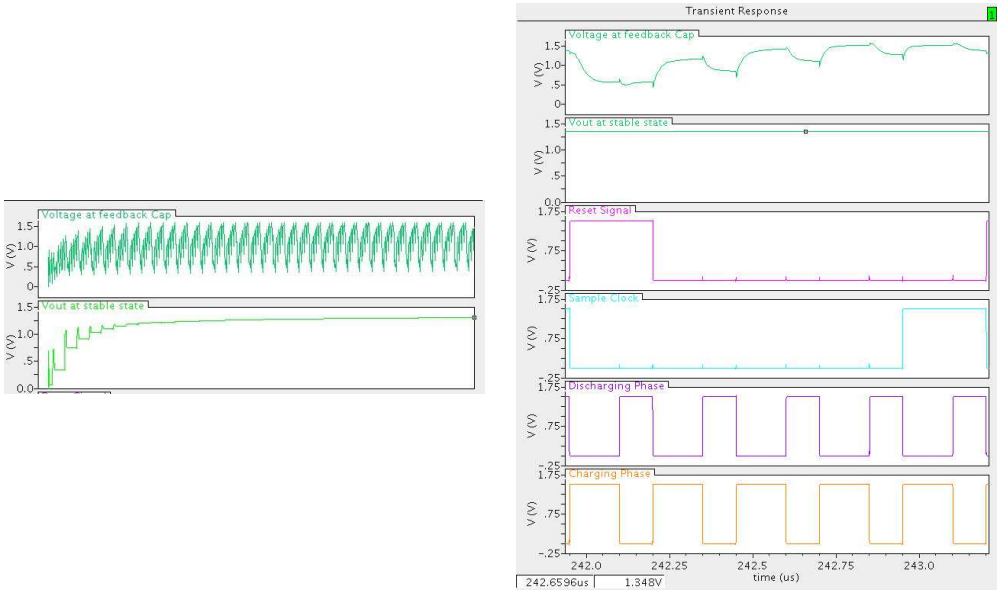

Figure 6.4: Transient responses over more than 40 microseconds (left) and 3 complete charging and discharging cycles (right) of the voltage at C_{fk}, voltage at C_{out} and four clock signals (CLK4: reset signal, CLK3: sample clock, CLK2: discharging C_{fk} phase, and CLK1: charging C_{fk} phase), respectively from top to bottom. The left figure demonstrates how the output voltage can saturate. The circuit can be tuned based on the saturation data to find the dynamic range of the system.

Results

This capacitive sensor has been fabricated in the MIT/Lincoln Labs 3D SOI 0.15 μm process. The fabricated chip is pictured in Figure 6.5. However, experimental characterization has not been finished. Initial testing showed the op amp is functioning properly with less than 1 millivolt offset with nominal common mode and supply voltages. The amplifier's offset is within several millivolts when common mode level and supply voltages are varied.

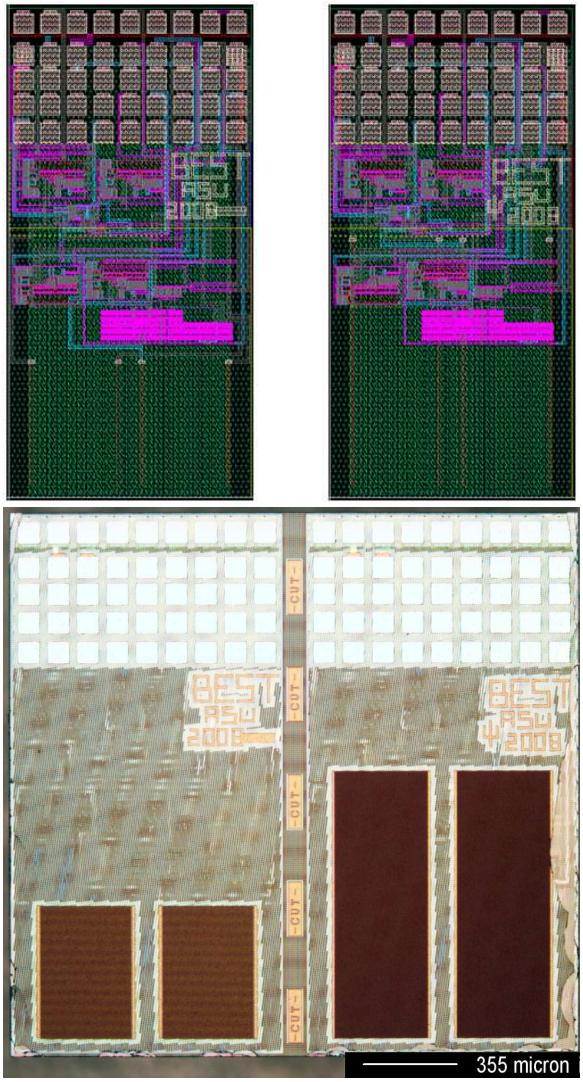

Figure 6.5: Layout (upper) and microphotograph (lower) of the two versions of the capacitance sensing chip.

6.2 Cellular Capacitance Monitoring

We have also fabricated a chip suitable for cell culture experimentation using the SensoNor MultiMEMS process. The MultiMEMS process consists of a silicon wafer, with various P and N doped regions (see Figure 4.2), between two layers of glass that can be etched to form cavities which expose the silicon surface. We have designed a cell culture area with an area of approximately 2.2 mm $\times$ 2.2 mm cut through the top glass

which is approximately 0.5 mm thick. This left an exposed area of silicon that was divided into four equal areas with each area containing a photodiode, an ISFET, and an interdigitated electrode structure (IDES) as seen in Figure 6.6. The IDES structures can be used for cellular level monitoring. The chip was fabricated but problems with post-processing did not allow extensive testing of this chip as a biological sensing environment. Therefore, this section presents the progress made on the post-processing and a cellular capacitance monitoring system using a commercially available sensor.

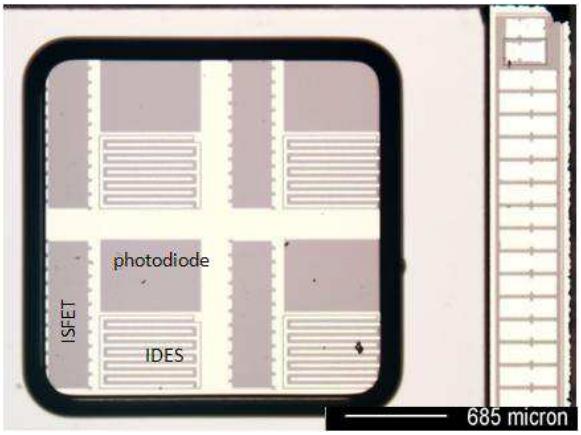

Figure 6.6: Top view of the biosensing array on the MultiMEMS chip with bond pad connections on the right. A 2×2 array of sensing regions can be seen with each region containing a photodiode, an ISFET, and an IDES.

Electroless Plating

The IDES structure was made using the aluminum top metal layer. Aluminum is the most common metal used in integrated circuit manufacturing processes, but significant problems arise when it contacts liquids, particularly biological media [82]. Aluminum forms a natural oxide of Al_2O_3, about 10 nm thick, when exposed to air. However, in saline based biological media corrosion occurs. This is due to a combination of the electrochemical potential and the pH of the solution as indicated in Figure 6.7. Chloride ions, which are abundant in media, absorb to the surface and create local acidic conditions that are harmful to both the aluminum and the cells potentially grown

on the metal. The use of copper in microelectronic fabrication is increasing, but it is affected by similar oxidation and corrosion problems.

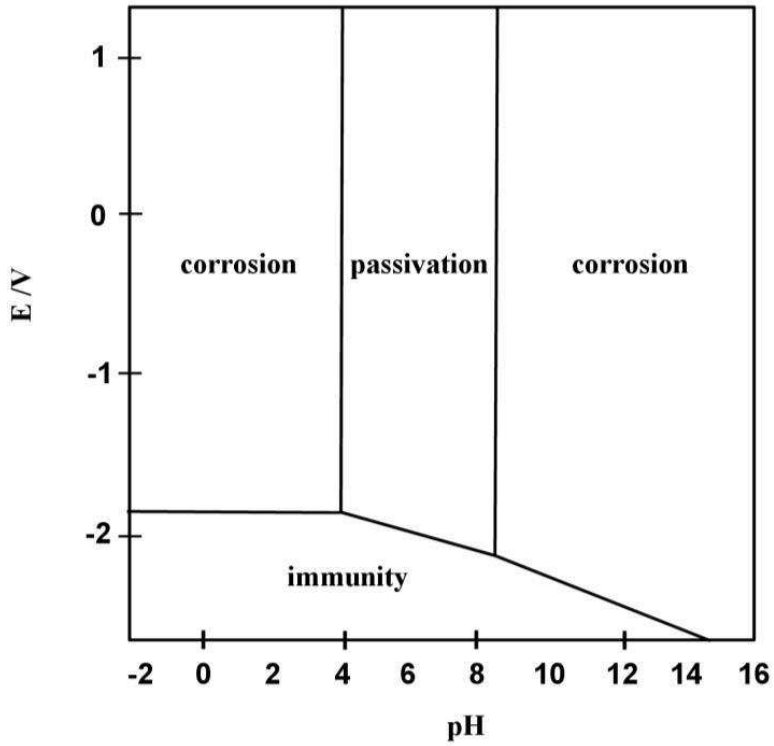

Figure 6.7: Pourbaix diagram for aluminum from [82]. The regions are determined from the Nernst equation and show a dependance on both pH and electrode potential (E).

To alleviate the problem of exposed aluminum we attempted to electrolessly plate the aluminum with gold. Electroless plating is preferred over electroplating because no electrical connection to the electrodes is necessary. The process involved first replacing the aluminum oxide layer with zinc, then plating a layer of nickel, and finally depositing a layer of gold [83]. Zincate, Nickelex, and Bright Electroless Gold were all obtained from Transene Company Inc. (Danvers, MA) and recommended immersion times and temperatures were followed. Our results were not ideal as seen in Figure 6.8.

The two biggest issues we encountered with electroless plating of gold on aluminum were a lack of adhesion and uncontrolled deposition. The initial zinc step, a two

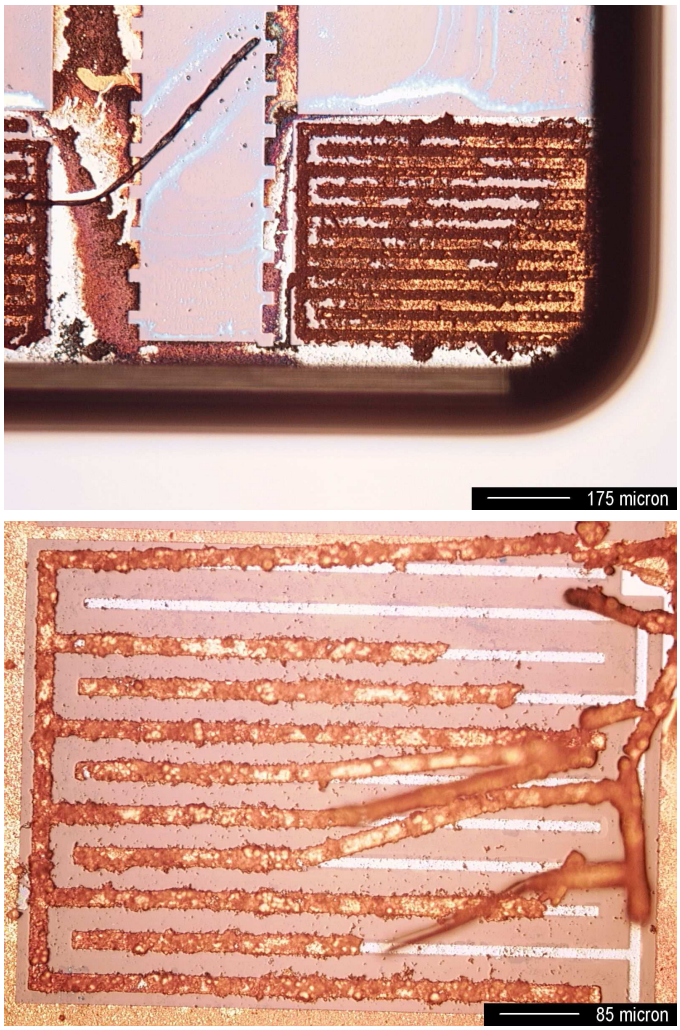

Figure 6.8: Non-ideal electroless plating results are shown. Shorting of electrical connections is seen in the top figure. Poor adhesion is observed in the bottom figure where deposited gold has detached from the aluminum.

step process to achieve better adhesion [84], is difficult to control for thin aluminum substrates because all of the aluminum can quickly be removed by zinc replacement. Initially we believed that post-processing exposed aluminum would be a viable method to create electrodes exposed to biological media but these results confirmed otherwise. We concluded that the aluminum metal layers would only be useful as sensors if a passivation layer is present. Alternatively, separate electrodes composed of a noble, biologically inert metal such as gold that are added after manufacturing would also be an

option. However, gold patterning would require lithography steps that would increase the complexity so avoiding this is desired.

6.3 Capacitance Sensor Implementation

Due to issues with electroless plating, the IDES we incorporated onto our chip could not be used for cell culture monitoring. Therefore, we tested cellular capacitance monitoring using the commercially available BioNAS metabolic chip SC1000 (BioNAS GmbH, Rostock, Germany). This chip has incorporated IDES structures made of palladium that are suitable for cell culture. For preliminary capacitance monitoring, we have measured the decay time of the capacitor on the BioNAS chip when it was arranged in a low pass filter configuration as in Figure 6.9.

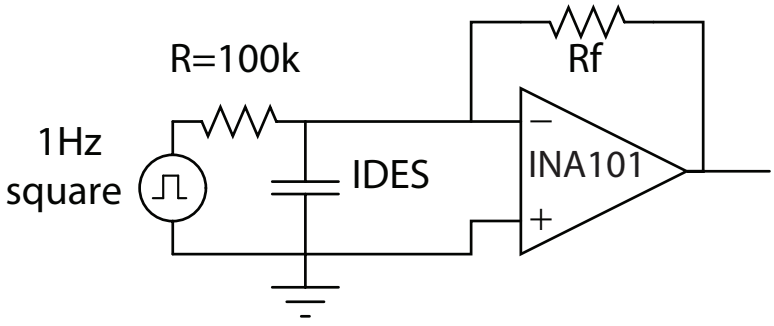

Figure 6.9: Low pass circuit configuration used to determine capacitance of IDES. The INA101 is an instrumentation amplifier with gain set by R_f. The input is a square wave with a frequency of 1 Hz and a duty cycle of 50%.

The output of the amplifier was read by a 1408FS data acquisition box from Measurement Computing (Norton, MA) and recorded using MATLAB (Mathworks, Natick, MA). The decay time was measured and related to capacitance using the equation $V(t) = V_0 e^{-\frac{t}{RC}}$, where $V(t)$ is the voltage at time t, V_0 is the initial voltage, R is the resistor used in the low pass filter, and C is the capacitance of the IDES.

Using this method, we successfully monitored capacitance in real time with readings about every 2 seconds - much faster than we would expect to see any changes

from biological phenomena. Figure 6.10 shows capacitance monitored over one hour with the addition of trypsin, a protease which detaches cells from the surface, to a confluent culture of NIH 3T3 cells after 30 minutes (1800 seconds).

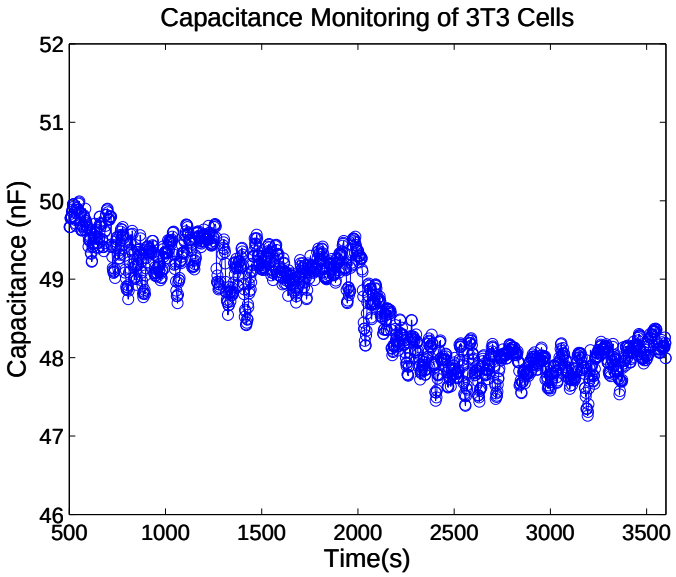

Figure 6.10: Raw IDES capacitance data. Cells were cultured on the BioNAS chip to confluence and continuously monitored for one hour. After 30 minutes (1800 seconds) trypsin was added to the solution, so a change in capacitance can be seen due to cells detaching from the surface.

These results demonstrate proficiency in obtaining capacitance measurements using an RC circuit and MATLAB for capacitance monitoring in real time. The fabricated system was designed for a similar measurement setup, allowing us to observe cell attachment and proliferation over time. Improved electroless plating capabilities would allow further work with this device.

Chapter 7

CARDIAC CELL MONITORING

Metal electrodes have been used successfully for measurements in biological environments for decades [85] [86]. Advances in microfabrication in the 1980s allowed for the development of microelectrode sensing arrays with dimensions similar to cells (ranging from one to hundreds of microns). Many sensors used today make use of these microelectrode arrays as passive elements of sensing systems [87–89], with the electrodes connected to separate signal processing hardware and software. Biological signals are small, usually only micro or millivolts, and small variations in these signals often contain large amounts of information [90]. Performing filtering and amplification of these signals after transmitting the signal away from the microelectrode sensing areas can add noise therefore losing some of the signal that contains biological information. With this project we work toward improving these active sensing devices by including the sensing microelectrodes on the signal processing substrate to provide for better resolution as well as lowering the total power consumption.

This chapter shows progress made towards combining the amplification and filtering of action potential signals of a cardiac cell with the sensing of the data onto one device. The improvements in resolution and power consumption will make this system well-suited for analysis of electrical recordings of living cells. This work was completed in collaboration with Jianan Song, a fellow member of Dr. Blain Christen's research group.

7.1 Background

Electrical signals in a biological environment occur due to the creation of ion gradients. The potential created across a cell membrane by ions is described by the Nernst

equation,

$$E_{ion} = \frac{60}{Z} \log \frac{C_o}{C_i} \tag{7.1}$$

where E_{ion} is the equilibrium potential for an ion, Z is the valence of the ion, and C_i and C_o are the intracellular and extracellular concentration of the ion respectively. Nerve and muscle cells are the most common types of electrically active cells, but some endocrine, immune, and reproductive cells are also capable of producing action potentials [90], making electrical recording applicable to many cell types. Cardiac cells are particularly of interest because of their strong electrical response and relative ease of culturing compared to nerve cells. In cardiac cells the three ions with the most influence on action potential firing are potassium, sodium, and calcium. The total potential for a cardiac cell will therefore be a combination of the Nernst equation for each of these ions while also accounting for the relative permeabilities of each ion. This is given by the Goldman equation

$$V_m = 60 \log \frac{P_K[K_o] + P_{Na}[Na_o] + P_{Ca}[Ca_o]}{P_K[K_i] + P_{Na}[Na_i] + P_{Ca}[Ca_i]} \tag{7.2}$$

where V_m is the total potential and permeabilities are given by P_{ion} [90]. The change in permeability of each ion is due largely to the opening and closing of ion channels during the action potential. The shape of an action potential produced in cardiac cells and the derivatives are shown in Figure 7.1.

The intracellular signal shown in Figure 7.1 is taken across the membrane. Microelectrode recordings only see an extracellular potential so the signal will be the second derivative of the action potential due to the low seal resistance between the cell and the electrode [91]. The second derivative signal occurs very quickly compared to the intracellular response making achieving better resolution even more important.

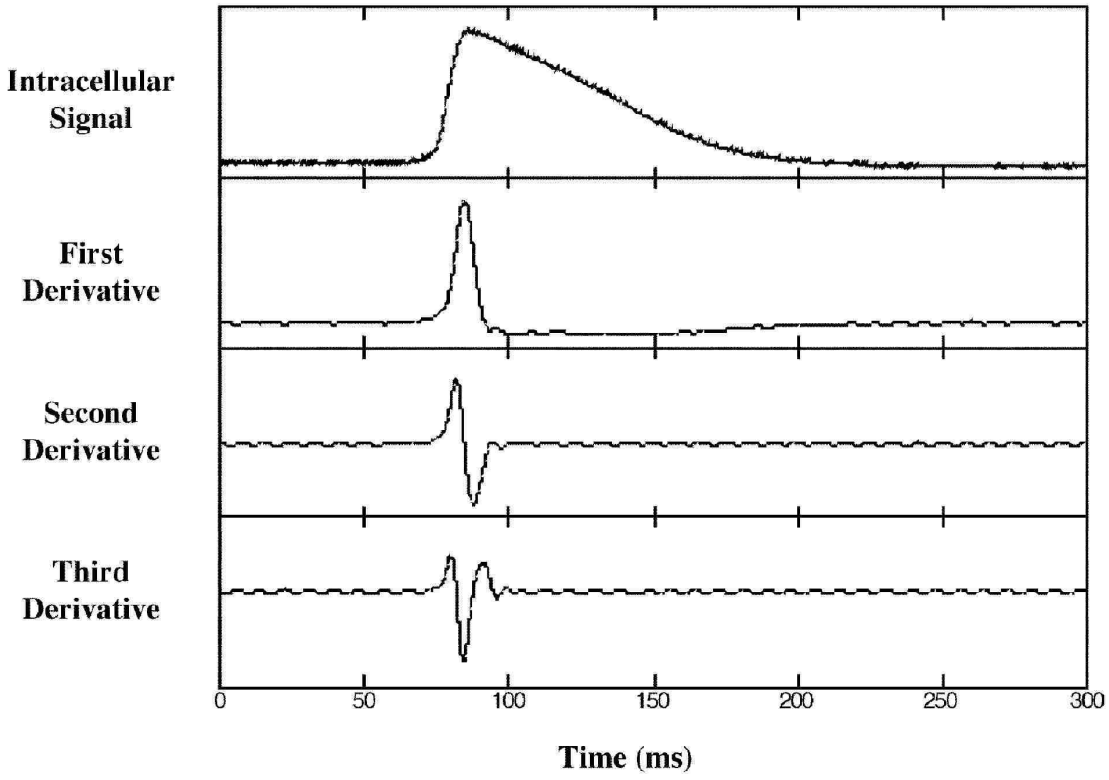

Figure 7.1: A typical HL-1 intracellular signal recorded with whole-cell patch clamp and the derivatives are shown. Extracellular recordings resemble the second derivative [89].

7.2 Circuit Design and Simulation

The challenge in measuring the extracellular cardiac action potentials is the small signal amplitude, low signal to noise ratio, and DC drift. Creating a biologically suitable interface for recording these signals is also difficult. The extracellular action potential is $1-2$ mV peak-to-peak with a bandwidth of 2 kHz to 4 kHz and a signal to noise (SNR) ratio of less than 10. For low frequency measurements the noise floor is pushed up by the flicker noise (1/f noise), so high-pass filtering was included. The first design receives the signal input from one sensing electrode and grounds the solution to the circuit ground as a reference. The second design utilizes two separate sensing electrodes

in a differential configuration to eliminate the need to connect the cell solution to the circuit ground. The circuit diagrams for two configurations of multi-stage amplification and filtering circuits are shown in Figure 7.2.

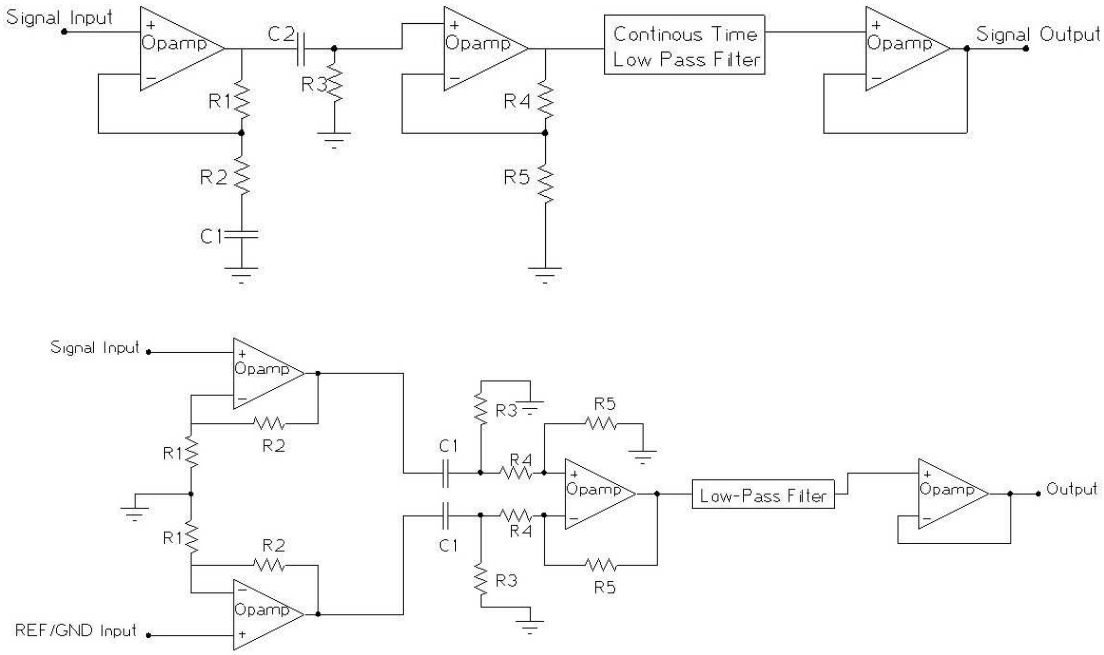

Figure 7.2: Single-ended and differential designs are shown. Both circuits contain two gain stages, a low-pass filter stage and a buffer stage. Values for components are shown in Table 7.1.

Single-Ended Configuration

Our single-ended configuration uses an electrode directly connected to the active components in the 50× pre-amplification stage. This maintains the signal to noise ratio since initial filtering with passive devices would further decrease the SNR. Rather than using a coupling capacitor to mitigate the effects of DC drift, we use a higher SNR design with a capacitor between the non-inverting gain resistors and ground. Additionally we add an AC coupling capacitor between the first and second gain stages to further remove the DC offset. This capacitor is also part of the high pass filter after the first stage that has a cutoff frequency of 6 Hz. The second stage of the circuit is a non-inverting

amplifier with a gain of 20. This is followed by a continuous time 10^{th} order linear phase low-pass filter with a cutoff frequency of 5 kHz which is defined by the ratio of resistors. The continuous time filter was selected because it does not require a clocking signal for operation that would add noise to the circuit and result in more components. The final stage is a buffer for a possible low impedance load. All of the amplifiers used are LinCMOS precision chopper-stabilized op amps with a low offset voltage of $1\,\mu V$, a low temperature drift of less than $0.003\,\mu V/^{\circ}C$, and a common-mode input voltage range that accounts for possible DC drift. The circuit was simulated in Cadence IC Virtuoso 5.141 Environment (Cadence, San Jose CA) with ideal components. In our experiments the transition time at the cutoff frequency is much shorter than simulation results since we use a 10^{th} order filter. The simulations show a 60 dB gain, low-pass filtering at 5 kHz and high-pass filtering at 6 Hz as expected from the design parameters in Table 7.1.

Differential Configuration

Although the single-ended design is sufficient for filtering and amplification, we can further improve the design with a differential configuration. Single-ended circuits are susceptible to many noise sources including induction noise. Differential circuits will improve the performance of the system by canceling out noise from connections and other parasitics. Since almost all of the noise is common to both input nodes, amplification circuits with good common-mode rejection ratio (CMRR) will be nearly immune to common mode noise. We have redesigned the circuit as a differential modified instrumentation amplifier. The differential configuration has a gain of 10 at the pre-amplification stage to give higher resolution and better SNR performance. Because our measurements are in a solution, we must ensure the common mode range for the circuit includes any possible DC offset.

Table 7.1: The values for each of the single-ended circuit (SEC) and differential circuit (DC) components in Figure 7.2.

Parameter	**SEC**	**DC**	**Function**
R1	196 kΩ	1.8 kΩ	Gain for first stage
R2	4 kΩ	15 kΩ	Gain for first stage
R3	40 kΩ	39 kΩ	Set 2^{nd} stage DC operating point
R4	98 kΩ	1.8 kΩ	Gain for second stage
R5	5 kΩ	39 kΩ	Gain for second stage
C1	10 μF	1 μF	Remove DC offset
C2	1 μF	N/A	AC coupling, DC filtering

7.3 Materials and Methods

We fabricated a microelectrode array with gold electrodes using the following procedure:

1. A $2inch \times 3inch$ glass slide was first cleaned with isopropyl alcohol and water to achieve a clean surface.

2. Shipley Microposit S1813 (Rohm Haas, Marlborough, MA) positive photoresist was spun to a thickness of 1 μm. The spin recipe was 500 RPM for 10 seconds followed by 3000 RPM for 30 seconds.

3. The resist was baked at $115^{\circ}C$ for 30 minutes. This was a change from the suggested recipe to account for heat transfer through the glass.

4. The resist was exposed for eight seconds with an aligner exposure power of approximately $25 mJ/s$.

5. Development was performed using 351 Developer (Microchem) mixed in a 5 : 1 ratio (water:developer). The pattern would fully develop in approximately 45 seconds. The device was cleaned with water after development.

6. Metal evaporation was performed in a Cressington 308R evaporator (Ted Pella Inc., Redding, CA) with a LT300 dual output power supply. Approximately $30\,nm$ of a chrome was evaporated to form an adhesion layer. A chrome rod served as the source for the metal (CRW-1, RD Mathis, Long Beach, CA). Immediately following the chrome deposition, approximately $70\,nm$ of gold (99.999% pure) was evaporated using a ME5-.005W source (RD Mathis).

7. Coated samples were place in an acetone bath with sonication to remove the patterned resist and therefore selectively lift off the metal.

A second photoresist layer was patterned (using the same S1813 resist patterning procedure) to only expose gold areas of about $25\,\mu m$ by $100\,\mu m$ to act as sensing electrodes. This resist layer effectively insulated the rest of the gold wiring so we would only observe electrical activity at the exposed regions. A 4×4 array of electrodes provides 16 channels for measurement.

A polydimethylsiloxane (PDMS) structure was placed on top of the electrodes to isolate the fluid needed for cell culture from the bond pads used for electrical connections. The PDMS was simply used to form a deep well for cell culture. The PDMS was bonded to the glass after plasma treatment for 1 minute at high power using oxygen as the process gas.

A jig, shown in Figure 7.3, was constructed of Lexan and Delrin and machined to hold the microelectrode array as well as 16 pogo pins to provide electrical connections to the bondpads connected to each of the electrodes. The pogo pins (PP8, Solarbotics, Calgary, AB, CAN) are placed in holders (PPH1, Solarbotics) to allow removal when an electrical connection is not needed. This jig allowed for quick, reliable and non-permanent connections between the micro-scale electrodes and the macro-scale connections to the circuit on the custom designed PCB.

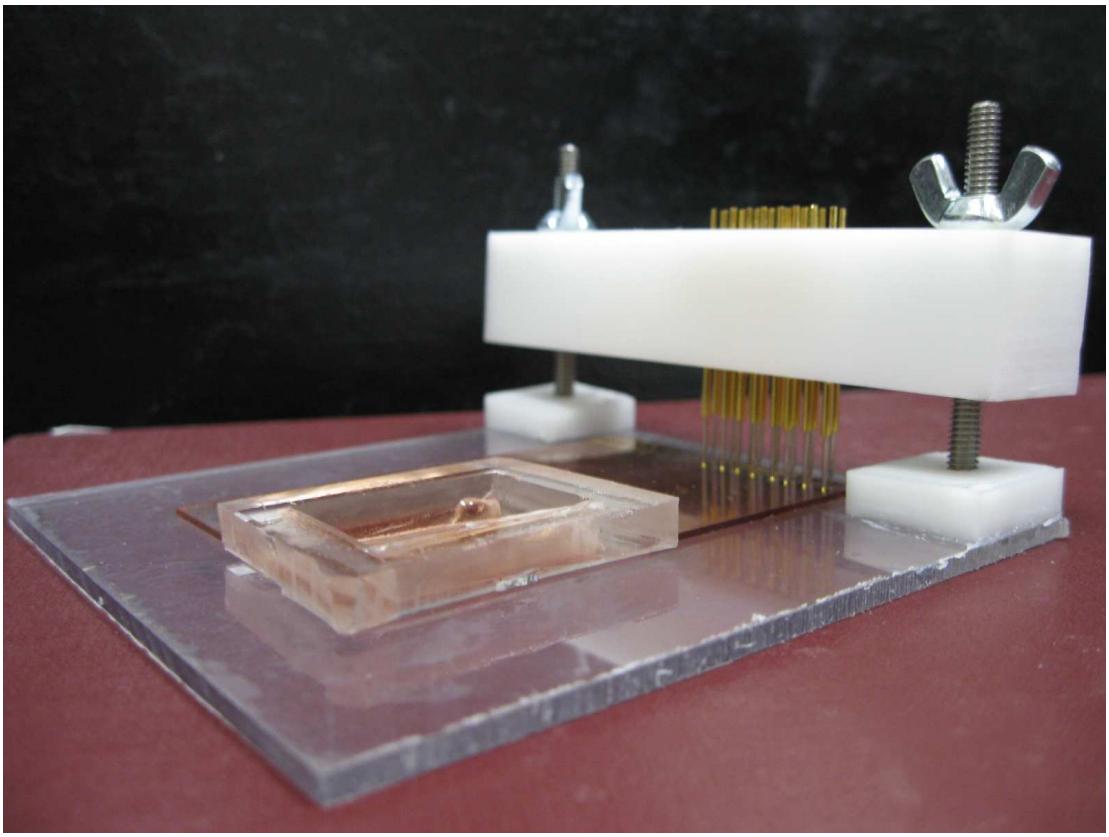

Figure 7.3: Pogo pin jig holding the microelectrode array with cells in a PDMS well. Connections to bond pads are made by pogo pins. The connections between the pogo pins and the PCB are made with microclip connectors.

HL-1 Cell Culture

The HL-1 cell line, derived from AT-1 cells (mouse cardiomyocyte tumor), retains the ability to contract spontaneously as well as cardiac morphological, biochemical, and electrophysiological properties through serial passages [92]. HL-1 cells have been used in other work with microelectrodes [88] [89] and provide electrical activity that is easily measured and will provide results for comparison. Cells were cultured in Claycomb media (Sigma, St. Louis MO) with 10% fetal bovine serum (Sigma), 1% 0.1mM norepinephrine (Sigma), 1% 2mM l-glutamine (Invitrogen, CA), and 1% 100 U/ml : 100 $\mu g/ml$ penicillin/streptomycin (Invitrogen). Surfaces were pretreated with

a 0.02% gelatin (Fisher Scientific, Pittsburg PA) and fibronectin (Sigma) mixture for 24 hours before cell introduction. The electrode device was autoclaved prior to pre-treatment with gelatin. Cells were allowed to grow to confluent in an incubator at $37\,^{\circ}C$ before testing, about $2-4$ days.

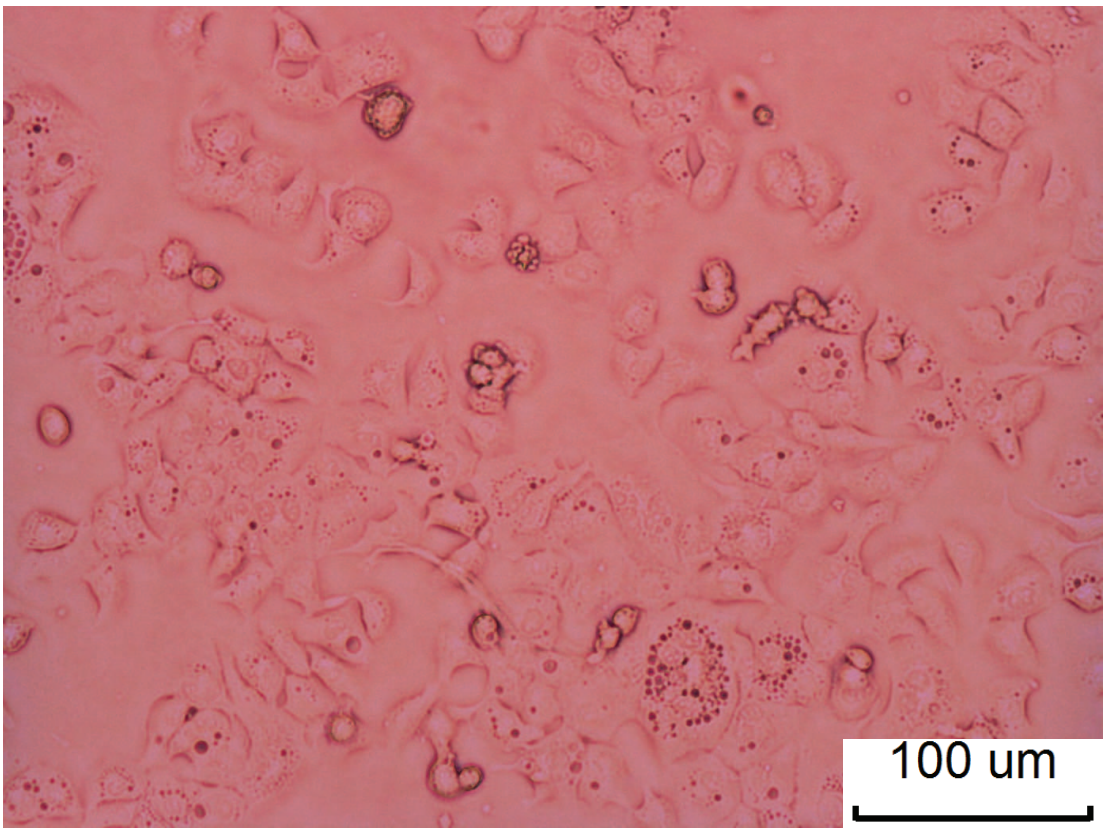

Figure 7.4: Micrograph of HL-1 cells. The cells exhibit spontaneous electrical activity.

Custom Designed Printed Circuit Board

We designed two custom, two-layer PCBs (3×3 square inches for the single-ended design, 3×4 square inches for the differential design) using PCB Artist (Advanced Circuits, Aurora CO). The single-ended design is shown in Figure 7.5. Both PCBs contained versions of the circuit requiring jumpers to manually complete some of the connections to allow for separate testing after each stage.

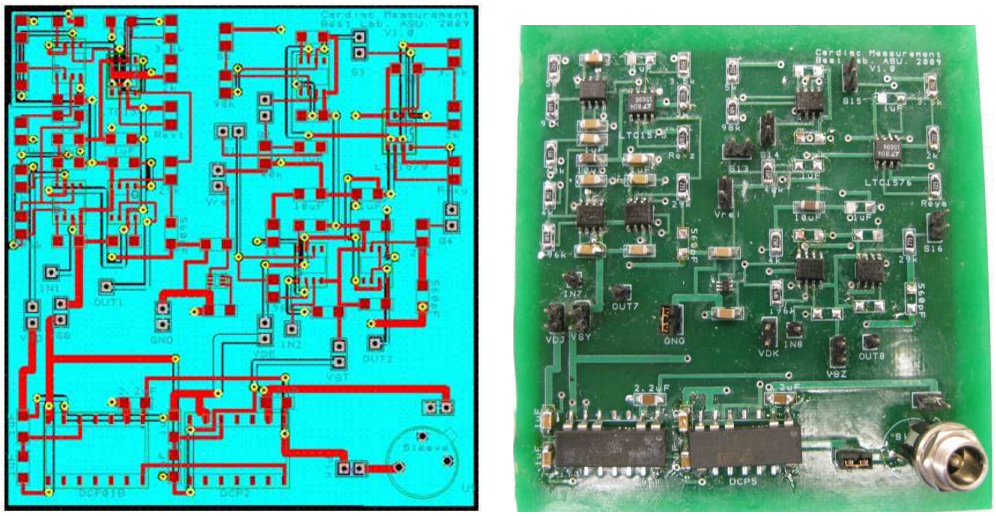

Figure 7.5: Custom designed printed circuit board layout (left) and picture (right) are shown. The design included the complete circuit chain on the left side of the board and debugging circuit with jumper connection points on the right.

7.4 Results

Stand-alone measurements of the circuit were conducted to determine circuit performance prior to testing with cells. The circuit was tested with various input waveforms and frequencies from a Keithley 3390 Arbitrary Waveform Generator (Keithley, Cleveland OH). Testing validated both the gain and frequency performance of the circuit. We were able to confirm the circuit worked with a range of DC offsets on the input from -3 V to +2 V. The AC response of the circuit corresponded very well with the simulation results. Initial testing using noisy square wave inputs was performed with varying frequencies for both designs. As the frequency of the square wave was increased from 500 Hz to 2.5 kHz, we were able to observe the output change from a noisy square wave to a clean sine wave. An input signal similar to the expected cardiac signals but with an amplitude of 6.3 mV pk-pk (minimum allowable amplitude) was tested with the differential design using the arbitrary waveform generator. The input signal and the output of the circuit are shown in Figure 7.6. The input signal from the arbitrary wave-

form generator is noisy and the peak of each pulse is hard to differentiate. However the output from the amplification and filtering circuit are clearly defined pulses. Figure 7.7 shows the power spectrum of the input and output signals. The original input signal from the arbitrary waveform generator contains a great deal of high frequency noise, but these higher frequency components are filtered as seen in the output of the differential circuit.

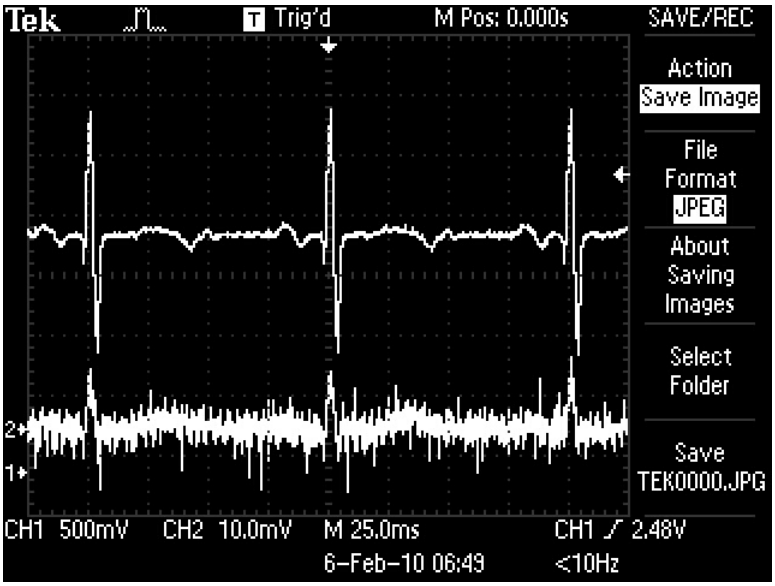

Figure 7.6: The transient response of the differential circuit (upper waveform) to the arbitrary waveform generator's output signal resembling the expected cellular signal (lower waveform). Note the two waveforms are plotted on different vertical scales.

We have designed and tested single-ended and differential designs of amplification circuits for measuring cardiac action potentials. The circuit performance was consistent with simulation results having expected gain and cutoff frequencies. We designed and fabricated the microelectrode array and Pogo pin jig as an interface between the circuit and the cells. Preliminary testing using HL-1 cells, the Pogo pin jig, and the amplification circuit demonstrated the setup will be sufficient to measure extracellular HL-1 action potentials. Our differential design was more robust for common mode noise suppression of induction noise and other environmental noise.

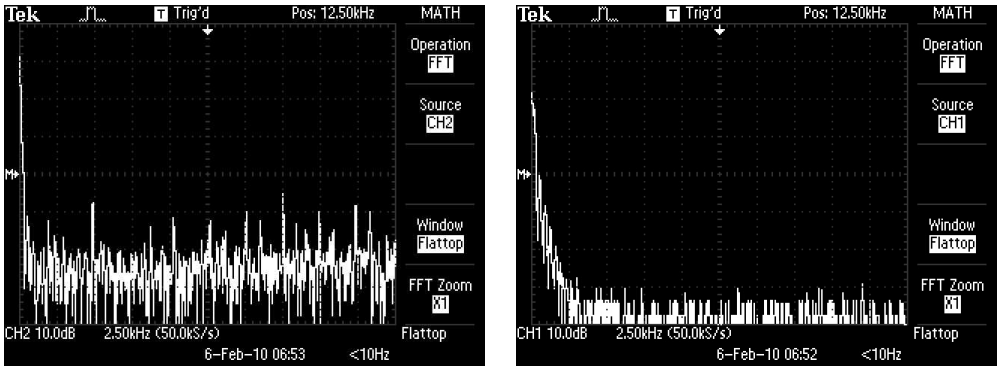

Figure 7.7: A fast Fourier transform was used to obtain the power spectrum of the original signal (left) and output from the differential circuit (right). The original signal and output signals are shown in Figure 7.6.

While the experiments and results shown are for discrete component PCB designs, the results are being used to better understand the transfer function of the system. This information is currently being used to improve our integrated circuit design. The final version of our system will allow for cell growth and signal measurement on a single chip that contains the integrated circuit, microelectrodes, and cell culture substrate. Once integration is complete we expect the entire device to be approximately $1inch \times 1inch \times 0.5inch$ for a sixteen channel system including accompanying microfluidics and packaging. The integrated system will allow for higher resolution outputs and lower power consumption than is currently possible.

Chapter 8

ION SENSITIVE FIELD EFFECT TRANSISTOR

Ion-sensitive field effect transistors (ISFETs) were introduced as pH sensitive devices by Bergveld over 40 years ago [93]. ISFETs are an attractive means of measuring pH because of their small size, low-power consumption, robustness, compatibility with on-chip circuit integration, and the low manufacturing cost by batch processing using integrated circuit technology [94]. However, their use in commercial applications thus far have been limited. One problem is the development of effective packaging. ISFETs, like other chemical sensors, need to be in contact with the solution being measured so isolation of fluids from the electrical circuitry is necessary. Chapter 12 will address packaging in more detail. The other major obstacle is drift in the sensor output.

This chapter will provide an introduction to the ISFET device. We also present a new method of mitigating the effects of drift in ISFETs by cycling the electric fields present in the device. This work was completed in collaboration with Sahil Shah, a fellow member of Dr. Blain Christen's research group.

8.1 Background

The functionality of ISFETs is well understood [96]. ISFETs are simply MOSFETs with the gate connection separate from the device in the form of a reference electrode present in solution. A schematic representation of an ISFET is shown in Figure 8.1. ISFETs work by modulating the semiconductor surface potential, usually the insulator-electrolyte interface, using the field-effect principle. The drain current in an ISFET is given by the same equations as MOSFETs:

$$I_d = C_{ox}\mu\frac{W}{L}[(V_{gs}-V_t)V_{ds}-\frac{1}{2}V_{ds}^2] \tag{8.1}$$

with C_{ox} the oxide capacitance per unit area, W and L the width and length of the channel, V_t is the threshold voltage, and μ the electron mobility in the channel. When

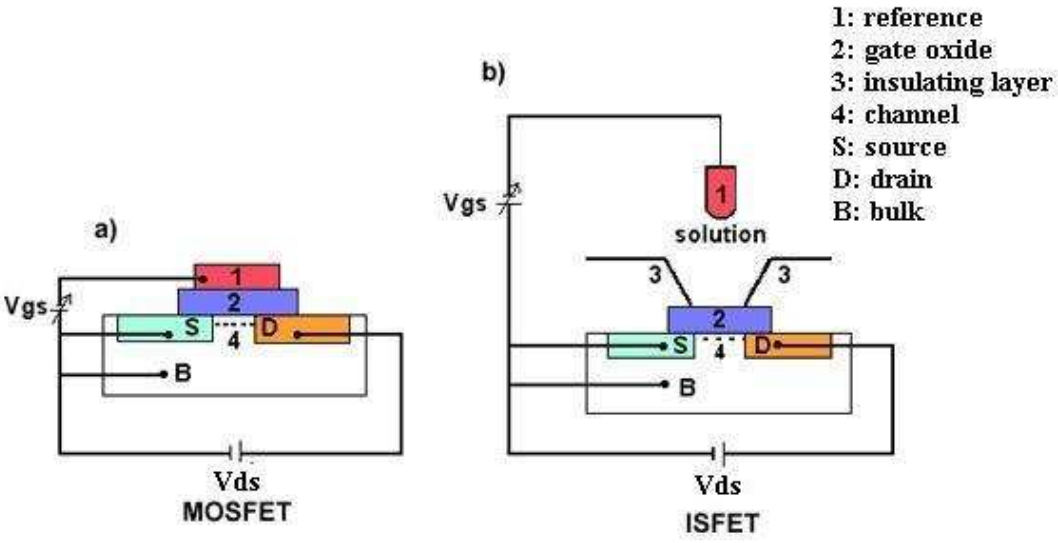

Figure 8.1: Schematic representation of MOSFET and ISFET [95]. The pH of the solution above the gate causes V_{gs} to change which changes I_d.

V_{ds} is held constant, the drain current, I_d, is a unique function of the input voltage V_{gs} which is controlled by the number of ions present in the solution. For this application, the number of ions present is the pH. Alternatively, holding I_d constant allows changes in V_{gs} to reflect changes in pH. The pH sensitivity of an ISFET occurs through changes in the threshold voltage of the device caused by modification of the flat band voltage, V_{FB}. The flat band voltage is defined as

$$V_{FB} = E_{ref} - \frac{1}{q}\Phi^{Si} - \psi_0 - \frac{Q_i}{C_i} + \chi^{Sol} + \delta_\chi \tag{8.2}$$

where E_{ref} is the reference electrode potential relative to vacuum, $1/q\Phi^{Si}$ is the work function of Si, ψ_0 is the potential drop in the electrolyte at the insulator-electrolyte interface, Q_i and C_i are the insulator effective charge and capacitance, χ^{Sol} is the surface dipole potential of the solvent, and δ_χ is a collection of a number of variations in χ. The insulator used in an ISFET contains charge at various locations, all of which affect

the operation of the device. The total effective insulator charge can be expressed as

$$Q_i = Q_f + Q_{it} + \frac{d_c}{d_i} Q_m \tag{8.3}$$

where Q_f is the fixed charge, Q_{it} is the charge trapped in surface states, and the last term is the charge distributed at the insulator, Q_m, taking into account the distance to the centroid of the insulator d_c and the insulator thickness d_i. In total, the flat-band voltage is influenced by three terms that depend on the electrolyte composition. The first is ψ_0, the potential drop in the electrolyte at the electrolyte-insulator interface. The second is $(d_c/d_i)Q_m/C_i$, the effect of the mobile ionic charge which can be modulated by the electrolyte. The final component is $Q_{it}C_i$, which is the effect of the surface state density that can change from diffusion of the electrolyte into the insulator.

ISFETs suffer from drift caused by a number of different factors, some of which are not fully understood. Drift has been shown to be temperature dependent [97], pH dependent [98–100], insulating gate dependent [98], transport dependent [101], and split between a fast and slow response [102]. Attempts to mitigate the effects of drift by means of software compensation [94], hardware configurations [103], or a combination of both [100, 104, 105] have shown progress in making ISFETs adequately stable for commercial application.

Jamasb *et al.* developed a physical model for drift behavior in ISFET devices [101]. They hypothesized that much of the drift phenomenon is associated with transport through the gate insulator. Their model focuses on the chemical modification of the oxide surface by hydration when exposed to aqueous solutions. Changes in the oxide insulating layer modify the overall permittivity, therefore altering the capacitance (C_i) and the amount of channel inversion in the ISFET. Because these changes occur slowly over time, they show up as drift in the output signal of the devices.

8.2 Experimental

Device Fabrication

We have fabricated a chip with ISFET pH sensors using the SensoNor MultiMEMS process. The ISFET was made using the same process as the capacitance sensor in Chapter 6. The ISFETs we designed in the MultiMEMS process are P-channel devices. The P-doped regions are composed of PSC and PBC (see Figure 4.2) with a channel length of 6 μm. There are 21 fingers each with a length of 260 μm for a total channel width of 5460 μm. The ISFET structure is contained in the N-Epi layer. The gate insulating material is thermally grown oxide. The ISFET area can be seen in Figure 6.6.

ISFET Characterization

We measured electrical characteristics using a Keithley 2636A source measurement unit (Keithley Instruments, Inc., Cleveland, Ohio) controlled by MATLAB (Mathworks, Natick, MA). Devices were characterized with buffer solutions with pH of 4.01, 7.0, and 10.01 (Oakton Instruments, Vernon Hills, IL). A gold wire was used as a reference electrode, and all experiments were conducted in a Faraday cage.

We verified a pH response from the device as shown in Figure 8.2. The device gives a calculated sensitivity of 45 mV/pH. It is important to note that the values of V_{ref} required to operate the ISFETs varied greatly between devices. The V_{ref} required to operate varied between about $-20V$ and $-2V$, depending on the device. The huge range is likely due to the fact that the fabrication was not designed to make ISFETs. Once we determined the proper V_{ref} for a device to operate, the value was fairly consistent.

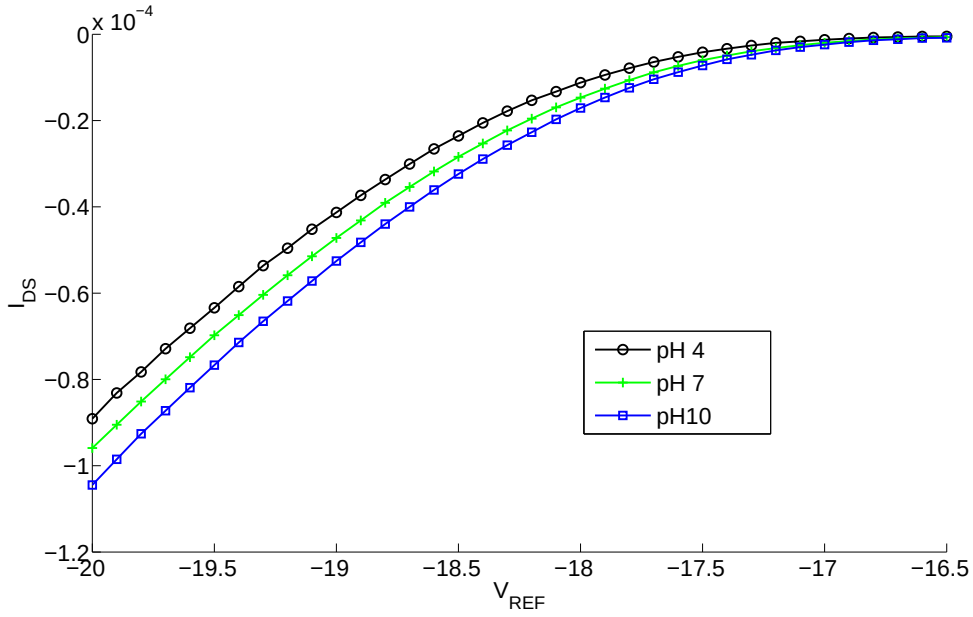

Figure 8.2: The pH response of an ISFET using buffer solutions of pH of 4, 7, and 10. The value of V_{ref} was swept, and the current I_{DS} was recorded.

Voltage Cycling

We examined the cycling of two electric fields present within the ISFET. The first field is the vertical field of the device which depends on the voltage between V_{ref} and the channel potential. The vertical field was cycled by switching the value of V_{ref} between the operating voltage (ISFET on) and the value at the source (ISFET off). We also investigated cycling of the horizontal electric field between the source and drain. The horizontal field was controlled by switching the voltage on the drain of the device. MATLAB was used to control all of the voltages applied to the device by the Keithley 2636A.

Modeling

A model of the ISFET was created using Silvaco TCAD to understand the physics of the drift and the reset behavior. A physical-based simulation was performed in ATLAS

to examine the physical mechanism of ISFET threshold voltage drift. The ATHENA process simulation framework was used to create a p-channel field effect transistor with the same properties and dimensions as the ISFET. The simulated model was fabricated according to the steps provided in the SensoNor MultiMEMS design guide.

TCAD can model the fabricated device, but the electrolyte cannot be modeled directly. Therefore, a user defined material was deposited on top of the oxide layer to emulate the electrolyte. All user defined materials in ATHENA are considered insulators with properties that can be altered to meet the requirements for a simulation. We modified the properties of the user defined material to align with the conditions of an ionic solution as specified by Chung *et al.* [106]. In an ionic solution the charge distribution (φ) in the ionic double layer is given by the Poisson-Boltzmann equation,

$$\frac{\delta^2\varphi}{\delta x^2} = -\frac{q}{\varepsilon}\left[C_0^{Na^+}\exp\left(\frac{-q\varphi}{kT}\right) - C_0^{Cl^-}\exp\left(\frac{-q\varphi}{kT}\right)\right] \tag{8.4}$$

where $C_0^{Na^+}$ and $C_0^{Cl^-}$ are the concentration of Na^+ and Cl^- in the electrolyte, k is Boltzmann's constant, T is the temperature in Kelvin, ε is the permittivity of the electrolyte, and q is the total charge of the ions in the double layer equal to the charge number of the ion (z) multiplied by the elementary charge (e) ($q = ze$). This equation can be modified to give the Fermi-Dirac distribution of electrons and holes given by

$$\frac{\delta^2\varphi}{\delta x^2} = -\frac{q}{\varepsilon}\left[p_0\frac{1+e^{\frac{E_i-E_v}{kT}}}{1+e^{\frac{E_i-E_v}{kT}}e^{\frac{q\varphi}{kT}}} - n_0\frac{1+e^{\frac{E_c-E_i}{kT}}}{1+e^{\frac{E_c-E_i}{kT}}e^{\frac{q\varphi}{kT}}}\right] \tag{8.5}$$

so that an intrinsic semiconductor can be used to model the electrolyte. In equation (8.5), n_0 and p_0 are electron and hole concentration, E_i is energy of fermi level in an intrinsic semiconductor, E_c is the energy of the conduction band, and E_v is the energy of the valence band. For equation (8.5) to be true, the band gap (E_g) of the intrinsic semiconductor should satisfy the equation $\frac{E_g}{2} - q\varphi \gg kT$.

The density of states for the valence band and conduction band, (N_c and N_v respectively), were specified according to the molar concentration of the ionic solution.

This set the bandgap to $1.5eV$. This model required a Debye length larger than the size of the simulated ions in solution. The Debye length decreases as the ionic concentration increases; therefore, the maximum concentration we could simulate was approximately $500mM$.

The relative permittivity of the defined material was set to 80 to match the properties of water. The mobility of electron and holes was set to the values for Cl^- and Na^+ ions in water ($6.88 \times 10^{-4} cm^2V^{-1}s^{-1}$ and $4.98 \times 10^{-4} cm^2V^{-1}s^{-1}$ respectively). Properties for electron affinity ($3.9eV$) and the recombination lifetime of electrons ($1 \times 10^{-3} s^{-1}$) and holes ($1 \times 10^{-3} s^{-1}$) were set by curve fitting the simulated and experimentally obtained curves. Gold was used as a reference electrode to match the experimental setup. The final structure of the modeled ISFET is shown in Figure 8.3.

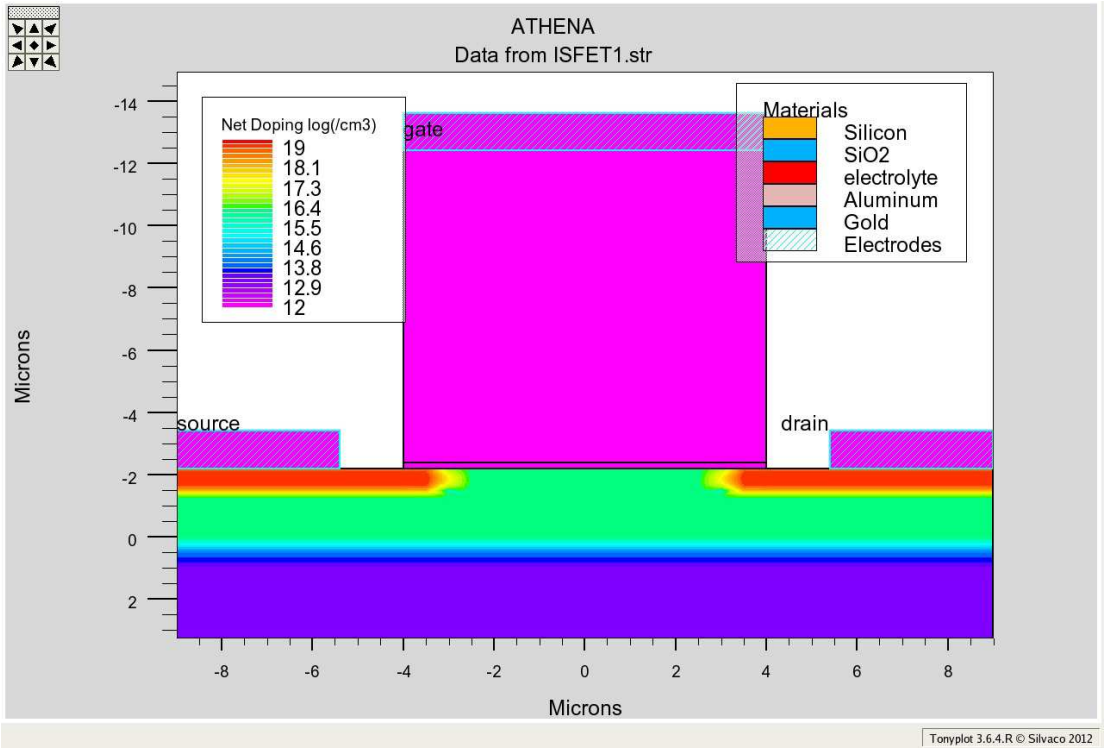

Figure 8.3: The structure of the ISFET as modeled in Silvaco TCAD. Doping levels and materials are indicated.

The Shockley-Read-Hall(SRH) and Lombard mobility models were used to simulate the drift in threshold voltage and the reset characteristics. These are standard models used for MOSFET simulations. SRH was used to model the generation and recombination inside the semiconductor. The Lombard mobility model considers mobility due to the transverse electric field. The curve fitting was done using I_{DS} vs V_{ref} values obtained from the static DC solution. The gate voltage was ramped from $0V$ to $-20V$ while keeping the drain at $-2V$ to obtain the I_{DS} vs V_{ref} curves. During simulations, the source and the substrate were kept at $0V$, while the drain was held at $-2V$. The reference voltage was kept at $-10V$ while performing transient simulations. All of the voltages used in the model reflect the experimental conditions. Simulations were performed for a model with a unit width so the current obtained was per μm of device width. The width of our fabricated ISFET was $5460\,\mu m$; the current values obtained during simulations are multiplied by the width to compare to our experimental results.

8.3 Experimental Results

Figure 8.4 shows the experimental ISFET drift results when using a pH 4 buffer. The ISFET had a steady drift when no switching was applied. Cycling V_{DS} showed no change in the overall drift of the device; drift appears to continue even when V_{DS} is not applied. Cycling V_{ref} shows a repeatable drift pattern. The cycling of V_{ref} effectively resets the device and causes identical drift every time the cycle is started. The reset characteristics showed some dependence on the on and off time proportions as well as the pH of the solution, but an appropriate vertical electric field reset time was easily determined by trial and error.

8.4 Simulation Results

Figure 8.5 shows simulation results of the same switching procedures shown in Figure 8.4. The simulations demonstrate the same behavior as our experimental results.

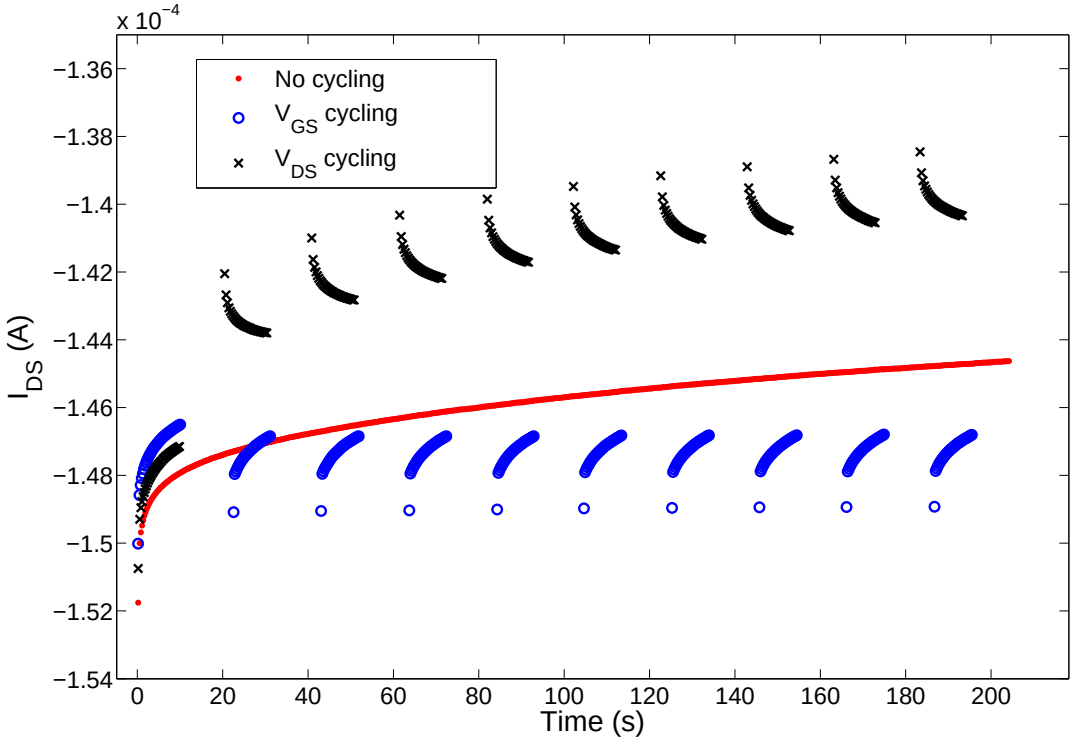

Figure 8.4: Experimental results showing drift in drain current, the effect of V_{ref} cycling, and the effect of V_{DS} cycling.

Cycling of V_{ref} effectively resets the device while cycling V_{DS} has little effect on the overall drift. We simulated a unit ISFET width so the currents were much smaller than experimental values.

8.5 Discussion

Cycling the vertical electric field of an ISFET is a promising method of drift compensation. Our experimental results showed a clear reset in the drift profile of a commercially fabricated ISFET when switching V_{ref}. Cycling V_{DS} did not produce a reset; instead, the ISFET output continued to drift throughout operation. The difference in drift direction between experimental and simulation results is likely due to producing an electrolyte solution within TCAD. The direction of drift has been shown to depend on the pH of the measured solution [102]. The electrolyte concentration, and thus the pH and direction

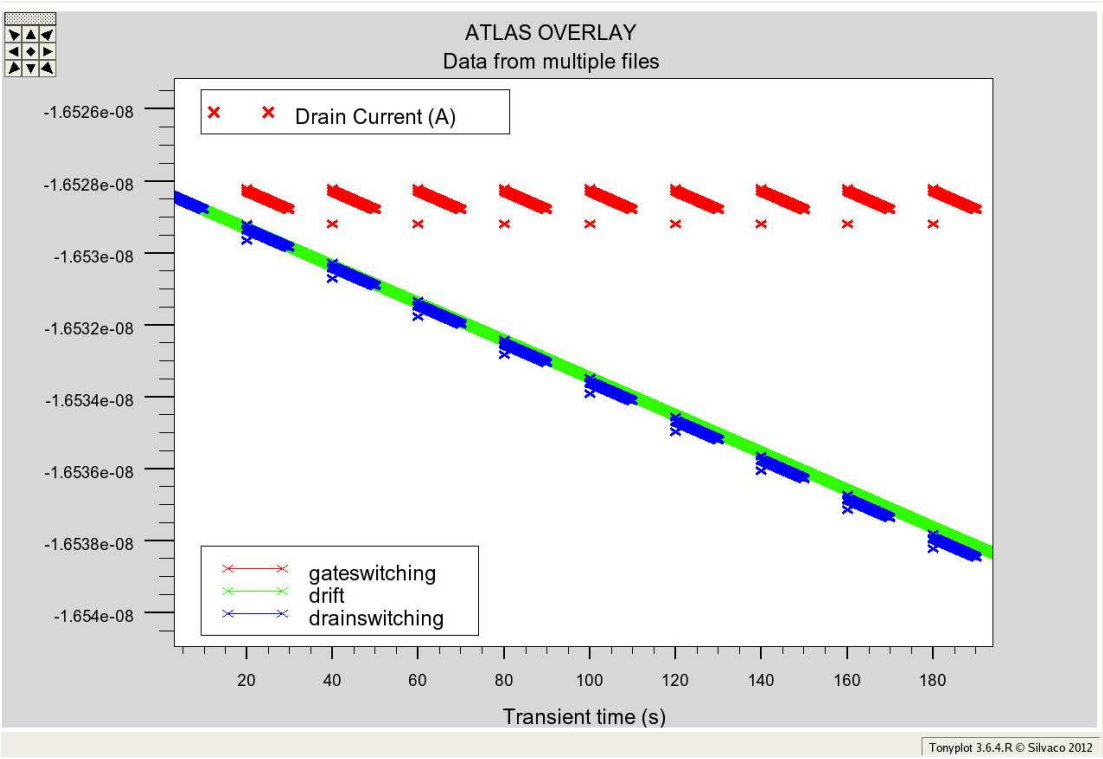

Figure 8.5: Simulated results showing the drift in drain current, the effect of V_{ref} cycling, and the effect of V_{DS} cycling.

of drift, cannot be modeled very accurately in TCAD. The simulated ISFET current values matched well with the experimental value; multiplying the simulated unit current (approximately 1.65×10^{-8}) by the total device length($5460\,\mu m$) gives $90\,\mu A$, which is very close to the experimental values of $146\,\mu A$.

Our simulation confirmed our experimental results of a drift reset when switching V_{ref} and enabled us to determine the cause for the drift. Under the influence of an electric field, ions accumulated at the interface between the oxide and the electrolyte. Switching the vertical electric field off for sufficient time allowed the ions to diffuse away from the surface. When the vertical electric field was restored, the ions would again accumulate at the surface but their accumulation would be identical to when the device was first turned on. Conversely, horizontal field cycling showed no effect on

the distribution of ions because the vertical field was maintained. The resetting of the device through vertical field cycling thus allows a predictable drift pattern. The off time required for a reset varied with the pH of the solution and the amount of time the device was in the on state.

Overall, these results show the cycling of V_{ref} gives a repeatable drift pattern easily accounted for with either software or hardware. Compensation of a known error would allow for drift resistant ISFET operation. Multiple devices could use V_{ref} cycling to achieve constant pH measurement. Such a setup is possible with the small size of the ISFET and their compatibility with on-chip circuit integration.

Other published work on ISFET drift attempts to actively fight against the behavior of the device. This work demonstrates the idea of drift management, allowing the device to drift normally, but in a repeatable pattern. Extensive compensation techniques for longer term monitoring are not necessary when the device shows repeatable operation using shorter measurement times. This voltage cycling technique thus shows potential in expanding the use of ISFETs in long term, continuous monitoring applications.

Chapter 9

DISCRETE ISFET

As discussed in Chapter 8, ISFETs are solid state devices for sensing pH. Early ISFETs were fabricated exactly as MOSFETs, except the gate contact was removed and the gate oxide exposed directly to a solution. This leaves a structure as seen in Figure 8.1. Further work with ISFETs revealed that the structure is essentially an ion sensitive electrode with a field effect transistor used for detection [107]. Because of this concept, extended gate structures were developed which used a simple metal connection to connect the pH sensitive region to a MOSFET for detection [108]. This has been demonstrated more recently by Prodromakis *et al.* using a discrete MOSFET with the gate connected to a metal electrode covered with a pH sensitive nitride layer [109]. This work uses the term "discrete ISFET" interchangeably with "extended gate ISFET" because the design uses a discrete, commercially made MOSFET.

The discrete ISFET behaves in the same manner as a regular ISFET. However, using a discrete design allows much more design freedom than a traditional implementation. The sensing region does not need to be on the same piece of silicon the transistor is fabricated on. Therefore, the sensing region can have various geometries or parameters that are only limited by the fabrication process of the sensor instead of the entire MOSFET structure. Changes can be made to the sensing portion without regard to the MOSFET operation. Excluding the MOSFET from the fabrication process reduces the time and cost of the sensor. Discrete component MOSFETS are incredibly cheap when produced by commercial foundries; the commercially produced devices utilized in this work were only $0.46 each. Fabrication of a similar quality MOSFET in a research lab is neither feasible or comparable, in terms of both cost and time. For instance, production of CMOS ISFETs (as in Chapter 11) takes a minimum of four months just to receive a design from a commercial process. The fabrication of a custom sensing re-

gion, on the other hand, is feasible in a research scale nanofabrication facility. The time required to fabricate just the sensing region is on the order of hours, so many iterations of the devices can be produced.

9.1 Discrete ISFET Fabrication

The design for the discrete ISFET used in this system went through many iterations. The first design was almost identical to the design used by Prodromakis *et al.* [109]. A key difference was the base substrate used. Prodromakis *et al.* used glass whereas we chose to fabricate on top of a silicon wafer to allow easier dicing. The design for metal deposition is shown in Figure 9.1.

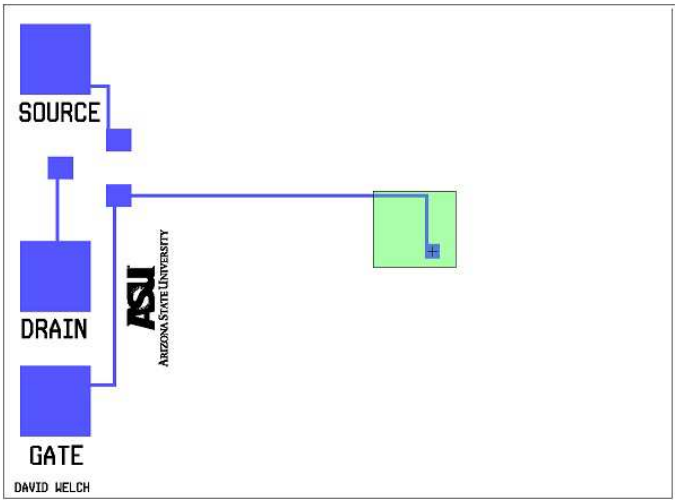

Figure 9.1: Masks used for the first discrete ISFET design. The blue represents areas of chrome and gold while the green represents nitride. The total area of the design is 24 mm $\times$ 18 mm.

The fabrication protocol for the first discrete ISFET design was as follows:

1. A clean, $<100>$ silicon wafer was used as the substrate
2. Shipley Microposit S1813 (Rohm Haas, Marlborough, MA) positive photoresist was spun to a thickness of 1 μm. The spin recipe was 500 RPM for 10 seconds followed by 3000 RPM for 30 seconds.

3. The resist was baked at $115\,^{\circ}C$ for 1 minute.

4. The resist was exposed for eight seconds with an aligner exposure power of approximately $25\,mJ/s$. The mask was aligned with the wafer flat to ensure the patterns could be diced cleanly.

5. Development was performed using 351 Developer (Microchem) mixed in a $5:1$ ratio (water:developer). The pattern would fully develop in approximately 45 seconds. The device was cleaned with water after development.

6. Metal evaporation was performed in a Cressington 308R evaporator (Ted Pella Inc., Redding, CA) with a LT300 dual output power supply. Approximately $30\,nm$ of a chrome was evaporated to form an adhesion layer. A chrome rod served as the source for the metal (CRW-1, RD Mathis, Long Beach, CA). Immediately following the chrome deposition, approximately $70\,nm$ of gold (99.999% pure) was evaporated using a ME5-.005W source (RD Mathis).

7. Coated samples were placed in an acetone bath with sonication to remove the patterned resist and therefore selectively lift off the metal.

8. Approximately $65\,nm$ of silicon nitride was deposited using a Plasma Enhanced Chemical Vapor Deposition (PECVD) at $350\,^{\circ}C$.

9. Another layer of S1813 resist was spun, baked, exposed, and developed using a nitride patterning mask to provide a protective layer over the sensing electrode area.

10. The nitride was etched using reactive ion etching (RIE). This process removed nitride not protected by the S1813 and exposed the gold bonding pads.

11. The device was rinsed with acetone to remove the S1813 etch mask.

This process is summarized in Figure 9.2.

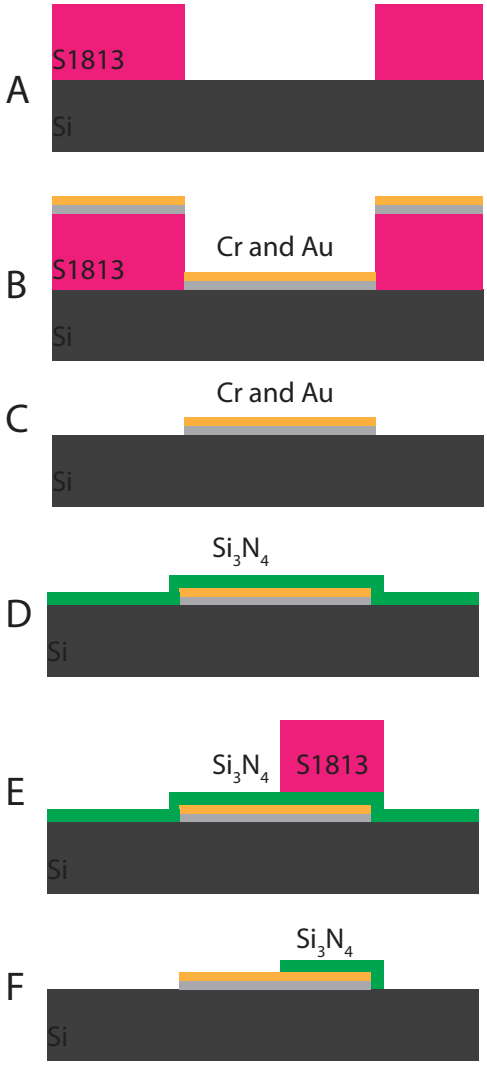

Figure 9.2: Process flow for the first discrete ISFET design. The steps include resist patterning (A), gold and chrome evaporation (B), lift-off to leave patterned gold (C), PECVD nitride deposition (D), resist patterning (E), and RIE of nitride and resist removal (F).

This device was tested for use as a pH sensing device and showed pH sensitivity. However, there was not an integrated reference electrode on the device. Using an external electrode was difficult because it had to be changed often and was not at a consistent distance from the sensing area. This caused significant variations in the

signals recorded and difficulty in calibrating for a pH value. This device also needed to be used in a microfluidic environment so we wanted to avoid trying to integrate a macroscale reference electrode.

The second iteration of the design integrated an on-chip reference electrode onto the device. The fabrication protocol was the same as described for the first device in Figure 9.2. Different masks were used for the resist patterning steps, shown in Figure 9.3. The problem with this design was a lack of insulation between the silicon substrate and the deposited metal. This was not an issue in the first design because there was only one connection made to the device. With the reference electrode integrated onto the same substrate, we enabled the sensing region to short to the reference electrode through the semiconducting silicon. The short rendered the devices useless as pH sensors.

The third version of the discrete ISFET sensor corrected the shorting issue by thermal growth of oxide on the silicon as an insulating layer. The remainder of the fabrication protocol was the same except for the nitride patterning. Instead we inverted the pattern used for the nitride patterning. The new mask design is shown in Figure 9.4. The summarized fabrication protocol is shown in Figure 9.5.

The change to the nitride patterning had no implications to the function of the ISFET as a pH sensor. In version two, nitride was left only on top of the electrode that was to be pH sensitive. Nitride was removed elsewhere to allow for off chip electrical connections and for reference electrode access to the solution. To ensure these electrical connections, the RIE was programmed to etch past the depth of the nitride and into the silicon dioxide. However, this excess etching produced a significant step from the total height of the chrome/gold/nitride stack down to the silicon dioxide layer. This step proved to be an issue when attempting to bond a microfluidic device on top of the discrete ISFET sensor. As shown in Figure 9.6, a good bond was formed between the

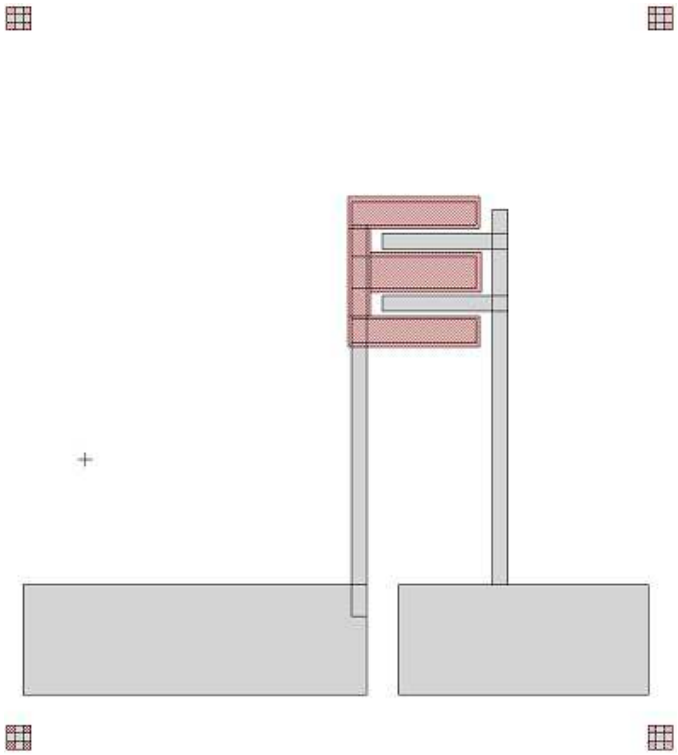

Figure 9.3: Masks used for the second discrete ISFET design. The grey represents areas of chrome and gold, and the red-checkered area represents nitride covered regions. Alignment marks at the corners of the mask are not part of the ISFET. The total area of the design is 24 mm $\times$ 21 mm.

nitride layer and the PDMS, but no bonding occurred outside of this area. The problem was corrected by only etching the nitride over the reference electrode and the bondpads. The etched areas of the final version are indicated by the green mask in Figure 9.4. This discrete sensor design was ultimately chosen for use in the feedback system.

9.2 Results

The discrete ISFETs could be tested for electrical characteristics using a Keithley 2636A source measurement unit (Keithley Instruments, Inc., Cleveland, Ohio) controlled by MATLAB (Mathworks, Natick, MA). Devices were characterized with buffer solutions with pH of 4.01, 7.0, and 10.01 (Oakton Instruments, Vernon Hills, IL). An external reference electrode was necessary to test the first discrete design. The fabri-

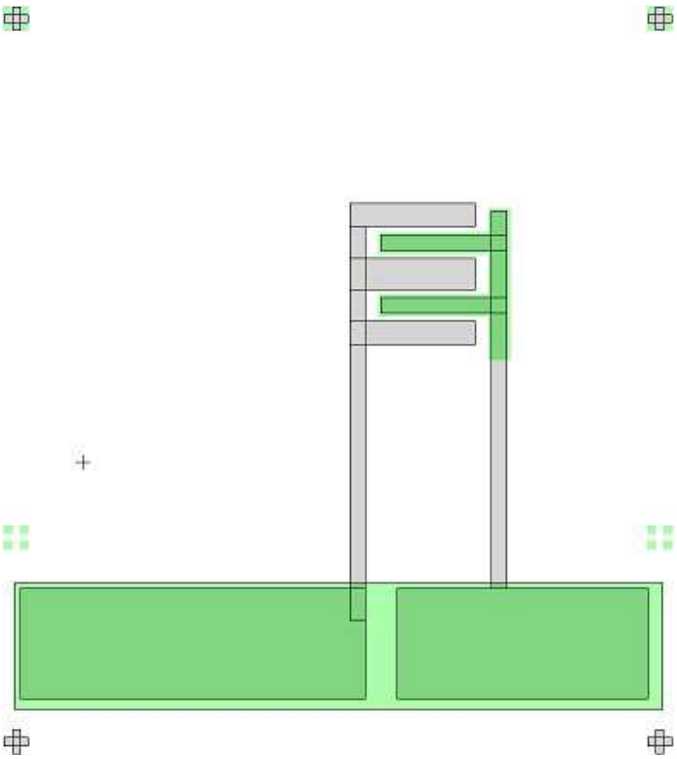

Figure 9.4: Masks used for the third discrete ISFET design. The grey represents areas of chrome and gold; the green represents areas NOT covered by nitride. The total area of the design is 24 mm $\times$ 21 mm.

cated sensor was attached to a cuvet to enable easy interaction with fluid for testing. The testing setup is shown in Figure 9.7. Initial testing was performed with a Ag/AgCl electrode.

An ISFET characterization curve for the first discrete device design is shown in Figure 9.8. The device shows pH dependence, but the results were highly variable and often switched their order, so determining the sensitivity was impossible.

The variations likely had many causes. The reference electrode required constant upkeep so it had to be removed and replaced frequently. This made it impossible to maintain a constant reference electrode position relative to the sensing region. Additionally, liquid needed to be changed out in order to test different pH values. Drying

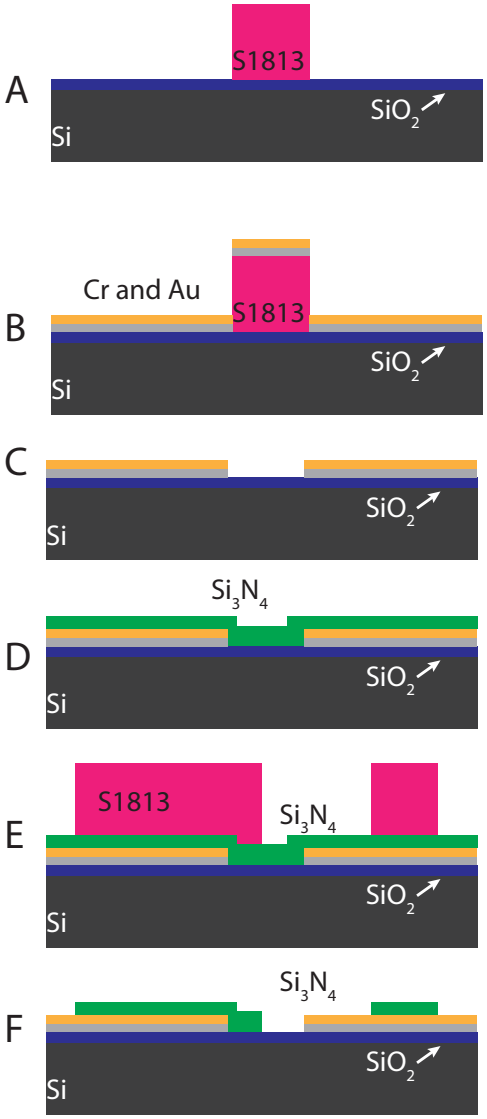

Figure 9.5: Process flow for the third discrete ISFET design. The steps include resist patterning on top of SiO_2 (A), gold and chrome evaporation (B), lift-off to leave patterned gold (C), PECVD nitride deposition (D), resist patterning (E), and RIE of nitride and resist removal (F).

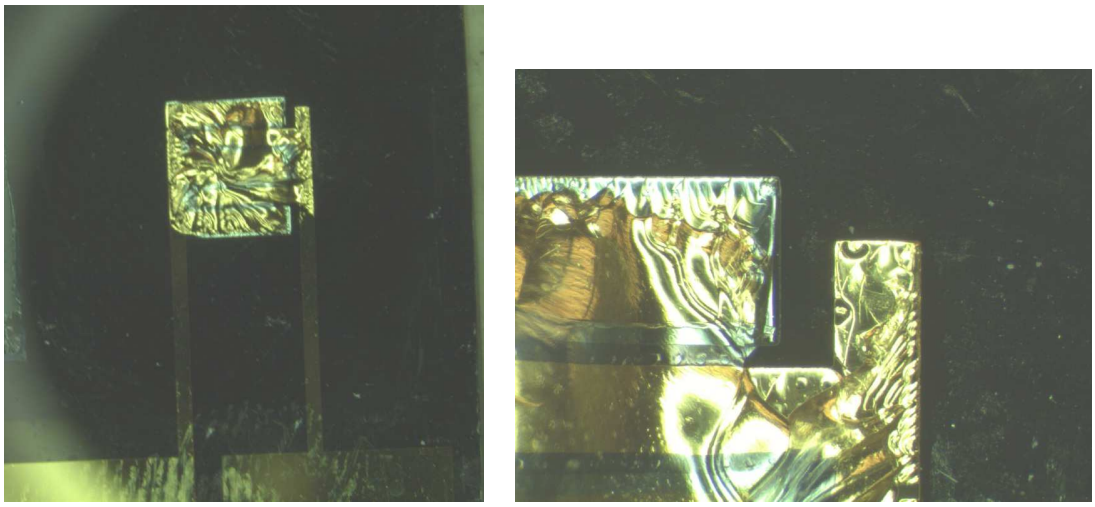

Figure 9.6: Micrograph of unsuccessful PDMS bonding onto the microfabricated ISFET (left). Bonding only occurred on the raised areas of gold or nitride (right). The width of the gold extending pad to the sensing region where attachment occurred is $500\,\mu m$.

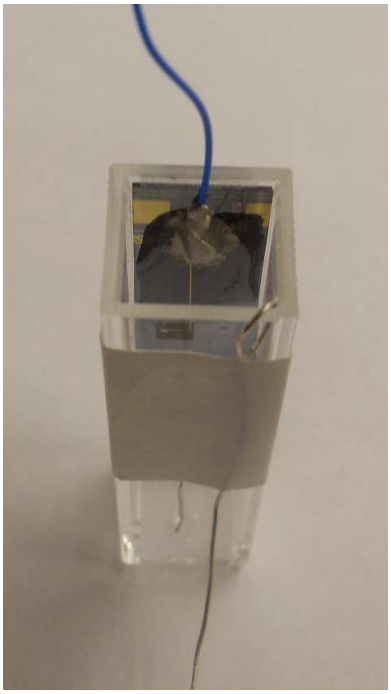

Figure 9.7: First discrete ISFET design in cuvet for characterization. The reference electrode was secured a fixed distance from the pH sensitive region.

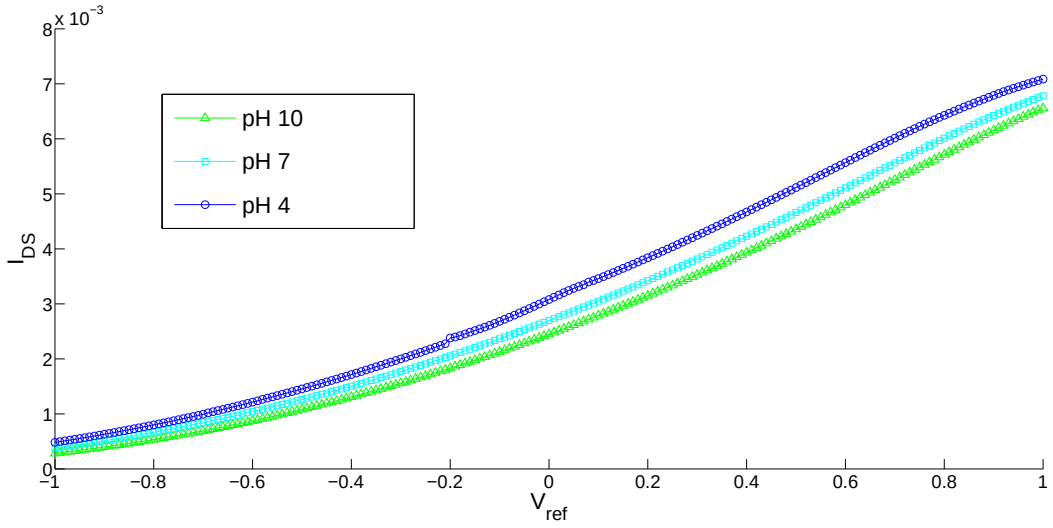

Figure 9.8: Characteristic ISFET curve for a discrete device. The V_{ref} value was swept while maintaining a constant V_{DS}. A different curve is obtained for each pH buffer value.

and changing fluids likely moved the reference electrode. The drift of the device was perhaps the greatest problem. To demonstrate drift, V_{ref} versus I_{DS} was continuously swept over a long period of time. As is seen in Figure 9.9, the device continued to drift over the full hour of testing. The constant drift behavior made full characterization difficult.

Subsequent designs integrated a reference electrode onto the substrate. This reduced some variability in ISFET performance. However, as explained in Chapter 8, drift is an inherent problem. Controlling the ISFET environment as much as possible helps to reduce drift. This can be done effectively using microfludics, as demonstrated in Chapter 10.

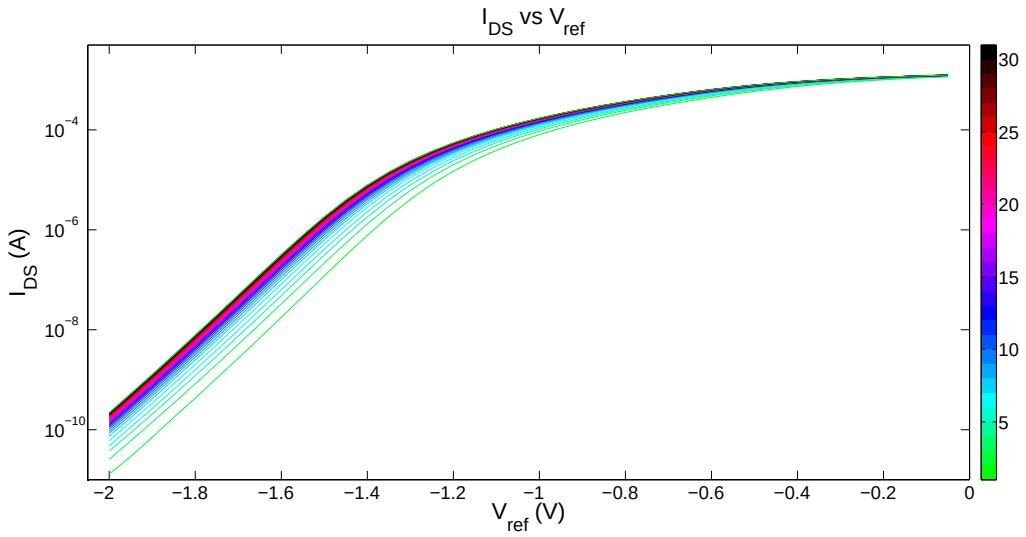

Figure 9.9: Drift behavior of a discrete ISFET device over 60 minutes. V_{ref} was swept repeatedly at a steady pace for one hour. The device was tested in a cuvet using pH 4 buffer. The order the curves were taken is indicated by color.

Chapter 10

MICROFLUIDIC FEEDBACK CONTROL OF pH

This work aims to look at the technologies and engineering principles that have evolved since cell culture was first introduced and analyze these new ideas to improve biological cell culture. One of the most important concepts that will be investigated is feedback control. Programmable control over the cellular environment will transform the way experimentation is perceived. Feedback will also provide the opportunity for variable control throughout an experiment instead of specifying only the starting parameters. Feedback control is fundamental to many engineering applications and implementing it for biological environments has numerous advantages to improve cell culture practices.

Current cell culture practices have a number of methods that attempt to control the environment, but most are focused on macroscale control. However, the cell microenvironment has been shown to be an equal or even more important factor. The microenvironment has a distinct physiological character defined by the physicochemical properties such as pH, oxygen tension, temperature, and osmolality [110] as well as the physical properties [111]. Recent research has shown that small variations in these factors affect cell behavior [112–117]. Stem cells are influenced by factors including growth factors, other cells, and extracellular matrix components to such a large degree that their microenvironment regulates cell survival, self-renewal, and differentiation [118–120]. Control of the microenvironment is also important in cancer research [121]. Hypoxic microenvironments have been shown to induce metastasis in tumors. Furthermore, levels of pH, glucose, and lactate also affect metastasis of tumors [122]. While cell culture has been used since the 1950s to produce human viral vaccines, only recently has the cell microenvironment been examined as a factor influencing their production [123]. Biopharmaceuticals rely on animal cells to glycosylate proteins, and maintaining a consistent glycosylation profile between batches is

important. Culture parameters such as nutrient concentration, dissolved oxygen, pH, temperature, batch age, ammonia, shear stress, and even media perfusion can affect glycosylation making consistent biopharmaceutical production difficult [124]. Precision control over the microenvironment would solve many of these problems.

This chapter presents a control system for microenvironment pH control. This is an excellent example of combining microscale biosensors into a biological environment.

10.1 Background

The pH of a solution is a dimensionless measurement of the molar hydrogen ion concentration ($[H^+]$) in a solution. The pH, which stands for "power of hydrogen", is calculated with

$$pH = -log_{10}[H^+] \tag{10.1}$$

Similarly, the pOH is the measurement of the molar hydroxide ion concentration ($[OH^-]$), which is calculated using

$$pOH = -log_{10}[OH^-] \tag{10.2}$$

The values of pH and pOH are related by the dissociation of water

$$2H_2O \rightleftharpoons H_3O^+(aq) + OH^-(aq) \tag{10.3}$$

where H_3O^+ is the equivalent to H^+, with an equilibrium constant (K_w) of

$$K_w = [H^+][OH^-] = 10^{14} \tag{10.4}$$

The values for pH and pOH are therefore related by

$$pOH \approx pH - 7 \tag{10.5}$$

when the temperature is $25\,^{\circ}C$. Thus water is at equilibrium when the pH and pOH are both 7, which is considered a neutral pH value. A solution with a $pH > 7$ is considered

basic and a solution with a $pH < 7$ is considered acidic. The usual range for pH or pOH is from 0 to 14.

The strength of an acid or base is determined by how much the compound making up the solution dissociates in water. Strong acids such as HCl and strong bases such as NaOH completely dissociate in water. Because strong acids and bases dissociate completely, their pH can be easily calculated using equations (10.1), (10.2), and (10.5). Weak acids and bases do not completely dissociate so their pH must be calculated based on their respective dissociation constants (denoted as K_a for an acid).

A buffer is a solution consisting of a mixture of a weak acid and its conjugate base, or a weak base and its conjugate acid. It is referred to as a buffer because their pH changes very little when adding a small amount of strong acid or base. Buffers are used to keep pH values close to constant and thus have many applications in cell culture and other biological applications. A property that distinguishes one buffer from another is the K_a value. The negative log of the K_a gives the pK_a, which is the pH value around which the weak acid provides buffering. Some weak acids used as buffers, such as potassium dihydrogen phosphate (KH_2PO_4), can lose more than one proton and thus have more than one K_a value. These weak acids are known as polyprotic acids.

Feedback Control

Control systems are generally in two categories: open loop systems and closed loop systems. An open loop system modifies the inputs to a system without monitoring the outputs. Open loop configurations thus have no way to tell if the changes made to the system actually perform as desired. Closed loop systems implement a feedback loop in the control path. The closed loop system inputs a value into a system, monitors the output, and then compares the output to the desired output characteristic to determine how to change the input value. Feedback systems thus offer increased stability, reduced

noise, reduced sensitivity to variations in input characteristics, and ultimate control over the output.

A common method to implement feedback control is through PID (proportional integral derivative) control. The control sequence of a PID system is illustrated in Figure 10.1. The system first monitors the output of a process. The output value is then fed back and compared to the setpoint of the system, which is set externally. The difference produces an error value. The error value is multiplied by "proportional," "integral," and "derivative" terms which are then summed to vary the input to the process. Each of the

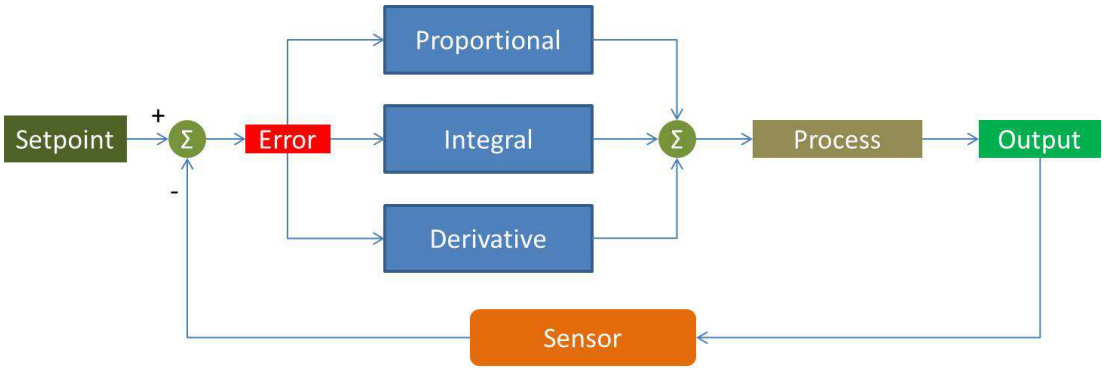

Figure 10.1: Control sequence for a PID system.

three PID elements of the controller has a different effect on the function of a system. Proportional control provides information on the current setpoint error. Integral control provides information on what has happened to the system in the past. The derivative portion provides information on how the system will perform in the future. These systems are often used concurrently but control systems also exist which only utilize one or two of these elements. Overall, the system can be described mathematically through equation 10.6 where $E(t)$ is the error, K_P, K_I and K_D are the proportional, integral, and derivative constants respectively, and $C(t)$ is the control output of the system.

$$C(t) = K_P \times E(t) + K_I \int_0^t E(t)dt + K_D \frac{dE(t)}{dt} \tag{10.6}$$

As shown in equation 10.6, the formula for calculating the input to the system is a continuous function. Since most modern control systems operate in discrete time, it is necessary to convert the continuous function into discrete-time function. This transformation requires approximations for both the integral and derivative portions of the equation to obtain the discrete-time PID formula. We use a simple first order approximation with t_S as the sample period to derive equation 10.7.

$$C(n) \cong K_P E(n) + \left[E(n) - E(n-1)\right]/t_S + t_S \sum_{0}^{n} E(n) \tag{10.7}$$

10.2 Fabrication

The feedback system used for this work uses a discrete ISFET for sensing pH. PDMS microfluidics are employed to control the microenvironment using incorporated valve structures. The microfluidics are joined to the ISFET to form an integrated testing platform. ISFET readout, valve control, and PID control are performed with a DAQ and a computer running MATLAB.

The fabrication for this device can be categorized into four parts. The first part is the fabrication of the discrete ISFET, discussed in Chapter 9. The remaining three parts are addressed in this chapter and include fabrication of the microfluidic environment, the ISFET readout circuit, and the valve control system. These four parts are integrated to form a feedback control system.

System Integration

There were multiple components necessary to make this feedback controlled microfluidic system work. Every part of the system was ultimately controlled using MATLAB. The computer used a National Instruments USB-6212 DAQ to interface all of the electrical connections necessary. The ISFET sensor was attached to a readout circuit which produced a signal read into the DAQ for MATLAB analysis. The microfluidic valves were controlled using an output from the DAQ.

All of the fluidic connections were made using tygon tubing. The system used gravity feeds to produce pressure driven flow through the device. The use of gravity for pressure flow was especially advantageous because it eliminated the need for pumping apparatus.

A picture of the complete system is shown in Figure 10.2. Specifics for the operations of the components are in the following sections.

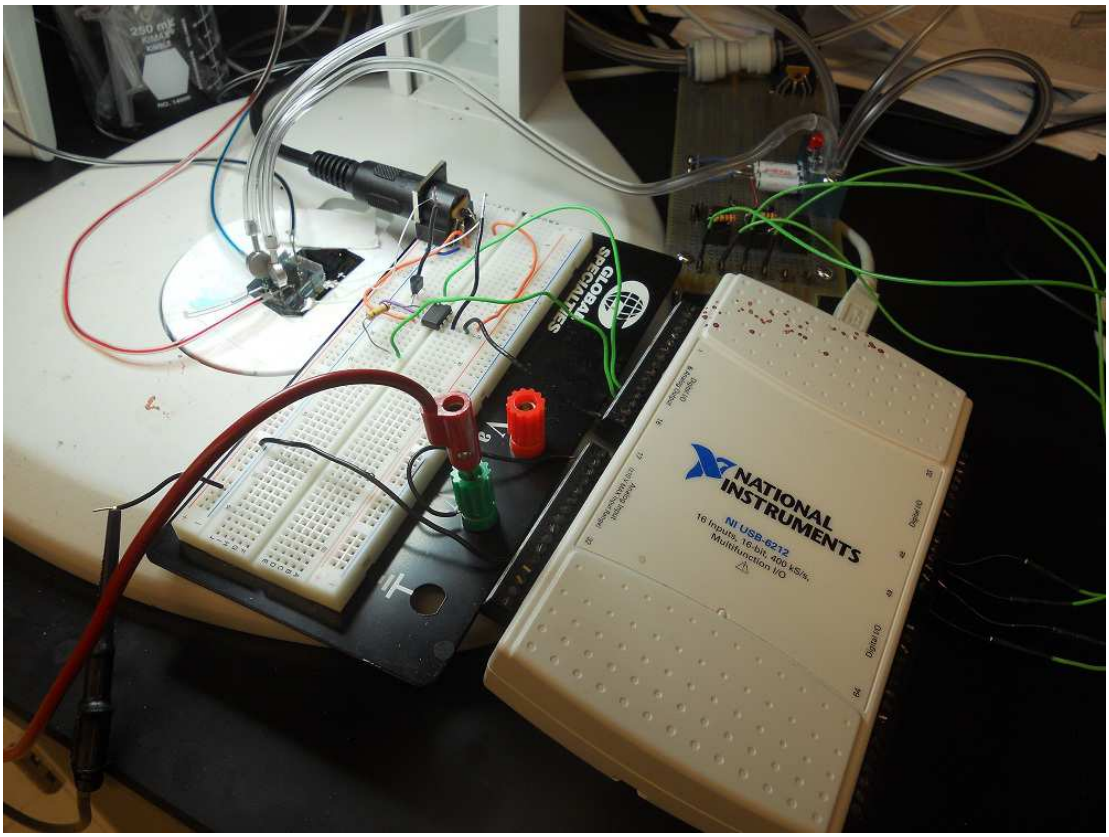

Figure 10.2: Picture showing all the components of the feedback system. The microfluidic device is shown with multiple fluidic inputs. Pressurized air is also input in the microfluidics for valve control. The flow of pressurized air is controlled by solenoid valves shown in the upper right. The ISFET readout circuit was implemented on a breadboard. The DAQ controls the ISFET readout circuit as well as the valve control circuitry.

PDMS Microfluidics

All of the microfluidic devices were made using standard fabrication techniques as presented in Chapter 3.

The design for the PDMS microfluidic interface also went through many iterations. The first device design is shown in Figure 10.3. The multilayer PDMS design featured a central processing chamber and two valves. The valves were to control the entry of fluid from either of the side channels. The chamber was to be centered over the pH sensitive electrode on the first discrete ISFET design. This design did not work well because of the symmetry; directing fluid to flow from one port to another was very difficult. The small chamber size was also inadequate for multiple electrodes. Another drawback to this design was the line around the outside of the pattern. A slight misalignment between the fluid and valve layers would cause one of the port areas to overlap with the line around the outside. When this happened, the line, which was only meant as a cutting aid, would turn into a channel. If the line was cut at any time during fabrication (which happened often, since it was designed to be cut) the channel would be open to air; thus fluid would leak out through the cutting line channel. This line was eliminated in subsequent designs and instead replaced with corner alignment markers.

The second design iteration featured two different analysis area options. One design, as shown in Figure 10.4, featured a large chamber area that would be situated over the sensing electrode and reference electrode. Two valves were still included but their angle was changed to allow for better spacing of the port connections. The length of the channel between the point of mixing area and the analysis area was also increased. The increase in length allowed better mixing in the laminar flow environment.

The second version of the second design iteration featured a different analysis area, as shown in Figure 10.5. This design replaced the chamber analysis area with a

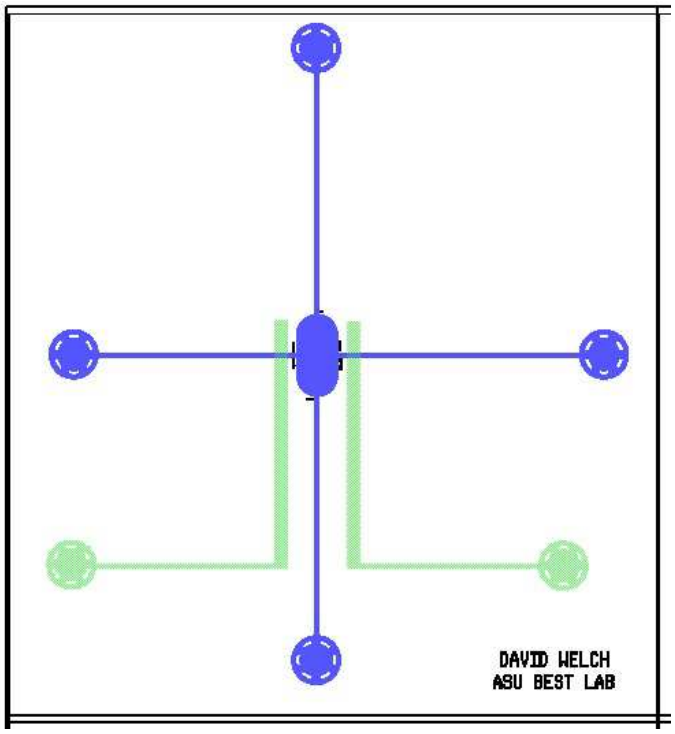

Figure 10.3: Mask designs for the first microfluidic design. The fluid layer is shown in blue, and the control valve layer is shown in green. It was designed to fit over the first ISFET device. The total area of the design is 16 mm $\times$ 17 mm.

small fluidic channel that would pass over the sensing area multiple times. This design helped to reduce the number of bubbles that were being trapped in the chamber designs.

Both designs during the second design iteration failed to allow flow as desired. The increased length of the channel before the analysis area had an adverse effect on the system because it increased the fluidic resistance. The increased resistance made fluid flow in that direction less likely than fluid flow into one of the valved channels or the bottom input channel. The small size of the channels used up to this point (100 μm across) limited fluid flow throughout the device. A faster fluid flow between the mixing region and the analysis region would reduce dead time in the feedback loop and thus make control easier. The microfluidic design was changed to allow greater flow rates in the third version. This version, shown in Figure 10.6, removed the lengthy mixing area

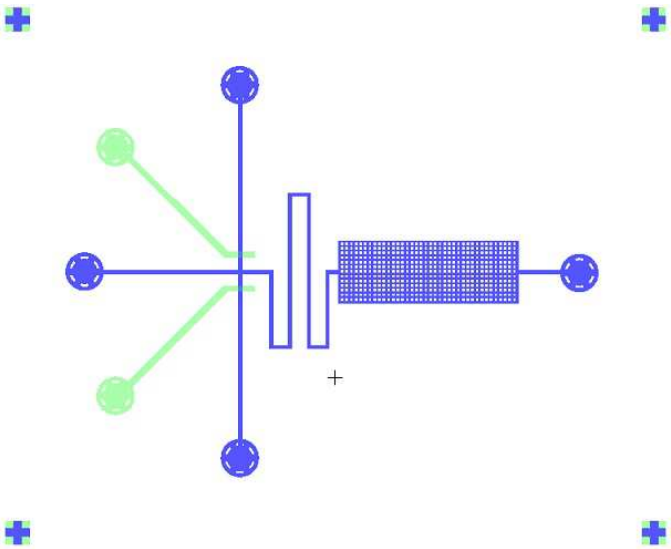

Figure 10.4: Mask designs for the second set of microfluidic designs. This design uses a chamber area for analysis. The fluid layer is shown in blue, and the control valve layer is shown in green. It was designed to fit over the second and third ISFET devices. The total area of the design is 21 mm $\times$ 17 mm.

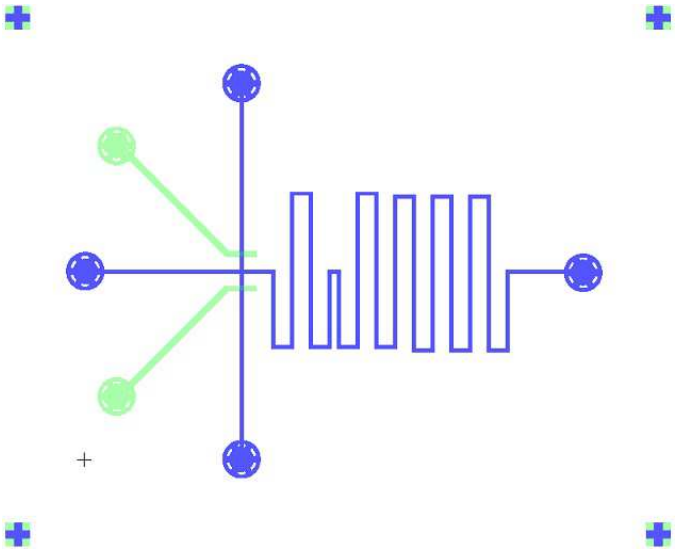

Figure 10.5: Mask designs for the second set of microfluidic designs. This design uses a serpentine channel arrangement over the sensing region. The fluid layer is shown in blue, and the control valve layer is shown in green. It was designed to fit over the second and third ISFET devices. The total area of the design is 21 mm $\times$ 17 mm.

with high resistance. All of the input and output channels were also increased in size to allow quicker flow throughout the system. The output channel was increased to larger than the input channels to encourage flow towards the analysis area. This design was used in the presented feedback system. The final PDMS microfluidics were bonded to the discrete sensor chip using oxygen plasma surface activation. This activation allowed irreversible bonding of the PDMS to the sensor devices.

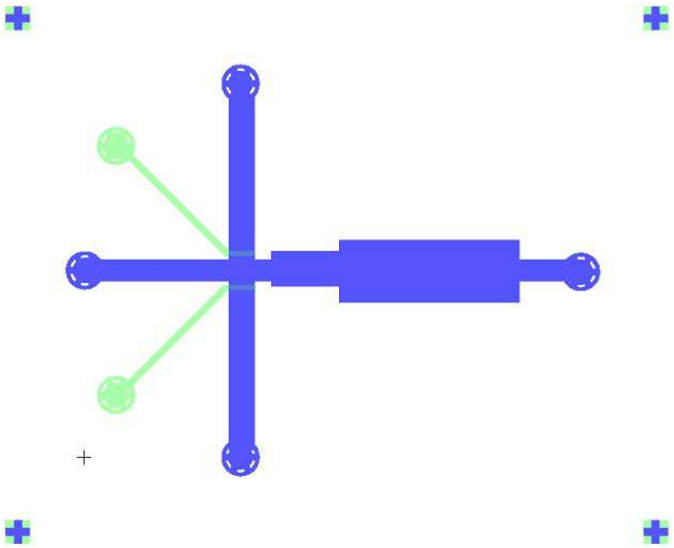

Figure 10.6: Mask designs for the third set of microfluidic designs. This design uses larger channels throughout the device to allow for greater flow. The output channel is larger than the input channels to encourage fluid flow in that direction. The fluid layer is shown in blue, and the control valve layer is shown in green. It was designed to fit over the second and third ISFET devices. The total area of the design is 21 mm $\times$ 17 mm.

Valve Control

The microfluidic valves are controlled by air pressure. When pressurized, the valves block flow in the fluidic channel they cross. An illustration of the valve action is shown in Figure 3.2. The flow of air into the valve channels is controlled by solenoid valves (LHDA1211111H, The Lee Company, Westbrook, CT). Photographs of solenoid valves are shown in Figure 10.7. The valves have two positions and can be switched by ap-

plying a 12V DC signal. The valves can switch positions at up to 300Hz. Due to the high voltage required, an isolation circuit is used to protect the DAQ and computer. The circuit, shown in Figure 10.9, uses a photocoupler to isolate the DAQ digital input from the solenoid connections. The valves are operated in a normally closed configuration; therefore, the valves will only open to allow pressurized airflow when a voltage is applied through the DAQ. Figure 10.8 illustrates the solenoid operating positions. The system uses 15 *psi* compressed air during operation.

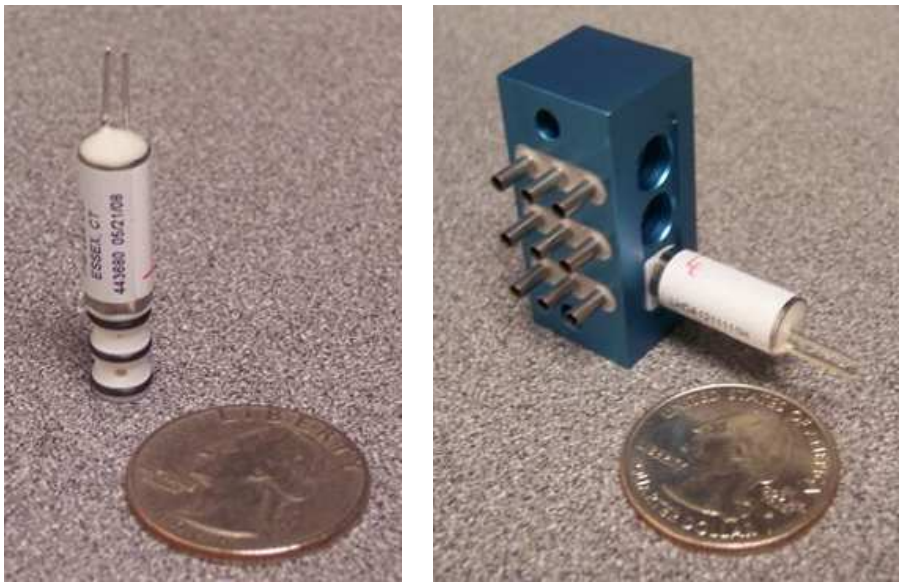

Figure 10.7: Photograph of an individual solenoid valve (left) and the valve position within a manifold.

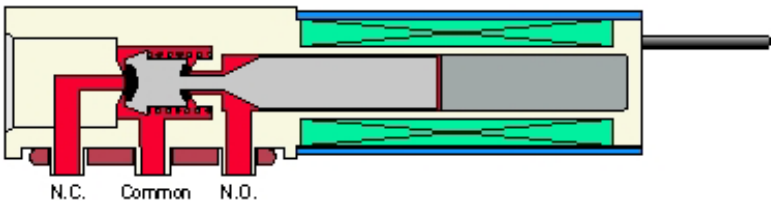

Figure 10.8: Cross section of solenoid valve showing the normally open (NO), common, and normally closed (NC) positions [125].

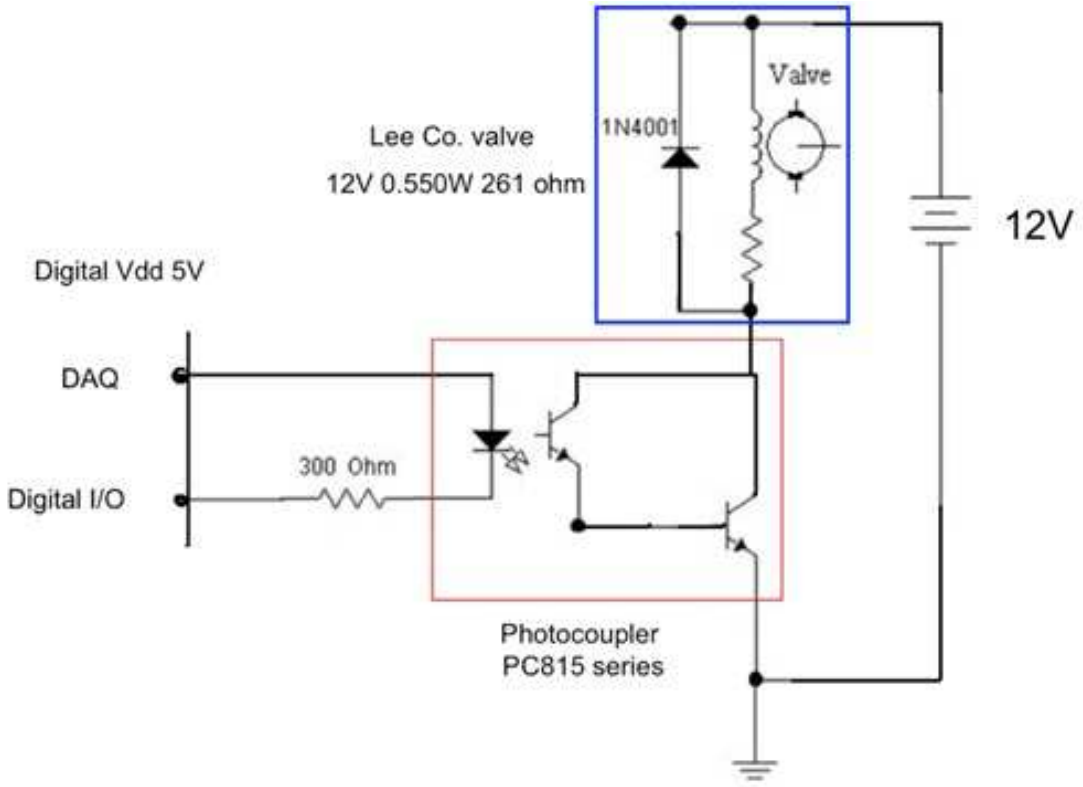

Figure 10.9: The schematic of the isolation circuit used for valve control. The photocoupler prevents high voltages from reaching the DAQ.

ISFET Readout

The device fabricated for pH detection cannot operate independently. The device only incorporates a pH sensitive nitride layer over an electrode; a transistor is needed to operate. This discrete ISFET configuration relies on a commercially fabricated MOSFET to operate. The pH sensing region acts like an extended gate connection and the operation is analogous to a regular ISFET. Using a metal connection to reduce the distance between the sensing region and the FET oxide is commonplace; even ISFETs made entirely in a CMOS process employ stacked metal layers to reduce the effective distance [126].

The ISFET device requires additional circuitry to provide an easy readout. We used the same circuit configuration as Dun *et al.* because it provides a simple readout [102]. The circuit, shown in Figure 10.10, uses a resistor with a known voltage drop to set a constant current through the MOSFET. The reference voltage applied to the solution changes depending on the pH of the solution. This circuit provides a simple means of readout by monitoring the reference voltage. This work used an LND150N3-G N channel MOSFET (Supertex, San Jose, CA) with the gate connected to the pH sensing region. The amplifier was an LF356N JFET input operational amplifier (Texas Instruments, Dallas, TX). During operation, the current through the MOSFET was set at $1\,\mu A$ by applying $0.182\,V$ across the $182\,k\Omega$ resistor.

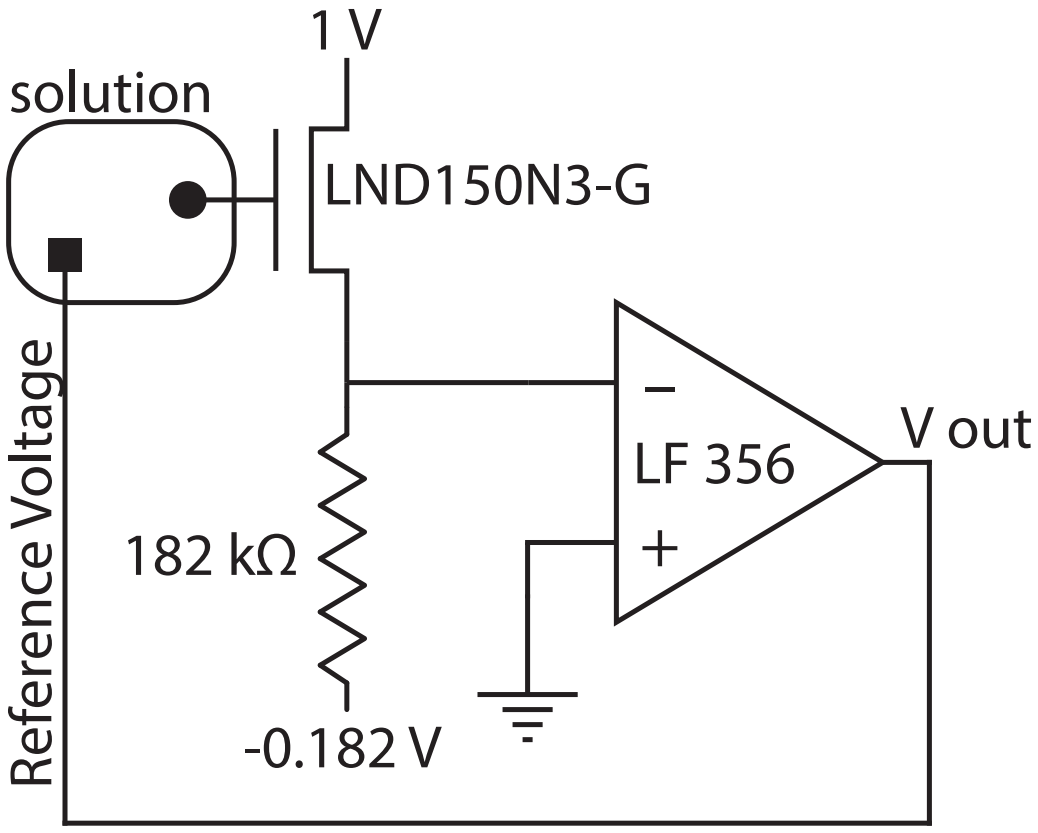

Figure 10.10: Schematic of the ISFET readout circuit. The ISFET kept at a constant current. Changes in pH are reflected in changes to the reference voltage.

Fluids

Fluid choice was critical for successful feedback operation as explained in section 10.1. This work used mixing of a weak acid, KH_2PO_4, with a strong base, $NaOH$. The solution therefore provides buffering around the region of interest, pH 7. The solutions were dyed, KH_2PO_4 with red food coloring and $NaOH$ blue food coloring, to aid in visualization of mixing. Both fluids were suspended approximately $50\,cm$ above the microfluidic device to provide pressurized flow from gravity. The mixed solution was free to drain throughout the experiment.

10.3 Results

pH Sensitivity

Standard pH buffers were used to determine the sensitivity of the discrete ISFET. Buffer values of pH 4, pH 7, and pH 10 were obtained from Oakton Instruments (Vernon Hills, IL). The buffers were introduced to the device one at a time, and the calibration value was recorded. The three point calibration shown in Figure 10.11 indicates a pH sensitivity of $33\,mV/pH$. This value is in agreement with the results of $36.5\,mV/pH$ by Prodromakis *et al.* using a similar device structure [109].

Feedback Control of pH

Figure 10.12 demonstrates the pH feedback control capabilities of this microfluidic system. The setpoint was adjusted in $5\,mV$ increments to show the response characteristics of the system. During tuning we discovered the necessity of an error value for the system to control the pH. The error provides the appropriate mixing ratio of the two reagents. Because a persistent offset was necessary for our operating region, we eliminated the use of the integral component of the control system and instead just used proportional and derivative values. Leaving the integral error factor would have caused wind up and loss of system control since the integral could never correct the offset.

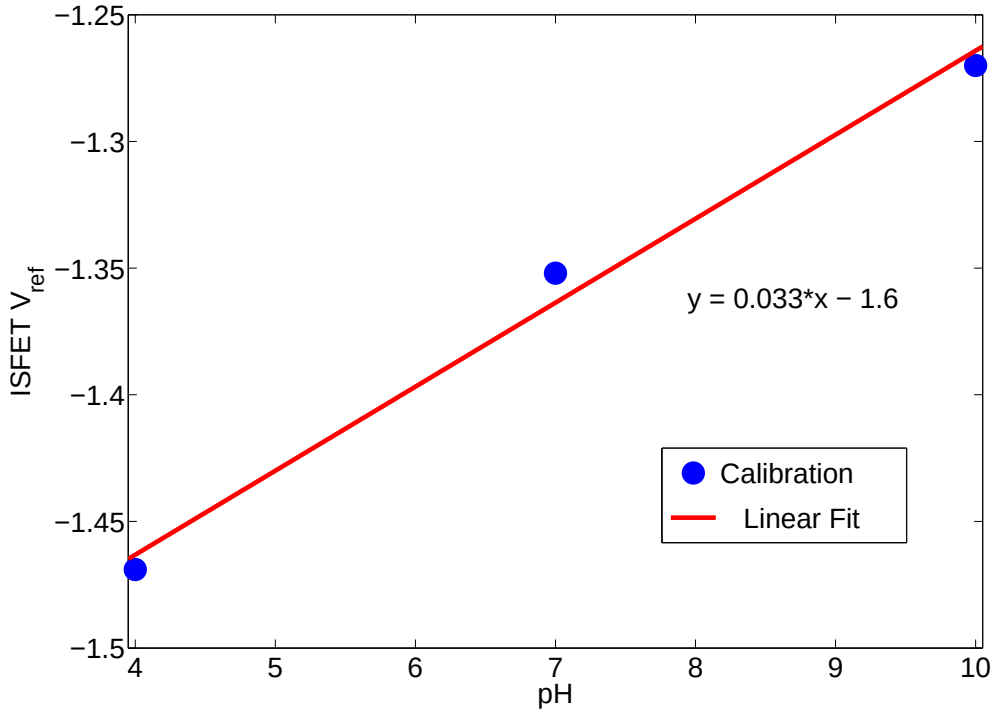

Figure 10.11: The three point calibration curve for the ISFET gives a sensitivity of 33 mV/pH.

The methods to complete the feedback loop for this system provided interesting behavior. The error signal was a difference in voltages between the set point and the measured value. The error signal was simply a voltage. However, the valves operated on a digital signal. A pulse width modulated (PWM) signal was created to convert the variable amount of error into a digital signal for valve operation. The error in volts was converted to a time using the tuning parameters of the feedback controller. The maximum operating frequency of the valve was 300Hz so the minimum pulse width was set to 0.01 second. Even periods of PWM signal were maintained by capping the sum of the pulse on and off time.

The error between the setpoint and measured pH value (V_{ref}) showed a linear relationship. The fit line for the error is shown in Figure 10.13. We were able to subtract

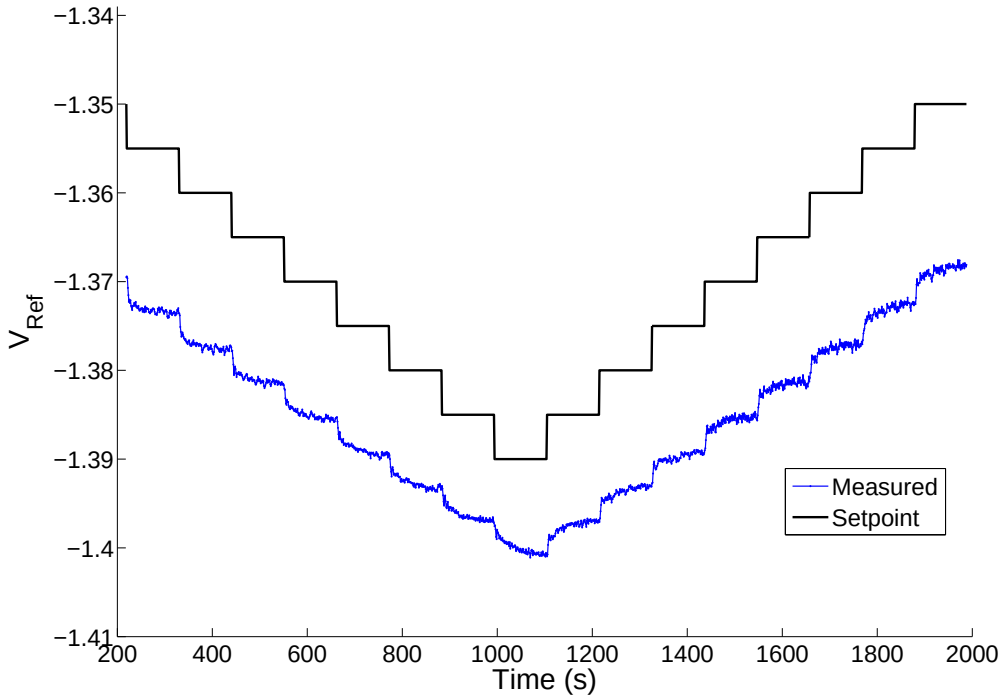

Figure 10.12: Feedback controlled steps in pH. An offset between the setpoint and the V_{ref} is necessary to maintain a specific pH value.

this error from the setpoint value to better demonstrate our control over the system. The modified setpoint is shown compared to the measured values in Figure 10.14. Each step in the measured pH value represents a 0.14 pH change. The system was tested for multiple hours and showed consistent control over the measured pH value. Drift in sensor operation was present but minimal over a two hour test at a consistent setpoint. Results are shown in Figure 10.15.

Range of pH Control

An example titration curve for a polyprotic acid is shown in Figure 10.16. The steps within the titration occur because of the progression through different chemical reactions, summarized in table 10.1. The use of KH_2PO_4 produces buffering due to the

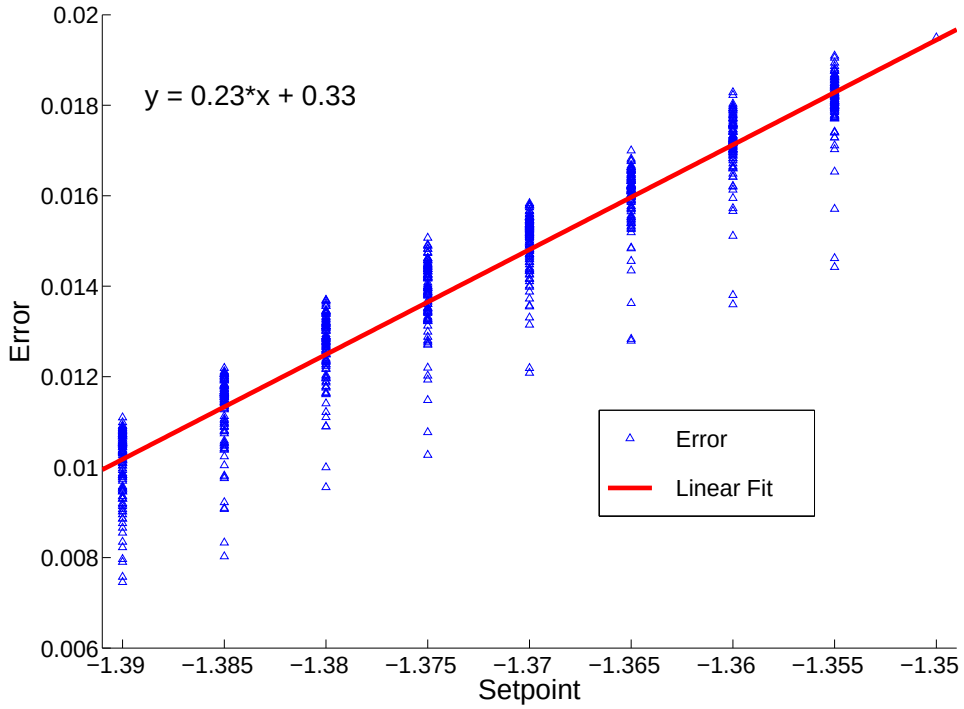

Figure 10.13: Error for a given setpoint. Error values converge to the fit line when the setpoint changes values. The relationship is approximately linear over the buffering region.

common ion effect. This means we introduce phosphoric acid H_3PO_4 to the system by means of its conjugate base, KH_2PO_4, which completely dissociates.

Table 10.1: Reaction equations during a titration of KH_2PO_4 and their pK_a values.

Reaction	pK_a
$KH_2PO_4 \rightarrow K^+ + {H_2PO_4}^-$	dissociates completely
$H_3PO_4 \rightleftharpoons {H_2PO_4}^- + H^+$	$pK_{a1} = 2.15$
${H_2PO_4}^- \rightleftharpoons {HPO_4}^{2-} + H^+$	$pK_{a2} = 6.82$
${HPO_4}^{2-} \rightleftharpoons {PO_4}^{3-} + H^+$	$pK_{a3} = 12.38$

Feedback control of pH is very difficult because pH is on a logarithmic scale and can rapidly change with very small additions. These points of rapid change are called equivalence points and are seen at points of very high slope on a titration curve.

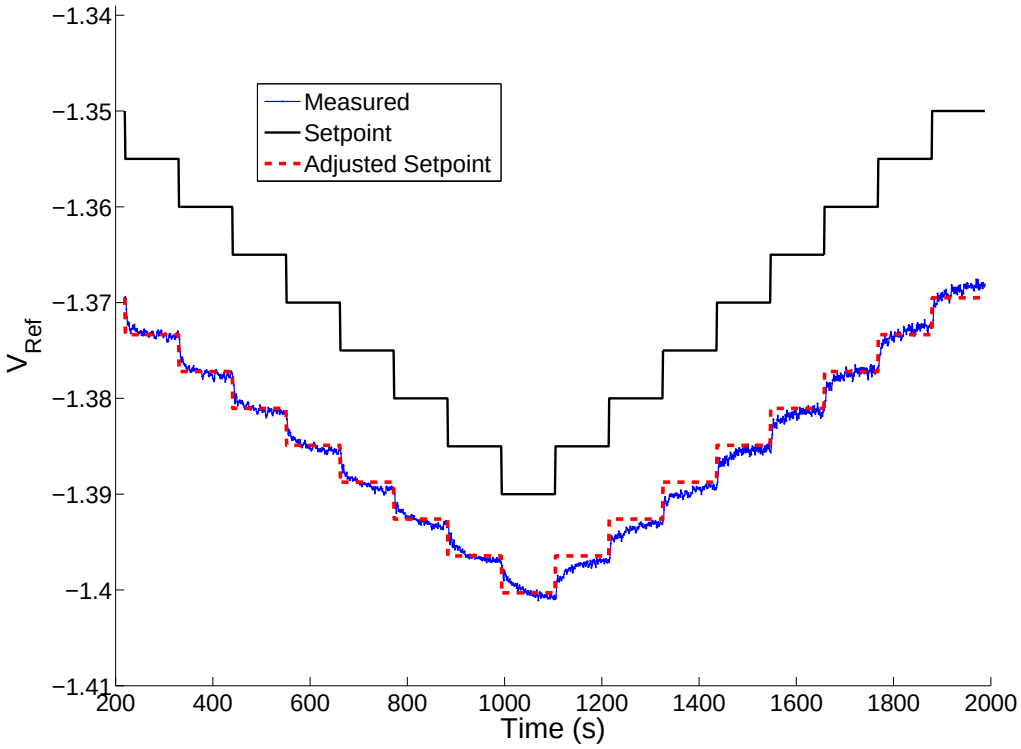

Figure 10.14: Feedback controlled steps in pH compared to the modified setpoint shows a well controlled feedback system. Each step in V_{ref} is approximately 0.12 pH.

Titrating a strong acid with a strong base yields an equivalent point close to pH 7. The pH is most sensitive around these equivalence points so it is extremely difficult to control pH in these regions. Therefore, this work demonstrates control using KH_2PO_4, a weak acid, titrated with $NaOH$, a strong base. This utilizes polyprotic buffering behavior to decrease the slope of the titration curve in the region of interest. With a decreased slope, feedback control in this region is more easily attained.

The range of pH for the system is demonstrated with a controlled titration of a weak acid (KH_2PO_4) and strong base ($NaOH$). Results from this titration are shown in Figure 10.17. As expected, the system was not stable near the equivalence points of the

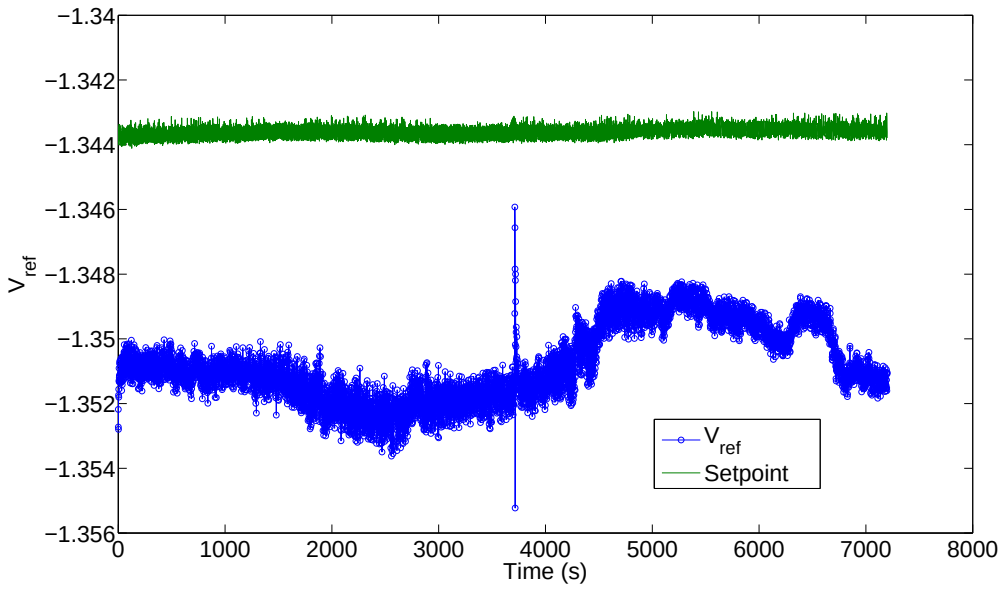

Figure 10.15: Drift in sensor output over a two hour test with a consistent setpoint.

system. The pH changes at these points still represent a multiple order of magnitude change in $[H^+]$, even though we are using a buffered solution.

The system required serial operations to read the input signal, process the error, and then execute the controlling PWM signal. The reading and processing time created delays between the PWM signal. The delay caused both valves to be open for a short amount of time regardless of the error signal produced. This small amount of leakage limited the pH range of the system because mixing always occurred in some amount. The effects were seen when the PWM signal period was shortened from two seconds, shown in Figure 10.17, to only one second, shown in Figure 10.18. The range of pH attainable is noticeably lower with the shorter PWM. However, the shorter PWM signal allows finer control over the biological buffering region. A longer PWM reduces the proportion of processing time to PWM period. The smaller proportion minimizes the total amount of unwanted mixing during processing.

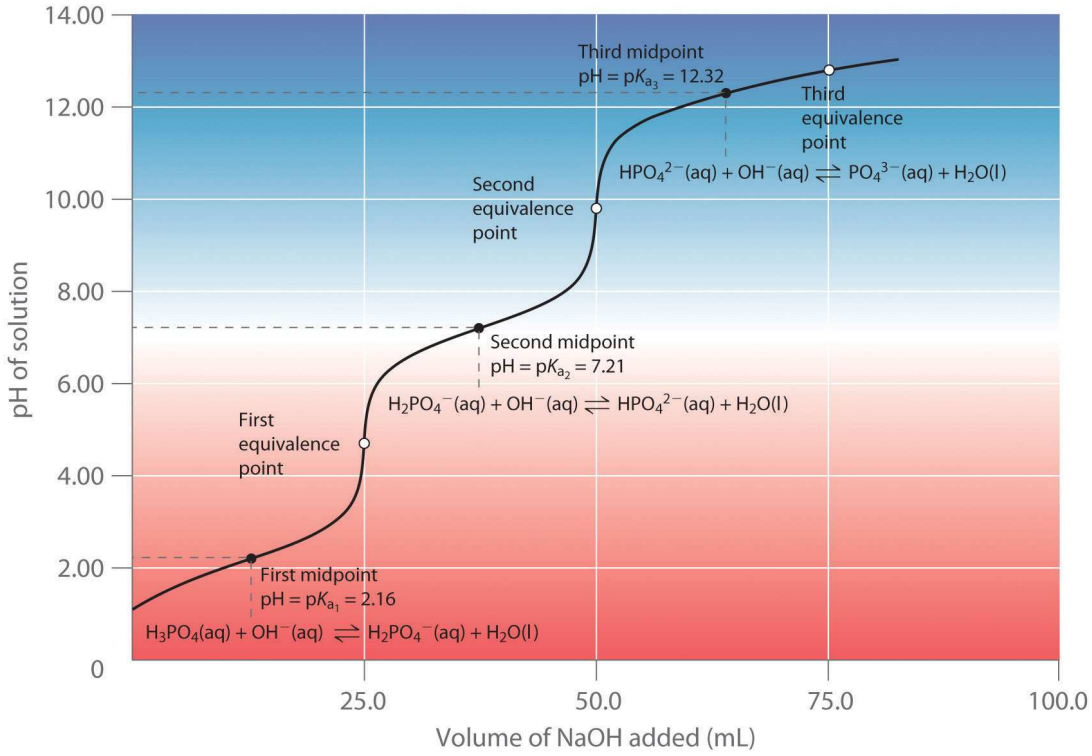

Figure 10.16: A sample titration curve for a polyprotic acid, H_3PO_4 [127]. The titration for KH_2PO_4 has a similar shape but different pK_a values.

Comparing Figures 10.17 and 10.18 also shows the drift problems of the pH sensor. Significant time passed between the calibration and the titration in Figure 10.18 so the pH levels are not accurate.

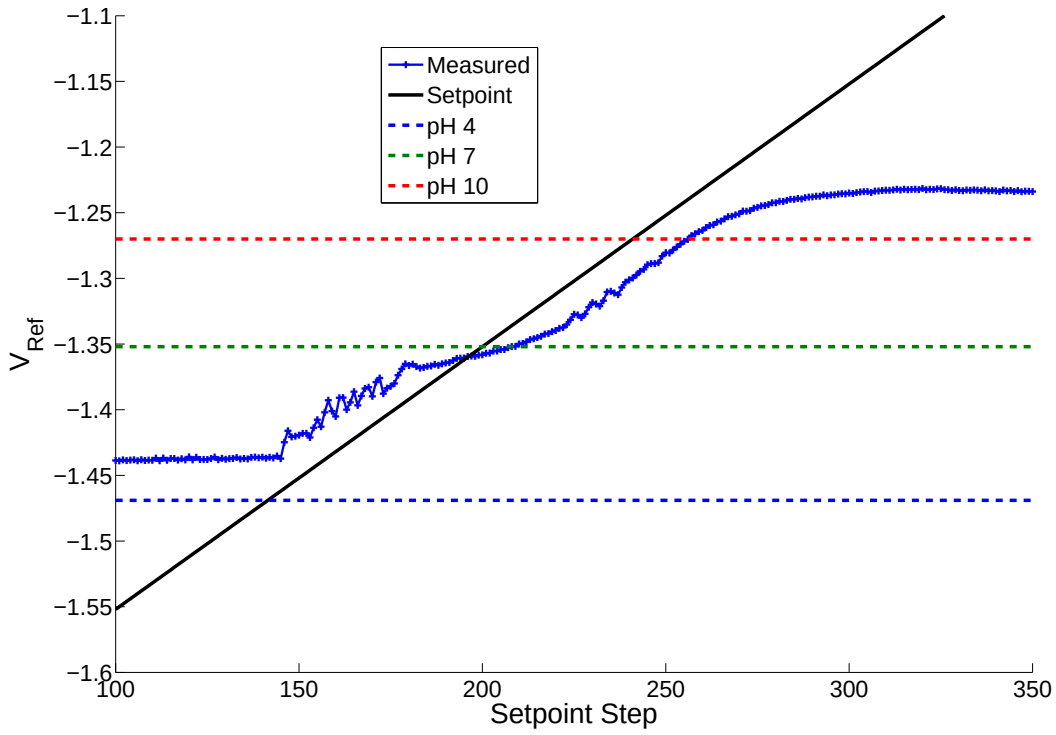

Figure 10.17: Feedback controlled titration using a weak acid (KH_2PO_4) and a strong base ($NaOH$). The polyprotic titration shape, as shown in Figure 10.16, is clearly defined. Equivalence points for the titration prevent stable feedback control. Indicated pH levels were measured with calibrated buffer solutions. The PWM signal had a period of two seconds.

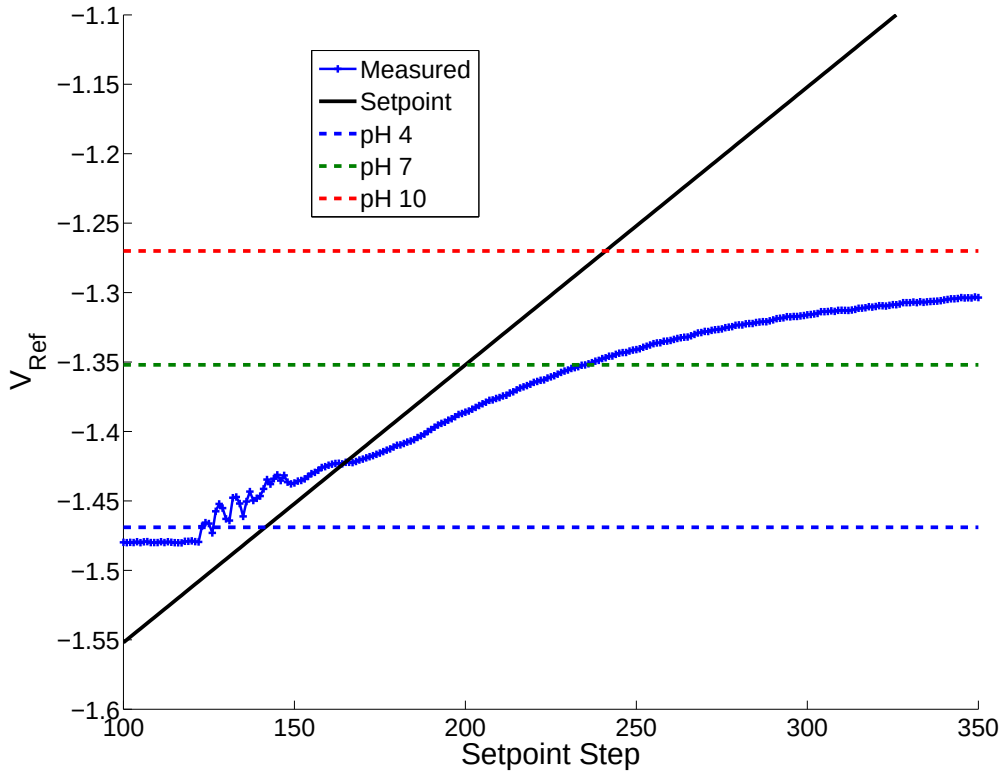

Figure 10.18: Feedback controlled titration using a weak acid (KH_2PO_4) and a strong base ($NaOH$). The range of pH is significantly reduced due to the reduced PWM period. Drift in the pH signal is also apparent when compared to Figure 10.17.

Chapter 11

CMOS BIOLOGICAL SENSORS

One of the most appealing methods to create lab-on-a-chip systems is to integrate the microfluidic and biological reagents with CMOS technology. CMOS technology offers integrated circuits, programmability and control, and embedded sensors in one device to perform many of the functions needed for a lab-on-a-chip. Furthermore, the shrinking sizes of CMOS features allow for the circuits created to be approximately the same size as the cells and bioparticles being analyzed [128]. CMOS technology has been used to create microelectrodes, microcoils, photodiodes, bipolar transistors, and ion sensitive field effect transistors (ISFETs) that serve as front end detection devices for a variety of applications ranging from temperature sensing to pH sensing to glucose monitoring to dielectrophoretic manipulation [80].

In examining the measurement techniques for LOC and μTAS systems, the vast majority of these systems are based on the measurement of basic quantities: voltage, current, charge, impedance, optical power, etc. A vast library of circuits is already available to make many of these measurements. The hurdle to making a complete system is now to design specifically for biological applications. New designs need to emphasize the eventual integration into a biological system. The best methods for creating electrical interfaces using the CMOS architecture also need to be determined.

This chapter presents two CMOS chip designs for biological sensing applications. Both designs were focused on their eventual integration into microfluidic systems. Special considerations were made for their eventual testing and packaging. Along with Chapter 12, this work makes significant progress towards fully integrated CMOS technology for biological applications.

11.1 CMOS Process Overview

Both of these chips were produced through the MOSIS Integrated Circuit Fabrication Service. The service allows for small quantity fabrication runs specifically designed for research and education purposes.

The process used for both chips allowed the definition of three metal layers and two poly layers. The process is designed for $5V$ operation. Both chips were the same die size, 3 mm $\times$ 1.5 mm. Circuit simulation and layout was performed in Cadence using the amis_c5_pdk.Rev2.18 design kit.

11.2 First CMOS Chip

This chip was designed with the goal of performing on-chip cell culture monitoring. The chip included six different sensing regions. Each region contained an ISFET, a Clark-type oxygen sensor, and a capacitance sensor. The ISFETs and the Clark sensors were directly connected to bond pads for off-chip processing. The capacitance sensor was connected to a capacitive feedback amplifier to convert the capacitance value to a voltage output. A separate amplifier test structure with the capacitive feedback removed was included so the amplifier could be tested independently.

The layout of the total chip area was important to the design. All of the bond pads were secluded to one end of the chip, while the sensing regions were pushed to the other. The goal of this design was to maximize the space available to seal the analysis area, which would contain liquids, from the electrical connection area. The bond pads were arranged in two rows and wire bonding was planned as the method of forming electrical connections. A picture of the entire chip layout is shown in Figure 11.1.

ISFET

The ion sensitive field effect transistor was made as an NPN transistor without a gate. The ISFET was designed with the intention of removing most of the passivation ox-

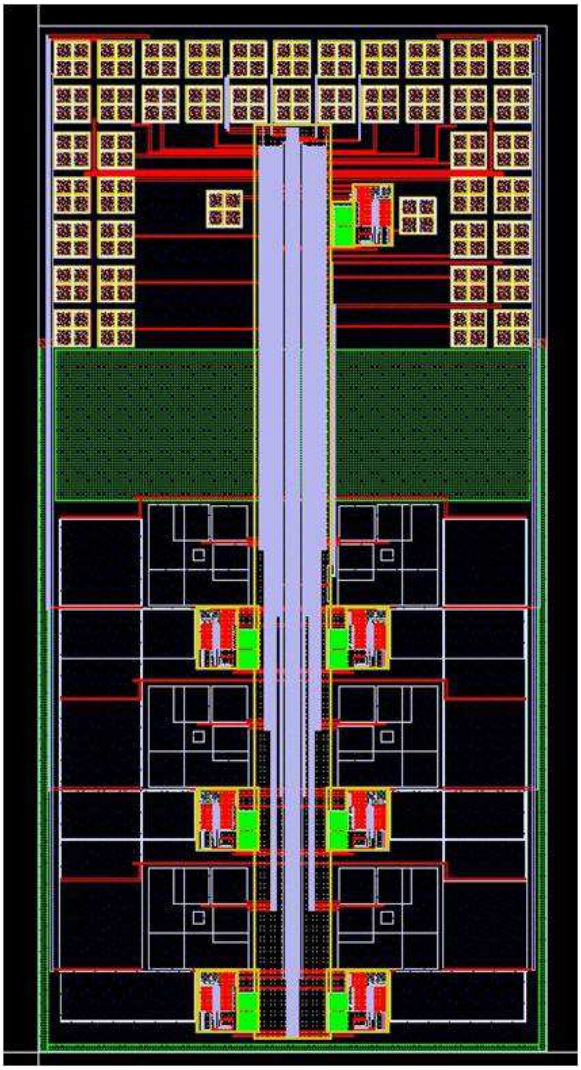

Figure 11.1: The complete Cadence layout for the first CMOS chip design. The layout is for a die size of 3 mm $\times$ 1.5 mm.

ide above the gate region with post-processing. Two layers of metal were included to cover the drain and source areas. The metal was included to act as a shield during post-processing so only passivation above the gate would be removed. This shielding method was designed to increase the ISFET response by decreasing the gate oxide thickness and therefore increasing the capacitance and sensitivity to hydrogen ion concentration. The layout of a single unit of the ISFET is shown in Figure 11.2. The gate length of the ISFET is 1.0 μm and the total width is 9000 μm (36 rows $\times$ 250 μm).

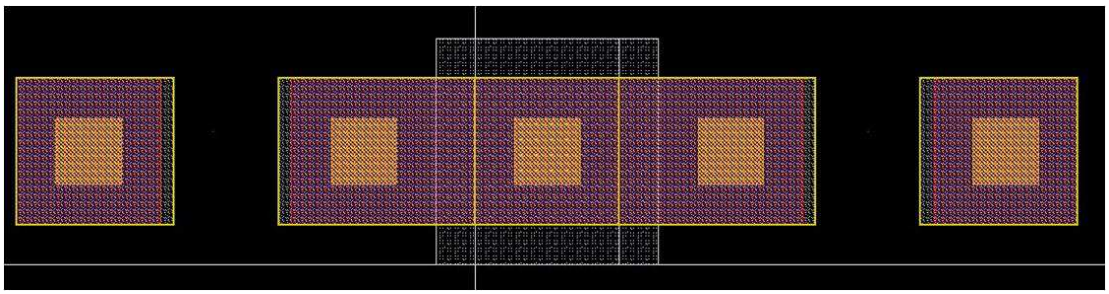

Figure 11.2: Layout of an individual unit of the ISFET. The middle area would act as the source. Drain connections are on both sides. The two gate areas are the undefined regions between the source and the drain. Each gate area is 1.0 μm long. Metal layers are defined to cover the source and drain connections. The metal layers also act as shielding during etching.

Capacitance Sensing

To sense capacitance, an interdigitated electrode structure (IDES) was designed with all three metal layers stacked on top of each other. Stacked metals were included with chip postprocessing mind. The goal was to remove the passivation between the stacked metal layers using a postprocessing etch. Without passivation, the capacitance could be simplified to a parallel plate structure. This would allow the analyte to reach the area between the IDES fingers with the goal of maximizing capacitance.

It was necessary to calculate the expected capacitance of the IDES, so we could correctly measure the capacitance. We assumed a parallel plate capacitance neglecting any fringing capacitance values. There were 100 rows of the stacked metals creating

200 spaces. The area of the “parallel plate” capacitor is found by taking the length of each row and multiplying by the height of the three metals when stacked. Using the relative permittivity (ε_r) value of water, we found an approximate capacitance value of 64.3 pF. In the expected range for capacitance sensing we were able to calculate an appropriate feedback capacitor to use in an electrometer op amp configuration. We chose a value of 1 pF for the feedback capacitor, so we would get a large gain from the amplifier. The feedback capacitor was made on-chip using the two poly layers.

The electrometer circuit, designed to output a voltage value representing a measured capacitance, is seen in Figure 11.3.

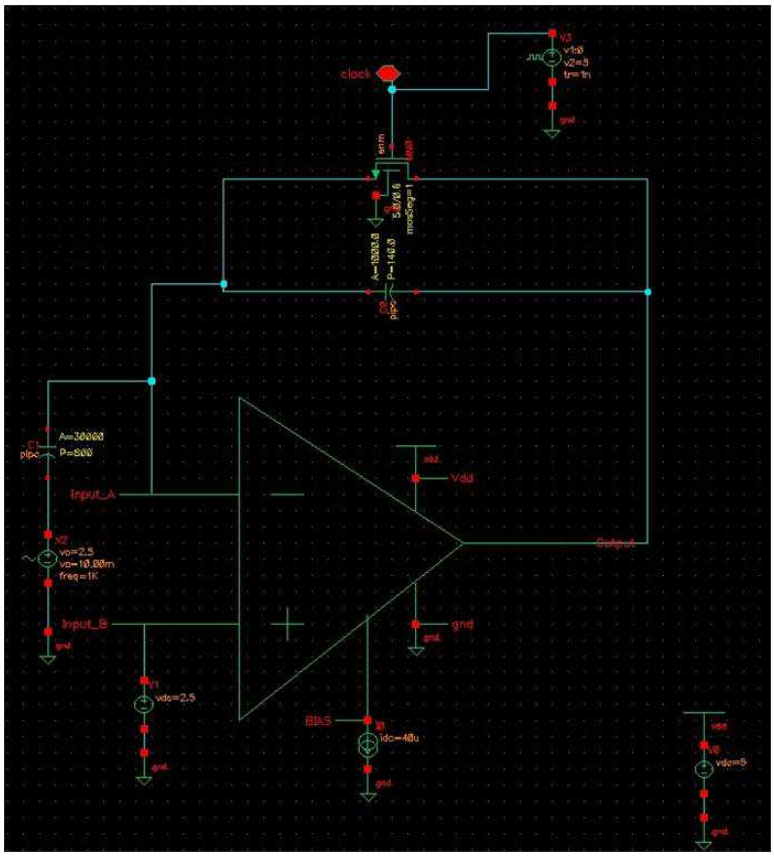

Figure 11.3: The schematic for the electrometer op amp charge amplifier circuit is shown in a test configuration.

Amplifier Design

The op amp is a large swing operational transconductance amplifier (OTA) with large input transistors to reduce noise from the noisy biological system. The schematic for the transistor layout of the amplifier is shown in Figure 11.4 with the W/L values included in the figure. The electrometer is reset through the feedback path using an external clock signal.

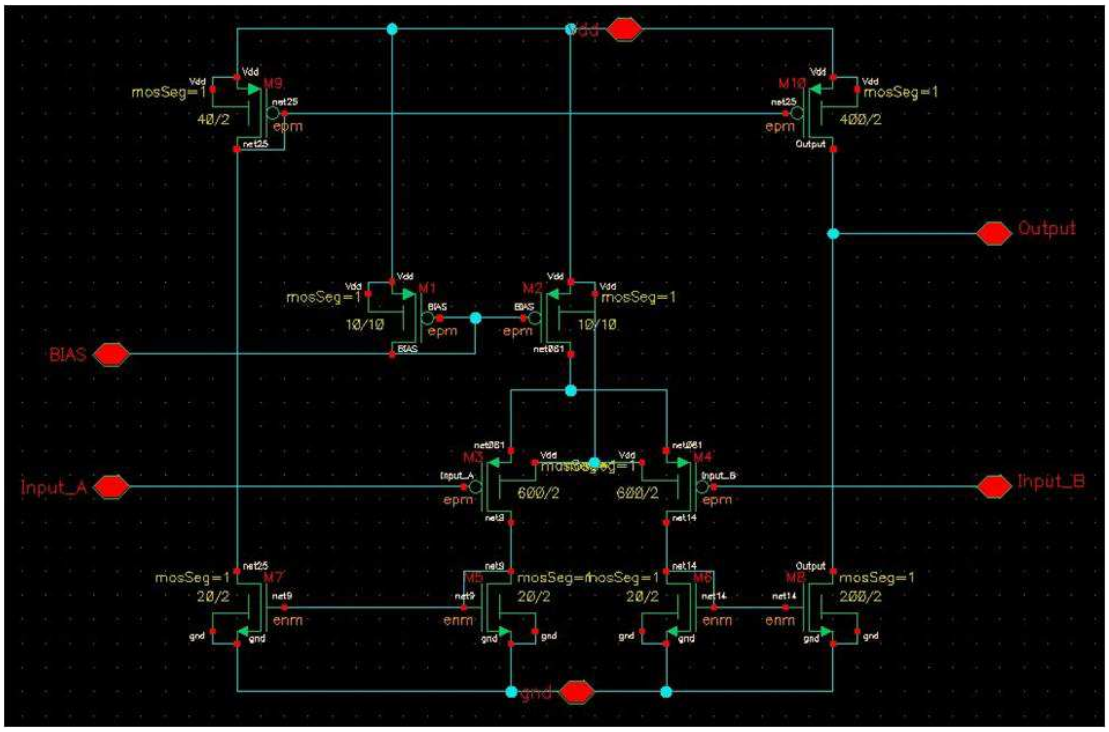

Figure 11.4: The transistor layout for the OTA is shown. W/L values are included for each transistor.

Clark Sensor

A Clark-type sensor is simply a three electrode design for measuring oxygen concentration. This design used three electrodes with different sizes: a small working electrode, a larger reference electrode, and an even larger counter electrode. The electrodes were made by stacking all three metal layers and with the plan of exposing them with passi-

vation removal during postprocessing. The Clark-type sensor was included in each of the six sensor areas along with the capacitance IDES and the ISFET.

First Chip Results

We discovered a number of design flaws during the testing of the fabricated chip, shown in Figure 11.5. The first flaw was the design for the amplifier biasing. The design included a biasing transistor for every amplifier on the chip, including the test structure. A better design would have used just one biasing transistor and mirrored the output to each amplifier. This error caused the biasing current to reflect the parallel combination of every bias transistor on the chip. When adjusted for this flaw the biasing behavior matched the simulated values.

Figure 11.5: Micrograph of the first CMOS chip.

Besides confirming the correct biasing, little analysis was performed on the chip. The chips quickly became inoperable during testing, likely due to electrostatic discharge (ESD). This design didn't include ESD protection, but this served as a reminder to why it was necessary.

The method for generating a reference voltage on this chip was also poorly executed. The amplifier required a $2.5V$ reference voltage for proper operation. In lieu of a bandgap reference, a voltage divider was made on chip using high resistance poly. Using a voltage divider was not a good option because of the variations in resistance values; matching problems between resistors could potentially cause incorrect voltage division. Additionally, this voltage divider was repeated for every amplifier instead of one instance that was connected throughout the chip. Because of this design, it was likely the reference values were different for each amplifier.

Overall this design required too much post-processing. Both the IDES and ISFET design required extensive etching through passivation. The materials and thicknesses included in the passivation were not disclosed, so a plan for etching could not be predicted. Furthermore, if the etching were successful, we would have left exposed aluminum. As discussed in Chapter 6, exposed aluminum needs to be plated before inclusion in a biological monitoring system. Electroless plating was not successful so these chips were not tested further.

11.3 Second CMOS Chip

The second chip was designed to correct many of the errors in the first version. First, the new design was restructured to accommodate better packaging methods for direct exposure biological environments. The chip architecture was completely changed to include a pad ring structure with the sensing regions centered on the chip. This sequestered the fluidic area to the middle of the chip while allowing electrical connections to extend in

all directions. This allowed for an increased pad count. The design geometry was used for the packaging method presented in chapter 12.

Another big change was the elimination of exposed aluminum in the sensing area, thus avoiding the problem of effective electroless plating. The Clark sensor design was eliminated in favor of additional circuit configurations for both capacitive sensing and ISFETs. A picture of the layout for this chip is shown in Figure 11.6.

ESD Protection

Each bondpad was designed with electrostatic discharge (ESD) protection. The ESD protection is a simple design but provides ample protection for our circuit. The schematic is seen in Figure 11.7. Protection was provided using diode connected transistors. One transistor was forward biased from the pad to VDD when the signal voltage was higher than approximately 5.7 V. Another diode connected transistor was forward biased from ground to the pad. This diode turns on to protect the circuit when the voltage was below approximately -0.7 V.

Amplifier Design

A single amplifier design was made and reproduced throughout the chip design. The design is a wide swing output transconductance amplifier (OTA). It was designed largely around the work by Harrison and Charles [129]. The design schematic, shown in Figure 11.8, was used in their neural amplifier. In this design, the transistor sizes were changed and the cascode transistors were omitted. Transistor sizes were tweaked to center the output by balancing the PMOS and NMOS. Large transistors (W/L=800/4) were used as input transistors to decrease noise. The OTA was designed to run on a 30 μA bias current with $Vdd = 5V$.

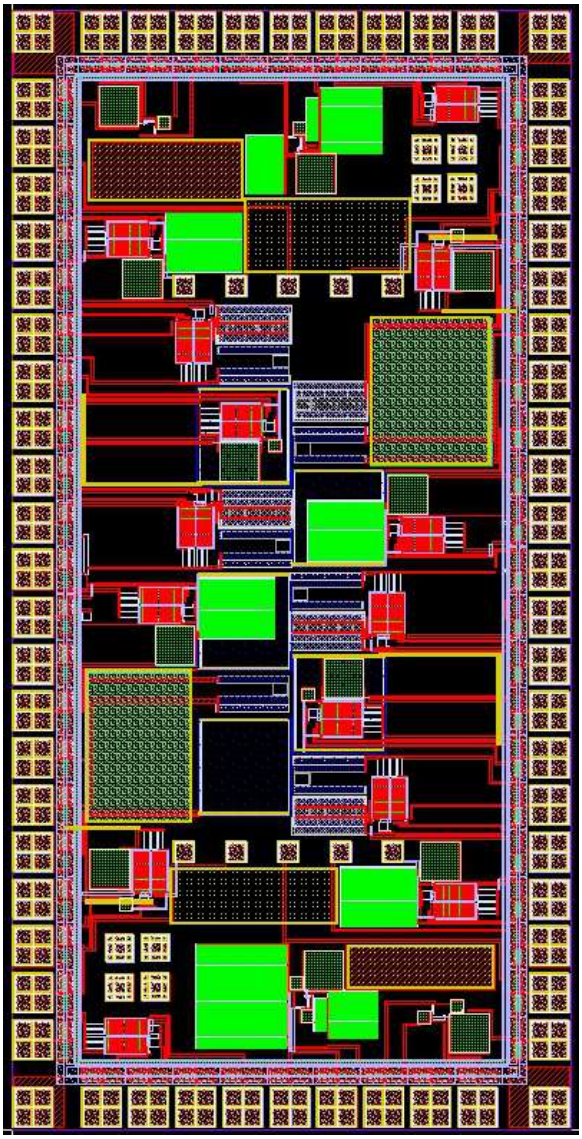

Figure 11.6: The complete Cadence layout for the second CMOS chip design. The layout is for a die size of 3 mm $\times$ 1.5 mm.

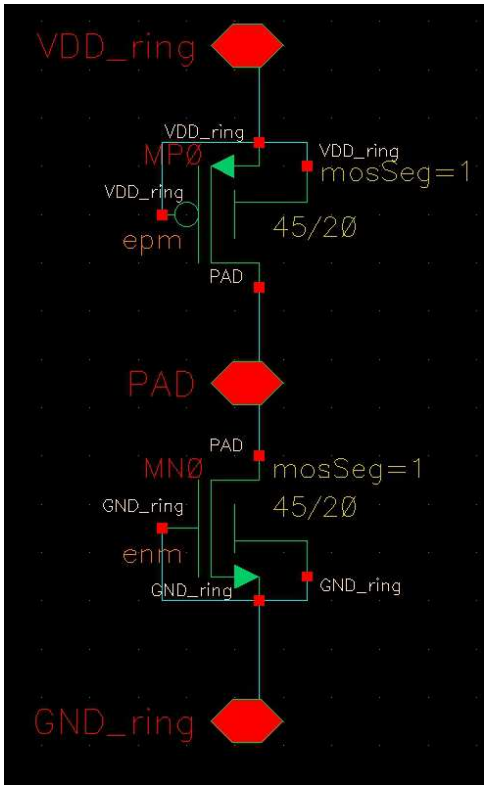

Figure 11.7: ESD pad schematic.

ISFET

CMOS ISFET designs differ from normal ISFET configurations [130] due to the large amount of oxide above the gate region as well as the need for a polysilicon gate for self-aligned source and drain regions [126]. Therefore, this version of our chip uses a CMOS ISFET similar to the design by Bausells [126] which stacked levels of metal connected to the ISFET gate. The metal is left floating and simply acts as a gate connection closer to the sensing oxide surface. Multiple ISFETs were included on the chip with both PMOS and NMOS configurations. We designed the ISFETs to separate the drain and source metal contacts from the floating gate to minimize noise [131]. Many of the NMOS ISFETs were connected to readout circuitry on chip. We employ a design from Morgenshtein et. al [103], the indirect complementary ISFET/MOSFET

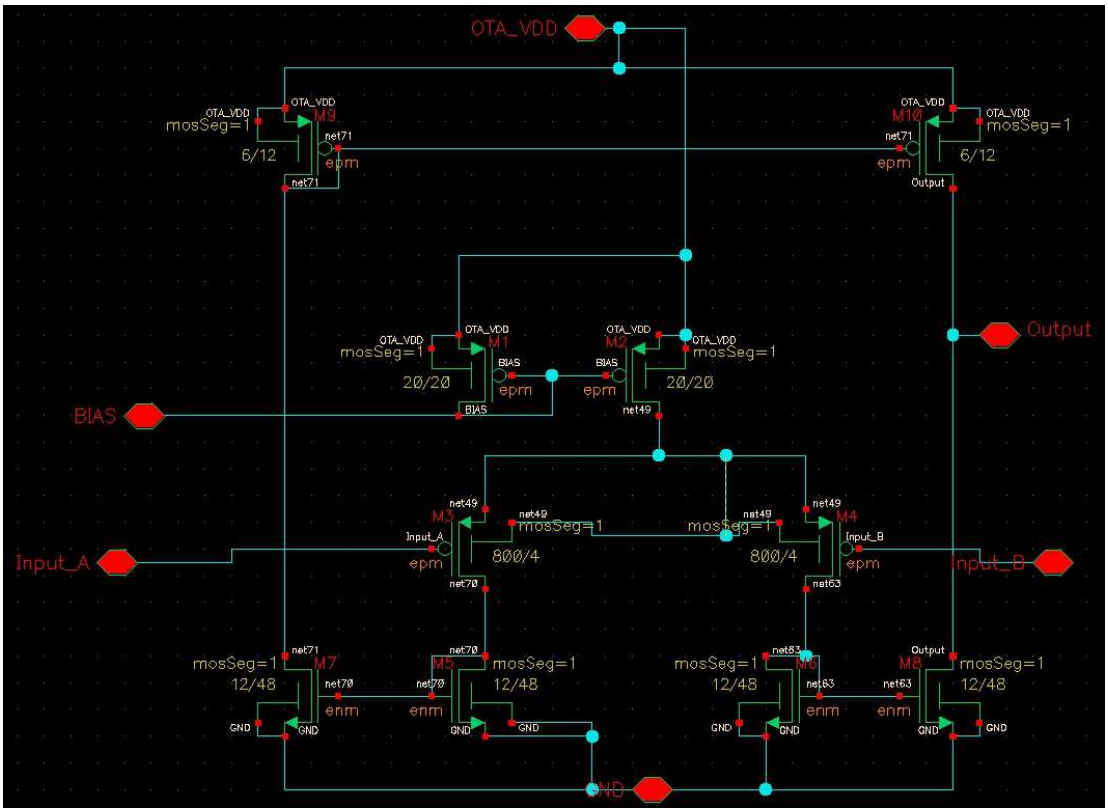

Figure 11.8: Schematic of OTA used in all capacitance sensing circuits.

pair configuration (Fig. 11.9). This design eliminates body effect that can shift the threshold voltage and the calculated pH value. The size of the ISFET was chosen to be approximately the same size as the work by Morgenshtein to allow for a performance comparison.

Capacitance Sensing

The chip included four designs for capacitance monitoring, each a combination of one of two sensing methods and one of two monitoring circuits. The first sensing method utilized the top metal of the CMOS process to create an IDES. This structure is designed to have a capacitance of 1pF. The top metal has a passivation layer over it, so it can be directly exposed to a biological environment without fowling due to aluminum. Any change to capacitance will be due to a change in fringe capacitance. Fringe ca-

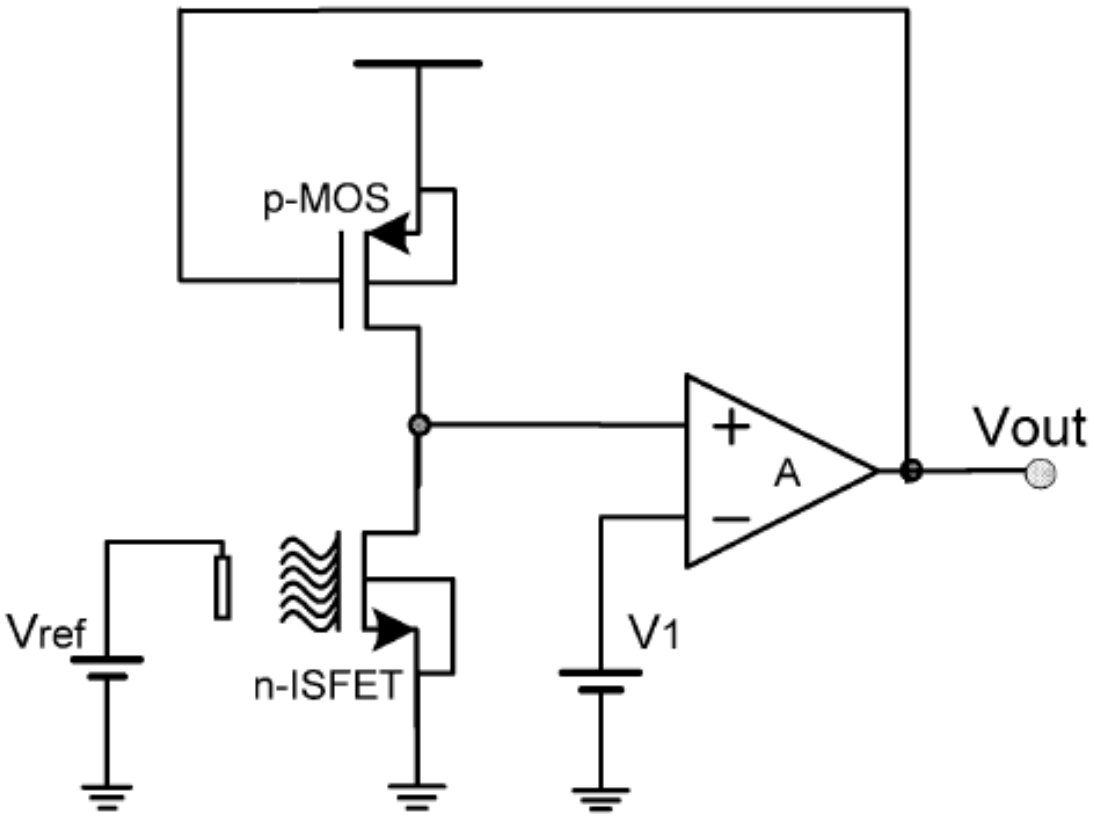

Figure 11.9: Indirect complementary ISFET/MOSFET schematic from [103].

pacitance is small compared to the total capacitance between two plates so only small variations were expected from this sensor. Therefore, this design relied heavily on a large amplification to get a detectable result.

The second capacitance sensor was also an IDES but required post-processing. The IDES was designed to be formed using patterned gold structures on top of the passivation layer, similar to the methods used by Zhang et al. [132]. The sensor could be produced using a lift-off method. An appropriate metal thickness would create a base capacitance of 1pF, similar to the other sensor design. Unlike the other design, this sensor allows cells to culture between the capacitor “plates” to create larger capacitance changes.

Two different circuit configurations were included on the chip. Both designs were based on an electrometer op amp charge amplifier circuit [133] [81]. Figure 11.10 shows the schematic of the circuit. Charge collects on the sensing capacitor and is amplified based on the value of the feedback capacitor. The resistive feedback provides a DC path to ground for the negative input terminal of the op amp. The transfer function of the circuit is $A = -\frac{C_{sense}}{C_{feedback}}$ when the frequency of excitation is much greater than the RC time constant [134]. We wanted large values of resistors so we could work at low frequencies using a lower power amplifier design. Our second circuit design uses a method of creating large resistors using MOS-bipolar pseudoresistors as demonstrated by Harrison and Charles [129]. Harrison showed resistance values greater than 1GΩ, a resistance that would be prohibitively large to make in a standard CMOS process.

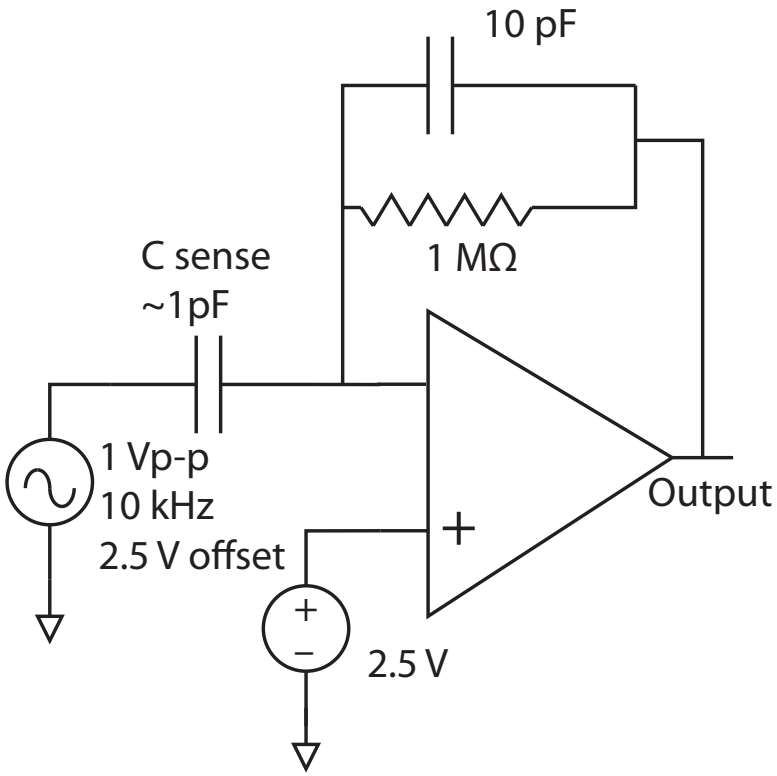

Figure 11.10: Basic electrometer circuit schematic.

Second Chip Results

A micrograph of the second fabricated chip is shown in Figure 11.11. Two chips were wire bonded for electrical characterization without fluid interaction.

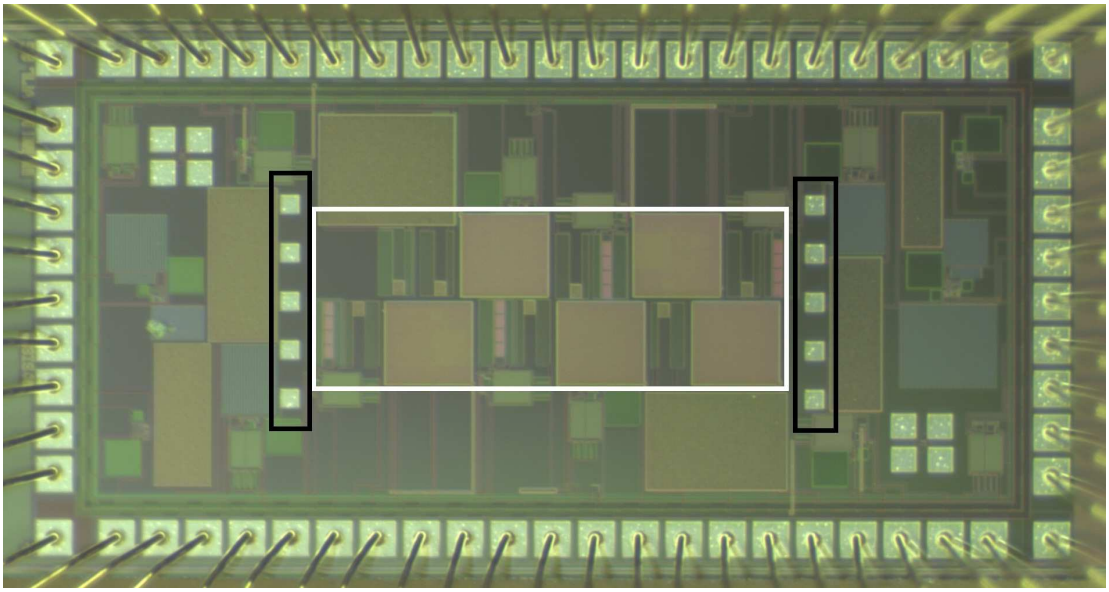

Figure 11.11: Micrograph of second fabricated chip modified to indicate the sensing region (white box) and the interior pad connections (black box). The chip is wire bonded for easy electrical analysis. The chip size is 3 mm $\times$ 1.5 mm.

Amplifier Testing Results

Testing of amplifier performance began by verifying the biasing conditions. An I_{DS} versus V_{DS} sweep was performed on the biasing PMOS, and we determined that a voltage of 2.35 V provides a 30 μA bias current. The amplifier was then configured with unity gain feedback to confirm the amplifier could act as a buffer. To see the input common-mode range, the input voltage was swept from 0 V to 5 V with $V_{DD} = 5$V and $V_{SS} = 0$V. The input common-mode range of the circuit was found to extend from 800 mV to 4.2 V. The open loop amplification was examined by setting the negative input to 2.5 V while a sine wave with a 2.5 V DC offset was applied to the positive

input. Because of the high gain of the circuit and limitations on the minimum output signal from the Keithley 3390 arbitrary waveform generator (Keithley Instruments Inc., Cleveland, OH), a voltage divider was used to attenuate the input signal. Using a TDS 2004B oscilloscope (Tektronix, Beaverton, OR), the peak to peak values were recorded and the gain of the amplifier was calculated to be 48 dB. While keeping the same open loop gain configuration, the input frequency was increased until finding the 3 dB point at 1.65 kHz. The CMRR was found by setting both amplifier inputs to a sinusoidal input centered at 2.5 V. The CMRR was calculated to be 72 dB.

The pH and capacitive sensing circuits could not be fully tested due to packaging problems. Progress on solving these issues is presented in Chapter 12.

Chapter 12

FLIP CHIP CMOS-MICROFLUIDIC PACKAGING

Small, complex integrated circuits are now commonplace with technology such as complementary metal-oxide-semiconductor (CMOS) processes. CMOS processes have been used to make sensors, actuators, and stimulators, as well as the circuits to amplify and process data, all in one device. Because CMOS is well-established commercially, there is the added advantage of reliable production methods and the economies of scale. CMOS integrated circuits are similar to microfluidics because both branches of research have followed a trend of miniaturization and integration [135]. Microfluidics matured into a major research field thanks in part to adapting many of the fabrication procedures used to make integrated circuits. Microfluidic devices allow controlled introduction of fluids, maintenance of a biocompatible environment, and sophisticated flow control for sample mixing, separation, and reactions. Successful integration of CMOS sensors with microfluidics would advance the testing and eventual commercialization of many lab-on-a-chip technologies.

Several challenges exist before all of the benefits of combining the technologies can be realized to create complete lab-on-a-chip systems [136]. One challenge is finding reliable and simple methods to seal microfluidics with integrated circuits. Another obstacle is making electrical connections to a printed circuit board and incorporating microfluidics onto the same board while isolating the fluids from the electronics. All packaging methods must be compatible with the integrated circuit process, *i.e.* no anodic bonding or very high temperatures. Another hindrance is a mismatch in device footprints. Microfluidic devices usually have dimensions in centimeters while CMOS die have dimensions in millimeters. Finally, creating reliable electrical connections in the presence of fluids also causes problems. Formulation of a methodology to solve all

of these issues concurrently is a significant problem in advancing lab-on-a-chip technology.

This chapter demonstrates a new technique for integrating CMOS technology with microfluidics. The system merges the capabilities of CMOS integrated circuits with the flexibility of soft lithography microfluidics to create a platform capable of numerous testing applications.

12.1 Background

An early method to combine CMOS chips with microfluidics involved depositing layers of polymer directly onto a chip and removing a sacrificial layer to create a channel [137]. Fluidic connection ports were etched through the bottom of the substrate to access the microfluidics constructed on the surface. The design also required extensive fabrication on the CMOS chip as well as machining of the package used to hold the chip. Work by Rasmussen *et al.* [138] involved designing the microfluidic system using layers within the CMOS chip. The channels were formed by bulk etching of the silicon substrate to eliminate the need for additional deposition. Other work has shown creation of multilayer fluidic structures on top of a CMOS substrate [139]. All of these methods produced simple channels for interface with the CMOS electronics but lacked valves or other methods of fluidic control.

More recent methods have focused on simplifying the hybrid system and addressing electrical connection issues [4]. A number of hybrid systems have been created that utilize wire bonding for electrical connections [140–143]. These systems limit chip area available for bond pads due to the path of the microfluidic channel. Additionally, the integrated microfluidics are incapable of performing flow control operations because they lack valves. Others have utilized flip chip bonding to make electrical connections with microfluidics fabricated from glass [144] [145] and injection molded plastic [146].

The presented work describes fabrication of a hybrid CMOS microfluidic system using flip chip electrical connections. The new method of creating flip chip electrical connections seals against liquids and provides mechanical support without using an underfill after bonding. Additionally, the system accommodates polydimethylsiloxane (PDMS) microfluidics made with common soft lithography methods. A method of bonding PDMS to flexible polyimide is also presented.

12.2 Experimental

System Design

A profile of our assembled system is shown in Figure 12.1. The central component of the system is a flexible printed circuit board (PCB) made of polyimide. All electrical connections are made on one side while fluids are confined to the other. The polyimide has low moisture absorption and high dielectric strength to provide adequate insulation between liquids and electronics. A small opening in the polyimide provides an area for fluids to interact directly with the CMOS surface. Electrical connections are made by first patterning the PCB copper to match the bond pad configuration of a CMOS die. A photo-patternable epoxy (SU-8) is then used to define open areas for electrical bonds. Solder paste is screen printed using the epoxy as a stencil, and then the CMOS die is flip chip bonded. Microfluidics are fabricated using established soft lithography methods with integrated valves and directly bonded to the polyimide using a combination of oxygen plasma and chemical bonding. The process flow for the electrical connections is shown in Figure 12.2, and the fluidic connection scheme is shown in Figure 12.11.

Flexible Printed Circuit Board

The flexible printed circuit board we used was Pyralux AC182500R obtained from Dupont (Wilmington, Delaware). Pyralux consists of 25.4 μm polyimide covered with 0.5 oz/ft^2 copper (18 μm thick) and comes as a large sheet that can be cut into custom shapes. A sample of the pyralux is shown in Figure 12.3. Pyralux is commonly used to

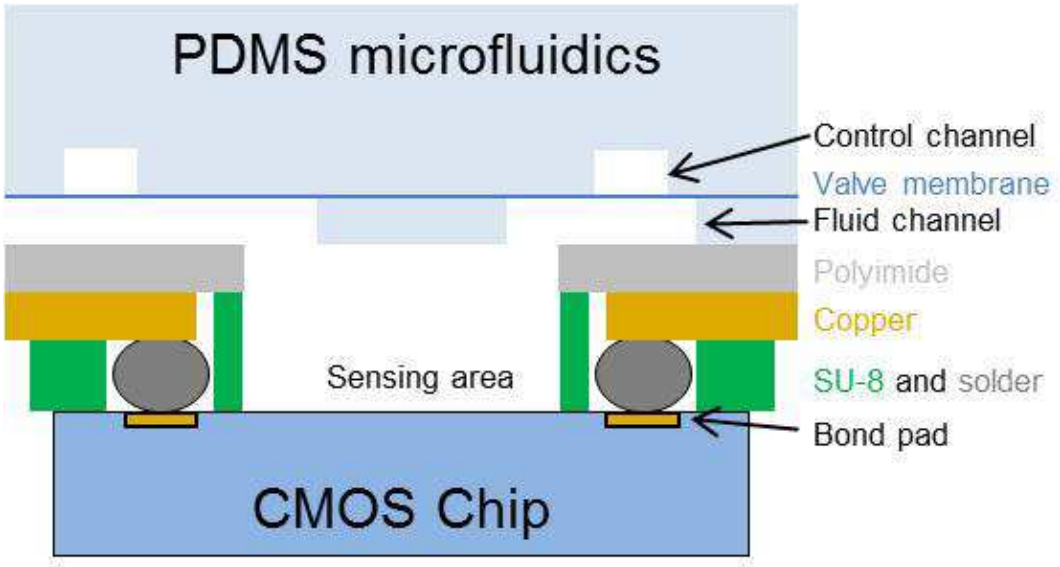

Figure 12.1: Schematic of hyrbid CMOS and microfluidic system. Flexible polyimide separates electrical connections from fluids. The chip is sealed from fluids by SU-8 resist. Not to scale.

make flexible circuits for automotive, computing, consumer electronics, aerospace, and even medical applications since it is biocompatible. Dupont provided the materials free of charge. Dupont also provided a coverlay material. The coverlay is used to protect and insulate the copper electrical connections after fabrication but was not used with this system. The Pyralux was cut to the desired size and attached to a glass slide using tape for easier handling during processing.

PCB Layout

The PCB layout was designed using L-Edit. The only electrical use of the PCB was to provide a connection between the flip chip bonding area and test equipment. No other components were included on the PCB. The layout of the mask for patterning is shown in Figure 12.4. The wires are spaced to fit into an eight pin flexible flat cable socket with $2.54\,mm$ spacing, part number $538-15-25-4081$ from Mouser (Mansfield, TX).

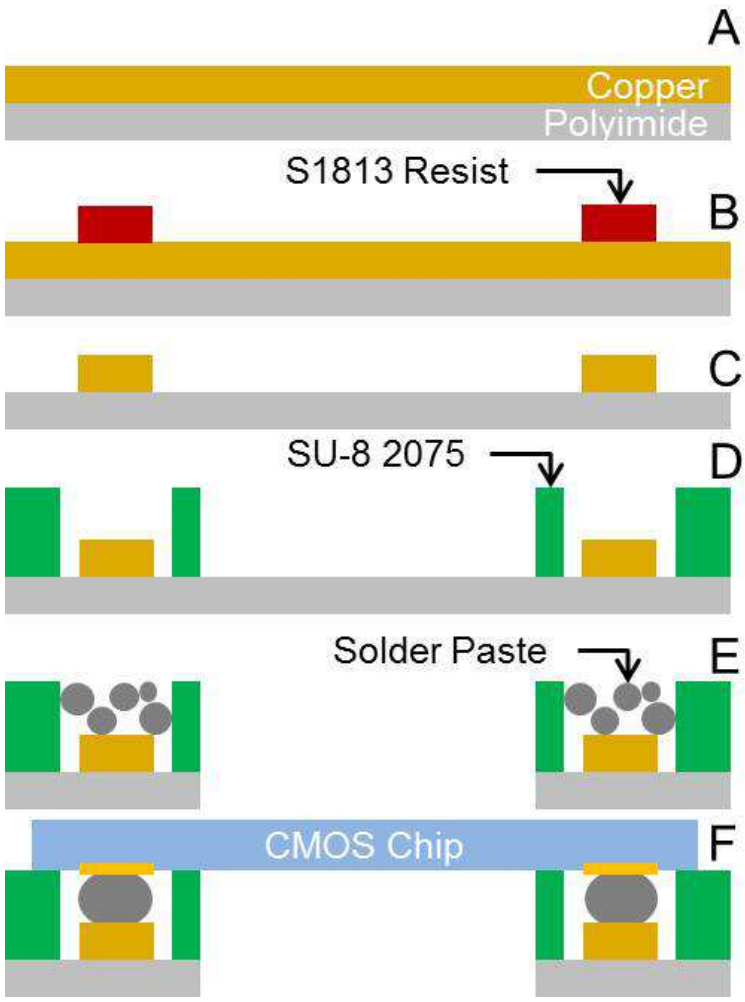

Figure 12.2: Electrical connections to a CMOS chip are made on a flexible PCB (A) by patterning S1813 positive resist (B), etching copper to leave traces and bonding sites on the board (C), and then patterning SU-8 (D). Cavities above copper bonding areas are filled with a solder paste and an opening is cut in the polyimide to allow access to the sensing region of the chip (E). Finally, a CMOS chip is flip chip bonded while in contact with the SU-8 layer to simultaneously create electrical connections and insulate them from fluids (F).

Figure 12.3: Photograph of Pyralux shown folded over to expose the copper side. Coverlay material is shown rolled next to the Pyralux and can also be cut to size.

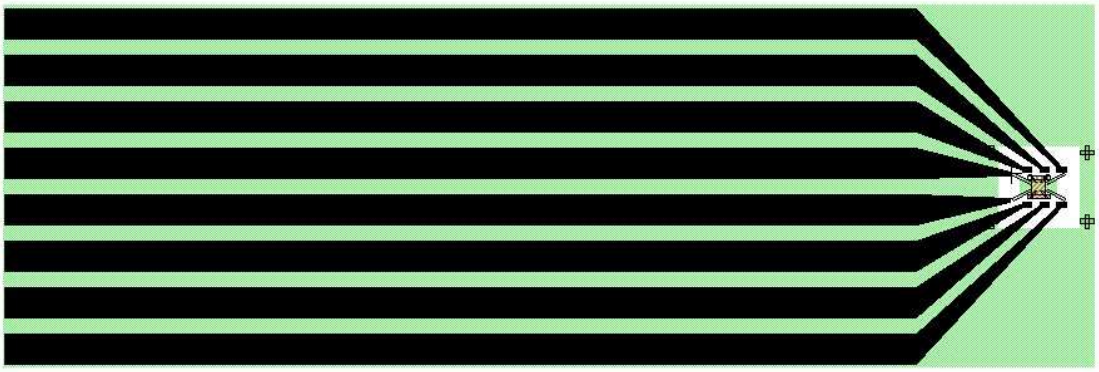

Figure 12.4: The layout of the PCB mask is indicated by the black layer. The connections are designed to connect between a CMOS sized chip and a flat flexible connection socket. The mask color is inverted when used but is shown here with the opposite polarity to better indicate the position of the CMOS chip. The green mask layer represents SU-8 patterning. The total area of the layout shown is about 3 inches $\times$ 1 inch.

PCB Fabrication

The PCB fabrication protocol was as follows:

1. The Pyralux was cut into a two inch by three inch rectangle and attached to a glass slide of the same size using scotch tape, copper side up.

2. Shipley Microposit S1813 (Rohm Haas, Marlborough, MA) positive photoresist was spun to a thickness of 1 μm on the Pyralux. The spin recipe was 500 RPM for 10 seconds followed by 3000 RPM for 30 seconds.

3. The resist was baked at $115\,^{\circ}C$ for 15 minutes. This is increased from the one minute suggested bake time on the datasheet to account for the slower heat transfer through the insulating glass.

4. The resist was exposed for eight seconds with an exposure power of approximately $25 mJ/s$.

5. Development was performed using 351 Developer (Microchem) mixed in a $5:1$ ratio (water:developer). The pattern would fully develop in approximately 45 seconds. The device was then ready for copper etching.

6. Copper was etched in ferric chloride (MG Chemicals, Surrey, BC, Canada) while brushed with a foam brush to aid in even etching rates across the PCB. The etching rate was fairly fast, so it was easy to over etch and remove small features if care was not taken. To avoid loss of small features, the brushing was performed over areas with large copper features until they were fully developed. Areas with small features were etched last. The samples were rinsed with water immediately upon completion of etching the small features to stop etching.

7. The resist etch mask was removed by rinsing the PCB with acetone, therefore exposing the copper.

SU-8 Patterning

SU-8 was patterned to expose areas of the copper for electrical connections to a silicon chip. The fabrication protocol was as follows:

1. SU-8 2075 (Microchem, Newton, MA) negative photo resist was spun to 60 μm thick on top of the flexible patterned PCB (still attached to a glass slide). The spin recipe was 500 RPM for 10 seconds followed by 4000 RPM for 30 seconds.

2. The SU-8 was soft baked at $65^{\circ}C$ for five minutes and then $95^{\circ}C$ for 15 minutes.

3. The SU-8 was exposed for 40 seconds with an exposure power of approximately $25 mJ/s$. The mask, shown as the green layer in Figure 12.4, is designed to only leave SU-8 in a small area around the electrical connection sites.

4. A post exposure bake is performed at $65^{\circ}C$ for five minutes and then $95^{\circ}C$ for 15 minutes.

5. The SU-8 was developed for approximately four minutes using SU-8 Developer (Microchem).

The completed PCB with patterned SU-8 is shown in Figure 12.5. The copper traces on the PCB are 18 μm tall, therefore this protocol gives about 42 μm of SU-8 above the copper areas. SU-8 was removed away from the die attachment area to maintain flexibility and allow for electrical connections to test equipment. Excess SU-8 across the PCB decreases flexibility and can cause deformation. An area where chip sensors can be accessed was also left open to allow for easier removal of the polyimide layer to expose the sensing region of the chip.

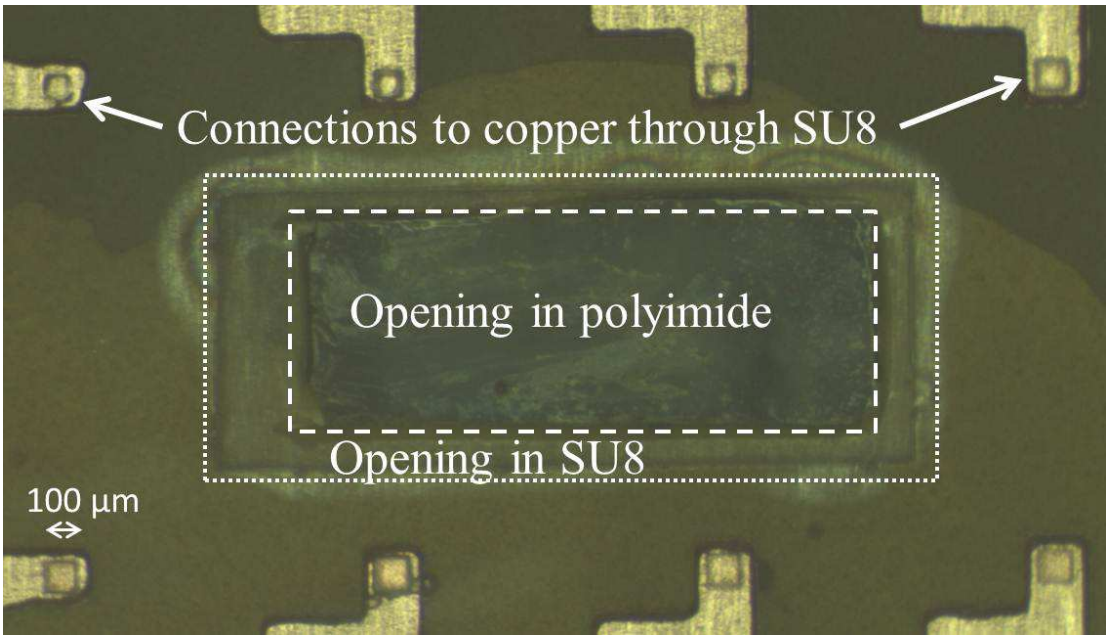

Figure 12.5: Micrograph of patterned copper on flexible PCB with a SU-8 patterned on top. Holes in the SU-8 layer expose the copper pads for electrical connections. An area of SU-8 in the middle of the bonding area was removed to allow polyimide to be cut out for access to the die sensing area after flip-chip attachment.

Test CMOS Style Die Fabrication

To simulate a CMOS die we have created test structures with metal connections identical in size to those seen in CMOS processes. Commerical CMOS bond pads are typically aluminum but nickel-gold under bump metallization (UBM) is common to prevent oxidation before flip chip bonding [147]. To simplify fabrication, our metal connections exclude the aluminum and subsequent UBM process and instead consist of evaporated gold. This process also works with aluminum bond pads but results are not shown. Metal connections were made on a silicon wafer using a lift off process. The fabrication protocol for the test CMOS die was as follows:

1. First, a 100 nm layer of silicon dioxide was thermally grown on a silicon wafer. This was to insulate any electrical connection through the silicon wafer.

2. Shipley Microposit S1813 (Rohm Haas, Marlborough, MA) positive photoresist was spun to a thickness of 1 μm. The spin recipe was 500 RPM for 10 seconds followed by 3000 RPM for 30 seconds.

3. The resist was baked at $115\,^{\circ}C$ for 1 minute.

4. The resist was exposed for eight seconds with an aligner exposure power of approximately $25\,mJ/s$.

5. Development was performed using 351 Developer (Microchem) mixed in a $5:1$ ratio (water:developer). The pattern fully developed in approximately 45 seconds. The device was cleaned with water after development.

6. Metal evaporation was performed in a Cressington 308R evaporator (Ted Pella Inc., Redding, CA) with a LT300 dual output power supply. Approximately $30\,nm$ of a chrome was evaporated to form an adhesion layer. A chrome rod served as the source for the metal (CRW-1, RD Mathis, Long Beach, CA). Immediately following the chrome deposition, approximately $70\,nm$ of gold (99.999% pure) was evaporated using a ME5-.005W source (RD Mathis).

7. Coated samples were placed in an acetone bath with sonication to remove the patterned resist and therefore selectively lift off the metal.

8. Samples were rinsed with isopropyl alcohol and water before dicing into pieces that are approximately 1.5 mm $\times$ 3 mm, a common size of CMOS die.

A micrograph of the completed test die is shown in Figure 12.6.

Flip Chip Bonding

Flip chip bonding was performed on a Finetech Picoplacer multi-purpose die bonder, shown in Figure 12.7 (Finetech GmbH & Co. KG, Berlin, Germany). Bonding simul-

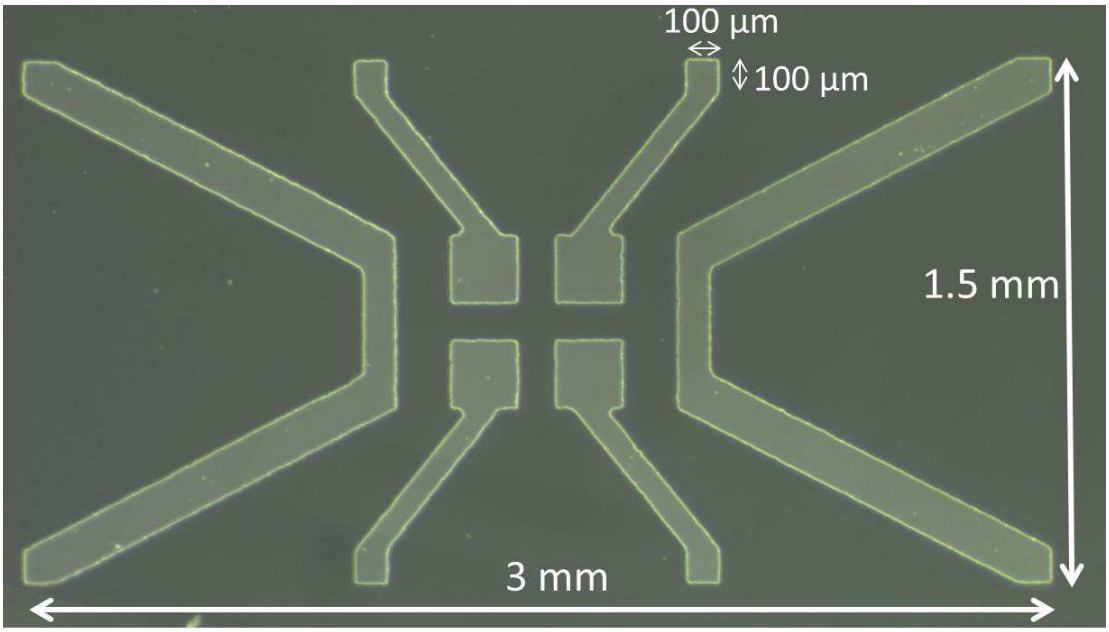

Figure 12.6: Micrograph of patterned metal connections for electrical testing. The connections simulate the size of a typical CMOS die, 1.5 mm $\times$ 3 mm, and bond pad sizes, 100 μm $\times$ 100 μm.

taneously created the electrical connections and sealed the test die against the SU-8. The procedure for the bonding was as follows:

1. After completion of SU-8 patterning on the PCB, the polyimide was manually cut from the center of the pad region using an X-Acto. The rectangular opening in the SU-8 allowed easy removal of the polyimide in this area. The PCB is still attached to the glass slide.

2. ChipQuik No Clean Solder Paste (Chip Quik Inc., Mashpee, MA) was applied to the patterned SU-8 and wiped repeatedly across the openings until filled. The wiping was performed with a plastic cell scraper (Fisher part 08-773-2) acting as a squeegee. The surface was also wiped with a kim-wipe to remove flux residue from the SU-8 surface that will bond with the chip. The solder paste has a lim-

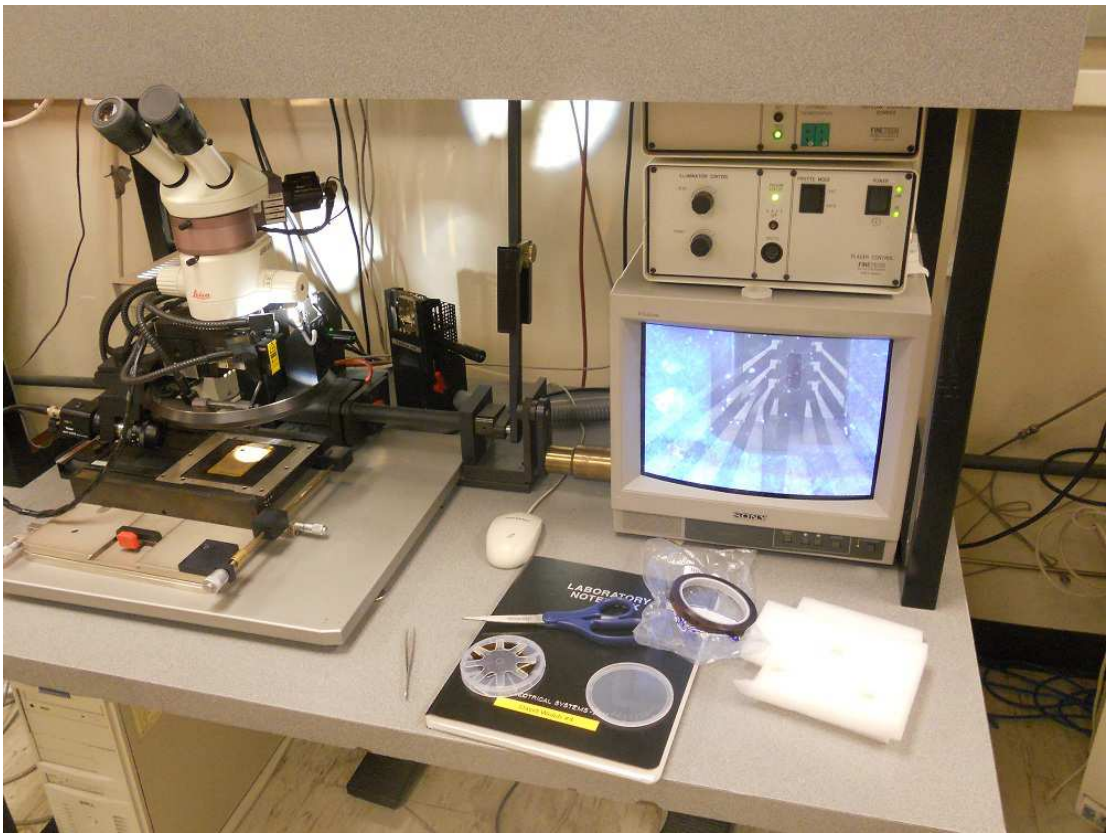

Figure 12.7: Photograph of the Finetech Picoplacer used for flip chip assembly. Assembly is done on the heated stage under the microscope, shown on the left side of the picture. A monitor, on the right, is attached to the microscope to aid in alignment. The chip and stage can be heated independently using computer control.

ited time before it dries out, so the next steps were performed immediately after application.

3. The flexible PCB was then removed from the glass slide, turned over, and the polyimide side was washed using a water dampened kim-wipe. This step cleans any residue from liquids (such as SU-8 developer) used during processing. If this is not performed the residue will become sticky from heating during the flip chip bonding process, making quality PDMS bonding impossible.

4. The flexible PCB was attached to the heating plate of the die bonder using high temperature polyimide tape (105AC120, Techni-Tool, Worcester, PA).

5. A test chip was picked up using the die bonder tool and aligned to the bonding area on the flexible PCB. The chip was then brought into contact with the PCB. A force of 50 Newtons was applied during chip bonding to aid in attachment.

6. The chip and flexible PCB were heated to maximum temperatures of $300\,^{\circ}C$ and $200\,^{\circ}C$ respectively over 90 seconds. The bonding system cooled for two minutes before removing the 50 Newton force and detaching the assembled structure.

Chip heating was adequate to liquify the solder paste. Surface tension forces in the liquid solder caused it to gather and increase in height to allow contact with the die bond pads. The change in height can be seen on solder balls that were liquified but not bonded to a CMOS chip in Figure 12.8. A seal between the die and the SU-8 was formed by exceeding the glass transition temperature ($210\,^{\circ}C$) of SU-8 while applying adequate pressure [148].

PDMS Molding and Attachment

Microfluidic Fabrication

Multilayer microfluidic structures were made using standard soft lithography techniques. The procedure for producing them was as follows:

1. SU-8 2007 (Microchem, Newton, MA) negative photo resist was spun to 10 μm thick on top of a silicon wafer. The spin recipe was 500 RPM for 10 seconds followed by 2000 RPM for 30 seconds.

2. The resist was soft baked for three minutes at $95\,^{\circ}C$.

3. The resist was exposed for 20 using the mask aligner with an exposure power of approximately $25\,mJ/s$.

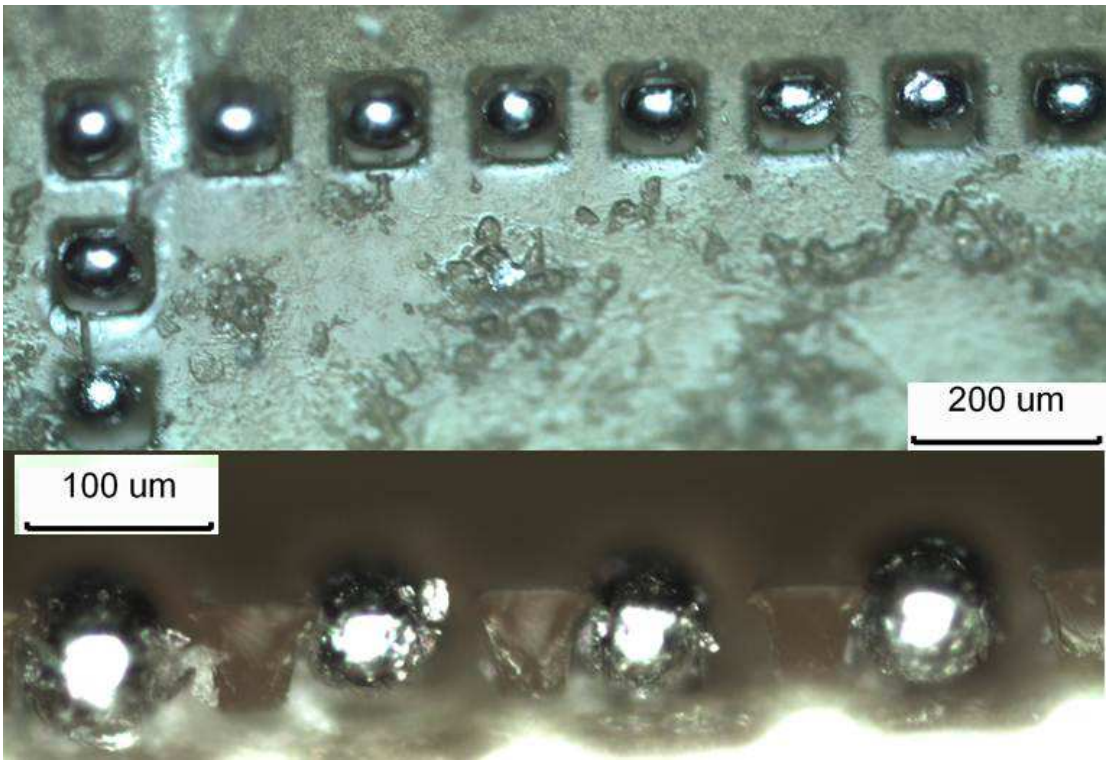

Figure 12.8: Micrographs of solder connections separated by SU-8 resist. A CMOS die would normally be aligned on top of these connections while the solder was still a paste. Surface tension formed the solder into a spherical shape when it was liquified. The spherical shape has an increased height to allow contact with a CMOS die bond pad.

4. The resist was given a post exposure bake for four minutes at $95\,^{\circ}C$.

5. The resist was developed for approximately two minutes in SU-8 developer.

6. The resist was hard baked at $250\,^{\circ}C$ for five minutes.

7. PDMS was mixed in a $10:1$ ratio (part A:part B) and degassed in a vacuum chamber until no bubbles were present.

8. The fluidic layer was made by spinning PDMS onto an SU-8 mold using a spin speed of 500 RPM for 10 seconds followed by 3500 RPM for 30 seconds.

9. The valve layer was made by pouring PDMS over an SU-8 mold to the depth of about one centimeter.

10. The PDMS and molds (both for the fluidic and valve layers) were put into an oven at $70\,^{\circ}C$ for at least two hours for curing.

11. PDMS was peeled away from the valve SU-8 mold to release the microfluidics.

12. Both the released valve PDMS structure and the fluidic structure (still attached to the mold) were plasma cleaned (Harrick Plasma, Ithaca, NY) using oxygen as the process gas and high RF power for 60 seconds.

13. Immediately upon completion of the plasma cleaning the valve layer was aligned with the fluidic layer and brought into contact. The layers attached immediately and were put into an oven at $70\,^{\circ}C$ for 10 minutes to ensure good bond strength.

14. The multilayer PDMS structure was peeled away from the fluidic mold. At this point the device was cut down to size using a razor blade.

15. Finally, a 20 gauge straight blunt needle (NE-251PL-C, Amazon Supply, Seattle, WA) was used to punch holes through the PDMS structure. This was to allow access to the valve and fluidic layers after the PDMS structure is bonded to a final surface.

PDMS to Polyimide Bonding

The attachment of PDMS to the flexible polyimide backbone of the Pyralux proved extremely difficult. The original plan was to bond the PDMS microfluidics to the polyimide side of the flexible PCB using the room temperature bonding method from Tang and Lee [149] shown in Figure 12.9. First, both the polyimide flexible PCB and the PDMS structure were plasma cleaned (Harrick Plasma, Ithaca, NY) using oxygen as the process gas and high RF power for 60 seconds. Immediately upon removal from the

plasma clean the PDMS was placed in a 1% solution of 3-Aminopropyltriethoxysilane (APTES, 99%)(Sigma-Aldrich, St. Louis, MO) and the flexible PCB was placed in a 1% solution of 3-Glycidoxypropyltriethoxysilane (GPTES, 99%)(Gelest, Morrisville, PA), both at room temperature. After 20 minutes the pieces were removed, rinsed with water, dried with nitrogen, and then aligned and brought into conformal contact. The device was allowed to set for at least 1 hour at room temperature to form a strong amine-epoxy bond.

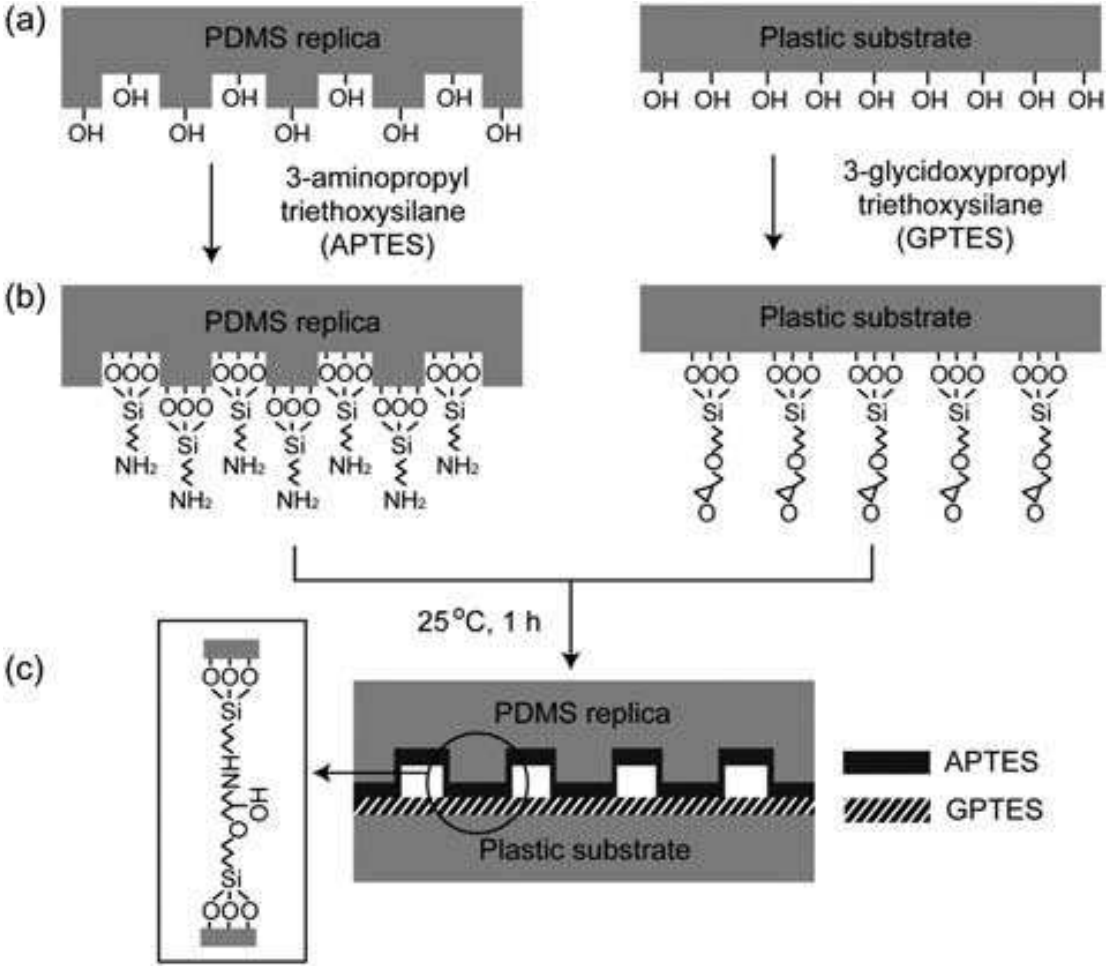

Figure 12.9: Bonding strategy from [149]. (a) Surface hydroxylation of PDMS and plastic substrates by O_2 plasma treatment for one minute. (b) Aminosilane and epoxysilane anchoring on the O_2 plasma-treated PDMS and plastic substrates, respectively. (c) Conformal contact of the two substrates at room temperature for one hour.

This process achieved favorable results when performed by Tang and Lee, but testing with our flip chip PCB yielded poor performance. The devices did not seal evenly so leakage occurred. An example of the poor sealing is shown in Figure 12.10. The bonding problem appeared to arise from the fact that the PDMS did not immediately bond with the polyimide. The procedure by Tang and Lee required the two pieces to sit in constant contact for at least an hour. This could not be achieved with our devices because we had already bonded the CMOS test chip to the other side of the polyimide. The chip was significantly smaller than the PDMS, so the PDMS could not sit evenly on the polyimide. Thus, a bond could not form.

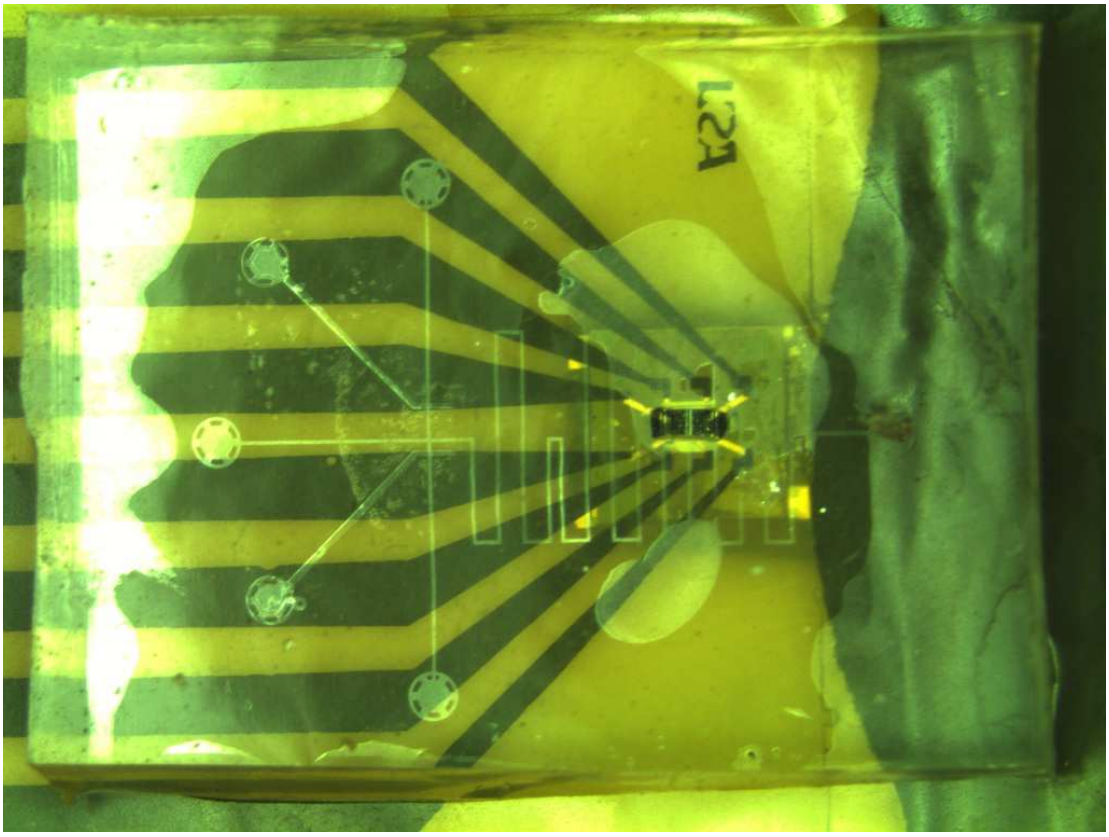

Figure 12.10: A micrograph of the poor bonding achieved with the APTES-GPTES bonding strategy. The port area on the right side is not sealed so the device is inoperable. The PDSM is approximately 16 mm $\times$ 17 mm.

A number of bonding methods were investigated as possible solutions to the PDMS to flexible polyimide bonding problem. The six attempted bonding strategies are summarized in Table 12.1. Materials used in these attempts included PDMS primer adhesive (SS4120, RS Hughes, Sunnyvale, CA), 5% APTES at $80^{\circ}C$, 5% GPTES at $80^{\circ}C$, and uncured PDMS. The standard plasma treatment was for 1 minute at high power using oxygen as the process gas. All strategies allowed the materials to sit in an oven for 30 minutes at $60^{\circ}C$ after they were brought into contact.

Table 12.1: Summary of attempted PDMS to flexible PCB bonding methods.

Strategy	**Flexible Polyimide Preparation**	**PDMS Microfluidics Preparation**
A	Spun on adhesion primer at 1000 RPM, allowed to dry for 20 minutes, then spun a layer of PDMS at 3500 RPM	Not modified
B	Brushed on adhesion primer (thicker than spinning), dry for 20 minutes	Stamped into a layer of uncured PDMS spun at 3500 RPM
C	Plasma treatment, submerged in APTES for 5 minutes, spun a layer of PDMS at 3500 RPM	Plasma treatment, stamped into a layer of uncured PDMS spun at 3500 RPM
D	Plasma treatment, submerged in APTES for 5 minutes	Plasma treatment
E	Plasma treatment, submerged in GPTES for 5 minutes, spun a layer of PDMS at 3500 RPM	Plasma treatment, stamped into a layer of uncured PDMS spun at 3500 RPM
F	Plasma treatment, submerged in GPTES for 5 minutes	Plasma treatment

The devices were tested for quality by attaching a pressurized air supply and increasing the pressure until leakage was heard. Strategies C, E, and F failed to hold even a base pressure of 50 kPa. Strategy B held up to 100 kPa, and strategy A held up to 125 kPa. Strategy D performed the best, holding up to 400 kPa before leaking. The leakage for strategy D was around the air supply connection, not between PDMS and the polyimide. Therefore the bond can likely hold much more than 400 kPa of pres-

sure. The pressure test also revealed a downfall of using stamped PDMS for adhesion promotion such as with strategies B, C, and E; some of the uncured PDMS entered the channels during stamping and cured, completely blocking flow.

The quality of each bond was also tested by a peel test. This was performed by simply holding onto the PDMS and attempting to peel it off of the polyimide. The only devices that did not come off as an entire piece were bonded with strategy D. These devices appeared to form a permanent bond with the polyimide because the PDMS structure broke before the bond with the polyimide.

Bonding strategy D has previously been demonstrated to work with bonding PDMS to other materials [150] [151]. However, this strategy had not been applied to flexible polyimide bonding. A more detailed procedure for this bonding strategy is shown in Figure 12.11. Polyimide substrates were first plasma cleaned using oxygen as the process gas and high RF power for 60 seconds. Immediately upon removal from the plasma clean, the polyimide PCB was placed in a 5% solution of APTES at $80^{\circ}C$ for 20 minutes. The 20 minutes is a change from strategy D above, allowing more time for APTES adhesion to the surface. The polyimide PCB pieces were then removed and dried with nitrogen while PDMS pieces were plasma cleaned for 60 seconds concurrently. Immediately upon completion of the plasma cleaning, the PDMS pieces were brought into contact with the surface modified polyimide PCB. The assembly was placed in an oven at $60^{\circ}C$ for 30 minutes to allow formation of a strong bond.

Bonding Strength Test

Additional experiments were performed to examine the APTES bonding strategy when used with the complete flip chip assembly. Again, a burst test was used since it is the common method for testing microfluidic devices. This is different from the previous burst test because the microfluidic devices were filled with water dyed with food col-

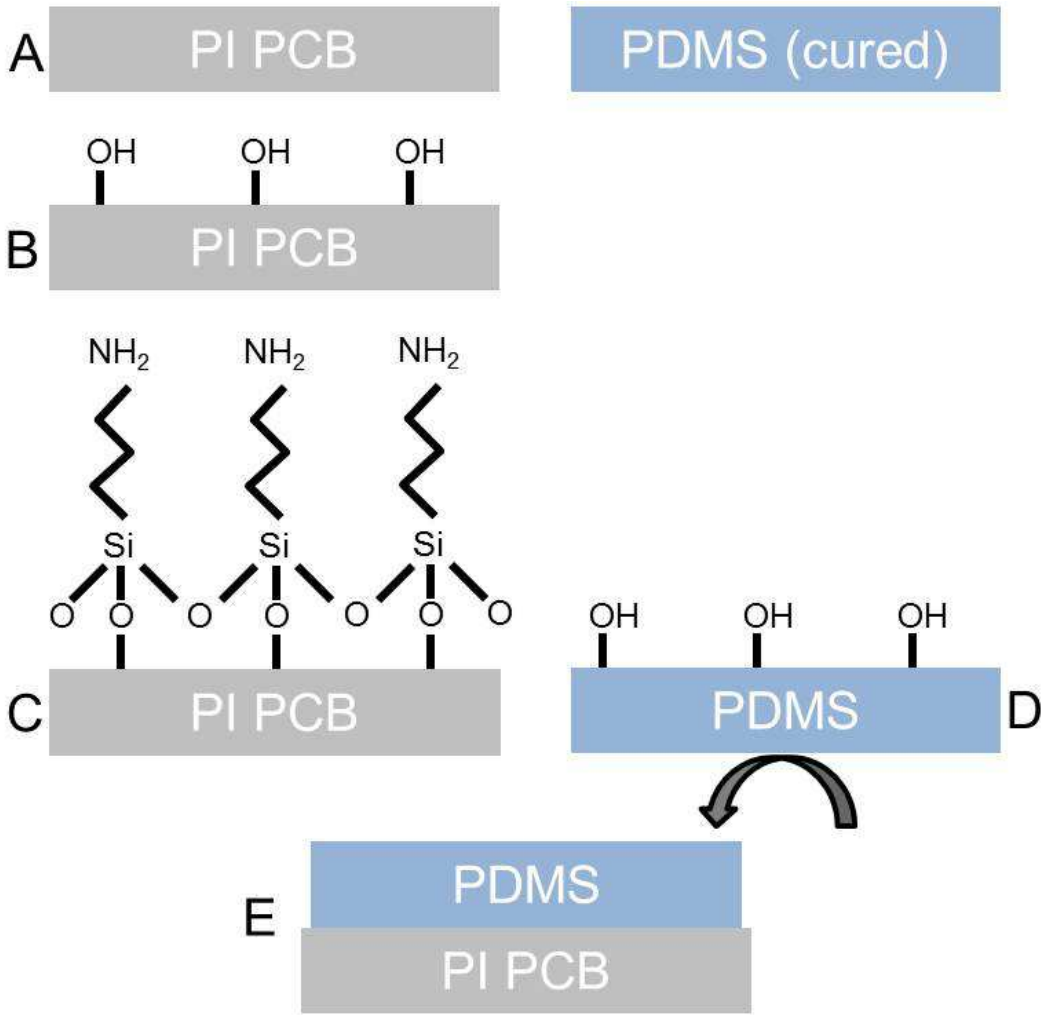

Figure 12.11: PDMS to polyimide bonding strategy. Starting with clean substrates (a), the polyimide is first hydroxylized by O_2 plasma treatment for 1 min (b). The polyimide is then placed in 5% APTES at $80\,^{\circ}C$ for 20 minutes (c) while the PDMS is hydroxylized by O_2 plasma treatment for 1 min (d). Substrates are brought into contact and bond instantly (e).

oring and placed on an absorbent towel for easy observation of leakage of fluid at the point of chip attachment. Fluidic connections to the microfluidic device were made with 20 gauge blunt needles and 0.030 inch inner diameter Tygon micro bore PVC tubing (Amazon Supply, Seattle, WA). Pressure was applied and controlled through a regulated air supply. The initial pressure of 50 kPa was applied and the system was

checked for leaks. The pressure was increased incrementally and continuously checked until leakage was observed.

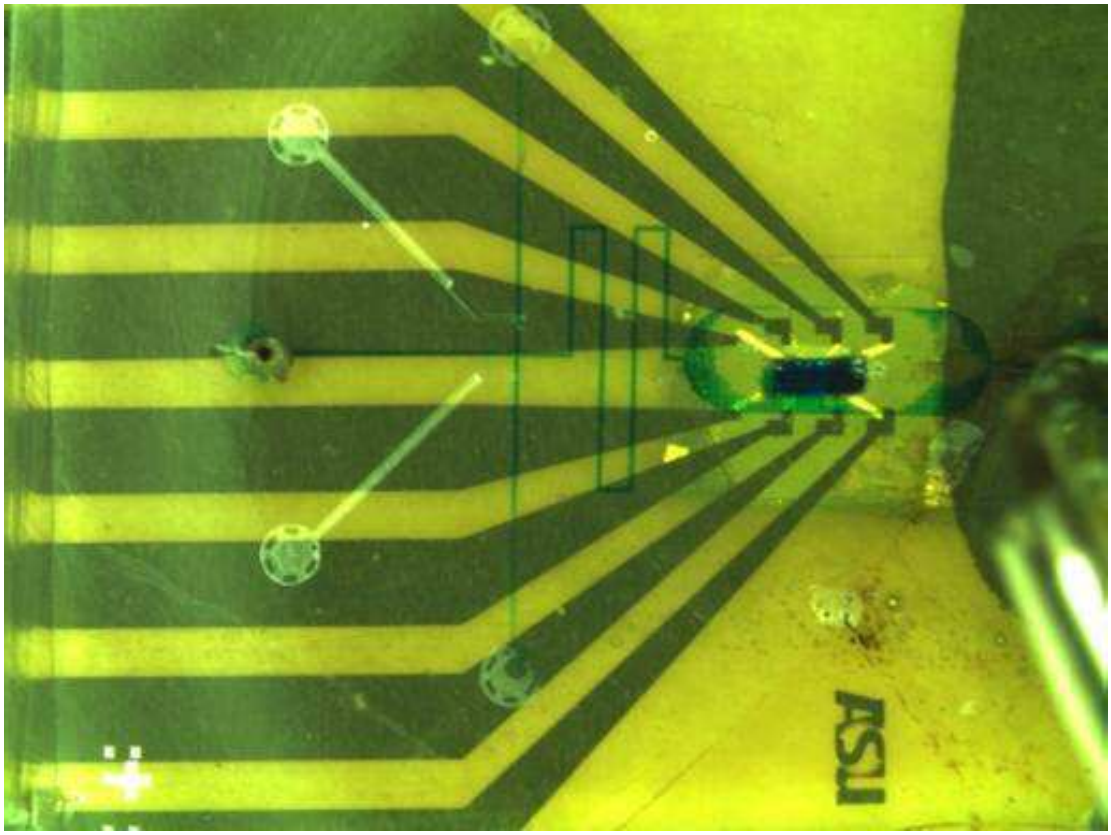

Figure 12.12: Fully assembled device filled with dye before leakage test. Air pressure was incrementally increased until a leak was observed to determine the overall bonding strength.

Electrical Connection Testing

Connections made via flip chip bonding were tested for both their conductivity and insulation from other connections. The deposited gold connections on the chip were tested for their resistance before bonding on a probe station (Semiprobe, Winooski, VT) using a Keithley 2636A source measurement unit (Keithley Instruments, Inc., Cleveland, OH). Insulation of the connections from one another was also verified with the same setup. Electrical connection quality after flip chip bonding was measured through the copper PCB connections. The electrical path we analyzed, shown in Figure 12.13,

includes resistance from the PCB (R_{copper}), the two solder connections (R_{bond}), and the on chip gold connections (R_{chip}).

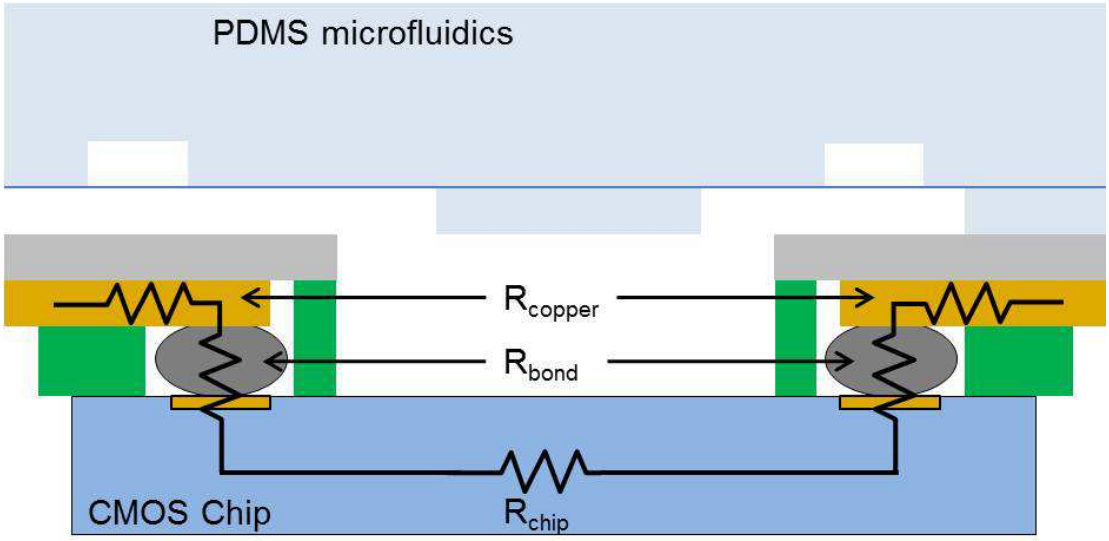

Figure 12.13: Complete electrical resistance path consisting of five resistances in series. Resistance was measured from one copper PCB connection to another to get the total resistance.

12.3 Results

We successfully packaged a CMOS-sized chip with a PDMS microfluidic device, as shown in Figure 12.14. This work demonstrates a number of advances in the fabrication of hybrid CMOS and microfluidic systems. Producing flip chip electrical connections with patterned SU-8 as a permanent stencil allows the use of solder paste, a common and inexpensive laboratory material, in place of expensive solder ball formation and placement technology. Leaving the SU-8 throughout solder placement and bonding helps ensure that the electrical connections are properly insulated from each other. Because the SU-8 both bonds and seals the chip to the polyimide, additional fabrication steps are eliminated. Additional underfill is not needed to provide mechanical stability between the flexible PCB and the chip. Furthermore, the SU-8 application by spin coating creates a flat surface for bonding chips which reduces the possibility of leak-

age. The planar bonding surface also creates equal height solder connections across the entire area of the chip.

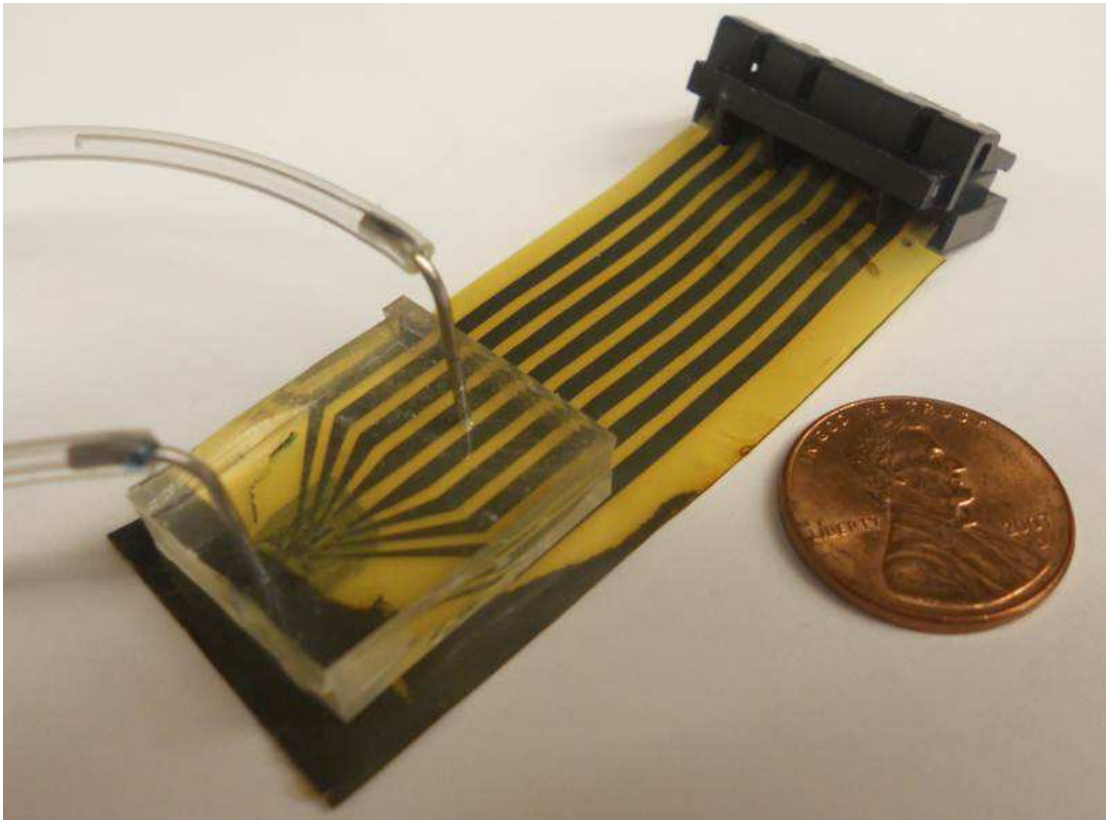

Figure 12.14: A completely assembled device is shown plugged into a socket for easy electrical connections. Microfluidic channels can be easily accessed while being insulated from all electrical connections.

Electrical connections between the flexible PCB and the test chip were characterized for the new bonding strategy. The resistance of the solder bond was evaluated by subtracting the values of the serial resistive components. Measurements are summarized in Table 12.2. We calculated R_{bond} to be $-8.2 \pm 7.9\ \Omega$ for each soldered connection. Additionally, isolated electrical connections remained as open circuit connections after the bonding process. No leakage current was measured between adjacent electrical bonds.

The value for R_{bond} is essentially a short circuit connection. The negative resistance is likely caused by the solder connection effectively shortening the total length of the on-chip electrical connection. The bond pad areas are collectively almost 10% of the total length of the on-chip connections; reducing the effective length of the connection by 10% causes a drop in the total resistance by about $7\,\Omega$. This drop in resistance is very close to our measured result and explains the negative resistance value. The high variation is likely due to alignment problems during flip chip bonding. The high reflectivity of the test CMOS die made optical alignment difficult with our system. Improved optics would significantly improve device yield.

Table 12.2: Measured resistance values for each component of the measurement path. R_{bond} is calculated from the measured values.

Parameter	**Resistance(Ω)**
R_{chip}	74.2 ± 3.8
R_{copper}	0.76 ± 0.05
Total series resistance	58.5 ± 16.3
R_{bond}	-8.2 ± 7.9

A complete device assembly was evaluated for leakage with emphasis on two key bonding areas. The first area was the ability of the PDMS to bond directly to the polyimide substrate. PDMS bonded directly to an area of unmodified polyimide substrate held to a pressure of 400 kPa. The failure point of the device was at the connection of the Tygon tubing to the PDMS, suggesting that the ultimate strength of the polyimide to PDMS bond would be higher with a better connection. We next tested the strength of the entire assembly which included the chip bonded with electrical connections. The device was able to hold without leaks up to a pressure of 175 kPa. The failure point of the complete assembly was between the chip and the SU-8. Both the bonding between the PDMS and the polyimide, and between the chip and the SU8, are adequate to work with normal microfluidic applications which only reach pressures

up to 50 kPa. To our knowledge this is the first reported bonding of polyimide to PDMS using only APTES as a bonding intermediate. Other work involving polyimide to PDMS bonding [149] required additional activation of the PDMS surface. This is also the first reported use of a flip chip bonding assembly with a flexible PCB and PDMS microfluidic device. This bonding method eliminated the need for a PDMS adhesion layer as used by Wu *et al.* [145]. By using SU-8 for solder placement and this method for PDMS adhesion, we have shortened the gap between the surface of the chip surface and the microfluidics from 120 μm [145] to 85 μm.

Solder Volume Analysis

An interesting topic of analysis for this integrated packaging system is the formation of the solder electrical connection. During reflow, the solder balls that make up the solder paste form a continuous volume. The solder height must be more than the height of the SU-8 well surrounding the PCB pad to make an electrical connection between the PCB and a CMOS chip. If the volume is large enough, solder will come into contact with the chip at the top of the well. An electrical connection is not made if upon reflow the solder height is not sufficient to contact the chip. This dependence on solder volume is illustrated in Figure 12.15.

It is obvious that we want to achieve the greatest height of solder possible to get the best connection. The best height is achieved by maximizing the solder volume. Solder volume is determined by the solder paste used to fill the wells before reflow. Solder paste is composed of flux and spheres of solder, known as solder powder. The size of solder powder in the paste used in this work is not stated by the manufacturer. The most common size for powder for solder paste is currently type 4 solder so we can assume this value. Type 4 powder indicates the solder powder spheres have an average diameter of 29 microns. The size of the powder is therefore significant compared to the total dimensions of the well.

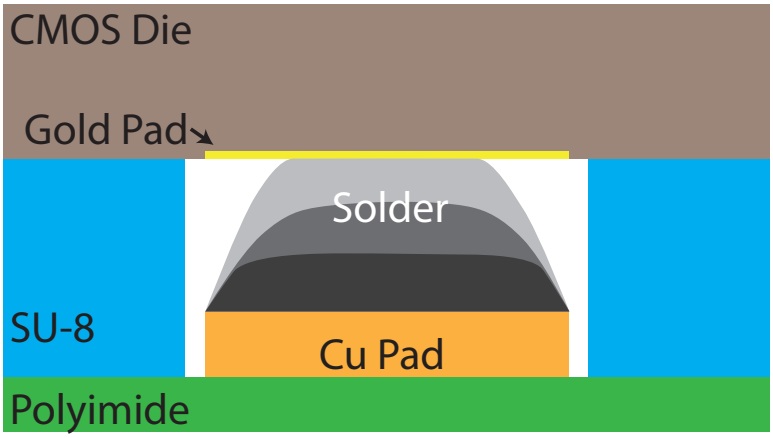

Figure 12.15: A profile view of the solder well showing the dependence on solder height to make an electrical connection. Different solder heights are illustrated with different shades of grey.

Knowing the dimensions of the spheres and wanting to maximize the total solder volume (and with it the height) therefore becomes a packing problem. The problem can be reduced to a two-dimensional problem for simplicity. The geometry is shown in Figure 12.16.

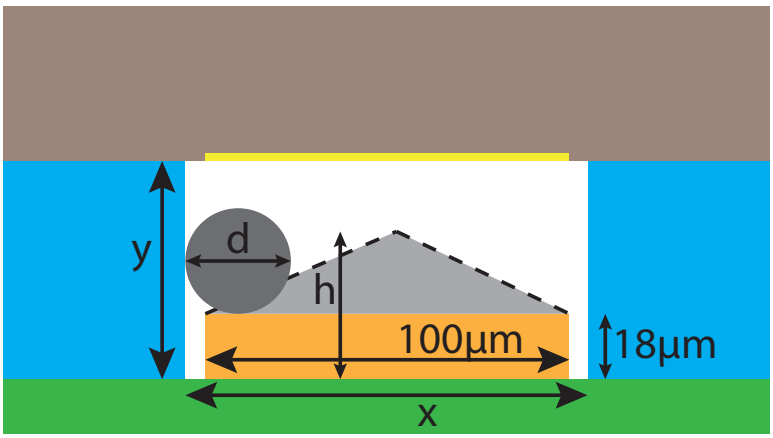

Figure 12.16: A profile view of the solder well dimensions used to calculate solder height.

The first step is to find the total volume of solder that can fit into a given well size. With the simplified two-dimensional problem, this means finding the number

of circles with the diameter of the solder ball (d) that fit into the area of the well (a rectangle of area $x \times y$). For simplicity, the number of circles that will fit in a given dimension x or y assumes a cubic packing pattern. A floor function is used to eliminate partial spheres because the solder powder size is significant with respect to the size of the well (*i.e.* only one $29\,\mu m$ sphere will fit in the y direction until $y > 58$). The copper pad is within the well area, so the constant area of the pad is multiplied by the density of a cubic lattice ($\pi/6$) and then subtracted from the total solder area. The final equation for the area of solder is

$$A = \left(\lfloor \frac{x}{d} \rfloor \times \lfloor \frac{y}{d} \rfloor \times \pi \times \left(\frac{d}{2} \right)^2 \right) - \left(1800 \times \frac{\pi}{6} \right) \tag{12.1}$$

where A is the area of solder in the two-dimensional model and the remaining variables are as indicated in Figure 12.15.

The area of solder will wet to the surface of the copper pad first. As the area increases it will grow in height, but the shape it takes is hard to define due to the internal forces of the liquid solder. The shape is simplified to be a triangle with a fixed base of $100\mu m$, the width of the pad. This assumption is quite generous since the solder shape will be much more rounded. Given this assumption, the height of the solder for a given well area is

$$h = \frac{A}{50} + 18 \tag{12.2}$$

which adds 18 to account for the height of the copper pad. The output of equation (12.2) is shown in Figure 12.17. From this data it is clear that a well width (x) close to the width of the copper pad ($100\,\mu m$) provides little chance for the solder to reach the top of the well to connect with the CMOS chip. The solder wells used in this work were exactly the same size as the copper pad, a possible explanation of the poor yield. When electrical connections were made, they had somewhat large resistances. The large resistances could be explained by a limited area of solder actually making contact between the pads. Future work with this packaging design should have the well be at

least 30% larger than the copper pad area for best results. Additionally, solder paste with a smaller powder size will generally increase the likelihood of achieving a height sufficient for contact.

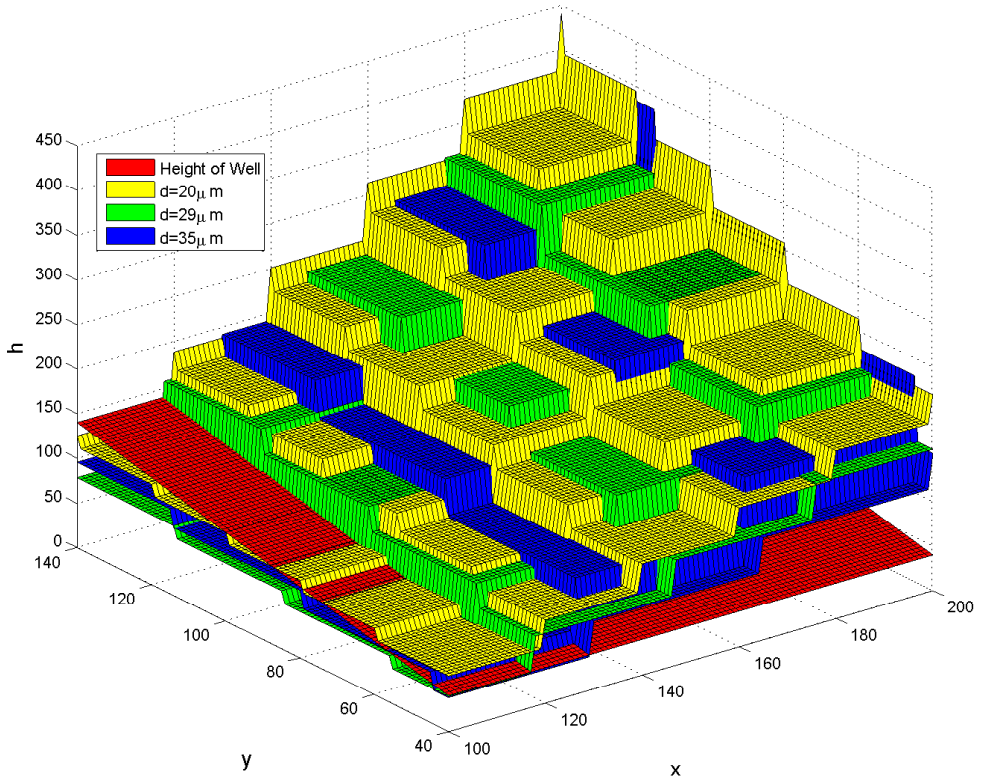

Figure 12.17: Plot of the estimated height of the solder in an SU-8 well with the given x and y dimensions for type 5 powder ($d = 20\,\mu m$), type 4 powder ($d = 29\,\mu m$), and type 3 powder ($d = 35\,\mu m$).

12.4 Discussion

This work presents a number of improvements over recent systems which interfaced microelectronic devices with microfluidics. Table 12.3 summarizes some distinguishing system parameters. Our design offers many advantages over other systems created to date. The integration of traditional soft lithography microfluidics with direct contact to microelectronic sensors is the most notable improvement.

Table 12.3: Comparison of CMOS and microfluidic integration methods

Packaging Method	Wire Bonds (W) or Flip Chip (F)	Number of Bond Pads Available (+/-)	Multiple Microfluidic Geometries (+/-)	Integrated Valves (Yes/No)	Direct Fluid Interaction (Yes/No)	Soft Lithography (Yes/No)	Number of Microfluidic Layers	Distance between Sensor and Microfluidics
[140]	W	-	-	N	Y	N	1	0
[142]	W	+	-	N	Y	N	-	0
[143]	W	+	+	Y	N	Y	No Limit	$2mm$
[144]	F	+	-	N	N	N	1	175μm
[145]	F	+	+	Y	Y	N	2	120μm
This Work	F	+	+	Y	Y	Y	No Limit	85μm

The demonstrated system provides flexibility in the choice of microfluidic features because of the modular assembly method. The structure of the microfluidics is independent of the electrical connections made; the only requirement is a testing chamber located over the sensing area of the chip. This flexibility also alleviates the problem of footprint mismatch between a CMOS chip and microfluidics. The microfluidic footprint is only limited by the flexible PCB area and is unrelated to the electrical connection placement.

This system design has many potential configurations to create lab-on-a-chip devices with multiple sensing areas. Multiple CMOS chips, each with a separate sensing, actuating, or stimulating function, could be joined to the same flexible PCB. Mi-

crofluidics could connect all of the exposed CMOS areas with channels and include pumps or mixers between them. The use of multiple, isolated sensing areas on the same CMOS chip is also a possibility. SU-8 can be patterned to create separate fluid wells in the same way the electrical connections isolate solder in this work. A well-designed arrangement of polyimide openings and associated microfluidics would make completely isolated fluid chambers on the same CMOS chip possible. This arrangement would allow for small signal detection through differential measurements on a single chip with associated signal processing.

Chapter 13

CONCLUSIONS

Multiple themes were present throughout this work. First, this work emphasized the necessity of good packaging design. Consideration of the operating environment in packaging enables seamless integration of microelectronics and sensors into biological systems. Second, this work delved into the theme of integrating different technologies for comprehensive interaction. Effectively interfacing sensors with readout circuits in a microscale biological environment enables complex systems. Finally, this work explored the control of sensor and microenvironment interaction. Tight microenvironment control opens numerous applications in biological processing. Tying these themes together when creating biological analysis systems can lead to nearly unlimited possibilities.

This work presented a number of unique contributions. Chapter 4 presented an original MEMS tilt sensor concept. The liquid pendulum design was inspired by the anatomy of the human vestibular system. The precision measurement of two-dimensional tilt is enabled by a differential measurement. The design is straightforward yet elegant, and the system is mechanically robust.

Much of the original research focused on ISFETs as pH sensitive devices. This work explored ISFETs fabricated in commercial CMOS and MEMS processes as well as extended gate devices independently fabricated within the lab. Chapter 8 demonstrated a theory for ISFET drift with both experimental and simulation results. These results indicated a method for producing a repeatable drift behavior. Chapter 10 exhibited an ISFET utilized in a complete feedback system which combined electronic sensing with microfluidic control. The system demonstrated control down to 0.12 pH

and real-time pH control. The system also showed long term control with minimal pH variation.

Significant contributions were made in CMOS system integration with microfluidics in Chapter 12. A new technique demonstrated seamless interfacing of CMOS with soft lithography. The new technique is an improvement over any existing system. The presented work advances the capabilities of using CMOS technology for biological analysis.

There is great potential in the integration of microelectronics, sensors, and microfluidics to form complete biological sensing systems. This dissertation presented a number of integration examples spanning from the whole-body level down to the molecular level. All of the systems demonstrated both the challenges and benefits of combining different areas of research which are often considered independently. While many systems have been addressed, there are numerous other possibilities to form complete sensor systems. As advances continue across the fields of microelectronics, sensors, and microfluidics, it will be important to continue to develop systems to combine these technologies.

REFERENCES

[1] R. G. Harrison, M. J. Greenman, F. P. Mall, and C. M. Jackson, "Observations of the living developing nerve fiber," *The Anatomical Record*, vol. 1, no. 5, pp. 116–128, 1907. [Online]. Available: http://dx.doi.org/10.1002/ar.1090010503

[2] Cell/tissue culture supplies market to exceed $6.0 billion by 2015, according to new report by global industry analysts, inc. [Online]. Available: http://www.prweb.com/releases/cell_culture _supplies/tissue_culture _supplies/prweb4640084.htm

[3] R. I. Freshney, *Culture of Animal Cells*. Wiley-Liss, 2005.

[4] J. Christen and A. Andreou, "Design, fabrication, and testing of a hybrid cmos/pdms microsystem for cell culture and incubation," *Biomedical Circuits and Systems, IEEE Transactions on*, vol. 1, no. 1, pp. 3 –18, march 2007.

[5] T. H. Park and M. L. Shuler, "Integration of cell culture and microfabrication technology," *Biotechnology Progress*, vol. 19, no. 2, pp. 243–253, 2003. [Online]. Available: http://dx.doi.org/10.1021/bp020143k

[6] H. Andersson and A. van den Berg, "Microfluidic devices for cellomics: a review," *Sensors and Actuators B: Chemical*, vol. 92, no. 3, pp. 315 – 325, 2003. [Online]. Available: http://www.sciencedirect.com/science/article/pii/S0925400503002661

[7] C. Yi, C.-W. Li, S. Ji, and M. Yang, "Microfluidics technology for manipulation and analysis of biological cells," *Analytica Chimica Acta*, vol. 560, no. 1-2, pp. 1 – 23, 2006. [Online]. Available: http://www.sciencedirect.com/science/article/pii/S0003267005020945

[8] T. Jain and J. Muthuswamy, "Bio-chip for spatially controlled transfection of nucleic acid payloads into cells in a culture," *Lab Chip*, vol. 7, pp. 1004–1011, 2007. [Online]. Available: http://dx.doi.org/10.1039/B707479D

[9] M. Ni, W. H. Tong, D. Choudhury, N. A. A. Rahim, C. Iliescu, and H. Yu, "Cell culture on mems platforms: A review," *International Journal of Molecular Sciences*, vol. 10, no. 12, pp. 5411–5441, 2009. [Online]. Available: http://www.mdpi.com/1422-0067/10/12/5411/

[10] J. El-Ali, P. K. Sorger, and K. F. Jensen, "Cells on chips," *Nature*, vol. 442, no. 7101, pp. 403–411, Jul. 2006. [Online]. Available: http://dx.doi.org/10.1038/nature05063

[11] G. Whitesides, E. Ostuni, S. Takayama, X. Jiang, and D. Ingber, "Soft lithography in biology and biochemistry," *ANNUAL REVIEW OF BIOMEDICAL ENGINEERING*, vol. 3, pp. 335–373, 2001.

[12] K. J. Regehr, M. Domenech, J. T. Koepsel, K. C. Carver, S. J. Ellison-Zelski, W. L. Murphy, L. A. Schuler, E. T. Alarid, and D. J. Beebe, "Biological implications of polydimethylsiloxane-based microfluidic cell culture," *Lab Chip*, vol. 9, pp. 2132–2139, 2009. [Online]. Available: http://dx.doi.org/10.1039/B903043C

[13] C.-W. Huang and G.-B. Lee, "A microfluidic system for automatic cell culture," *Journal of Micromechanics and Microengineering*, vol. 17, no. 7, p. 1266, 2007. [Online]. Available: http://stacks.iop.org/0960-1317/17/i=7/a=008

[14] G. Mehta, K. Mehta, D. Sud, J. Song, T. Bersano-Begey, N. Futai, Y. S. Heo, M.-A. Mycek, J. Linderman, and S. Takayama, "Quantitative measurement and control of oxygen levels in microfluidic poly(dimethylsiloxane) bioreactors during cell culture," *Biomedical Microdevices*, vol. 9, pp. 123–134, 2007, 10.1007/s10544-006-9005-7. [Online]. Available: http://dx.doi.org/10.1007/s10544-006-9005-7

[15] M. Polinkovsky, E. Gutierrez, A. Levchenko, and A. Groisman, "Fine temporal control of the medium gas content and acidity and on-chip generation of series of oxygen concentrations for cell cultures," *Lab Chip*, vol. 9, pp. 1073–1084, 2009. [Online]. Available: http://dx.doi.org/10.1039/B816191G

[16] J. Wegener, C. R. Keese, and I. Giaever, "Electric cell-substrate impedance sensing (ecis) as a noninvasive means to monitor the kinetics of cell spreading to artificial surfaces," *Experimental Cell Research*, vol. 259, no. 1, pp. 158 – 166, 2000. [Online]. Available: http://www.sciencedirect.com/science/article/pii/S001448270094919X

[17] C. Xiao, B. Lachance, G. Sunahara, and J. Luong, "An in-depth analysis of electric cell-substrate impedance sensing to study the attachment and spreading of mammalian cells," *Analytical Chemistry*, vol. 74, pp. 1333–1339, 2002.

[18] S. B. Prakash and P. Abshire, "On-chip capacitance sensing for cell monitoring applications," *Sensors Journal, IEEE*, vol. 7, no. 3, pp. 440 –447, 2007.

[19] L. Ceriotti, A. Kob, S. Drechsler, J. Ponti, E. Thedinga, P. Colpo, R. Ehret, and F. Rossi, "Online monitoring of balb/3t3 metabolism

and adhesion with multiparametric chip-based system," *Analytical Biochemistry*, vol. 371, no. 1, pp. 92 – 104, 2007. [Online]. Available: http://www.sciencedirect.com/science/article/pii/S0003269707004654

[20] E. Ghafar-Zadeh and M. Sawan, "A hybrid microfluidic/cmos capacitive sensor dedicated to lab-on-chip applications," *Biomedical Circuits and Systems, IEEE Transactions on*, vol. 1, no. 4, pp. 270 –277, 2007.

[21] P. J. Hung, P. J. Lee, P. Sabounchi, R. Lin, and L. P. Lee, "Continuous perfusion microfluidic cell culture array for high-throughput cell-based assays," *Biotechnology and Bioengineering*, vol. 89, no. 1, pp. 1–8, 2005. [Online]. Available: http://dx.doi.org/10.1002/bit.20289

[22] R. Gomez-Sjoberg, A. A. Leyrat, D. M. Pirone, C. S. Chen, and S. R. Quake, "Versatile, fully automated, microfluidic cell culture system," *Analytical Chemistry*, vol. 79, no. 22, pp. 8557–8563, 2007, pMID: 17953452. [Online]. Available: http://pubs.acs.org/doi/abs/10.1021/ac071311w

[23] B. Zhang, M.-C. Kim, T. Thorsen, and Z. Wang, "A self-contained microfluidic cell culture system," *Biomedical Microdevices*, vol. 11, pp. 1233–1237, 2009, 10.1007/s10544-009-9342-4. [Online]. Available: http://dx.doi.org/10.1007/s10544-009-9342-4

[24] E. Leclerc, Y. Sakai, and T. Fujii, "Cell culture in 3-dimensional microfluidic structure of pdms (polydimethylsiloxane)," *Biomedical Microdevices*, vol. 5, pp. 109–114, 2003, 10.1023/A:1024583026925. [Online]. Available: http://dx.doi.org/10.1023/A:1024583026925

[25] S.-M. Ong, C. Zhang, Y.-C. Toh, S. H. Kim, H. L. Foo, C. H. Tan, D. van Noort, S. Park, and H. Yu, "A gel-free 3d microfluidic cell culture system," *Biomaterials*, vol. 29, no. 22, pp. 3237 – 3244, 2008. [Online]. Available: http://www.sciencedirect.com/science/article/pii/S0142961208002664

[26] L. Kim, Y.-C. Toh, J. Voldman, and H. Yu, "A practical guide to microfluidic perfusion culture of adherent mammalian cells," *Lab Chip*, vol. 7, pp. 681–694, 2007. [Online]. Available: http://dx.doi.org/10.1039/B704602B

[27] Y. Xia and G. M. Whitesides, "Soft lithography," *Angewandte Chemie International Edition*, vol. 37, no. 5, pp. 550–575, 1998. [Online]. Available: http://dx.doi.org/10.1002/(SICI)1521-3773(19980316)37:5¡550::AID-ANIE550¿3.0.CO;2-G

[28] S. R. Quake and A. Scherer, “From micro- to nanofabrication with soft materials,” *Science*, vol. 290, no. 5496, pp. 1536–1540, 2000. [Online]. Available: http://www.sciencemag.org/content/290/5496/1536.abstract

[29] T. Thorsen, S. J. Maerkl, and S. R. Quake, “Microfluidic large-scale integration,” *Science*, vol. 298, no. 5593, pp. 580–584, 2002. [Online]. Available: http://www.sciencemag.org/content/298/5593/580.abstract

[30] R. Dai, R. Stein, B. Andrews, K. James, and M. Wieler, “Application of tilt sensors in functional electrical stimulation,” *Rehabilitation Engineering, IEEE Transactions on*, vol. 4, no. 2, pp. 63 –72, 1996.

[31] P. Minarro, P. Andujar, P. Garcia, and E. Toro, “A comparison of the spine posture among several sit-and-reach test protocols.” *J Sci Med Sport*, vol. 10, no. 6, pp. 456–462, 2007. [Online]. Available: http://ukpmc.ac.uk/abstract/MED/17298887

[32] Y.-L. Chen, “Application of tilt sensors in human-computer mouse interface for people with disabilities,” *Neural Systems and Rehabilitation Engineering, IEEE Transactions on*, vol. 9, no. 3, pp. 289 –294, 2001.

[33] B. L. Harrison, K. P. Fishkin, A. Gujar, C. Mochon, and R. Want, “Squeeze me, hold me, tilt me! an exploration of manipulative user interfaces,” in *Proceedings of the SIGCHI conference on Human factors in computing systems*, ser. CHI ’98. New York, NY, USA: ACM Press/Addison-Wesley Publishing Co., 1998, pp. 17–24. [Online]. Available: http://dx.doi.org.ezproxy1.lib.asu.edu/10.1145/274644.274647

[34] National Institute on Deafness and Other Communication Disorders. (2009). [Online]. Available: http://www.nidcd.nih.gov/health/hearing/coch.asp

[35] Johns Hopkins Medical Institutions. (2007, August) Electrical implant steadies balance disorder in animals. [Online]. Available: http://www.sciencedaily.com/releases/2007/08/070806112548.htm

[36] MedicaLook. (2009). [Online]. Available: http://www.medical-look.com/human_anatomy/organs/Inner_ear.html

[37] L. Tang, K. Zhang, S. Chen, G. Zhang, and G. Liu, “Mems inclinometer based on a novel piezoresistor structure,” *Microelectronics*

Journal, vol. 40, no. 1, pp. 78 – 82, 2009. [Online]. Available: http://www.sciencedirect.com/science/article/pii/S0026269208003157

[38] C. H. Lin and S. M. Kuo, "Micro-impedance inclinometer with wide-angle measuring capability and no damping effect," *Sensors and Actuators A: Physical*, vol. 143, no. 1, pp. 113 – 119, 2008. [Online]. Available: http://www.sciencedirect.com/science/article/pii/S0924424707006371

[39] J. H. Lee and S. S. Lee, "Electrolytic tilt sensor fabricated by using electroplating process," *Sensors and Actuators A: Physical*, vol. 167, no. 1, pp. 1 – 7, 2011. [Online]. Available: http://www.sciencedirect.com/science/article/pii/S092442471100015X

[40] H. Jung, C. J. Kim, and S. H. Kong, "An optimized mems-based electrolytic tilt sensor," *Sensors and Actuators A*, vol. 139, pp. 23–30, 2007.

[41] S. Billat, H. Glosch, M. Kunze, F. Hedrich, J. Frech, J. Auber, W. Lang, H. Sandmaier, and W. Wimmer, "Convection-based micromachined inclinometer using soi technology," in *Micro Electro Mechanical Systems, 2001. MEMS 2001. The 14th IEEE International Conference on*, 2001, pp. 159 –161.

[42] V. Milanović, E. Bowen, M. E. Zaghloul, N. H. Tea, J. S. Suehle, B. Payne, and M. Gaitan, "Micromachined convective accelerometers in standard integrated circuits technology," *Applied Physics Letters*, vol. 76, no. 4, pp. 508–510, 2000. [Online]. Available: http://link.aip.org/link/?APL/76/508/1

[43] D. Benz, T. Botzelmann, H. Kuck, and D. Warkentin, "On low cost inclination sensors made from selectively metallized polymer," *Sensors and Actuators A: Physical*, vol. 123-124, no. 0, pp. 18 – 22, 2005. [Online]. Available: http://www.sciencedirect.com/science/article/pii/S0924424705001974

[44] H. Ueda, H. Ueno, K. Itoigawa, and T. Hattori, "Micro capacitive inclination sensor utilizing dielectric nano-particles," in *Micro Electro Mechanical Systems, 2006. MEMS 2006 Istanbul. 19th IEEE International Conference on*, 2006, pp. 706 –709.

[45] L. Zhao and E. Yeatman, "Micro capacitive tilt sensor for human body movement detection," in *4th International Workshop on Wearable and Implantable Body Sensor Networks (BSN 2007)*, ser. IFMBE Proceedings, S. Leonhardt, T. Falck, and P. Mhnen, Eds. Springer Berlin Heidelberg, 2007, vol. 13, pp. 195–200.

[46] R. Yotter, R. Baxter, S. Ohno, S. Hawley, and D. Wilson, "On a micromachined fluidic inclinometer," *TRANSDUCERS*, 2003.

[47] O. Baltag, D. Costandache, and A. Salceanu, "Tilt measurement sensor," *Sensors and Actuators A: Physical*, vol. 81, no. 13, pp. 336 – 339, 2000. [Online]. Available: http://www.sciencedirect.com/science/article/pii/S0924424799001053

[48] B. Ando, A. Ascia, S. Baglio, and N. Savalli, "A novel ferrofluidic inclinometer," *Instrumentation and Measurement, IEEE Transactions on*, vol. 56, no. 4, pp. 1114 –1123, 2007.

[49] B. Ando, A. Ascia, and S. Baglio, "A ferrofluidic inclinometer in the resonant configuration," *Instrumentation and Measurement, IEEE Transactions on*, vol. 59, no. 3, pp. 558 –564, 2010.

[50] L. Rovati and S. Cattini, "Contactless two-axis inclination measurement system using planar flux-gate sensor," *Instrumentation and Measurement, IEEE Transactions on*, vol. 59, no. 5, pp. 1284 –1293, 2010.

[51] J. S. Bajic, D. Z. Stupar, L. M. Manojlovic, M. P. Slankamenac, and M. B. Zivanov, "A simple, low-cost, high-sensitivity fiber-optic tilt sensor," *Sensors and Actuators A: Physical*, vol. 185, no. 0, pp. 33 – 38, 2012. [Online]. Available: http://www.sciencedirect.com/science/article/pii/S0924424712004918

[52] Y. Zhao, J. Yang, B.-J. Peng, and S.-Y. Yang, "Experimental research on a novel fiber-optic cantilever-type inclinometer," *Optics & Laser Technology*, vol. 37, no. 7, pp. 555 – 559, 2005. [Online]. Available: http://www.sciencedirect.com/science/article/pii/S0030399204001653

[53] L. Amaral, O. Frazao, J. Santos, and A. Lobo Ribeiro, "Fiber-optic inclinometer based on taper michelson interferometer," *Sensors Journal, IEEE*, vol. 11, no. 9, pp. 1811 –1814, 2011.

[54] T. G. Constandinou, , and J. Georgiou, "Micro-optoelectromechanical tilt sensor," *Journal of Sensors*, 2008.

[55] H. Kato, M. Kojima, M. Gattoh, Y. Okumura, and S. Morinaga, "Photoelectric inclination sensor and its application to the measurement of the shapes of 3d objects," *Instrumentation and Measurement, IEEE Transactions on*, vol. 40, no. 6, pp. 1021 –1026, 1991.

[56] J.-H. Wu, K.-Y. Horng, S.-L. Lin, and R.-S. Chang, "A two-axis tilt sensor based on optics," *Measurement Science and Technology*, vol. 17, no. 4, p. N9, 2006. [Online]. Available: http://stacks.iop.org/0957-0233/17/i=4/a=N01

[57] R. Ragazzoni and S. R. Restaino, "An all-refractive optics for tilt sensing," *Optics Communications*, vol. 137, no. 13, pp. 6 – 10, 1997. [Online]. Available: http://www.sciencedirect.com/science/article/pii/S003040189782007X

[58] Z. Zhong, L. Zhao, and H. Lin, "Development and investigation of an optical tilt sensor," *Optics Communications*, vol. 261, no. 1, pp. 23 – 28, 2006. [Online]. Available: http://www.sciencedirect.com/science/article/pii/S0030401805012654

[59] C. R. Pollock, *Fundamentals of Optoelectronics*, 1st ed. Richard D. Irwin, Inc., 1995.

[60] C. L. Yaws, *Yaws' Thermophysical Properties of Chemicals and Hydrocarbons (Electronic Edition)*. Knovel, 2010.

[61] D. R. Lide, Ed., *CRC Handbook of Chemistry and Physics, 85th Edition*. CRC Press, 2004.

[62] B. Gilbert, "Translinear circuits: a proposed classification," *Electronics Letters*, vol. 11, no. 1, pp. 14 –16, 9 1975.

[63] U.S. Engergy Information Administration. [Online]. Available: http://www.eia.gov/cneaf/solar.renewables/page/solarphotv/table3_2.html

[64] J. Quero, C. Aracil, L. Franquelo, J. Ricart, P. Ortega, M. Dominguez, L. Castaner, and R. Osuna, "Tracking control system using an incident radiation angle microsensor," *Industrial Electronics, IEEE Transactions on*, vol. 54, no. 2, pp. 1207 –1216, 2007.

[65] C.-Y. Lee, P.-C. Chou, C.-M. Chiang, and C.-F. Lin, "Sun tracking systems: A review," *Sensors*, vol. 9, no. 5, pp. 3875–3890, 2009. [Online]. Available: http://www.mdpi.com/1424-8220/9/5/3875

[66] H. Mousazadeh, A. Keyhani, A. Javadi, H. Mobli, K. Abrinia, and A. Sharifi, "A review of principle and sun-tracking methods for maximizing solar systems output," *Renewable and Sustainable Energy Re-*

views, vol. 13, no. 8, pp. 1800 – 1818, 2009. [Online]. Available: http://www.sciencedirect.com/science/article/pii/S1364032109000318

[67] T. Bohnke, M. Edoff, and L. Stenmark, "Development of a moems sun sensor for space applications," *Sensors and Actuators A: Physical*, vol. 130-131, no. 0, pp. 28 – 36, 2006. [Online]. Available: http://www.sciencedirect.com/science/article/pii/S0924424705005510

[68] P. Ortega, G. Lopez-Rodriguez, J. Ricart, M. Dominguez, L. Castaner, J. Quero, C. Tarrida, J. Garcia, M. Reina, A. Gras, and M. Angulo, "A miniaturized two axis sun sensor for attitude control of nano-satellites," *Sensors Journal, IEEE*, vol. 10, no. 10, pp. 1623 –1632, oct. 2010.

[69] Zomeworks Corporation. [Online]. Available: http://www.zomeworks.com/photovoltaic-tracking-racks/

[70] C. de Boom, J. Leijtens, L. v. Duivenbode, and N. van der Heiden, "Micro digital sun sensor: System in a package," in *MEMS, NANO and Smart Systems, 2004. ICMENS 2004. Proceedings. 2004 International Conference on*, 2004, pp. 322 – 328.

[71] I. Maqsood and T. Akram, "Development of a low cost sun sensor using quad-photodiode," in *Position Location and Navigation Symposium (PLANS), 2010 IEEE/ION*, 2010, pp. 639 –644.

[72] A. Mäkynen, "Position-sensitive devices and sensor systems for optical tracking and displacement sensing applications," Ph.D. dissertation, University of Oulu, 2000. [Online]. Available: http://herkules.oulu.fi/isbn9514257804/isbn9514257804.pdf

[73] J. Wallmark, "A new semiconductor photocell using lateral photoeffect," *Proceedings of the IRE*, vol. 45, no. 4, pp. 474 –483, 1957.

[74] D. Qian, W. Wang, and I. Busch-Vishniac, "A method for measurement of multiple light spot positions on one position-sensitive detector (psd)," *Instrumentation and Measurement, IEEE Transactions on*, vol. 42, no. 1, pp. 14 –18, 1993.

[75] C. Liebe and S. Mobasser, "Mems based sun sensor," in *Aerospace Conference, 2001, IEEE Proceedings.*, vol. 3, 2001, pp. 3/1565 –3/1572 vol.3.

[76] C. Liebe, S. Mobasser, Y. Bae, C. Wrigley, J. Schroeder, and A. Howard, “Micro sun sensor,” in *Aerospace Conference Proceedings, 2002. IEEE*, vol. 5, 2002, pp. 5–2263 – 5–2273 vol.5.

[77] C. Liebe, “Solar compass chip,” *Sensors Journal, IEEE*, vol. 4, no. 6, pp. 779 – 786, 2004.

[78] F. Chen and J. Feng, “Analogue sun sensor based on the optical nonlinear compensation measuring principle,” *Measurement Science and Technology*, vol. 18, no. 7, p. 2111, 2007. [Online]. Available: http://stacks.iop.org/0957-0233/18/i=7/a=042

[79] W. D. Lubitz, “Effect of manual tilt adjustments on incident irradiance on fixed and tracking solar panels,” *Applied Energy*, vol. 88, no. 5, pp. 1710 – 1719, 2011. [Online]. Available: http://www.sciencedirect.com/science/article/pii/S030626191000471X

[80] E. Ghafar-Zadeh and M. Sawan, *CMOS Capacitive Sensors for Lab-on-Chip Applications*. Springer, 2010.

[81] E. Ghafar-Zadeh, M. Sawan, and D. Therriault, “A 0.18-[mu]m cmos capacitive sensor lab-on-chip,” *Sensors and Actuators A: Physical*, vol. 141, no. 2, pp. 454 – 462, 2008. [Online]. Available: http://www.sciencedirect.com/science/article/pii/S0924424707007054

[82] A. H. D. Graham, J. Robbins, C. R. Bowen, and J. Taylor, “Commercialisation of cmos integrated circuit technology in multi-electrode arrays for neuroscience and cell-based biosensors,” *Sensors*, vol. 11, no. 5, pp. 4943–4971, 2011. [Online]. Available: http://www.mdpi.com/1424-8220/11/5/4943/

[83] J. W. Ko, H. C. Koo, D. W. Kim, S. M. Seo, T. J. Kang, Y. Kwon, J. L. Yoon, J. H. Cheon, Y. H. Kim, J. J. Kim, and Y. J. Park, “Electroless gold plating on aluminum patterned chips for cmos-based sensor applications,” *Journal of The Electrochemical Society*, vol. 157, no. 1, pp. D46–D49, 2010. [Online]. Available: http://link.aip.org/link/?JES/157/D46/1

[84] M. Hino, K. Murakami, Y. Mitooka, K. Muraoka, and T. Kanadani, “Effects of zincate treatment on adhesion of electroless ni-p coating onto various aluminum alloys,” *Transactions of Nonferrous Metals Society of China*, vol. 19, no. 4, pp. 814 – 818, 2009. [Online]. Available: http://www.sciencedirect.com/science/article/pii/S1003632608603568

[85] D. A. Robinson, "The electrical properties of metal microelectrodes," *Proceedings of the IEEE*, vol. 56, pp. 1065–1071, 1968.

[86] R. C. Gesteland, B. Howland, J. Y. Lettvin, and W. H. Pitts, "Comments on microelectrodes," *Proceedings of the IEEE*, vol. 47, pp. 1856–1862, 1959.

[87] A. A. Werdich, E. A. Lima, B. Ivanov, I. Ges, M. E. Anderson, J. P. Wikswo, and F. J. Baudenbacher, "A microfluidic device to confine a single cardiac myocyte in a sub-nanoliter volume on planar microelectrodes for extracellular potential recordings," *Lab on a Chip*, vol. 4, pp. 357–362, 2004.

[88] J. Law, C. Yeung, B. Hofmann, S. Ingebrandt, J. Rudd, A. Offenhauser, and M. Chan, "The use of microelectrode array (MEA) to study the protective effects of potassium channel openers on the metabolically compromised HL-1 cardiomyocyte," *Physiological Measurement*, vol. 30, pp. 155–167, 2009.

[89] G. T. A. Kovacs, "Electronic sensors with living cellular components," *Proceedings of the IEEE*, vol. 91, pp. 915–929, 2003.

[90] E. P. Widmaier, *Vander's Human Physiology*. McGraw-Hill, 2006.

[91] D. A. Borkholder, "Cell-based biosensors using microelectrodes," Ph.D. dissertation, Stanford University, 1998.

[92] W. C. Claycomb, N. A. Lanson, B. S. Stallworth, D. B. Egeland, J. B. Delcarpio, A. Bahinski, and N. J. Izzo, "HL-1 cells: A cardiac muscle cell line that contracts and retains phenotypic characteristics of the adult cardiomyocyte," *Proceeding of the National Academy of Sciences, USA*, vol. 95, pp. 2979–2984, 1998.

[93] P. Bergveld, "Development of an ion-sensitive solid-state device for neurophysiological measurements," *Biomedical Engineering, IEEE Transactions on*, vol. BME-17, no. 1, pp. 70 –71, 1970.

[94] S. Jamasb, "An analytical technique for counteracting drift in ion-selective field effect transistors (isfets)," *Sensors Journal, IEEE*, vol. 4, no. 6, pp. 795 – 801, 2004.

[95] W. Wroblewski. Field effect transistors (fets) as transducers in electrochemical sensors. [Online]. Available: http://csrg.ch.pw.edu.pl/tutorials/isfet/

[96] L. Bousse, N. De Rooij, and P. Bergveld, “Operation of chemically sensitive field-effect sensors as a function of the insulator-electrolyte interface,” *Electron Devices, IEEE Transactions on*, vol. 30, no. 10, pp. 1263 – 1270, 1983.

[97] J.-L. Chiang, S.-S. Jan, J.-C. Chou, and Y.-C. Chen, “Study on the temperature effect, hysteresis and drift of ph-isfet devices based on amorphous tungsten oxide,” *Sensors and Actuators B: Chemical*, vol. 76, no. 1-3, pp. 624 – 628, 2001. [Online]. Available: http://www.sciencedirect.com/science/article/pii/S0925400501006578

[98] L. Bousse, H. van den Vlekkert, and N. de Rooij, “Hysteresis in al2o3-gate isfets,” *Sensors and Actuators B: Chemical*, vol. 2, no. 2, pp. 103 – 110, 1990. [Online]. Available: http://www.sciencedirect.com/science/article/pii/092540059080018U

[99] P. Hein and P. Egger, “Drift behaviour of isfets with si3n4-sio2 gate insulator,” *Sensors and Actuators B: Chemical*, vol. 14, no. 1-3, pp. 655 – 656, 1993. [Online]. Available: http://www.sciencedirect.com/science/article/pii/092540059385131S

[100] K.-M. Chang, C.-T. Chang, K.-Y. Chao, and C.-H. Lin, “A novel ph-dependent drift improvement method for zirconium dioxide gated ph-ion sensitive field effect transistors,” *Sensors*, vol. 10, no. 5, pp. 4643–4654, 2010. [Online]. Available: http://www.mdpi.com/1424-8220/10/5/4643/

[101] S. Jamasb, S. Collins, and R. L. Smith, “A physical model for drift in ph isfets,” *Sensors and Actuators B: Chemical*, vol. 49, no. 1-2, pp. 146 – 155, 1998. [Online]. Available: http://www.sciencedirect.com/science/article/pii/S0925400598000409

[102] Y. Dun, W. Ya-dong, and W. Gui-hua, “Time-dependent response characteristics of ph-sensitive isfet,” *Sensors and Actuators B: Chemical*, vol. 3, no. 4, pp. 279 – 285, 1991. [Online]. Available: http://www.sciencedirect.com/science/article/pii/092540059180018F

[103] A. Morgenshtein, L. Sudakov-Boreysha, U. Dinnar, C. G. Jakobson, and Y. Nemirovsky, “Cmos readout circuitry for isfet microsystems,” *Sensors and Actuators B: Chemical*, vol. 97, no. 1, pp. 122 – 131, 2004. [Online]. Available: http://www.sciencedirect.com/science/article/pii/S0925400503006919

[104] S. Casans, D. R. Munoz, A. Navarro, and A. Salazar, “Isfet drawbacks minimization using a novel electronic compensation,” *Sensors and Actuators B: Chemical*, vol. 99, no. 1, pp. 42 – 49, 2004. [Online]. Available: http://www.sciencedirect.com/science/article/pii/S092540050300741X

[105] D. Chen and P. Chan, “An intelligent isfet sensory system with temperature and drift compensation for long-term monitoring,” *Sensors Journal, IEEE*, vol. 8, no. 12, pp. 1948 –1959, 2008.

[106] I.-Y. Chung, H. Jang, J. Lee, H. Moon, S. M. Seo, and D. H. Kim, “Simulation study on discrete charge effects of sinw biosensors according to bound target position using a 3d tcad simulator,” *Nanotechnology*, vol. 23, no. 6, p. 065202, 2012. [Online]. Available: http://stacks.iop.org/0957-4484/23/i=6/a=065202

[107] A. van den Berg, “Ion sensors based on isfet’s with synthetic ionophores,” Ph.D. dissertation, 1988.

[108] J. van der spiegel, I. Lauks, P. Chan, and D. Babic, “The extended gate chemically sensitive field effect transistor as multi-species microprobe,” *Sensors and Actuators*, vol. 4, no. 0, pp. 291 – 298, 1983. [Online]. Available: http://www.sciencedirect.com/science/article/pii/0250687483850355

[109] T. Prodromakis, Y. Liu, and C. Toumazou, “A low-cost disposable chemical sensing platform based on discrete components,” *Electron Device Letters, IEEE*, vol. 32, no. 3, pp. 417 –419, march 2011.

[110] E. W. K. Young and D. J. Beebe, “Fundamentals of microfluidic cell culture in controlled microenvironments,” *Chem. Soc. Rev.*, vol. 39, pp. 1036–1048, 2010. [Online]. Available: http://dx.doi.org/10.1039/B909900J

[111] G. M. Walker, H. C. Zeringue, and D. J. Beebe, “Microenvironment design considerations for cellular scale studies,” *Lab Chip*, vol. 4, pp. 91–97, 2004. [Online]. Available: http://dx.doi.org/10.1039/B311214D

[112] K. Kirchhof, A. Andar, H. B. Yin, N. Gadegaard, M. O. Riehle, and T. Groth, “Polyelectrolyte multilayers generated in a microfluidic device with ph gradients direct adhesion and movement of cells,” *Lab Chip*, vol. 11, pp. 3326–3335, 2011. [Online]. Available: http://dx.doi.org/10.1039/C1LC20408D

[113] L. Ponsonnet, M. Boureanu, N. Jaffrezic, A. Othmane, C. Dorel, and P. Lejeune, “Local ph variation as an initial step in bacterial

surface-sensing and biofilm formation," *Materials Science and Engineering: C*, vol. 28, no. 5-6, pp. 896 – 900, 2008. [Online]. Available: http://www.sciencedirect.com/science/article/pii/S0928493107002160

[114] T. M. Keenan and A. Folch, "Biomolecular gradients in cell culture systems," *Lab Chip*, vol. 8, pp. 34–57, 2008. [Online]. Available: http://dx.doi.org/10.1039/B711887B

[115] G. B. Udy, R. P. Towers, R. G. Snell, R. J. Wilkins, S.-H. Park, P. A. Ram, D. J. Waxman, and H. W. Davey, "Requirement of stat5b for sexual dimorphism of body growth rates and liver geneexpression," *Proceedings of the National Academy of Sciences*, vol. 94, no. 14, pp. 7239–7244, 1997. [Online]. Available: http://www.pnas.org/content/94/14/7239.abstract

[116] Y. Yan, D. Yang, E. D. Zarnowska, Z. Du, B. Werbel, C. Valliere, R. A. Pearce, J. A. Thomson, and S.-C. Zhang, "Directed differentiation of dopaminergic neuronal subtypes from human embryonic stem cells," *STEM CELLS*, vol. 23, no. 6, pp. 781–790, 2005. [Online]. Available: http://dx.doi.org/10.1634/stemcells.2004-0365

[117] A. Folch and M. Toner, "Microengineering of cellular interactions," *ANNUAL REVIEW OF BIOMEDICAL ENGINEERING*, vol. 2, pp. 227+, 2000.

[118] D. E. Discher, D. J. Mooney, and P. W. Zandstra, "Growth factors, matrices, and forces combine and control stem cells," *Science*, vol. 324, no. 5935, pp. 1673–1677, 2009. [Online]. Available: http://www.sciencemag.org/content/324/5935/1673.abstract

[119] A. Rosenthal, A. Macdonald, and J. Voldman, "Cell patterning chip for controlling the stem cell microenvironment," *Biomaterials*, vol. 28, no. 21, pp. 3208 – 3216, 2007. [Online]. Available: http://www.sciencedirect.com/science/article/pii/S0142961207002402

[120] C. M. Metallo, J. C. Mohr, C. J. Detzel, J. J. de Pablo, B. J. Van Wie, and S. P. Palecek, "Engineering the stem cell microenvironment," *Biotechnology Progress*, vol. 23, no. 1, pp. 18–23, 2007. [Online]. Available: http://dx.doi.org/10.1021/bp060350a

[121] L.-M. Postovit, N. V. Margaryan, E. A. Seftor, D. A. Kirschmann, A. Lipavsky, W. W. Wheaton, D. E. Abbott, R. E. B. Seftor, and M. J. C. Hendrix, "Human embryonic stem cell microenvironment suppresses the tumorigenic

phenotype of aggressive cancer cells," *Proceedings of the National Academy of Sciences*, vol. 105, no. 11, pp. 4329–4334, 2008. [Online]. Available: http://www.pnas.org/content/105/11/4329.abstract

[122] E. K. Rofstad, "Microenvironment-induced cancer metastasis." *International Journal of Radiation Biology*, vol. 76, no. 5, pp. 589 – 605, 2000.

[123] M. Butler, "Animal cell cultures: recent achievements and perspectives in the production of biopharmaceuticals," *Applied Microbiology and Biotechnology*, vol. 68, pp. 283–291, 2005, 10.1007/s00253-005-1980-8. [Online]. Available: http://dx.doi.org/10.1007/s00253-005-1980-8

[124] P. Hossler, S. F. Khattak, and Z. J. Li, "Optimal and consistent protein glycosylation in mammalian cell culture," *Glycobiology*, vol. 19, no. 9, pp. 936–949, 2009. [Online]. Available: http://glycob.oxfordjournals.org/content/19/9/936.abstract

[125] The Lee Company. [Online]. Available: http://www.theleeco.com

[126] J. Bausells, J. Carrabina, A. Errachid, and A. Merlos, "Ion-sensitive field-effect transistors fabricated in a commercial cmos technology," *Sensors and Actuators B: Chemical*, vol. 57, no. 1-3, pp. 56 – 62, 1999. [Online]. Available: http://www.sciencedirect.com/science/article/pii/S0925400599001355

[127] B. Averill and P. Eldredge, *Chemistry: Principles, Patterns, and Applications*. Prentice Hall, 2006.

[128] E. Ghafar-Zadeh, M. Sawan, and D. Therriault, "Cmos based capacitive sensor laboratory-on-chip: a multidisciplinary approach," *Analog Integrated Circuits and Signal Processing*, vol. 59, pp. 1–12, 2009, 10.1007/s10470-008-9239-9. [Online]. Available: http://dx.doi.org/10.1007/s10470-008-9239-9

[129] R. Harrison and C. Charles, "A low-power low-noise cmos amplifier for neural recording applications," *Solid-State Circuits, IEEE Journal of*, vol. 38, no. 6, pp. 958 – 965, 2003.

[130] P. Bergveld and A. Sibbald, *Analytical and Biomedical Applications of Ion-Selective Field-Effect Transistors*, Svehla, Ed. Elsevier, 1988.

[131] B. Paln, F. V. Santos, J. M. Karam, B. Courtois, and M. Husk, "New isfet sensor interface circuit for biomedical applications," *Sensors and Actuators*

B: Chemical, vol. 57, no. 1-3, pp. 63 – 68, 1999. [Online]. Available: http://www.sciencedirect.com/science/article/pii/S0925400599001367

[132] J. Zhang, Y. Huang, N. Trombly, C. Yang, and A. Mason, "Electrochemical array microsystem with integrated potentiostat," in *Sensors, 2005 IEEE*, 30 2005-nov. 3 2005, p. 4 pp.

[133] R. B. Northrop, *Introduction to Instrumentation and Measurement*. CRC Press, 1997.

[134] M. Haider, M. Mahfouz, S. Islam, S. Eliza, W. Qu, and E. Pritchard, "A low-power capacitance measurement circuit with high resolution and high degree of linearity," pp. 261 –264, 2008.

[135] H. Lee, D. Ham, and R. M. Westervelt, Eds., *CMOS Biotechnology*. Springer, 2007.

[136] H. Becker, "All i want for christmas..." *Lab Chip*, vol. 11, pp. 1571–1573, 2011. [Online]. Available: http://dx.doi.org/10.1039/C1LC90025K

[137] P. Man, D. Jones, and C. Mastrangelo, "Microfluidic plastic capillaries on silicon substrates: a new inexpensive technology for bioanalysis chips," in *Micro Electro Mechanical Systems, 1997. MEMS '97, Proceedings, IEEE., Tenth Annual International Workshop on*, 1997, pp. 311 –316.

[138] A. Rasmussen, M. Gaitan, L. Locascio, and M. Zaghloul, "Fabrication techniques to realize cmos-compatible microfluidic microchannels," *Microelectromechanical Systems, Journal of*, vol. 10, no. 2, pp. 286 –297, 2001.

[139] M. Agirregabiria, F. J. Blanco, J. Berganzo, M. T. Arroyo, A. Fullaondo, K. Mayora, and J. M. Ruano-Lopez, "Fabrication of su-8 multilayer microstructures based on successive cmos compatible adhesive bonding and releasing steps," *Lab Chip*, vol. 5, pp. 545–552, 2005. [Online]. Available: http://dx.doi.org/10.1039/B500519A

[140] E. Ghafar-Zadeh, M. Sawan, and D. Therriault, "Novel direct-write cmos-based laboratory-on-chip: Design, assembly and experimental results," *Sensors and Actuators A: Physical*, vol. 134, no. 1, pp. 27 – 36, 2007. [Online]. Available: http://www.sciencedirect.com/science/article/pii/S0924424706003712

[141] H. Lee, Y. Liu, D. Ham, and R. M. Westervelt, "Integrated cell manipulation system-cmos/microfluidic hybrid," *Lab Chip*, vol. 7, pp. 331–337, 2007. [Online]. Available: http://dx.doi.org/10.1039/B700373K

[142] L. Li and A. Mason, "Post-cmos parylene packaging for on-chip biosensor arrays," in *Sensors, 2010 IEEE*, nov. 2010, pp. 1613 –1616.

[143] J. Chediak, Z. Luo, J. Seo, N. Cheung, L. P. Lee, and T. D. Sands, "Heterogeneous integration of cds filters with gan leds for fluorescence detection microsystems," *Sensors and Actuators A: Physical*, vol. 111, no. 1, pp. 1 – 7, 2004, ¡ce:title¿Micromechanics section of Sensors and Actuators, based on contributions revised from the Technical Digest of the 16th IEEE International conference on Micro Electro mechanical Systems (MEMS 2003)¡/ce:title¿. [Online]. Available: http://www.sciencedirect.com/science/article/pii/S0924424703005272

[144] L. Hartley, K. V. I. S. Kaler, and O. Yadid-Pecht, "Hybrid integration of an active pixel sensor and microfluidics for cytometry on a chip," *Circuits and Systems I: Regular Papers, IEEE Transactions on*, vol. 54, no. 1, pp. 99 –110, jan. 2007.

[145] A. Wu, L. Wang, E. Jensen, R. Mathies, and B. Boser, "Modular integration of electronics and microfluidic systems using flexible printed circuit boards," *Lab Chip*, vol. 10, pp. 519–521, 2010. [Online]. Available: http://dx.doi.org/10.1039/B922830F

[146] R. Wimberger-Friedl, T. Nellissen, W. Weekamp, J. van Delft, W. Ansems, M. Prins, M. Megens, W. Dittmer, C. de Witz, and B. van Iersel, "Packaging of silicon sensors for microfluidic bio-analytical applications," *Journal of Micromechanics and Microengineering*, vol. 19, no. 1, 2009. [Online]. Available: http://stacks.iop.org/0960-1317/19/i=1/a=015015

[147] J. H. Lau, Ed., *Flip Chip Technologies*. McGraw-Hill, 1996.

[148] S. Serra, A. Schneider, K. Malecki, S. Huq, and W. Brenner, "A simple bonding process of su-8 to glass to seal microfluidic device." Proceedings 3rd International Conference on Multi-Material Micro Manufacture, October 2007. [Online]. Available: http://www.4m-net.org/files/papers/4M2007/367308/PID367308.pdf

[149] L. Tang and N. Y. Lee, “A facile route for irreversible bonding of plastic-pdms hybrid microdevices at room temperature,” *Lab Chip*, vol. 10, pp. 1274–1280, 2010. [Online]. Available: http://dx.doi.org/10.1039/B924753J

[150] K. Aran, L. A. Sasso, N. Kamdar, and J. D. Zahn, “Irreversible, direct bonding of nanoporous polymer membranes to pdms or glass microdevices,” *Lab Chip*, vol. 10, pp. 548–552, 2010. [Online]. Available: http://dx.doi.org/10.1039/B924816A

[151] M.-E. Vlachopoulou, A. Tserepi, P. Pavli, P. Argitis, M. Sanopoulou, and K. Misiakos, “A low temperature surface modification assisted method for bonding plastic substrates,” *Journal of Micromechanics and Microengineering*, vol. 19, no. 1, p. 015007, 2009. [Online]. Available: http://stacks.iop.org/0960-1317/19/i=1/a=015007

BIOGRAPHICAL SKETCH

David Welch is a PhD candidate in Biomedical Engineering at Arizona State University. In 2008, David joined the Bio Electrical Systems and Technology Laboratory as a graduate research assistant to Dr. Jennifer Blain Christen. While working as a graduate research assistant, David received an Arizona State University Biodesign Institute Graduate Research Fellowship, a Science Foundation Arizona Graduate Fellowship, and a National Science Foundation (NSF) GK-12 Fellowship. Prior to attending Arizona State University, David received a B.S. in Biomedical Engineering at Tulane University in 2007. David received a M.S. from Arizona State University in 2011. David will conclude the requirements for his Ph.D. in Biomedical Engineering in December 2012. David is active in science community outreach. As an NSF GK-12 Fellow, David worked as a biology teaching fellow at Superior High School, where he developed and published lesson plans focused on inquiry-based learning. Over the past three years, he has also volunteered as an Arizona Middle School Science Bowl Moderator, an Eta Kappa Nu Middle School Electrical Engineering Outreach Volunteer, and a National Nanotechnology Infrastructure Network Mentor. Since joining Dr. Blain Christen's laboratory, David's contributions have been widely recognized. In 2008, David's submission to the Stimulation Action on MEMS (STIMESI) International Design Contest won the Advanced Category. In 2010, David achieved first place in the Science Foundation Arizona Grand Challenges Conferences Poster Session.